A Lagrangian study of inhomogeneous turbulence

Nickolas Stelzenmuller

Communauté
UNIVERSITÉ Grenoble Alpes

THÈSE
pour obtenir le grade de

DOCTEUR DE LA COMMUNAUTE UNIVERSITÉ DE GRENOBLE-ALPES

Spécialité:
Mecanique des Fluides, Procedes, Energetique
Arrêté ministériel : 25 mai 2016

Présentée par

Nickolas STELZENMULLER

Thèse dirigée par:
M. Nicolas MORDANT, PROFESSEUR
UNIVERSITÉ DE GRENOBLE-ALPES

preparée au sien du
Laboratoire des Ecoulements Géophysiques et Industriels
École doctorale: **IMEP-2**

Étude Lagrangienne d'une turbulence inhomogène

Thèse soutenue publiquement le **20 octobre, 2017**
devant le jury composé de:

M. Emmanuel LÉVÊQUE, Rapporteur
Directeur de recherche , LMFA, École Centrale de Lyon

M. Nicholas T. OUELLETTE, Rapporteur
Associate Professor, Stanford University

M. Alain CARTELLIER,
Directeur de recherche, LEGI, Université de Grenoble-Alpes

Mme. Anne TANIÈRE,
Professeur, LEMTA, Université de Lorraine
Presidente de jury

M. Romain VOLK,
Maître de conférences, ENS Lyon

A Lagrangian study of inhomogeneous turbulence

Abtstract: Inhomogeneous turbulence is experimentally investigated in a Lagrangian framework. Measurements of tracer and non-tracer particles in a turbulent channel were made, and were used to extract Lagrangian statistics conditioned on their initial distance to the channel wall. Highly resolved in time and space, these measurements provide the three components of position, velocity, and acceleration along a particle trajectory from very close to the channel wall ($y^+ \approx 10$) to the channel center. Lagrangian time correlations allow the direct measurement of velocity and acceleration timescales in each direction, and characterize the inhomogeneity and anisotropy of the turbulent channel from the Lagrangian perspective. Small scale-anisotropy, characterized by the skewness and the correlation of the components of the acceleration, was found to be significant throughout the channel. Significant scale separation between the magnitude and components of acceleration was found across the channel, even in the near-wall region. Two classes of non-tracer particle trajectories were also measured, allowing direct comparison of tracer and non-tracer statistics from the highly-sheared anisotropic zone near the channel wall to the more homogeneous outer layer. Non-tracer acceleration statistics in the turbulent channel were found to be significantly different from similar results in homogeneous, isotropic turbulence. These statistics are necessary components of advanced Lagrangian stochastic models to predict dispersion and mixing in inhomogeneous turbulence.

Keywords: Turbulence, Lagrangian, Turbulent Channel, 3-D PTV

Résumé: Une turbulence inhomogène est étudiée expérimentalement dans un contexte lagrangien. La mesure des trajectoires de traceurs lagrangiens et de particules inertielles a été effectuée dans un canal plan turbulent et a été utilisée pour obtenir des statistiques lagrangiennes conditionnées à leur distance initiale par rapport à la paroi. Ces mesures à haute résolution en temps et en espace fournissent les trois composantes de la position, la vitesse et l'accélération le long de la trajectoire d'une particule individuelle depuis des distances très proches de la paroi (10 unités de paroi) jusqu'au centre du canal. Les corrélations temporelles lagrangiennes ont permis la mesure directe des échelles de temps de la vitesse et l'accélération dans chacune des trois directions. Ces échelles caractérisent l'inhomogénéité et l'anisotropie du canal turbulent dans une perspective lagrangienne. Une anisotropie à petite échelle, quantifiée par la "skewness", et les corrélations entre composantes de l'accélération sont observées dans tout le canal. Une séparation d'échelle significative entre les composantes de l'accélération et son amplitude a été mesurée au travers du canal notamment dans la zone proche de la paroi. Deux classes de particules inertielles ont été étudiées permettant ainsi la comparaison directe entre statistiques des traceurs et des non-traceurs dans la zone de fort cisaillement et de forte anisotropie proche de la paroi jusqu'à la région plus homogène du centre. Les propriétés statistiques des particules inertielles dans le canal turbulent sont significativement différentes de celles observées en turbulence homogène isotrope. Ces statistiques sont les ingrédients nécessaires à la construction de modèles stochastiques lagrangiens pour la prédiction de la dispersion et du mélange en turbulence inhomogène.

Mots-clés: Turbulence, Lagrangien, Canal turbulent, 3-D PTV

Acknowledgments

When I arrived at LEGI to start my PhD I spoke no French, but was determined to learn. As I began setting up the experiment, my fumbling attempts at communication led to a series of comical sketches, in which the long suffering technicians and staff were subjected to my extremely bad French supplemented with gestures. The humor, patience, and generosity with which I was received was remarkable, and will remain a fond memory for a long time to come.

In addition to their warm welcome, the technical expertise of Laure Vignal, Joseph Virone, Mile Kusulja, Gaby Moreau, Samuel Viboud, and Jean-Paul Thibault was invaluable to the success of the experiments.

Nicolas Mordant and I spent many an agreeable hour puzzling over the often counter-intuitive Lagrangian properties of turbulence. In my moments of self-doubt and discouragement(of which there were a few), his evident intellectual curiosity and enthusiasm for our subject were very encouraging.

I would like to thank the co-authors of the article that appears in this thesis, especially Juan Ignacio Polanco and Ivana Vinkovic, for their permission to include the article. It was a real pleasure to discuss and collaborate with them on this project.

Special thanks to Philippe Marmottant and Nicolas Plihon for the gracious loan of their high-speed cameras, without which these experiments would not have been possible.

Many thanks to the members of the thesis committee, especially the referees Emmanuel Lévêque and Nicholas Ouellette. Their time, insightful comments, and kind words at the thesis defense were very much appreciated.

My colleagues at LEGI, many of whom became close friends, provided discussion, a helping hand, technical support, and encouragement. The solidarity and conviviality I found among the PhD students and post-docs was a joy.

Finally, I would like to thank my partner Steph for her acceptance of my long nights at the lab, her encouragement when I was discouraged, and especially her unflagging faith in me.

To my mother, whose courage and perseverance showed me the way . . .

Contents

List of figures

List of Tables

Motivation

Our eyes are instinctively drawn to motion. Watching snowflakes in a storm, dust caught in a ray of sunlight, or leaves on the surface of a river can be almost hypnotic. This is turbulence as understood by children—following a bubble as it dances in the air. This intuitive view of turbulence is formalized by Lagrangian kinematics, which follows a particle trajectory in time.

The study of turbulence in a Lagrangian framework is not new: G. I. Taylor formulated a theory of the dispersion of particles in turbulence using a Lagrangian framework in 1921, and more sophisticated Lagrangian models for dispersion have been developed since. Nevertheless it is only in the last 20 years, with the development of new measuring technologies and increased computing power, that we have able to directly observe small particles in turbulence at high resolution. Measuring particle trajectories over time allows us to observe how the position, velocity, and acceleration evolve along the particle trajectory—how the particle experiences the turbulence. Statistics formed from these measurements provide a Lagrangian statistical description of turbulence. For example, statistics of the velocity along the trajectory at two times separated by a time-lag may be measured, e. g.

$$v(t) - v(t + \Delta t) \tag{1}$$

The shape of the probability density function of this Lagrangian velocity increment is approximately Gaussian for large Δt, but is increasingly non-Gaussian as Δt is decreased. For very small values of Δt the velocity increment is closely related to the acceleration:

$$a \equiv \lim_{\Delta t \to 0} \frac{v(t + \Delta t) - v(t)}{\Delta t} \tag{2}$$

which is a strongly intermittent quantity: accelerations up to *50 times* the root-mean-square acceleration have been measured experimental. Statistics in the time-correlations of velocity and acceleration, for example

$$\frac{a(t + \Delta t)\, a(t)}{\langle a^2 \rangle} \tag{3}$$

also provide a useful Lagrangian description of turbulence. The velocity decorrelates relatively slowly, and is directly related to the dispersion of fluid particles from a point-source in turbulence. Acceleration decorrelates rapidly, although the correlation of the magnitude of acceleration decays quite slowly in comparison.

Models of varying complexity have been proposed to explain and/or predict these observations. For example, multifractal models formulated in a Lagrangian framework have been used to predict the increasingly non-Gaussian distributions of the velocity increment, and of acceleration. Stochastic dispersion models use time-correlations of velocity and acceleration to recreate fluid particle trajectories. Multifractal random walk, and acceleration-orientation random walk models predict the rapid decorrelation of acceleration and the slow decorrelation of the magnitude of acceleration.

The vast majority of Lagrangian experiments, simulations, and models have focused on homogeneous isotropic turbulence (HIT). The symmetries of high-Reynolds number, homogeneous, isotropic turbulence create a simplified academic framework in which to study turbulence. Models developed in this framework may then be adapted, with varying degrees of success, to the more complicated, realistic cases of lower-Reynolds number, inhomogeneous, anisotropic turbulence. In order to adapt models developed in HIT to more realistic contexts, we must first understand how inhomogeneous turbulence differs from HIT. Inhomogeneous turbulence has long been studied from a practical perspective, as many engineering applications involve wall-bounded turbulence. Almost all of this work has considered inhomogeneous turbulence in an Eulerian framework. From the Lagrangian perspective we know very little about inhomogeneous turbulence. There are many open questions, e. g. in a wall-bounded turbulent flow, how do Lagrangian statistics change with distance to the wall? At what distance to the wall is statistical isotropy reestablished? Are Lagrangian statistics more or less susceptible to the large scale inhomogeneity than Eulerian statistics?

In addition to the behavior of the fluid turbulence, behavior of non-tracer particles in turbulence is also of considerable interest. A wide range of practical applications are concerned with how particles interact with turbulence. Non-tracer particles diverge from fluid particle trajectories, but where and how this divergence occurs is not fully known. Models and mechanisms have been proposed for some classes of particles, e. g. very small, heavy particles, but again, almost all of our understanding relates to particle dynamics in homogeneous isotropic turbulence.

This thesis attempts to respond to these gaps in our knowledge. We use the instruments and techniques developed in the last 20 years of high-resolution Lagrangian measurements and apply them to a turbulent channel flow. The turbulent channel flow in which these measurements were taken is a stationary, moderate-Reynolds number turbulent flow with a single direction of inhomogeneity. This relatively simple configuration allows the measurement of Lagrangian statistics from the highly sheared, strongly anisotropic near-wall region to the quasi-homogeneous center of the channel. Tracer particle measurements allow the extraction of Lagrangian statistics of the fluid turbulence. Two classes of non-tracer particles were also measured, allowing us to explore the effects of inhomogeneity on non-tracer particle statistics.

This thesis is organized as follows. Chapter 1 introduces fundamental concepts in turbulence, provides an overview of previous Lagrangian investigations in homogeneous turbulence, briefly outlines turbulent channel flow, and gives a survey of Lagrangian stochastic modeling. The experimental details are given in chapter 2, which also provides a discussion of the design and constraints involved in such measurements. Eulerian tracer particle results in the turbulent channel are presented in chapter 3, with a focus on the one-time statistics of acceleration across the turbulent channel. Chapter 4 presents Lagrangian results in position, velocity, and acceleration for tracer particles. Finally, non-tracer particles are considered in chapter 5.

Chapter 1

Introduction and Theory

> Moreover, I soon understood that there was little hope of developing a pure, closed theory, and because of the absence of such a theory the investigation must be based on hypotheses obtained in processing experimental data
>
> *A. N. Kolmogorov*

Contents

1.1 Fluid turbulence from a Lagrangian point of view

1.1.1 What is turbulence?

The dynamics of incompressible Newtonian fluids are given by the deceptively simple equations for the conservation of fluid mass

$$\frac{\partial \mathrm{U}_i}{\partial x_i} = 0 \tag{1.1}$$

and momentum

$$\frac{\mathrm{D}\mathrm{U}_i}{\mathrm{D}t} = -\frac{1}{\rho}\frac{\partial \mathrm{P}}{\partial x_i} + \nu\frac{\partial^2 \mathrm{U}_i}{\partial x_j \partial x_j} \tag{1.2}$$

where ρ and ν are the fluid material properties of density and kinematic viscosity, respectively (taken here to be constant), and U and P are the dynamical quantities of fluid velocity and pressure. Despite being compact and apparently simple, these equations model an incredible array of phenomenon encountered in natural and man-made systems, from the evolution of galaxies[6] down to the flow of fluid within a living cell.

It has long been observed that fluid flows are either calm and viscous or energetic and chaotic. In a classic experiment [7] Reynolds found that these two states of the flow—called laminar and turbulent, respectively—could be seen in water flowing through a glass pipe by changing what became known as the Reynolds number. The Reynolds number is the non-dimensional parameter that controls the transition between a laminar flow and a turbulent flow, and is written as

$$\mathrm{Re} = \frac{\mathscr{U}\mathscr{L}}{\nu} \tag{1.3}$$

where $\mathscr{U}$ and $\mathscr{L}$ are characteristic velocity and length scales of the flow. This parameter represents the balance between inertial forces and viscous forces, which may be seen directly when equation 1.2 is scaled with characteristic length and velocity scales $u^* = \mathrm{U}/\mathscr{U}$, $x^* = x/\mathscr{L}$, and $t^* = t/(\mathscr{L}/\mathscr{U})$:

$$\frac{\mathrm{D}\mathrm{U}_i^*}{\mathrm{D}t^*} = -\frac{1}{\rho}\frac{\partial p}{\partial x_i^*}\frac{1}{\mathscr{U}^2} + \frac{1}{\mathrm{Re}}\frac{\partial^2 \mathrm{U}_i^*}{\partial x_j^* \partial x_j^*} \tag{1.4}$$

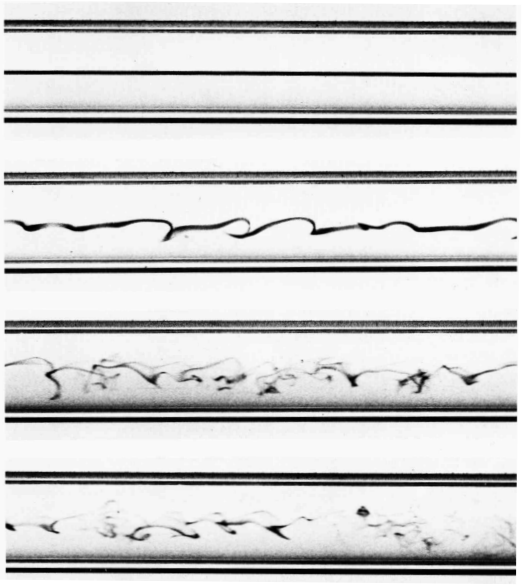

Figure 1.1: A streak of dye in a glass pipe at four Reynolds numbers, from laminar (top) to turbulent (bottom) flow. This photograph is of a recreation of Reynolds' classic experiment of 1883 using the original apparatus, made by N. H. Johannesen and C. Lowe. Reproduced from the collection of Van Dyke[5].

Reynolds found that for low-Reynolds-number conditions dye injected in the flow did not mix with the flow, implying that there were steady streamlines parallel to the direction of the flow. In fact, the momentum equation (also called the Navier-Stokes equations and abbreviated as N-S) admits an analytical solution for this problem: a parabolic streamwise profile that does not vary in time or streamwise direction. However, at a certain Reynolds number this system transitions to a turbulent state, which is characterized by a time-dependent velocity profile and mixing of the injected dye, shown in figure 1.1

In the years since Reynolds first quantified the differences between these two states in fluid flow many researchers have found common characteristics in a wide variety of turbulent flows. Turbulence has resisted a formal definition[8], but characteristics common to all turbulent flows include

1. **Randomness**: Instantaneous turbulent quantities are not predictable. The N-S equation is a deterministic equation that amplifies small perturbations at high Reynolds numbers. This is a qualitative explanation for the two very different flow states described above—at low Reynolds numbers small perturbations are damped by viscosity, and at high Reynolds numbers these perturbations are amplified. Deterministic systems with a high sensitivity to initial conditions are not predictable. However, statistical properties of multiple realizations may be stable and predictable, i. e. the instantaneous velocity $u_i(x_i, t)$ is not predictable, but the average velocity at that point and time over many realizations—the ensemble average $\langle u_i(x_i, t)\rangle$ is stable and may be predicted. This quality of turbulence motivates a statistical approach.

2. **Large range of interacting scales**: Turbulence is characterized by a wide range of scales, from the large scales that arise from external considerations such flow boundaries to small scales at which dissipation occurs. Interaction between scales is non-local and non-linear, a point which will be discussed further in the following section.

3. **Turbulence is dissipative and strongly diffusive**: Turbulence dissipates kinetic energy into heat, and is thus a thermodynamically irreversible process. Not coincidentally it is also very efficient at mixing. These two qualities are typically the aspects of turbulence important from a practical engineering perspective, resulting in costly turbulent friction in pipelines, but also highly effective mixing in industrial applications.

1.1.2 Turbulence theory

Lagrangian-Eulerian kinematics

The derivation of the Navier-Stokes equation for incompressible flow from first principles may be found in many textbooks[9, 10], and will not be reproduced here. Explicit in this derivation is the concept of a fluid particle, i. e. an infinitesimal material element which is accelerated by forces in accordance with Newton's second law. The fluid particle traces out a fluid-particle trajectory over time in response to external forces. If the individual fluid particles in a system of n fluid particles are arbitrarily labeled a_i for $i = 1...n$ then the material coordinate is defined as $\mathbf{X}(a_i, t)$. This fluid-particle path is also called a Lagrangian trajectory, and the first and second time derivatives may be taken to find the velocity and acceleration of the fluid particle

$$\frac{\partial \mathbf{X}(a_i, t)}{\partial t} = \mathbf{V}(a_i, t) \qquad \frac{\partial^2 \mathbf{X}(a_i, t)}{\partial t^2} = \mathbf{A}(a_i, t) \tag{1.5}$$

the latter of which is simply the time history of the external forces acting on the fluid particle a_i. This is the Lagrangian perspective, and arises naturally from Newtonian dynamics. Fluid particle trajectories are commonly labeled by their position $\mathbf{x}$ at some time t_0, convieniently written as $\mathbf{x}_0$. For example the Lagrangian position is written as $\mathbf{X}(\mathbf{x}_0, t|t_0)$. This labeling relates the Lagrangian and Eulerian positions as

$$\mathbf{x}_0 = \mathbf{X}(\mathbf{x}_0, t_0|t_0) \tag{1.6}$$

While the fluid particle kinematics are naturally considered from a Lagrangian perspective, the forces acting on a fluid particle depend on the local spatial gradients, which are best expressed from an inertial reference frame, i. e. the Eulerian perspective. Flow variables in this perspective are defined point-wise in space and time, for example the Eulerian velocity field $\mathbf{U}(\mathbf{x}, t)$. The Eulerian velocity is equal to the Lagrangian velocity at $\mathbf{x} = \mathbf{x}_0$ and $t = t_0$

$$\mathbf{V}(\mathbf{x}_0, t_0 | t_0) = \mathbf{U}(\mathbf{x}, t)|_{\mathbf{x}=\mathbf{x}_0,\ t=t_0} \tag{1.7}$$

a concept illustrated in the sketch shown here. This implies the general relation between Lagrangian and Eulerian expressions, written here in velocity

$$\mathbf{V}(\mathbf{x}_0, t | t_0) = \mathbf{U}(\mathbf{X}(\mathbf{x}_0, t | t_0), t) \tag{1.8}$$

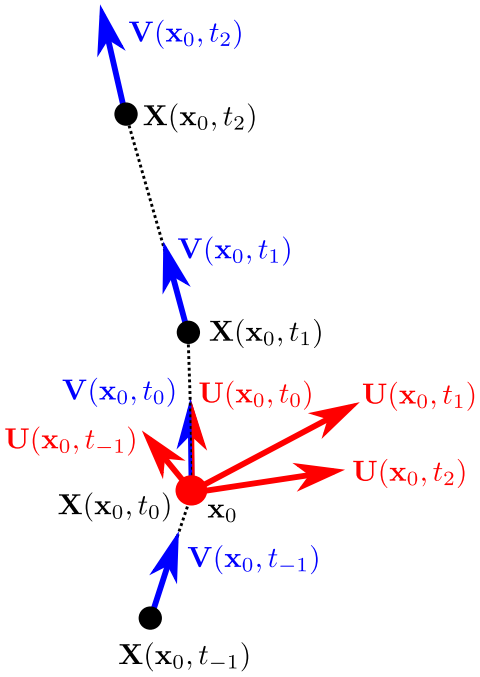

The Lagrangian acceleration $\mathbf{A}$ may be expressed in terms of the Eulerian velocity field

$$\mathbf{A}(\mathbf{x}_0, t | t_0) = \frac{\partial \mathbf{V}(\mathbf{x}_0, t | t_0)}{\partial t} \overset{eqn1.8}{=} \frac{\partial \mathbf{U}(\mathbf{X}(\mathbf{x}_0, t | t_0), t)}{\partial t} = \left[\frac{\partial \mathbf{U}(\mathbf{x}, t)}{\partial \mathbf{x}} \frac{\partial \mathbf{X}(\mathbf{x}_0, t | t_0)}{\partial t} + \frac{\partial \mathbf{U}(\mathbf{x}, t)}{\partial t} \frac{\partial t}{\partial t} \right]_{\mathbf{x}=\mathbf{X}(\mathbf{x}_0, t | t_0)} \tag{1.9}$$

considering the terms in the last expression

$$\left. \frac{\partial \mathbf{U}(\mathbf{x}, t)}{\partial \mathbf{x}} \right|_{\mathbf{x}=\mathbf{X}(\mathbf{x}_0, t | t_0)} = \nabla \mathbf{U}(\mathbf{x}, t)|_{\mathbf{x}=\mathbf{X}(\mathbf{x}_0, t | t_0)} \tag{1.10}$$

and

$$\frac{\partial \mathbf{X}(\mathbf{x}_0, t | t_0)}{\partial t} = \mathbf{V}(\mathbf{x}_0, t | t_0) = \mathbf{U}(\mathbf{x}, \mathbf{t})|_{\mathbf{x}=\mathbf{X}(\mathbf{x}_0, t | t_0)} \tag{1.11}$$

so equation 1.9 may be written as

$$\mathbf{A}(\mathbf{x}_0, t | t_0) = \left[\frac{\partial \mathbf{U}(\mathbf{x}, t)}{\partial t} + (\mathbf{U}(\mathbf{x}, \mathbf{t}) \cdot \nabla) \mathbf{U}(\mathbf{x}, \mathbf{t}) \right]_{\mathbf{x}=\mathbf{X}(\mathbf{x}_0, t | t_0)} = \left. \frac{\mathrm{D}\mathbf{U}(\mathbf{x}, t)}{\mathrm{D}t} \right|_{\mathbf{x}=\mathbf{X}(\mathbf{x}_0, t | t_0)} \tag{1.12}$$

or equivalently in completely Eulerian terms

$$\mathbf{A}(\mathbf{x}, t) = \frac{\partial \mathbf{U}(\mathbf{x}, t)}{\partial t} + (\mathbf{U}(\mathbf{x}, \mathbf{t}) \cdot \nabla) \mathbf{U}(\mathbf{x}, \mathbf{t}) \tag{1.13}$$

This development is shown here in order to stress that acceleration is a fundamentally Lagrangian quantity, and that the non-linearity of the N-S equation, the term $(\mathbf{U} \cdot \nabla)\mathbf{U}$, arises from the change in reference frame.

A statistical approach to turbulence

The random nature of turbulence motivates a statistical approach, in which the quantities of interest are not the instantaneous variables but the statistics of an ensemble of realizations. A classic example of this approach is the decomposition of variables into mean and fluctuating components, e. g. the Eulerian velocity $\mathrm{U}_i(x_i, t)$ and pressure $\mathrm{P}(x_i, t)$

$$\mathrm{U}_i(x_i, t) = \langle \mathrm{U}_i(x_i, t) \rangle + u_i(x_i, t) \qquad \mathrm{P}(x_i, t) = \langle \mathrm{P}(x_i, t) \rangle + p(x_i, t) \tag{1.14}$$

This decomposition is known as the Reynolds decomposition, and may be substituted into the N-S equations, here written without the explicit dependence on x_i and t for convenience

$$\frac{\partial}{\partial t}(\langle \mathrm{U}_i \rangle + u_i) + \frac{\partial}{\partial x_j}(\langle \mathrm{U}_i \rangle + u_i)\,(\langle \mathrm{U}_j \rangle + u_j) = \frac{-1}{\rho}\frac{\partial}{\partial x_i}(\langle \mathrm{P} \rangle + p) + \nu \frac{\partial^2}{\partial x_j \partial x_j}(\langle \mathrm{U}_i \rangle + u_i) \quad (1.15)$$

or

$$\frac{\partial \langle \mathrm{U}_i \rangle}{\partial t} + \frac{\partial u_i}{\partial t} + \frac{\partial}{\partial x_j}\langle \mathrm{U}_i \rangle \langle \mathrm{U}_j \rangle + \frac{\partial}{\partial x_j} u_i \langle \mathrm{U}_j \rangle + \frac{\partial}{\partial x_j}\langle \mathrm{U}_i \rangle u_j + \frac{\partial}{\partial x_j} u_i u_j = \frac{-1}{\rho}\frac{\partial \langle \mathrm{P} \rangle}{\partial x_i} + \frac{-1}{\rho}\frac{\partial p}{\partial x_i} + \nu \frac{\partial^2 \langle \mathrm{U}_i \rangle}{\partial x_j \partial x_j} + \nu \frac{\partial^2 u_i}{\partial x_j \partial x_j} \quad (1.16)$$

Writing the N-S equation with the Reynolds decomposition show clearly the terms that depend only on the mean flow topology, those that depend only on the fluctuating quantities, and those that depend on the interaction of the mean and fluctuating quantities. The ensemble average of equation 1.16 may be taken, and all terms containing a single fluctuating term go to zero by construction[1], leaving

$$\frac{\partial \langle \mathrm{U}_i \rangle}{\partial t} + \frac{\partial}{\partial x_j}\langle \mathrm{U}_i \rangle \langle \mathrm{U}_j \rangle + \frac{\partial}{\partial x_j}\langle u_i u_j \rangle = \frac{-1}{\rho}\frac{\partial \langle \mathrm{P} \rangle}{\partial x_i} + \nu \frac{\partial^2 \langle \mathrm{U}_i \rangle}{\partial x_j \partial x_j} \quad (1.17)$$

The above equation appears to be quite similar to the unaveraged N-S equation, with the exception of the term containing the mean of the product of the fluctuating velocities, $\langle u_i u_j \rangle$. This quantity, called the Reynolds tensor, it is a fundamental statistical quantity in the Eulerian analysis of turbulence that has a direct effect on the mean velocity (through equation 1.17), contains the turbulent kinetic energy ($\frac{1}{2}u_i u_i$), and contains information regarding turbulent anisotropy (in the off-diagonal components).

In the frame of a fluid particle the evolution of the kinetic energy per unit mass[2] $\mathrm{E} \equiv \frac{1}{2}\mathrm{U}_i \mathrm{U}_i$ of the fluid particle is simply the inner product of the fluid particle velocity and acceleration

$$\frac{\partial \mathrm{E}(\mathbf{x_0}, t|t_0)}{\partial t} = \mathbf{A}(\mathbf{x_0}, t|t_0) \cdot \mathbf{V}(\mathbf{x_0}, t|t_0) \quad (1.18)$$

In an Eulerian framework this evolution of kinetic energy is found by multiplying the N-S equation (equation 1.2) by the Eulerian velocity $\mathrm{U}_i(x_i, t)$ as follows.

$$\mathrm{U}_i \frac{\mathrm{D}\mathrm{U}_i}{\mathrm{D}t} = \mathrm{U}_i \left[-\frac{1}{\rho}\frac{\partial p}{\partial x_i} + \nu \frac{\partial^2 \mathrm{U}_i}{\partial x_j \partial x_j} \right] \quad (1.19)$$

A Reynolds decomposition separates the energy associated with the mean flow $\overline{\mathrm{E}} = \frac{1}{2}\langle \mathrm{U}_i \rangle^2$ and the turbulent kinetic energy $k = \frac{1}{2}\langle u_i u_i \rangle$. Development equations for these two quantities may be formed[3] from equation 1.19, resulting in

[1] also using the the fact that the ensemble average and differentiation operators commute.

[2] For the flow in which density is constant it is convenient to refer to the kinetic energy as one half the square of the velocity, leaving the "per unit mass" implied.

[3] For a full derivation see chapter 5 of *Turbulent Flows*[10]

$$\underbrace{\frac{1}{2}\frac{\partial \overline{\mathrm{E}}}{\partial t} + \langle \mathrm{U}_j \rangle \frac{\overline{\mathrm{E}}}{\partial x_j}}_{\text{Change in } \overline{\mathrm{E}}} + \underbrace{\frac{\partial}{\partial x_j}\left[\langle \mathrm{U}_i \rangle \langle u_i u_j \rangle + \frac{1}{\rho}\langle \mathrm{U}_j \rangle \langle \mathrm{P} \rangle \delta_{ij} - \nu \frac{\partial \overline{\mathrm{E}}}{\partial x_j} \right]}_{\text{Transport of } \overline{\mathrm{E}}}$$

$$= \underbrace{\langle u_i u_j \rangle \frac{\partial \langle \mathrm{U}_i \rangle}{\partial x_j}}_{\text{Production of } k} - \underbrace{\nu \left[\frac{\partial \langle \mathrm{U}_i \rangle}{\partial x_j} \frac{\partial \langle \mathrm{U}_i \rangle}{\partial x_j} \right]}_{\text{Dissipation due to mean flow}} \tag{1.20}$$

$$\underbrace{\frac{\partial k}{\partial t} + \langle \mathrm{U}_j \rangle \frac{\partial k}{\partial x_j}}_{\text{Change in } k} + \underbrace{\frac{\partial}{\partial x_j}\left[\langle u_j u_i u_i \rangle + \frac{1}{\rho}\langle u_i p \rangle \delta_{ij} - \nu \frac{\partial k}{\partial x_j} \right]}_{\text{Transport of } k} = \underbrace{-\langle u_i u_j \rangle \frac{\partial \langle \mathrm{U}_i \rangle}{\partial x_j}}_{\text{Production of } k} - \underbrace{\nu \left\langle \frac{\partial u_i}{\partial x_j} \frac{\partial u_i}{\partial x_j} \right\rangle}_{\text{Turbulent dissipation } \epsilon} \tag{1.21}$$

Equations 1.20 and 1.21 describe the evolution of kinetic energy in a turbulent flow, and are examined more closely in section 1.2 in the context of turbulent channel flow. Qualitatively, the interaction between the Reynolds stress and the mean-flow gradient transfer kinetic energy from the mean flow to the turbulence, where the kinetic energy is dissipated as heat by viscous friction. The dissipation of kinetic energy implies that a constant level of kinetic energy in a control volume requires the injection of energy into the control volume. This energy injection drives the mean flow and, by the the production term in equation 1.20, injects energy into the turbulence. The structure of this energy from its injection into the turbulence to its dissipation into heat is the subject of an important theory of statistical turbulence published by Kolmogorov in 1941.

Kolmogorov's 1941 theory of turbulence (K41)

In a series of papers[4] Kolmogorov proposed that in fluid turbulence with large Reynolds numbers the small scales of the turbulence becomes universal. This universality[5] implies a scaling based on dimensional analysis for the scales at which viscous dissipation occurs. These scales are therefore independent of the large scales in the turbulence.

$$\eta = \left(\frac{\nu^3}{\epsilon}\right)^{1/4} \quad \text{Dissipation length scale} \tag{1.22}$$

$$\tau_\eta = \left(\frac{\nu}{\epsilon}\right)^{1/2} \quad \text{Dissipation time scale} \tag{1.23}$$

$$u_\eta = (\nu\epsilon)^{1/4} \quad \text{Dissipation velocity scale} \tag{1.24}$$

where ν is the kinematic viscosity of dimension $[\mathrm{L}]^2[\mathrm{T}]^{-1}$ and

ϵ is the mean dissipation rate of dimension $[\mathrm{L}]^2[\mathrm{T}]^{-3}$

Further, there are range of scales small enough to be universal but too large to be affected by viscous dissipation. This *inertial range* is given as $\eta \ll l \ll l_0$, where l_0 is the large length scale of the turbulence. Turbulence statistics in the inertial range are self-similar, i. e. they

[4] The works of Kolmogorov are introduced and put in context quite clearly by Frisch in *Turbulence*[11]

[5] Which includes the assumption of local homogeneity and isotropy, more formally described as a restoration of statistical symmetries of the N-S equation, see [11]

depend only the scale l and of the mean rate of change of kinetic energy ϵ . The scale l is examined precisely with the longitudinal Eulerian structure function, defined as

$$S_p(l) \equiv \langle [(\mathbf{u}(\mathbf{r}+\mathbf{l},t) - \mathbf{u}(\mathbf{r},t)) \cdot \mathbf{l}/l]^p \rangle \tag{1.25}$$

Dimensional analysis requires

$$S_p(l) = C_p \epsilon^{p/3} l^{p/3} \quad \text{for } \eta \ll l \ll l_0 \tag{1.26}$$

Where C_p is dimensionless. For the case of $p = 3$ the exact result $C_3 = -4/5$ was derived directly from the Navier-Stokes equation and the assumptions of global homogeneity and isotropy. There is no similar theoretical result for the value of C_2, but a large body of experimental evidence has confirmed the validity of the scaling $S_2 \propto \epsilon^{2/3} l^{2/3}$. This relation may be interpreted as the amount of turbulent kinetic energy at a given length scale l.

For $p \neq 3$, and especially for $p > 3$ this scaling is complicated by the intermittency of turbulent dissipation. Refinements to K41 have been proposed, some of which are reviewed in the following section.

Kolmogorov developed this theory in the Eulerian framework, but an analogous relation was developed for the Lagrangian structure function by Obukhov and Landau[12] using the approximation[6] $\tau = \mathbf{r}/\delta\mathbf{u}(\mathbf{r})$. The Lagrangian structure function is defined as

$$S_p^L(\tau) \equiv \langle |\mathbf{V}(\mathbf{x}_0, t_0+\tau) - \mathbf{V}(\mathbf{x}_0, t_0)|^p \rangle \tag{1.27}$$

K41 predicts the scaling

$$S_p^L(\tau) \propto (\epsilon\tau)^{p/2} \quad \text{for } \tau_\eta \ll \tau \ll T_L \tag{1.28}$$

For $p = 2$ the Lagrangian structure function is commonly written as

$$S_2^L(\tau) = a_0 \epsilon^{3/2} \nu^{-1/2} \tau^2 \quad \text{for } \tau \ll \tau_\eta \tag{1.29}$$

$$S_2^L(\tau) = C_0 \epsilon \tau \quad \text{for } \tau_\eta \ll \tau \ll T_L \tag{1.30}$$

where T_L is the Lagrangian time scale, and a_0, C_0 are non-dimensional constants

This scaling in the Lagrangian structure function may be seen in the Lagrangian autocorrelation

$$\rho_L(\tau) \equiv \langle V(\mathbf{x}_0, t_0+\tau) V(\mathbf{x}_0, t_0) \rangle \tag{1.31}$$

using the kinematic relationship in stationary HIT:

$$S_2^L(\tau) = 2\langle u^2 \rangle [1 - \rho_L(\tau)] \tag{1.32}$$

The Kolmogorov scaling in shown in equation 1.30 implies that

$$\rho_L(\tau) = 1 - \frac{a_0 \epsilon^{3/2} \nu^{-1/2} \tau^2}{2\langle u^2 \rangle} \quad \text{for } \tau \ll \tau_\eta \tag{1.33}$$

$$\rho_L(\tau) = 1 - \frac{C_0 \epsilon \tau}{2\langle u^2 \rangle} \quad \text{for } \tau_\eta \ll \tau \ll T_L \tag{1.34}$$

Some results regarding the scaling of acceleration can be deduced using the kinematic relationship (valid for stationary statistics):

$$\langle a(\mathbf{x}_0, t_0+\tau) a(\mathbf{x}_0, t_0) \rangle = -\langle u^2 \rangle \frac{d^2}{d\tau^2} \rho_L(\tau) \tag{1.35}$$

using the scaling in equations 1.33-1.34 the autocorrelation of acceleration is

$$\langle a(t_0+\tau) a(t_0) \rangle = a_0 \epsilon^{3/2} \nu^{-1/2} \quad \text{for } \tau \ll \tau_\eta \tag{1.36}$$

$$\langle a(t_0+\tau) a(t_0) \rangle = 0 \quad \text{for } \tau \gg \tau_\eta \tag{1.37}$$

[6] Falkovich *et al*[13] offers an interesting recent discussion of the validity of this assumption and its implications for Lagrangian statistics.

This lack of dependence of the autocorrelation of acceleration[7] on the time lag τ is reflected in the constant curvature of the velocity autocorrelation in figure 1.2, and zero -correlation in the inertial range implies that acceleration is a fundamentally small-scale quantity with a time correlation approximately equal to the Kolmogorov time scale τ_η. The form of the autocorrelation of acceleration is not predicted from K41, although as the derivative of a stationary process the integral scale is expected to be zero in HIT[14].

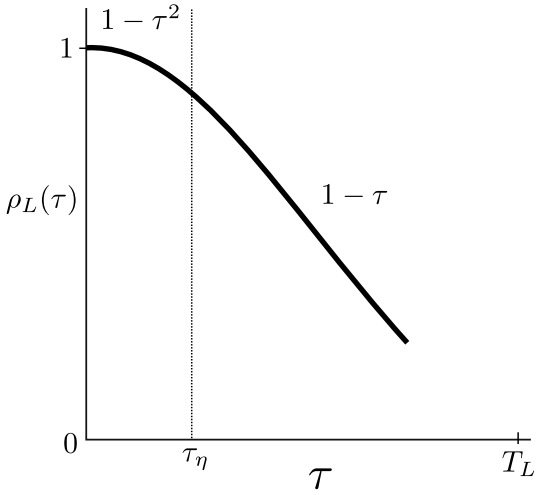

Figure 1.2: Schematic view of the Kolmogorov quadratic and linear scaling of the velocity autocorrelation.

The limits and extensions of K41

K41 predicts statistical similarity of velocity increments in the inertial range for HIT. Since the introduction of K41 many experimental results have shown that these statistics are scale dependent. This dependence may be seen in the results of Mordant *et al*[1] for the Lagrangian velocity increment, shown in figure 1.3. The evolution of the PDF of the normalized velocity increment $v(t_0+\tau)-v(t_0)$ from $\tau \approx T_L$ (approaching Gaussian) to $\tau \approx \tau_\eta$ (highly non-Gaussian) shows that these Lagrangian statistics are not self-similar in the inertial range. This lack of self-similarity is known as internal intermittency, and is known be greater in the Lagrangian framework[15]. Explanations of the behavior shown in figure 1.3 represent an active field of study in turbulence research.

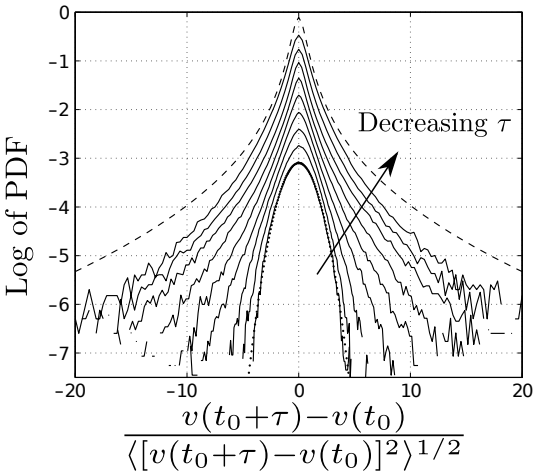

Figure 1.3: The probability density function of the normalized velocity increment for several values of τ. The dotted line represents the distribution of acceleration. Reproduced from Mordant *et al*[1].

The reason why K41 fails to capture the intermittency is that it implicitly assumes a constant dissipation rate in the structure function scaling shown in equation 1.26; an assumption made clear by noting that $\langle\epsilon^{p/3}\rangle \neq \langle\epsilon\rangle^{p/3}$ for $p \neq 3$ unless $\epsilon = \langle\epsilon\rangle$. Kolmogorov and Obukhov attempted to address this shortcoming by conditioning the scaling shown in equation 1.26 on the local instantaneous value of the dissipation rate volume averaged on the scale l, written here as ϵ_l

$$\langle[(\mathbf{u}(\mathbf{r}+\mathbf{l},t)-\mathbf{u}(\mathbf{r},t))\cdot\mathbf{l}/l]^p|\epsilon_l\rangle = C_p(\epsilon_l l)^{p/3} \tag{1.38}$$

and then modeling the distribution of ϵ as a function of scale. This approach, known as K62, is notable for two reasons. First, it directly links the instantaneous viscous dissipation—a small-scale scale quantity—with the scales in the inertial range. Second, it requires knowledge of the the distribution of ϵ_l, which general must be modeled and is related to the large scales of the turbulence. Kolmogorov suggested that the dissipation has a log-normal distribution, the specification of which allows the calculation of $\epsilon^{p/3}$ from $\langle\epsilon\rangle$. This approach has been

[7] The acceleration variance is simply equation 1.36 at $\tau = 0$, and is also referred to as the Heisenberg-Yaglom relation

used to collapse Lagrangian velocity increments[16] similar to those shown in figure 1.3, and used in the superstatistical approach[17, 18].

Another notable approach to intermittency is the multifractal model, which models the scaling exponent ζ_p in the Eulerian structure function

$$S_p(l) \sim l^{\zeta_p} \tag{1.39}$$

The exponent $\zeta_p(p)$ has been shown experimentally to have the following qualities: for $\zeta_p = 1$ at $p = 3$, confirming the exact result of Kolmogorov; approximately linear behavior at $p \leq 3$, reflecting the fact that K41 provides a close approximation for lower order statistics; and $\zeta_p(p)$ is increasingly curved for $p > 3$ reflecting the scale dependence of higher order statistics (e. g. the shape of the PDFs shown in figure 1.3). Note that for K41 ζ_p is linear in p: $\zeta_p = p/3$ (equation 1.28), and for K62[8]predicts a curved function: $\zeta_p = p/3 + \mu/18(3p - p^2)$, where $\mu \approx 0.2$ is thought to be universal.

The multifractal model attempts to predict this curved ζ_p in a universal manner without specifying the distribution of ϵ. The underlying idea is that turbulence has a range of fractal dimensions D that is scale dependent. The distribution of this dimension $D(h)$, where h is the scale, is thought to be universal. As a consequence the scaling of $S_p(l)$ is a superposition of power laws over the range of scales:

$$S_p(l) \sim l^{ph_1} l^{3-D(h_1)} + ph_2 l^{3-D(h_2)} + ...ph_n l^{3-D(h_n)} \tag{1.40}$$

$D(h)$ is not generally known a priori, and must be modeled and/or measured directly[20]. Multifractal formalism has been extended to the Lagrangian framework and provides a unified description of turbulence in the inertial and dissipative ranges[21, 22].

1.1.3 Turbulence investigations in the Lagrangian framework

As suggested by the quotation of A. N. Kolmogorov that opens this chapter, the study of turbulence has been largely driven by experimental investigation. Since the pioneering experiments of Reynolds the development of experimental methods have allowed researchers to measure turbulent quantities with ever increasing spatial and temporal resolution. Historically these instruments and techniques were focused on Eulerian measurements; instruments and techniques enabling Lagrangian measurements in turbulence are a relatively recent[9] development.

Fluid particle trajectories may be measured experimentally by measuring the position of a tracer particle over time, or extracted from a direct numerical simulation (DNS) of turbulence. The experimental system used in this study, an optical particle tracking velocimetry system than uses high-speed cameras to record tracer particle positions, is fairly typical of modern experimental Lagrangian measurements. DNS solves the N-S equations directly over a large grid of positions, such that all scales of the turbulence are resolved. Fluid particle trajectories are then integrated from the calculated Eulerian velocity field that is highly resolved in x, y, z, t (See e.g. Yeung[24] for details), allowing the extraction of high resolution Lagrangian statistics. Such simulations are computationally expensive for large Reynolds numbers, but increasingly available computational resources have allowed DNS at Reynolds numbers($Re_\lambda = 1000$) similar to many experiments[25].

[8] Following the assumption of the log-normality of ϵ, see e.g. Davidson[19] for this derivation

[9]With a few notable exceptions, among them a study of relative dispersion in the atmosphere by Richardson in 1922[23], in which balloons were released containing messages asking the finders to note where the balloons landed and to send Richardson the location by postcard.

Turbulence statistics may be divided, somewhat arbitrarily, into the following four categories, each of which corresponds to different measurements methods, and each of which is related to different areas of turbulence research:

Eulerian

- **One-point statistics**: A measurement at a single point, e.g. by a hot-wire or pitot tube. The "frozen turbulence" hypothesis of Taylor is often used with these measurement to deduce two-point statistics.
- **Many- point statistics**: Simultaneous measurements at two or more locations, which allow direct measurement of spatial structure. Modern optical measurement methods, such as particle image velocimetry (PIV), allow direct field measurements.

Lagrangian

- **Single-particle statistics**: The trajectory of a single particle. Typically measured optically (e. g. PTV) but at low particle-seeding levels.
- **Many-particle statistics**: Many *simultaneous* trajectory, such that the measurement of particle separation distance over time, the coherence of groups of particles over time (e. g. tetrads), etc., are possible. These statistics are typically measured with techniques similar to those used to measure single-particle statistics, but they require relatively high particle-seeding levels.

All four categories of statistics may be measured at a variety of temporal and spatial resolutions, depending on the measurement method and instrumentation used. Access to these statistics has allowed researchers to test theories and explore phenomena in turbulence. For example K41 was based on and supported by high-resolution hot wire measurements, which, using Taylor's frozen turbulence hypothesis, furnished Eulerian structure function statistics in the inertial range. Coherent structures and their role in turbulence were elucidated using PIV measurements, which allowed spatially resolved measurements of the velocity and vorticity fields.

Similarly, the more recently available high-resolution Lagrangian measurements allow the exploration of questions regarding fluid particle velocity and acceleration. The following discussion will focus on results related to single-particle statistics, which are also the focus of the present study.

Lagrangian velocity statistics in HIT

K41 in the Lagrangian framework predicts

$$\langle |\mathbf{V}(\mathbf{x}_0, t_0+\tau) - \mathbf{V}(\mathbf{x}_0, t_0)|^p \rangle \propto (\epsilon\tau)^{p/2} \quad \text{for } \tau_\eta \ll \tau \ll T_L \tag{1.41}$$

in the limit of large Reynolds numbers, but leaves many open questions. At what range of Reynolds is this scaling observed? What are the values of the proportionality constants, especially C_0?[10] How is the Lagrangian timescale T_L related to other turbulence quantities, such as more easily measured Eulerian statistics? These questions have important implications for Lagrangian modeling(discussed in more depth in section 1.3), as C_0, T_L, and Re_λ are basic ingredients of these models. A variety of experimental and DNS measurements have been reported, clearly summarized by Lien and D'Asaro[26]. A more recent DNS

[10] Where C_0 is the proportionality constant when $p = 2$

from Sawford and Yeung[27] consider the second-order K41 scaling over a wide range Reynolds numbers ($Re_\lambda = 43 - 1000$). C_0 is found to increase with Reynolds number, even at the relatively high Reynolds that have been tested. This result is consistent with the observation that the Eulerian inertial range is greater than the Lagrangian inertial range for a given Reynolds number.

The anomalous scaling of equation 1.1.3 was previously evidenced in the lack of self-similarity in the PDFs of the velocity increments shown in figure 1.3. This anomolous scaling is commonly written as

$$\langle |\mathbf{V}(\mathbf{x}_0, t_0 + \tau) - \mathbf{V}(\mathbf{x}_0, t_0)|^p \rangle \propto (\epsilon\tau)^{\xi_p^L} \tag{1.42}$$

Scaling exponents in the inertial range were measured directly by Mordant *et al*[1] and Xu *et al*[15], and were found to deviate more strongly from K41 (non-intermittent) values than the equivalent Eulerian exponents. While the power law scaling in equation 1.42 is expected in the inertial range $\tau_\eta \ll \tau \ll T_L$, it does not necessarily hold when $\tau \sim \tau_\eta$. Biferale *et al*[28] and Arneodo *et al*[22] report measurements from several dataset of the quantity

$$\zeta_p(\tau) = \frac{d\log[S_p^L(\tau)]}{d\log[S_2^L(\tau)]} \tag{1.43}$$

i. e the logarithmic derivative of the structure function of order p, normalized by the logarithmic derivative of the structure function of order 2. $\zeta_p(\tau)$ is a way of quantifying the deviation from non-intermittent behavior *at each scale* τ. Both groups report strong intermittence at $\tau/\tau_\eta \approx 2$. Intermittency of Lagrangian structure functions at small time-lags is closely related to the observed intermittency of fluid particle acceleration, as Lagrangian velocity increments at small times are closely related to fluid particle acceleration by the definition

$$\mathbf{a} \equiv \lim_{\tau \to 0} \frac{\mathbf{v}(\tau) - \mathbf{v}(0)}{\tau} \tag{1.44}$$

Acceleration in HIT

The acceleration of a fluid particle is proportional to the sum of the forces acting on the particle, and arises directly from the N-S equation. As such a fundamental quantity, as well as for its importance to Lagrangian stochastic modeling[29](discussed in below in section 1.3), the statistical properties of the fluid particle acceleration in turbulence have been studied extensively. Experimental[30, 31] and numerical[16, 32] studies have measured fluid particle accelerations, which were found to have "thick-tail", highly non-Gaussian distributions. Specifically, accelerations up to 50 times greater than the root-mean-square value have been measured[31]. The distribution of the acceleration may be inferred from the multi-fractal model, and agrees closely with experimental[31] and DNS[33] results.

The variance of acceleration has a scaling derived from K41 (equation 1.37), suggesting a universal constant a_0 exists at high Reynolds numbers. Sawford *et al*[34] assembled a several datasets to examine the dependence of a_0 on Reynolds number, and did not find evidence that a_0 is independent of Re_λ for $Re_\lambda < 1000$.

The autocorrelations of acceleration components were found to have short decorrelation times with respect to the autocorrelation of the magnitude of acceleration[35, 16]. Evidence for a connection between intense acceleration events and vortex filaments[36] suggests the difference between the correlation times of an acceleration component and the acceleration magnitude may be explained vortex trapping: in which a fluid particle has a relatively long-lived helical motion that follows a small vortical structure. As the particle

moves around the axis of rotation of the vortex, the acceleration direction decorrelates rapidly, but the acceleration magnitude stays relatively correlated. Further evidence of that vortex filaments are related to the intermittency of acceleration was reported by Toschi *et al*[37], who found that the component of the acceleration perpendicular to the velocity has different statistical properties than the component of acceleration parallel to the velocity. Specifically, intense acceleration events in the perpendicular component are correlated over a greater time than intense events in the parallel component.

In the vision of Kolmogorov, high Reynolds number turbulence is characterized by scale-separation; large scales are decoupled from small-scales. This suggests that velocity (associated with the large scales) and acceleration (associated with the small scales) are independent of each other. This assumption is implicit in second-order Lagrangian stochastic models[38, 39], which model acceleration and velocity as independent processes. In fact, several studies have shown strong dependence of the acceleration variance on velocity. Crawford *et al*[40] report experimental results showing that intense accelerations are correlated with high velocities in high Reynolds number turbulence. The dependence is shown to increase with Reynolds number, which is counterintuitive given the *increased* scale-separation at higher Reynolds numbers.

1.2 Turbulent Channel Flow

The previous section focused on the theory and previous work related to HIT, with a focus on investigations from a Lagrangian perspective. Similar investigations in inhomogeneous turbulence are much less common due to the theoretical and experimental/numerical complications associated with the inhomogeneity. However, inhomogeneous turbulence is ubiquitous in nature and engineering, motivating a deeper understanding of such turbulent systems. Technological advances in high-speed cameras and computing power increasingly allow experimental and numerical Lagrangian investigations of such turbulent flows. In order to limit the complexity introduced by the inhomogeneity there is a preference for "simple" inhomogeneous turbulence flows, such as turbulent channel flow. This section introduces turbulent channel flow, and describes selected characteristics of this flow relevant to the work presented in this thesis.

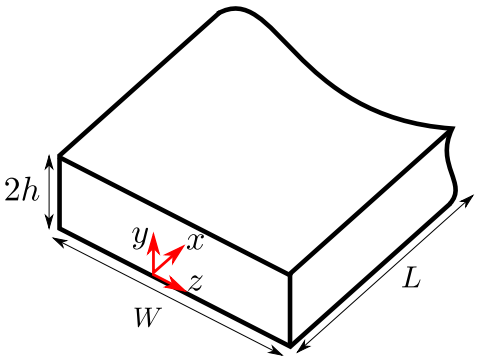

Figure 1.4: Schematic of a turbulent channel with coordinate system. A high aspect ratio ($h \ll$ W) and sufficient development length ($h \ll$ L) ensure statistical homogeneity in the streamwise(x) and spanwise (z) direction.

Turbulent channel flow is an internal, pressure-driven flow in a rectangular channel at sufficiently high Reynolds number. If the channel is sufficiently long and sufficiently high-aspect-ratio, the flow is homogeneous in the streamwise (x) and spanwise (z) directions; the only direction of inhomogeneity is the wall-normal (y) direction[11]. As such it is a convenient academic framework to study inhomogeneous turbulence.

By symmetry all statistics, e. g. the mean streamwise velocity, are symmetric about the

[11] This assumption is often implicit in the literature of turbulent channel flows, i. e. "turbulent channel flow" refers to the subset of turbulent channel flow for which this assumption holds.

mid-plane of the channel $y = h$

$$\langle \mathrm{U}_x(x, y^*, z)\rangle = \langle \mathrm{U}_x(x, 2h - y^*, z)\rangle \qquad 0 < y^* < 2h \tag{1.45}$$

Statistical homogeneity in the streamwise and spanwise direction, and the conservation of mass and momentum give the following results for the mean Eulerian velocity and pressure fields:

$$\langle \mathrm{U}_y(x, y, z)\rangle = 0 \tag{1.46}$$

$$\langle \mathrm{U}_z(x, y, z)\rangle = 0 \tag{1.47}$$

$$\left\langle \frac{d\mathrm{P}(x, y, z)}{dx} \right\rangle = \text{constant} \tag{1.48}$$

This constant streamwise mean pressure gradient drives the flow, and in stationary flow is balanced by the wall shear stress τ_w. The wall shear stress provides a convenient quantity by which to scale flow variables. Following the notation of Pope[10] this scaling is given as

$$u_\tau = \sqrt{\frac{\tau_w}{\rho}} \quad \text{Velocity wall-scale} \tag{1.49}$$

$$\delta_\nu = \nu\sqrt{\frac{\rho}{\tau_w}} \quad \text{Length wall-scale} \tag{1.50}$$

$$t_\tau = \frac{\nu\rho}{\tau_w} \quad \text{Time wall-scale} \tag{1.51}$$

These wall-scales are used to scale flow variables, which are then denoted with a "+" superscript, e. g.

$$y^+ = \frac{y}{\delta_\nu} \tag{1.52}$$

The Reynolds number typically chosen to characterize turbulent channel flows is formed with this velocity wall-scale as

$$\mathrm{Re}_\tau \equiv \frac{u_\tau h}{\nu} \overset{\text{Eqns. } 1.49,1.50}{=} \frac{h}{\delta_\nu} \tag{1.53}$$

This definition of the Reynolds number is convenient in that is gives a direct measure of length scale separation between the viscous wall length scale (δ_ν) and the largest length scale (h).

High Reynolds number channel flow varies qualitatively with respect to the distance from the wall (y^+). Attempts to describe and understand this variation from a purely statistical point of view has occupied researchers since Prandtl, and have led to advances such as the law of the wall and an understanding of the production-transport-dissipation of turbulent kinetic energy in the system. Another approach[12] focuses on the organization of vortical flow structures in the channel , and their role in the turbulence. A small selection of results from each approach are discussed here.

1.2.1 Eulerian statistics in a turbulent channel

Law of the wall

Dimensional analysis using the assumptions made above lead to the expression for the mean shear

$$\frac{d\langle \mathrm{U}_x^+\rangle}{dy} = \frac{1}{y^+} f\left(\frac{y}{\delta_\nu}, \frac{y}{h}\right) \tag{1.54}$$

[12] Tsinober[8] points out that it is impossible to draw a clear line between a "statistical" and a "structural" approach to turbulence; this distinction is made here simply for the purpose of introduction.

At high Reynolds number one may assume that there is a distance from the wall $\delta_\nu \ll y \ll h$ such that the mean shear is independent of both δ_ν and h, in which case the function f must be a constant, i. e.

$$\frac{d\langle U_x^+\rangle}{dy} = \frac{1}{\kappa y^+} \quad \text{for } \delta_\nu \ll y \ll h$$
$$\Rightarrow \langle U_x^+\rangle = \frac{1}{\kappa} ln(y^+) + B \quad \text{for } \delta_\nu \ll y \ll h \tag{1.55}$$

where κ is the von Kármán constant (≈ 0.41) and $B \approx 5.2$ for smooth walls. The layer in which this self-similar relation holds is called the log layer. Very close to the wall the dynamics are dominated by viscous stress, and between these two layers there is a transitional layer called the buffer layer. These three layers are defined[13] as

$$\text{Viscous layer: } 0 < y^+ < 5 \tag{1.56}$$
$$\text{Buffer layer: } 5 < y^+ < 30 \tag{1.57}$$
$$\text{Log layer: } y^+ > 30, \quad y/h < 0.3 \tag{1.58}$$

and are shown graphically with the mean velocity and velocity variance in figure 1.5. Note that peak of the streamwise variance occurs in the buffer layer, as does the peaks of turbulence production, dissipation, and turbulent kinetic energy (not shown in figure 1.5), highlighting the dynamical importance of this layer, despite how little of the channel it fills (less than 2% of the half-width of the channel at $Re_\tau = 1440$). The definition of the log-layer layer illustrates how the width of this layer depends on the Reynolds number

$$\text{Lower limit of log layer: } y^+ = 30 = 30\frac{h}{Re_\tau} \qquad \text{Upper limit of log layer: } 0.3h \tag{1.59}$$

i. e. for a given channel width h the upper limit of the log layer is fixed, and increasing Re_τ acts to shrink the viscous length scale, thus pushing the lower limit of the log layer towards the wall.

Dimensional analysis similar to the derivation of the log law (equation 1.55) gives

$$\frac{U_0 - \langle U_x\rangle}{u_\tau} = -\frac{1}{\kappa} ln\left(\frac{y}{h}\right) + B_1 \quad \text{for } y \ll h \tag{1.60}$$

where U_0 is the mean streamwise velocity at the centerline ($U_0 = \langle U_x(y)\rangle|_{y=h}$), and B_1 is a constant (≈ 0.2). Equations 1.55 and 1.60 can be combined yielding

$$\frac{U_0}{u_\tau} = \frac{1}{\kappa} ln\left(Re_0 \frac{u_\tau}{U_0}\right) + B + B_1 \tag{1.61}$$

which relates the ratio of velocity scales to the large-scale Reynolds number $Re_0 \equiv U_0 h/\nu$. This relation allows the estimation of the velocity scale u_τ directly from the centerline velocity, which is more practical experimentally, as a direct measurement of τ_w is often not possible.

Reynolds stresses: production, transport, and dissipation

The equation governing the kinetic energy in a turbulent flow, $\mathbf{U}\cdot\left[\frac{D\mathbf{U}}{Dt} = -\frac{1}{\rho}\frac{dP}{d\mathbf{x}} + \nu\nabla^2\mathbf{U}\right]$, was previously developed using the Reynolds decomposition (equations 1.20 and 1.21).

[13] This definition is taken from Pope[10], but definitions vary in the literature, e.g. Hoyas[41] take the log layer to be narrower: $y^+ > 100, \quad y/h < 0.2$

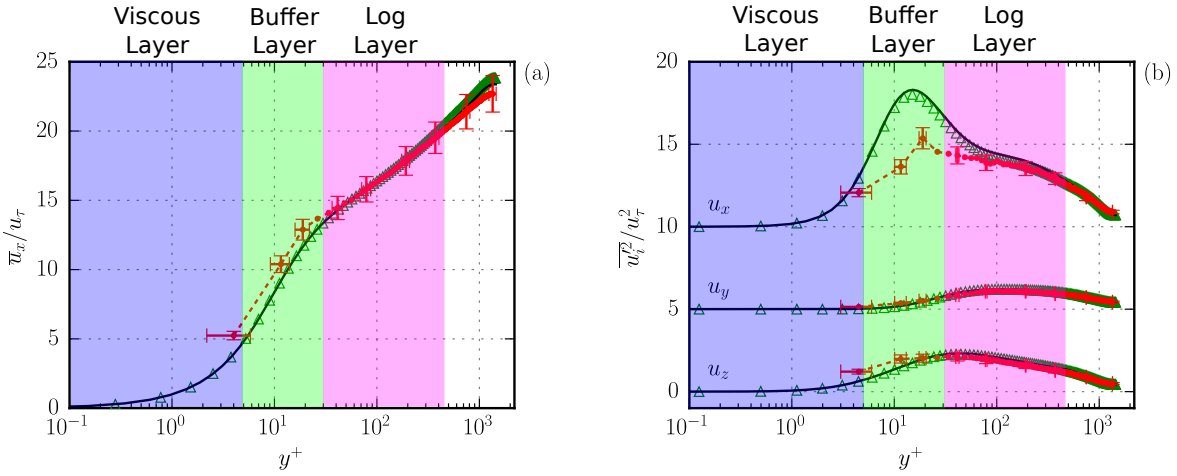

Figure 1.5: Profiles of mean streamwise velocity (left) and component-wise velocity variance (right), shown with the viscous layer, the buffer layer, and the log layer. Red symbols are experimental data, green symbols and black line are DNS. Velocity variance profiles are offset by $5u_\tau^2$ for clarity. Figure modified from Stelzenmuller *et al*[42].

Using the symmetries of turbulent channel flow, these equations are simplified to

$$\underbrace{\frac{\partial}{\partial y}\left[\langle \mathrm{U}_x\rangle\langle u_x u_y\rangle - \nu\frac{\partial \overline{\mathrm{E}}}{\partial y}\right] + \frac{1}{\rho}\frac{\partial\langle \mathrm{P}\rangle}{\partial x}\langle \mathrm{U}_x\rangle}_{\text{Transport of }\overline{\mathrm{E}}} = \underbrace{\langle u_x u_y\rangle\frac{\partial\langle \mathrm{U}_x\rangle}{\partial y}}_{\text{Production of } k} - \underbrace{\nu\left[\frac{\partial\langle \mathrm{U}_x\rangle}{\partial y}\frac{\partial\langle \mathrm{U}_x\rangle}{\partial y}\right]}_{\text{Dissipation due to mean flow}} \tag{1.62}$$

$$\underbrace{\frac{\partial\langle u_y u_x u_x\rangle}{\partial y}}_{\text{Turbulent transport}} + \underbrace{\frac{1}{\rho}\frac{\partial\langle u_y p\rangle}{\partial y}}_{\text{Pressure transport}} - \underbrace{\nu\frac{\partial^2 k}{\partial y^2}}_{\text{Viscous transport}} = \underbrace{-\langle u_x u_y\rangle\frac{\partial\langle \mathrm{U}_x\rangle}{\partial y}}_{\text{Production of } k} - \underbrace{\nu\left\langle\frac{\partial u_i}{\partial x_j}\frac{\partial u_i}{\partial x_j}\right\rangle}_{\text{Turbulent dissipation }\epsilon} \tag{1.63}$$

where $\overline{\mathrm{E}} = \frac{1}{2}\langle \mathrm{U}_x\rangle^2$ and $k = \frac{1}{2}(u_x^2 + u_y^2 + u_z^2)$. Some of the terms in these energy equations are easily measured experimentally, and will be presented in Chapter 3. Other terms, such as the fluctuating spatial velocity gradients and the fluctuating pressure, are generally not accessible in experiments. Results from DNS[43, 44], where all of the terms can be directly measured, have been published for a range of Reynolds numbers. The profiles of these terms across the channel show the following behavior in each layer.

- **Viscous layer**: In the viscous layer there is very little fluctuating velocity and thus very little production. Dissipation is highest at the wall, balanced by viscous transport term which brings energy towards the wall.

- **Buffer layer**: In the buffer layer all of the terms in equation 1.63 are important. The production term is highest in this layer, and is greater than the dissipation, which means the transport terms are working to bring energy toward the wall (by the viscous transport term) and away from the wall (by the pressure and turbulent transport term). The viscous and buffer layers have been shown to be dependent on the Reynolds number.

- **Log layer**: In the log layer the production and dissipation of energy are in balance, and the transport terms become negligible. The wall-scaled terms show little dependence on Reynolds number.

- **Beyond the log layer**: Between the log layer and the channel centerline the production declines to zero, and the dissipation is balanced by the transport terms.

Anisotropy

Turbulent channel flow is characterized by a high degree of anisotropy. The mean velocity is highly sheared, and the variance of fluctuating velocity components—$\langle u_x^2 \rangle, \langle u_y^2 \rangle, \langle u_z^2 \rangle$—differ significantly. These large-scale anisotropies are greatest near the wall, and relax to isotropy at the channel centerline. It remains an open question as to the extent to which the small scales of the flow are isotropic in the high Reynolds number limit, as predicted by Kolmogorov. In a turbulent channel DNS of $Re_\tau = 1000$, Pumir *et al*[45] found small-scale anisotropy up to the channel center, by some measures greater than that found in equivalent homogeneous shear turbulent flow. In another channel flow DNS at a similar Reynolds number Zamansky *et al*[3] found that the orientations of acceleration approach isotropy at $y^+ \approx 40$, i. e. the beginning of the log layer.

1.2.2 Vortical structures in a turbulent channel

Flow visualization techniques applied to wall-bounded turbulence have revealed organized motions in the turbulence. These organized motions have been studied extensively[2, 46, 47, 48], although there is a general lack of agreement in the literature about how to define these organized motions. For the purpose of this discussion an intuitive definition of a vortex will suffice.

Herpin *et al*[49] analyzed data from a channel flow DNS ($Re_\tau \approx 950$) with respect to the number and radii of vortices across the channel width. Streamwise vortices were found to be significantly more common than spanwise vortices in the buffer and log layers. This difference is minor beyond the log layer, but a small difference persists almost to the channel center. The overall number of vortices peaks at $y^+ \approx 100$ for both streamwise and spanwise vortices, and declines towards the center. Streamwise vortex radii were found to be smaller than those of the spanwise vortices in the near-wall region, and approximately equal elsewhere.

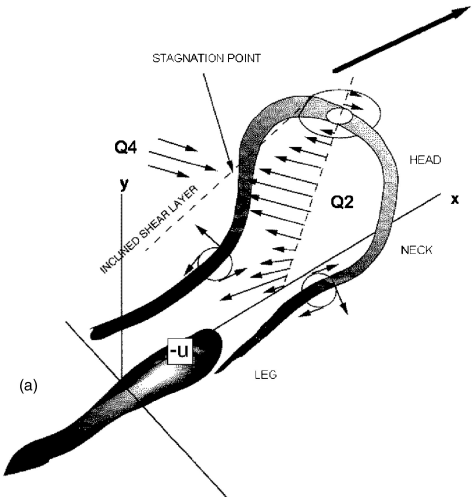

Figure 1.6: Sketch of a horseshoe vortex, showing two parallel streamwise legs close to the wall and spanwise elevated head. Reproduced from Adrian[2].

The qualitative picture given by these results is that turbulence near the center of the channel—3-D, quasi-isotropic, quasi-homogeneous turbulence—becomes more and more organized as one approaches the wall. This organization manifests as vortices increasingly aligned in the streamwise direction, i. e. a system between fully 3-D HIT and 2-D turbulence[14]. From a Lagrangian point of view, one in which high accelerations events and the long time correlations of acceleration magnitude are associated with fluid particles "trapped" in vortices, the organization of vortices is expected to have a significant effect on Lagrangian statistics.

[14] Clearly near wall turbulence is quite different from classical 2-D turbulence, but there are intriguing similarities such as the structure of aligned vortices and the inverse energy cascade.

1.3 Dispersion and Lagrangian stochastic models

One of the fundamental properties of turbulence is highly efficient mixing, an effect that is directly observed in the experiments of Reynolds (figure 1.1). This mixing effectiveness has important practical consequences for problems such as the dispersion of pollutants, heat transfer in fluid systems, and the mixing of chemical species in natural and engineering systems. Quantities such as temperature, non-reacting chemical species, etc., commonly have large Péclet numbers[15], and small particles often have low Stokes numbers[16] such that the dispersion of these quantities closely resembles the dispersion of fluid particles. The dispersion of fluid particles is naturally treated in the Lagrangian framework, for example the dispersion of pollution from a point source $\mathbf{x_0}$ at a time t_0 is described by the PDF of an ensemble of Lagrangian trajectories $\mathbf{X}(\mathbf{x_0}, t|t_0)$.

One approach to this problem is to generate particle trajectories with a stochastic process of the form

$$\mathbf{X}_{n+1} = f(\mathbf{X}_n) + \mathrm{S} \quad \text{where S is a stochastic forcing term} \tag{1.64}$$

Multiple realizations of equation 1.64 result in an ensemble of fluid particle trajectories, from which the PDF of $\mathbf{x_0}$ at a time t_0 may be extracted. This is the approach of Lagrangian stochastic models, which have applications in dispersion problems, as well as statistical descriptions of turbulence (PDF methods), subgrid modeling in LES, and the modeling of inertial particles in turbulence.

1.3.1 Single particle dispersion

In a classic paper from 1921[50] G. I. Taylor showed that in stationary HIT the dispersion of a fluid particle particle position was related to the time for which the Lagrangian velocity is correlated. Following this reasoning, but allowing for stationary inhomogeneous anisotropic turbulence, a fluid particle trajectory conditioned on an initial position $\mathbf{x}_0$ at time t_0 is written as

$$\mathbf{X}(\mathbf{x}_0, t|t_0) = \int_{t_0}^{t} \mathbf{V}(\mathbf{x}_0, \tau|t_0)\, d\tau + \mathbf{x}_0 \tag{1.65}$$

The covariance of an ensemble of such trajectories is given as

$$\langle \mathrm{X}_i(\mathbf{x}_0, t|t_0)\mathrm{X}_j(\mathbf{x}_0, t|t_0)\rangle = \int_{t_0}^{t}\int_{t_0}^{t} \langle \mathrm{V}_i(\mathbf{x}_0, t'|t_0)\mathrm{V}_j(\mathbf{x}_0, t''|t_0)\rangle\, dt'\, dt'' \tag{1.66}$$

Defining the general form of the normalized correlation[17]

$$\rho_{ij}(\tau) \equiv \frac{\langle \mathrm{V}_i(\mathbf{x}_0, t_0|t_0)\mathrm{V}_j(\mathbf{x}_0, t_0+\tau|t_0)\rangle}{\sqrt{\langle \mathrm{V}_i^2(\mathbf{x}_0, t_0|t_0)\rangle \langle \mathrm{V}_j^2(\mathbf{x}_0, t_0+\tau|t_0)\rangle}} \quad \text{where } \tau = t - t_0 \tag{1.67}$$

For convenience this normalization factor is written as

$$\sigma_{ij}(\tau) \equiv \langle \mathrm{V}_i(\mathbf{x}_0, t_0|t_0)\rangle \langle \mathrm{V}_j(\mathbf{x}_0, t_0+\tau|t_0)\rangle \tag{1.68}$$

[15] The Péclet number defines the ratio of the advective rate of transport to the molecular diffusion rate of transport.

[16] The Stokes number defines the ratio of characteristic times of the particle and the flow—in the limit of small Stokes number particles tend to follow fluid particles faithfully.

[17] This choice of normalization factor is not unique, but is standard in the literature.

The Lagrangian velocity integral time scale, or equivalently the Lagrangian integral scale, is defined as

$$\mathrm{T}_{\mathrm{L},ij} \equiv \int_0^\infty \rho_{ij}(\tau)d\tau \tag{1.69}$$

The r.h.s. of equation 1.66 can be rewritten to reduce the double integral to single integral[18]

$$\langle \mathrm{X}_i(\mathbf{x}_0, t|t_0)\mathrm{X}_j(\mathbf{x}_0, t|t_0)\rangle = 2(t-t_0)\int_{t_0}^{t} \sigma_{ij}(\tau)\rho_{ij}(\tau)d\tau - 2\int_{t_0}^{t} \tau\sigma_{ij}(\tau)\rho_{ij}(\tau)d\tau \tag{1.70}$$

Equation 1.70 clarifies the asymptotic behavior of dispersion. For short time lags $\tau \ll \mathrm{T}_{\mathrm{L},ij}$ the velocity is highly correlated so $\rho_{ij} \approx 1$, also $\sigma_{ij}(\tau) \approx \sigma_{ij}(0)$. Using these approximations in equation 1.70 gives

$$\langle \mathrm{X}_i(\mathbf{x}_0, t|t_0)\mathrm{X}_j(\mathbf{x}_0, t|t_0)\rangle \approx \tau^2\sigma_{ij}(0) \quad \text{for } \tau \ll \mathrm{T}_{\mathrm{L},ij} \tag{1.71}$$

At long time lags $\tau \gg \mathrm{T}_{\mathrm{L},ij}$ the velocity is uncorrelated and $\rho_{ij} \approx 0$ indicating that the dispersion at long times may be estimated by neglecting the second term in equation 1.70

$$\langle \mathrm{X}_i(\mathbf{x}_0, t|t_0)\mathrm{X}_j(\mathbf{x}_0, t|t_0)\rangle \approx 2\tau\int_{t_0}^{t} \sigma_{ij}(\tau)\rho_{ij}(\tau)d\tau \tag{1.72}$$

Note that the normalization factor $\sigma_{ij}(\tau)$ samples the inhomogeneity of the flow and may not be brought out of the integral, illustrating the difficulty in calculating dispersion in inhomogeneous turbulence. For the special case of HIT

$$\sigma_{ij}(\tau) = u'^2, \quad \rho_{ij}(\tau) = \rho(\tau), \quad \mathrm{T}_{\mathrm{L},ij} = \mathrm{T}_\mathrm{L} \tag{1.73}$$

And Taylor's results for the asymptotic scaling of dispersion in HIT are found

$$\begin{aligned} \langle \mathrm{X}^2(\mathbf{x}_0, t_0+\tau|t_0)\rangle &= \tau^2\langle u'^2\rangle \quad \text{for } \tau \ll \mathrm{T}_\mathrm{L} \\ \langle \mathrm{X}^2(\mathbf{x}_0, t_0+\tau|t_0)\rangle &= 2\tau\langle u'^2\rangle\mathrm{T}_\mathrm{L} \quad \text{for } \tau \gg \mathrm{T}_\mathrm{L} \end{aligned} \tag{1.74}$$

Taylor constructed a stochastic model of Lagrangian trajectories in the spirit of equation 1.64 that replicated his findings for turbulent dispersion. This model is equivalent to the Langevin equation, which models Lagrangian velocity.

1.3.2 The Langevin equation

The Langevin equation is a stochastic differential equation of the form

$$d\mathrm{V}(t) = \gamma\mathrm{V}(t) + \mathrm{L}(t) \tag{1.75}$$

Where $\mathrm{L}(t)$ is a Gaussian stochastic process with zero mean ($\langle \mathrm{L}(t)\rangle = 0$) and is delta-correlated in time ($\langle \mathrm{L}(t)\mathrm{L}(t')\rangle = \Gamma\delta(t-t')$). This model was developed by Langevin to describe Brownian motion,[19] where the change in particle motion $d\mathrm{V}$ is equal to a deterministic term (proportional to the fluid velocity) and a stochastic term that models molecular collisions with the particle. Equation 1.75 can be solved as an initial value problem:

$$\mathrm{V}(t) = \mathrm{V}_0\exp(-\gamma t) + \exp(-\gamma t)\int_0^t \exp(\gamma t)\mathrm{L}(t')dt \tag{1.76}$$

[18] See derivation in *Turbulent flows*[10] p. 502

[19] A review and English translation of this paper is available from Lemons and Gythiel[51].

Using the properties of the stochastic process $L(t)$ the mean autocorrelation is found to be

$$\langle V(t)V(t+\tau)\rangle \equiv \rho(\tau) = \frac{\Gamma}{2\gamma}\exp(-\gamma\tau) \quad \text{in the limit of } t \to \infty \tag{1.77}$$

Substituting equation 1.77 into the HIT form of the Taylor relation for the variance of dispersion (equation 1.66)

$$\begin{aligned}\langle X^2(\tau)\rangle &= \int_0^\tau \int_0^\tau \frac{\Gamma}{2\gamma}\exp(-\gamma\tau)\,d\tau' d\tau'' \\ \langle X^2(\tau)\rangle &= \frac{\Gamma}{2\gamma^2}\left[\tau - \frac{1}{\gamma}\left(1-\exp[-\gamma\tau]\right)\right]\end{aligned} \tag{1.78}$$

Using the following substitutions

$$\begin{aligned} T_L = \frac{1}{2\gamma}, \quad \Gamma = \frac{2\langle u'^2\rangle}{T_L} \\ \rightarrow \langle X^2(\tau)\rangle = \langle u'^2\rangle T_L\left[\tau - T_L\left(1-\exp[-\tau/T_L]\right)\right]\end{aligned} \tag{1.79}$$

recreates the Taylor scaling for single particle dispersion in HIT (equation 1.74), as shown here:

$$\langle X^2(\tau)\rangle = \langle u'^2\rangle T_L\left[\tau - T_L\left(1-1+\frac{\tau}{T_L}-\frac{\tau^2}{T_L^2}+\mathcal{O}\left(\frac{\tau^3}{T_L^3}\right)\right)\right] \approx \langle u'^2\rangle\tau^2 \quad \text{for } \tau \ll T_L \tag{1.80}$$

$$\langle X^2(\tau)\rangle = \langle u'^2\rangle T_L\left[\tau - T_L\left(1-\exp[-\tau/T_L]\right)\right] \approx \langle u'^2\rangle T_L\tau \quad \text{for } \tau \gg T_L \tag{1.81}$$

Writing the Langevin equation with coefficient determined in this manner results in

$$dV(t) = -\frac{V(t)}{T_L}dt + \sqrt{\frac{2\langle u'^2\rangle}{T_L}}dW(t) \tag{1.82}$$

where $V(t)$ is the Lagrangian velocity, T_L is the Lagrangian velocity integral time scale, $\langle u'^2\rangle$ is the Eulerian velocity variance, and $\rho(\tau) = \exp(-|\tau|/T_L)$ is the velocity autocorrelation function. The stochastic term is rewritten

$$L(t) = \sqrt{\frac{2\langle u'^2\rangle}{T_L}}dW(t) \tag{1.83}$$

where $W(t)$ is a normalized Gaussian process (zero mean, unit variance) called a Weiner process.

The scaling of K41 may be applied to this model by considering the second order Lagrangian structure function $S_2^L = \langle|\mathbf{V}(\mathbf{x}_0, t_0+\tau) - \mathbf{V}(\mathbf{x}_0, t_0)|^2\rangle$

$$\begin{aligned} S_2^L(\tau) &= C_0\langle\epsilon\rangle\tau \quad \text{for } \tau_\eta \ll \tau \ll T_L \quad \leftarrow \text{K41 scaling} \\ &= 2\langle u'^2\rangle[1-\rho_L(\tau)] \quad \leftarrow \text{Kinematic relationship in HIT} \\ &= 2\langle u'^2\rangle[1-\exp(-\tau/T_L)] \quad \leftarrow \rho_L \text{ from Langevin model} \\ &= 2\langle u'^2\rangle[1-1+\tau/T_L+\mathcal{O}((\tau/T_L)^2)] \quad \leftarrow \text{Taylor series expansion around } \tau = 0 \\ \rightarrow C_0\langle\epsilon\rangle &= \frac{2\langle u'^2\rangle}{T_L} \quad \text{for } \tau_\eta \ll \tau \ll T_L \end{aligned} \tag{1.84}$$

Using the result in isotropic turbulence that $\langle u'^2 \rangle = \frac{2}{3}k$ (where k is the turbulent kinetic energy) the inverse of the time scale may be written as

$$\frac{1}{T_L} = \frac{3C_0\epsilon}{4k} \tag{1.85}$$

The Langevin model may be written for high Reynolds number stationary HIT with zero mean flow as

$$dV(t) = -\frac{3C_0\epsilon}{4k}V(t)dt + (C_0\epsilon)^{1/2}dW(t) \tag{1.86}$$

For this highly idealized turbulent flow this model is compatible with K41 scaling and single particle dispersion scaling by construction. Equation 1.86 is an example of an Ornstein-Uhlenbeck process, and as such is a stationary Gaussian stochastic process with additive noise.

This form of the Langevin equation has been the foundation of the Lagrangian stochastic modeling of turbulence. This model has several important limitations, which have been addressed with a wide variety of approaches. The nature of these approaches depends on the model application and the specific statistical results sought, e.g. models used to predict pollution in the atmospheric boundary layer have different requirements than the models used to predict mixing of chemical species in an engineering application. The literature regarding Lagrangian stochastic models in turbulence is vast, and a complete summary is not attempted here. This section attempts rather to identify three important limitations of equation 1.86—the assumptions of Reynolds number independence, homogeneity, and Gaussianity—and present selected attempts to overcome these limitations. The emphasis is naturally placed on models applicable to flow in a turbulent channel.

As a common point of reference for the following discussion equation 1.82 is rewritten to be as general as possible

$$d\mathbf{X} = A(\mathbf{X}, t)dt + B(\mathbf{X}, t)dW \tag{1.87}$$

where $\mathbf{X}$ is a state vector containing the variables of state necessary to model the system, e. g. velocity, acceleration, dissipation, etc. A and B are typically referred to in the literature as the drift and diffusion tensors, respectively, and may depend on the state vector and time.

1.3.3 Reynolds number dependence

Only one turbulence time scale appears in the Langevin equation of velocity, which implies that the Reynolds number is approaching infinity. One way of seeing this directly is to consider the Kolmogorov scaling $Re \approx (T_E/\tau_\eta)^2$, where T_E and τ_η are the Eulerian integral time-scale and the Kolmogorov time-scale, respectively. The Kolmogorov time-scale τ_η is represented in equation 1.86 as approaching zero, a consequence of the delta-correlated stochastic term, thus as $\tau_\eta \to 0$, $Re \to \infty$. The K41 scaling shown in equation 1.84 also is valid in the limit of $Re \to \infty$. Turbulent flows are characterized principally by Reynolds number, and so the

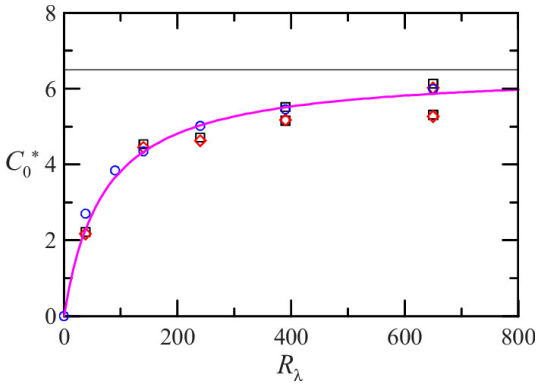

Figure 1.7: The Kolmogorov "constant" C_0^* as a function of Reynolds number in DNS of isotropic turbulence (points), shown with an empirical fit (line). Figure reproduced from Sawford *et al*[52]

Reynolds number independence of the Langevin equation as formulated in equation 1.86 may be problematic, especially for low Reynolds number flows.

A simple way to introduce Reynolds number dependence to equation 1.86 is to let the Kolmogorov "constant" C_0 be a function of Reynolds number $C_0^*(Re_\lambda)$, as shown in figure 1.7. This Reynolds number dependent scaling is clearly contrary to the spirit of K41, but allows the simple adaptation of equation 1.86 to low Reynolds number flows. Pope[53] showed that Langevin model results using this approach closely match DNS results in isotropic turbulence for second order Lagrangian structure functions for $\tau > 20\tau_\eta$, although at shorter times the model does not reproduce the DNS results.

Another approach to introduce Reynolds number dependence into the Langevin equation is to model increments of acceleration instead of increments of velocity. This approach was first proposed by Sawford[38], who introduced the following model for a component of the acceleration in HIT:

$$\begin{aligned} du(t) &= a(t)dt \\ da(t) &= -\alpha a(t)dt - \beta u(t)dt + \left(2\langle a'^2\rangle\gamma\right)^{1/2} dW(t) \end{aligned} \tag{1.88}$$

Where α, β, and γ are constants related to the two length scales of the turbulence. In this framework the increments of acceleration are directly modeled with deterministic terms linear in acceleration and velocity and a stochastic term with similar properties to that shown in equation 1.86. The velocity is simply the time integral of the acceleration. A model of this type has the advantage of allowing a time scale associated with the acceleration, which implies: a non-delta acceleration autocorrelation function, a realistic velocity autocorrelation function[20], and a natural inclusion of Reynold number dependence.

The Sawford model results are in close agreement with low Reynolds number Lagrangian statistics obtained from DNS[54]. Unlike models of velocity, the Sawford model is able to accurately model Lagrangian statistics at short time lags.

This model was formulated under the assumptions of isotropic turbulence and is constrained with K41 theory and DNS results relating the ratio of time scales with the Reynolds

Timescales and "noise" in the Langevin equation:
The use of a delta-correlated "noise" term is clearly justified in systems where there is external noise with a time scale that is short relative to the slow system variable. Brownian motion was the original application and illustrates clearly the separation between the stochastic noise—in this case molecular forces—and particle velocity. This concept is much less physically justified in the case of turbulence due to the fact that there is no "noise" from external sources. The application of the Langevin equation is loosely justified if there is a large time scale separation between the modeled variable and its time derivative. This is clear in the case of equation 1.86 in the limit of $Re \to \infty$, but much less clear for models of acceleration. Good agreement between the results of such models and numerical and experimental results seem to indicate that a timescale separation indeed exists between the acceleration and its time derivative, but there is no theoretical prediction for this separation or how it scales with other quantities.

[20] The velocity autocorrelation function $\exp(-|\tau|/T_L)$ associated with equation 1.86 is non-differential at $\tau = 0$; a non-zero acceleration time scale acts to smooth this cusp, resulting in a differential velocity autocorrelation function at $\tau = 0$.

number. The full 1-D model is as follows:

$$du(t) = a(t)dt \tag{1.89}$$

$$da(t) = -\left(\frac{1}{\tau} + \frac{1}{T_\infty}\right) a(t)dt - \left(\frac{1}{\tau T_\infty}\right) u(t)dt + \left(2\langle a'^2\rangle \left(\frac{1}{\tau} + \frac{1}{T_\infty}\right)\right)^{1/2} dW(t) \tag{1.90}$$

where T_∞ is related to the Lagrangian integral scale T_L as

$$T_\infty = \frac{T_L}{1 + \left(\frac{16a_0^2}{C_0^2} Re\right)^{-1/2}} \tag{1.91}$$

and the small time scale associated with the acceleration is given as

$$\tau = \frac{\langle u'^2\rangle}{\langle a'^2\rangle T_\infty} \tag{1.92}$$

This approach naturally incorporates Reynolds number dependence but remains limited in several important ways. Notably, the Sawford model results in a Gaussian distribution of acceleration increments. The non-Gaussianity of velocity increments was seen in figure 1.3 to increase as the velocity increments approach the limit of acceleration. The use of a Gaussian noise term in the Sawford model is therefore less justified than its use in the Langevin equation of velocity. The other limits are similar to those of the simple Langevin model in velocity, namely, the model is valid only in HIT, only a single component of a or v is modeled, and the lack of correlation between components is assumed.

Development of Lagrangian stochastic models in acceleration have continued, notably by Pope[55] and Reynolds[39]. These models are discussed in the following sections.

1.3.4 Lagrangian stochastic models in inhomogeneous turbulence

The assumption of homogeneity is extremely helpful in the construction and constraint of Lagrangian stochastic models. The general case, in which the drift and diffusion tensors (A and B in equation 1.87) are functions of position and are anisotropic, present theoretical and technical problems to development. Some of the more important of these problems are

- **Parameter constraint:** The drift term in the simple Langevin model (equation 1.86) was constrained with Taylor dispersion and Kolmogorov scaling results assuming homogeneity and isotropy. Thomson[56] suggested using a "well-mixed condition", i. e. once well mixed fluid particles should stay well-mixed, as a condition to constrain the drift tensor, but also noted that it is not sufficient for a unique specification.

- **Multiplicative noise:** If the diffusion tensor is dependent on position then the noise term becomes dependent on the signal itself: multiplicative noise. This multiplicative noise presents a technical challenge to the use of Langevin-type models, see references[57, 58] for details.

One of the more common forms of Lagrangian stochastic model for inhomogeneous turbulence is the Generalized Langevin Model (GLM), which provides a framework models for specific inhomogeneous flows, e. g turbulent free shear turbulent flow, boundary layer turbulence, etc.

Generalized Langevin Model (GLM)

The GLM, introduced by Pope[59], is given as

$$
\begin{aligned}
d\mathrm{X}_i(t) &= \mathrm{V}_i(t)\,dt \\
d\mathrm{V}_i(t) &= \left[-\frac{1}{\rho}\frac{\partial \langle p \rangle}{\partial x_i} + \nu \frac{\partial^2 \langle \mathrm{U}_i \rangle}{\partial x_j^2} + \mathrm{G}_{ij}(\mathrm{X}_i)[\mathrm{V}_j(t) - \langle \mathrm{V}_j \rangle] \right] dt + (\mathrm{C}_0 \epsilon)^{1/2} d\mathrm{W}_i(t)
\end{aligned} \tag{1.93}
$$

where G_{ij} is a function of position, and is evaluated at the instantaneous position $\mathrm{X}_i(t)$. The GLM bears a clear resemblance to the N-S equation, where the first and second terms on the r.h.s are the contributions from the mean pressure and mean velocity, and the third and fourth terms model the instantaneous contribution to the velocity increment. The GLM retains the stochastic term of the simple Langevin model (equation 1.86) , which ensures consistency with K41, and avoids problems associated with multiplicative noise. Models for specific flows are found by specifying the drift tensor G_{ij}. This model was shown to provide good agreement with experimental results in a variety of homogeneous turbulent flows[60].

Extensions to the GLM

For homogeneous shear flow, Pope[61] made an explicit connection between the drift and diffusion tensors A and B in the model

$$
du_i = -\mathrm{A}_{ij} u_j + \mathrm{B}_{ij} d\mathrm{W}_j \tag{1.94}
$$

and two measurable quantities: the anisotropic Lagrangian correlation tensor $\mathrm{R}_{ij}(\tau) = u_i(t_0+\tau)u_j(t_0)$ and the normalized Reynolds stress tensor $\langle u_i u_j \rangle / k$. Specifically,

$$
\begin{aligned}
\mathrm{T}_{ij} &= \int_0^\infty \frac{\langle u_i(t_0+\tau)u_j(t_0)\rangle}{\langle u_i \rangle \langle u_j \rangle} d\tau \\
\mathrm{C}_{ij} &= \langle u_i u_j \rangle / k \\
\mathrm{A}_{ij} &= (\mathrm{T}_{ij}^{-1})^{\mathrm{T}} \qquad (1.95) \\
\mathrm{B}_{ij}^2 &= \mathrm{A}_{ik}\mathrm{C}_{kj} + \mathrm{C}_{ik}\mathrm{A}_{kj}^{\mathrm{T}} \qquad (1.96)
\end{aligned}
$$

Although strictly valid only for homogeneous flow, this method may be extended to inhomogeneous flows by assuming approximate local homogeneity. In this case T_{ij} and C_{ij} become functions of position. This idea was extended to inhomogeneous pipe flow by Veenman[62], and the Lagrangian statistics necessary to constrain A were measured experimentally by Walpot *et al*[63].

Tanière *et al*[64] applied this reasoning to turbulent channel flow in the context of the modeling of inertial particles. The Lagrangian correlation tensor $\mathrm{R}_{ij}(\tau, y_0)$ and Reynolds stress tensor $\mathrm{C}_{ij}y_0$, written here showing the dependence on the wall-normal position y_0 at t_0, was extracted from DNS of channel flow at $\mathrm{Re}_\tau = 180$, and used to calculate the drift and diffusion tensors following the method of Pope.

Acceleration models in inhomogeneous turbulence

Pope developed a general model for acceleration[55] very similar to the GLM:

$$dX_i(t) = V(t)\,dt \tag{1.97}$$

$$dV_i(t) = -\left[\frac{1}{\rho}\frac{\partial\langle P\rangle}{\partial x_i}\right]_{X_i(t)} - \left[\frac{1}{\rho}\frac{\partial P^r}{\partial x_i}\right]_{X_i(t)} + a_i^0(t) \tag{1.98}$$

$$dA_i(t) = -[C_{ij}A_j^0(t) + D_{ij}v_j(t)]\,dt + B_{ij}\,dW_j \tag{1.99}$$

where the rapid pressure is modeled separately. In a manner analogous to the development shown above, specifically equations 1.95-1.96, a direct link can be made between the Lagrangian statistics and the parameters of this model in the case of homogeneous shear flow. In this case the required statistics are the Lagrangian correlation tensors in velocity, acceleration, and mixed velocity-acceleration. Presumably the same approach taken by Tanière *et al*—make an assumption of local homogeneity and calculate C, D, and B as a function of position—could be attempted, but this has not yet been attempted. This model, like the Sawford model, results in Gaussian acceleration statistics.

Reynolds[65] proposed a model in acceleration constrained by Thomson's well-mixed condition, Kolmogorov scaling, and a model for the fluctuating dissipation rate (See the section on superstatistical models below). Acceleration components are considered to be independent, i. e. the crosscorrelations are zero. This model was applied to channel flow DNS ($Re_\tau = 400$), and appears to agree fairly closely some DNS results for $y^+ > 100$, although there are not enough published details to make thorough assessment.

1.3.5 Intermittency

Incorporating the effects of intermittency in Lagrangian stochastic models is an active area of research[66], and consequently there are a wide variety of approaches.

Superstatistical approach

The superstatistical approach allows model coefficients to themselves be modeled random variables. Lagrangian results from DNS[16] suggest that non-Gaussian Lagrangian velocity increments may be collapsed to a quasi-Gaussian distribution when conditioned on the local, instantaneous rate of energy dissipation[21]. This finding, together with the K62 scaling framework using the instantaneous local value of the dissipation rate, motivate a modeling approach that jointly models the dissipation rate and the velocity. A model of this type proposed by Pope and Chen[67], in which the log the dissipation rate $\chi(\mathbf{x}, t) = ln[\epsilon(\mathbf{x}, t)/\langle\epsilon\rangle]$ is modeled with the Langevin-type equation:

$$d\chi = -\frac{\chi - \langle\chi\rangle}{T_\chi}\,dt + \left(\frac{2\sigma_\chi^2}{T_\chi}\right)^{1/2} dW \tag{1.100}$$

Velocity is modeled jointly with the GLM, with the refinement that the diffusion term in equation 1.93—$(C_0\langle\epsilon\rangle)^{1/2}$ —is replaced with the $(C_0\epsilon(\mathbf{x}, t))^{1/2}$, where $\epsilon(\mathbf{x}, t)$ is the *instantaneous, local*, value of ϵ taken from the dissipation model (equation 1.100). Note that the Gaussian distribution of $ln(\epsilon)$ implied in equation 1.100 is consistent with the K62 hypothesis of the log-normality of the dissipation rate.

[21] Technically the pseudo-dissipation was used for this normalization, see [16] for details.

This superstatistical approach was extended to Lagrangian stochastic models of acceleration by Reynolds[17, 18]. The dissipation model shown in equation 1.100 models the dissipation rate jointly with the acceleration (using the Sawford model, equation 1.90). Result from this model show good agreement with the experimentally measured high Reynolds number acceleration statistics[68, 30]. Further work in this direction from Lamorgese *et al*[69] suggests that the acceleration conditioned on the pseudo-dissipation has a cubic-Gaussian distribution, and the superstatistical approach of Reynolds should be refined accordingly.

Independent modeling of the magnitude and direction of acceleration

Mordant *et al*[70] experimentally measured the Lagrangian velocity increment $\Delta v(\tau) = v(t_0+\tau) - v(t_0)$, fitted the scaling exponent ζ_p to $\Delta v(\tau)^p \propto \tau^{\zeta_p}$, and found that ζ_p is quadratic in p—consistent with the multifractal model of intermittency. Using the observation that the decorrelation time of $|\Delta v(\tau)|$ is much slower than that of $\Delta v(\tau)$ itself, they constructed a stochastic model in which the direction and magnitude of the stochastic force were modeled as two independent processes. This model, which corresponds to a multifractal random walk model[71], is able to recreate the PDF of acceleration and other intermittency related statistics.

In a similar spirit, Sabel'nikov *et al*[72] proposed a stochastic model for use in LES in which the decomposition of acceleration into magnitude and direction is made explicitly

$$a_i = |a|\hat{e}_i \tag{1.101}$$

and these to quanities are modeled as independent stochastic processes. Using the K62 relation

$$\langle a_i a_j | \epsilon \rangle = \frac{a_0 \epsilon^{3/2}}{\nu^{1/2}} \delta_{ij} \tag{1.102}$$

the magnitude of acceleration is modeled as a log-normal process following the approach of Pope and Chen[67]. The direction of acceleration is modeled as a Gaussian random walk on a unit sphere, with a time scale equal to the Kolmogorov time τ_η. This model was used in a LES of turbulent channel flow by Zamansky *et al*[3] and found to provide good agreement with the DNS in measures such as the PDFs of acceleration, in which intermittency plays an important role.

1.4 Lagrangian statistics in inhomogeneous turbulence

Studies of inhomogeneous turbulence in a Lagrangian framework are rare, and at the time of this writing only a handful of articles have been published on the subject. Researchers have primarily focused on high-Reynolds-number HIT as a natural context in which to study the Lagrangian statistics of acceleration and the universality of the theories of Kolmogorov and their extensions, such as the multi-fractal model of intermittency. Turbulence that is inhomogeneous and anisotropic is inherently more complex than HIT, and presents several additional challenges to the researcher. Turbulence statistics must be conditioned on position, and their components (e.g. in x, y, z) are in general not identical. This conditioning requires more data to converge statistics *at each position*. The interpretation of such results is also more complicated, as both large-scale flow conditions (e.g. boundaries, mean flow, mean shear, etc.) and small-scale turbulence properties (e.g. the Kolmogorov scales) are a function of position.

Both experimental measurement and DNS of inhomogeneous turbulence are also subject to additional technical challenges. In experiments, a mean flow sweeps particles through the measurement volume, and therefore limits the length of measured particle trajectories. Some work using instruments that are displaced with the mean flow[73, 74] has been successful, despite large technical difficulties. The various limitations and compromises associated with Lagrangian measurements in inhomogeneous turbulence are discussed in chapter 2. DNS of inhomogeneous turbulence also faces technical challenges: full resolution of the boundary layer, fewer periodic boundary conditions, and the need for a large computational domain. These factors render DNS of inhomogeneous turbulence more complex and more computationally expensive than equivalent[22] DNS of HIT.

Previous work in this area has focused on turbulent channel flow[75, 64, 76, 77, 3, 76, 78], although turbulent pipe flow[79, 80], turbulent boundary layers[73, 81], and very recently a turbulent jet[82] have also been studied. All of these turbulent flows (with the exception of the turbulent jet) are statistically stationary and contain a single direction of inhomogeneity: the wall-normal direction. Lagrangian quantities measured in these flows are typically conditioned on the distance to the wall y_0 at a given time t_0. One of the fundamental questions in this domain is simply: How do Lagrangian statistics—quantities such as Lagrangian time scales, acceleration time scales, etc.—change as a function of distance to the wall? Eulerian quantities such as dissipation, local Reynolds number, Reynolds stresses, etc. are also dependent on distance to the wall, motivating the question: To what extent does the change in Eulerian quantities with wall-distance explain the change in Lagrangian quantities with wall-distance? Wall-bounded flows are known to be highly anisotropic in the near-wall region, even at small scales, relaxing towards isotropy as wall-distance increases. To what extent is this phenomenon observed in Lagrangian statistics, and how does it differ from the what is seen in Eulerian statistics?

These questions have begun to be addressed. The isotropy and dependence on wall distance of several Lagrangian statistics was investigated in the DNS of a turbulent channel by Choi *et al*[75], including the Lagrangian time scale, the Kolmogorov constants a_0, C_0, and the autocorrelations of acceleration. Simulations of $Re_\tau = 200$ and $Re_\tau = 400$ channel flow (equivalent to a maximum $Re_\lambda \approx 30$ and 50 near the channel center, respectively) show significant differences in all of the Lagrangian statistics as expected given the low Reynolds numbers. Autocorrelations of acceleration were found to be highly anisotropic near the wall, with the streamwise component correlated significantly longer than the other components. Choi *et al* compared the values of C_0, a_0, and the timescale ratio T_L / t_η against the expected values from HIT given the local Reynolds number. These quantities are fairly well predicted by the local value of Re_λ, except near the wall.

The Lagrangian time scales were also measured in a numerical study of turbulent channel flow by Tanière *et al*[64], a similar study by Kuerten and Brouwers[77] at higher Reynolds number, and a combined experimental-numerical study of turbulent pipe flow by Walpot *et al*[79, 63], all three of which focused on Lagrangian velocity statistics in the context of Lagrangian stochastic model development. Drift and diffusion coefficients were found from DNS results (and experimental results in the case of Walpot) as discussed above in section 1.3, then the model results were evaluated. Similar efforts have yet to be made for Lagrangian stochastic models of acceleration.

Acceleration statistics in DNS of the turbulent channel have been examined by Yeo *et al*[78], Lee *et al*[76], and Zamansky *et al* [3]. Lee *et al* found that acceleration statistics near the wall are closely related to the coherent structures found near the wall. Specifically, the effect of vortex filaments on acceleration (strong centripetal acceleration, long correlation

[22] Equivalent is used here loosely, to mean of roughly similar Re_λ.

of acceleration magnitude) found in HIT also exists near the wall, and the preferential alignment of these vortex filaments parallel to the wall may be seen in the acceleration statistics. Yeo *et al* considered the PDFs of the components of acceleration in a turbulent channel, as well as the decomposition of acceleration in the pressure-gradient contribution and the viscous contribution. In the buffer layer the PDF of acceleration was found to be extremely intermittent and anisotropic. Near the wall, the viscous contribution to the streamwise acceleration is important, but this contribution is negligible for the wall-normal and transverse components of acceleration. Zamansky *et al* consider the magnitude and direction of acceleration, in the context of the development of a subgrid stochastic model for LES. The magnitude of acceleration was found to be log-normally distributed throughout the channel, even very close to the wall ($y^+ = 5$). The orientation of acceleration was shown to be anisotropic near the wall, relaxing to isotropy at approximately $y^+ = 40$.

The experimental studies in this area are quite limited. Gerashchenko *et al*[73] measured inertial particle in a turbulent boundary layer; these results are discussed in more depth in chapter 5. The acceleration PDF was measured by Schroder *et al*[81], but data was used from particle trajectories mixed over the entire logarithmic layer in a turbulent boundary layer. Selected Lagrangian acceleration statistics were measured in a turbulent pipe flow by Oliveira *et al*[80], but a complete analysis similar that of Choi *et al*[75] was not reported, nor was the near-wall boundary layer well resolved. No experimental Lagrangian measurements for turbulent channel flow have been reported. More broadly, there does not appear to be published results for fully resolved, 3-D Lagrangian experimental measurements that report the evolution of Lagrangian statistics of velocity and acceleration with position.

If DNS is capable of simulating turbulence at increasingly high Reynolds numbers, it is tempting to ask whether these kinds of experiments continue to be necessary. Almost all of the results available experimentally are also available from the DNS, and the DNS has access to other data (e. g. dissipation, other spatial gradient information) that is very difficult to measure experimentally. There are at least two justifications for doing experiments in this context. First, inhomogeneous DNS still requires experimental validation, especially when extracting Lagrangian results. Issues relating to domain length in channel flow DNS for example are still not settled. Second, DNS that resolves particles is much more demanding than the integration of point-particles trajectories in the domain, and moderate to high Reynolds number DNS with finite-size particles is still beyond current computational resources.

Chapter 2

Experimental methods

Aristotle maintained that women have fewer teeth than men; although he was twice married, it never occurred to him to verify this statement by examining his wives' mouths.

Bertrand Russell

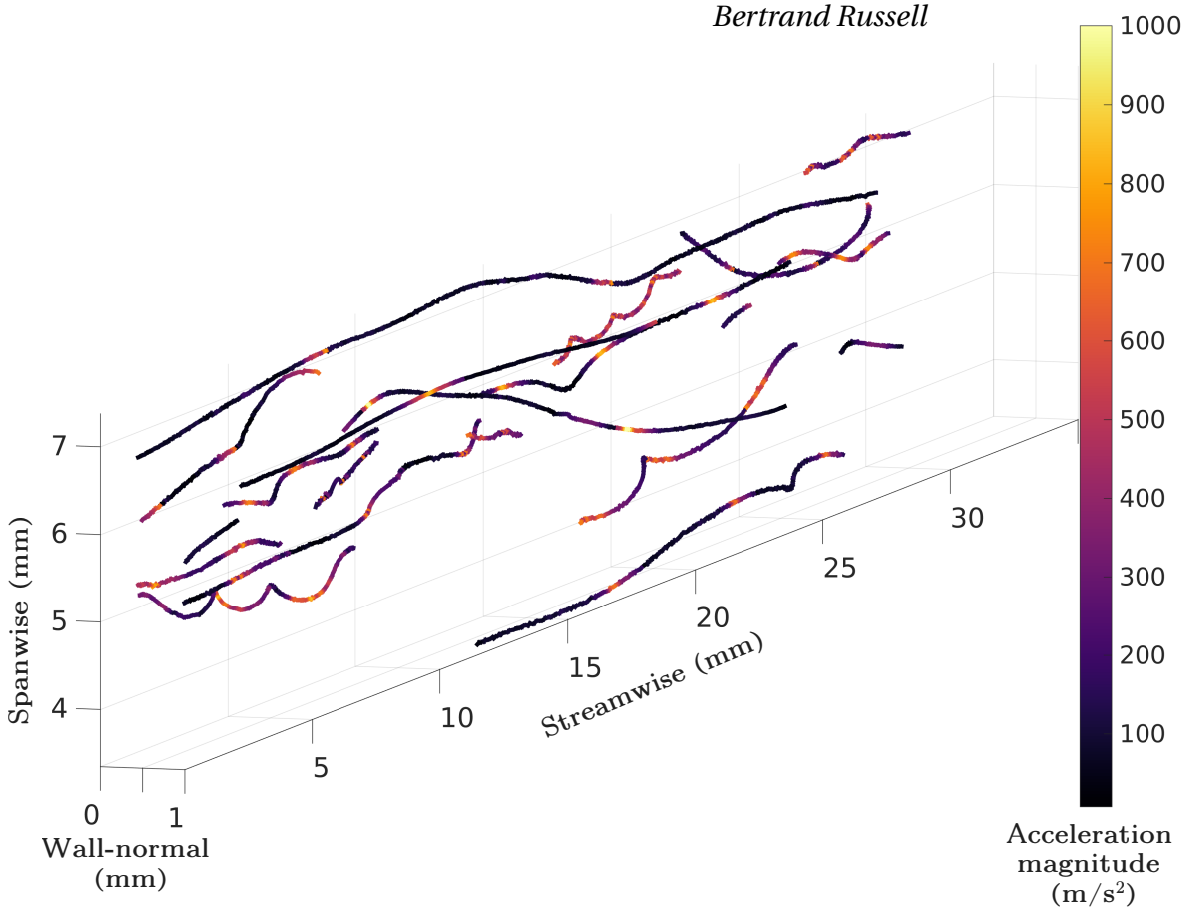

Figure 2.1: Selected tracer particle trajectories in the near wall region ($y^+ = 0 - 75$) of a turbulent channel, representing the first fully resolved Lagrangian measurements ever made in such a flow. Note the extreme accelerations, up to 100 times that of gravity.

The experimental results reported in this thesis were calculated from Particle Tracking Velocimetry (PTV) measurements performed in a turbulent channel at the Laboratoire des Ecoulements Geophysiques et Industriels (LEGI). PTV is an experimental technique that measures the position of particles entrained in a flow over time, i.e. particle trajectories, and is thus a natural and often-used technique for studying turbulence from a Lagrangian point of view. This chapter begins with a detailed description of the turbulent channel in which these measurements were made, including a discussion of the design of the experimental setup and the relevant experimental parameters. The PTV method is described in section 2.2. As this thesis reports the first such measurements performed in a turbulent channel, an emphasis is placed on the unique and challenging aspects of using PTV to study this type of flow. Section 2.3 describes the data processing techniques that allow the extraction of Lagrangian statistics in acceleration and velocity from raw particle trajectories.

Contents

2.1 The turbulent channel

The turbulent channel used in these experiments consists of a high-aspect-ratio rectangular test section in a closed-loop water tunnel. A schematic view of the test section is shown in figure 2.2. The design goals of the experimental system are to approach as closely as possible the idealized turbulent channel discussed in Section 1.2, and facilitate the PTV measurements. The following subsections enumerate these design goals, the manner in which the design goals were realized, and the tests performed to verify them.

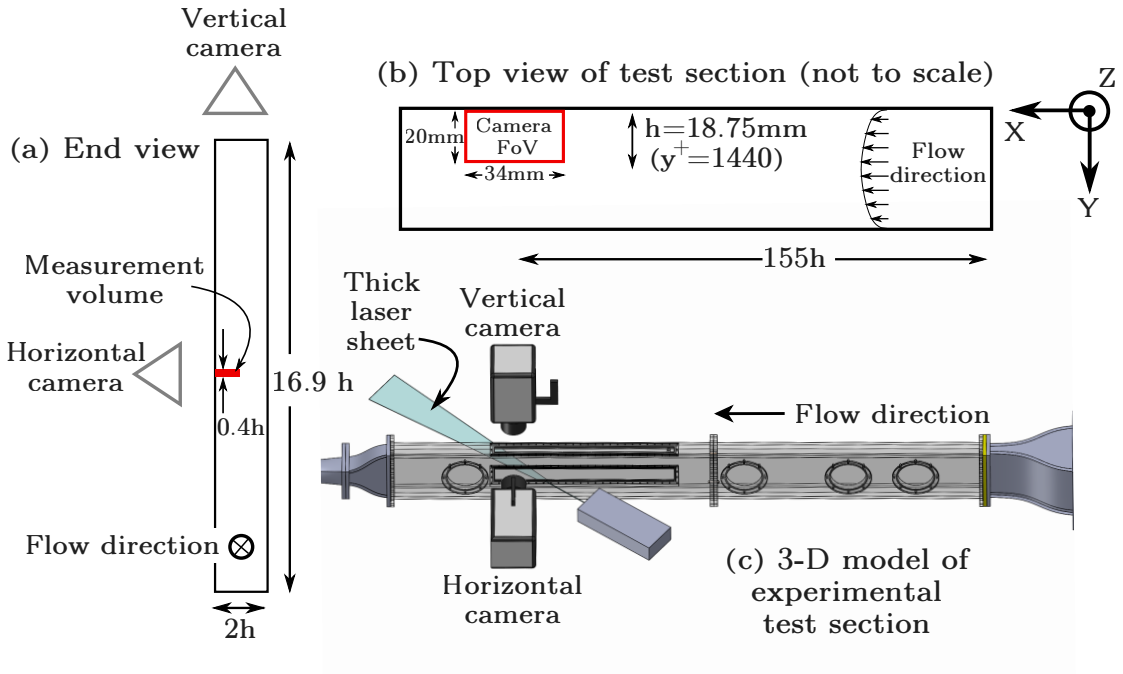

Figure 2.2: Sketch of the turbulent channel used in the experiment. Subfigure (a) is a sketch of the end view of the channel showing the aspect ratio of the channel (the spanwise distance is $16.9h$) and the end view of the measurement volume, as well as the position of the two cameras. Subfigure (b) shows a top view of the channel, with the field of view (FoV) of the vertical camera highlighted. Subfigure (c) shows a 3-D rendering of the experimental setup, including the relative positions of the two high speed cameras and the thick laser sheet used to illuminate the measurement volume.

2.1.1 Target Reynolds number

For these experiments the target friction Reynolds number was $Re_\tau = 1440$, corresponding to a Reynolds number of $Re_0 = 6.2 \times 10^4$, where $Re_0 \equiv \frac{2hU_0}{\nu}$, U_0 is the mean centerline velocity, h is the channel half-width, and ν is the kinematic viscosity. This moderate Reynolds number represents a balance: it is a Reynolds number high enough such that typical features of a moderate Reynolds number turbulent channel flow are observed, such as the appearance of an overlap region and reasonable scale separation over most of the channel (see the theoretical discussion of channel flow in section 1.2), while at the same time not exceeding the limitations on the Reynolds number imposed by the experimental setup. These limitations include the maximum volumetric flow rate of the previously existing recirculating water tunnel, the maximum pressure drop across the water tunnel (especially critical for the high aspect ratio test section), and the limitations imposed by the PTV system. The PTV system limits the Reynolds number by the size of the measurement volume. The measurement volume size limits the velocity scale (U_0) because a high mean

flow results in a low particle residence time in the measurement volume. The measurement volume also limits the length scale (h), because the measurement volume should ideally encompass the half-width of the channel.

The basic scaling of the experimental parameters for a similar experiment at double the friction Reynolds number is presented here in order to highlight the compromises described above.

$$\mathrm{Re}_\tau^{new} = 2 \times \mathrm{Re}_\tau \approx 2900 \tag{2.1}$$

Using the scaling given by Pope [10] to estimate the bulk Reynolds number:

$$\mathrm{Re}_\tau \approx 0.09\mathrm{Re}^{0.88} \quad \text{Note that here} \quad \mathrm{Re} \equiv \frac{\overline{\mathrm{U}}h}{\nu}, \quad \overline{\mathrm{U}} \equiv \frac{1}{h}\int_0^h \langle \mathrm{U} \rangle dy \tag{2.2}$$

$$\frac{\mathrm{Re}_\tau^{new}}{\mathrm{Re}_\tau} = 2 \approx \frac{0.09\mathrm{Re}_{new}^{0.88}}{0.09\mathrm{Re}^{0.88}} \quad \Rightarrow \quad \mathrm{Re}_{new} \approx 2.2\mathrm{Re} \tag{2.3}$$

If we assume that the minimum tracer particle diameter is fixed (set by the limitation of the PTV system, for example), and use the particle diameter (D_p) scaling:

$$\mathrm{D}_p \approx \delta_\nu \quad \text{and} \quad \mathrm{Re}_\tau = \frac{h}{\delta_\nu} \quad \Rightarrow \quad h \approx \mathrm{Re}_\tau \mathrm{D}_p \quad \Rightarrow \quad h_{new} = 2h \tag{2.4}$$

Substituting this value of h into the expression for the bulk Reynolds number

$$\mathrm{Re}_{new} = \frac{\overline{\mathrm{U}}_{new} h_{new}}{\nu} \approx 2.2\mathrm{Re} \quad \Rightarrow \quad \overline{\mathrm{U}}_{new} \approx 1.1\overline{\mathrm{U}} \tag{2.5}$$

We estimate the volumetric flow rate Q by

$$\mathrm{Q} \approx \mathrm{A}\overline{\mathrm{U}}, \text{ where } \mathrm{A} \equiv 2hl, \text{ and the aspect ratio } \mathrm{R} \equiv \frac{l}{h} \quad \Rightarrow \quad \mathrm{Q} \approx 2h^2\mathrm{R}\overline{\mathrm{U}} \tag{2.6}$$

Substituting in the new values of h_{new} and $\overline{\mathrm{U}}$ gives

$$\mathrm{Q}_{new} = 2h_{new}^2 \mathrm{R}\overline{\mathrm{U}}_{new} \approx 2(2h)^2\mathrm{R}(1.1)\overline{\mathrm{U}} \approx 4.4\mathrm{Q} \quad \text{(assuming a constant aspect ratio)} \tag{2.7}$$

Finally, the centerline velocity is found from the scaling (also taken from Pope [10])

$$\frac{\mathrm{U}_0}{u\tau} \approx 5log_{10}\mathrm{Re} \tag{2.8}$$

Using $u_\tau^{new} = u_\tau$ and $\mathrm{Re}_{new} = 2.2\mathrm{Re}$

$$\mathrm{U}_0^{new} \approx \left(1 + \frac{log(2.2)}{log(\mathrm{Re})}\right)\mathrm{U}_0 \approx 1.07\mathrm{U}_0 \tag{2.9}$$

To summarize, the doubling of the friction Reynolds number while keeping the viscous length scale constant requires doubling the width and height of the canal and increasing the volumetric flow rate by a factor of 4.4. To allow the channel flow to become fully developed (which occurs at $\mathrm{L} \approx 140h$) the length of the channel must also be doubled. The doubling of the channel width would require a doubling of the measurement volume width to continue to allow measurement from the wall to the channel centerline (although little streamwise expansion of the measurement volume would be required due to the almost unchanged centerline velocity). This, plus the fourfold increase in pump capacity, would be quite large modifications to the experimental system in order to achieve a relatively modest increase in friction Reynolds number.

2.1.2 Working fluid

Water was chosen as a working fluid over air (the other typical choice for such experiments). To see why, the scaling of an equivalent (i. e. equal friction Reynolds number) channel flow is briefly considered here. From the scaling of the friction and bulk Reynolds numbers shown in equation 2.2 and the scaling of the particle diameter shown in equation 2.4 we can show that the channel width and velocity are functions of the friction Reynolds number, fluid viscosity, and particle diameter as follows:

$$\text{From equation 2.2} \quad \Rightarrow \quad \mathrm{Re} \approx \left(\frac{\mathrm{Re}_\tau}{0.09}\right)^{1/0.88} \quad \Rightarrow \quad \overline{\mathrm{U}} \approx \frac{\nu}{h}\left(\frac{\mathrm{Re}_\tau}{0.09}\right)^{1/0.88} \tag{2.10}$$

using the scaling in equation 2.4 in place of h

$$\overline{\mathrm{U}} \approx \frac{\nu}{\mathrm{Re}_\tau \mathrm{D}_p}\left(\frac{\mathrm{Re}_\tau}{0.09}\right)^{1/0.88} \quad \Rightarrow \quad \overline{\mathrm{U}} \approx 15.4\frac{\nu}{\mathrm{D}_p}\mathrm{Re}_\tau^{0.14} \tag{2.11}$$

From equation 2.11 we see directly that for equal particle diameters the bulk velocity in the channel scales simply with viscosity

$$\frac{\overline{\mathrm{U}}_{air}}{\overline{\mathrm{U}}_{water}} \approx \frac{\nu_{air}}{\nu_{water}} \approx 15.6 \quad \text{assuming P} = 1\,\text{bar, T} = 20\,^\circ\text{C} \tag{2.12}$$

If we assume an equal particle diameter and Re_τ then it follows from equation 2.4 that the channel widths are equal. The bulk velocity is a measure of the residence time of the particles in the PTV measurement volume. Equation 2.12 shows that for channels with similar friction Reynolds numbers, particle diameters, and measurement volume sizes the particle residence time in water is approximately fifteen times longer than in air.

The foregoing discussion assumed that the same particle diameters could be used in air and water. For tracer particles intended to measure acceleration, it has been shown [83] that using particle of unequal density to that of the carrier fluid produced significant bias in acceleration measurement, even when the Stokes numbers of the particles are within the range typically considered to be tracer particles. Tracer particles practical for use in PTV systems that are isodense with air are limited to helium soap bubbles, which have effective minimum diameters of 1 mm [84].

For a turbulent channel in air with $\mathrm{Re}_\tau = 1440$ and $\mathrm{D}_p = 1\,\text{mm}$, from equation 2.4

$$h = \mathrm{Re}_\tau \mathrm{D}_p = 1.45\,\text{m}$$

and from equation 2.11

$$\overline{\mathrm{U}} \approx 15.4\frac{\nu}{\mathrm{D}_p}\mathrm{Re}_\tau^{0.14} \approx 0.7\,\text{m}\,\text{s}^{-1}$$

The minimum particles diameter possible with helium bubbles is quite limiting. Following the above calculations and using the same aspect ratio and development length ratio as the water channel used in this experiment, the turbulent air channel would need to have dimensions of 3 m × 25 m × 225 m, a size clearly impractical despite the modest bulk velocity requirement. Note that equation 2.4 implies that these geometrical constraints are independent of viscosity, so this estimation of channel size is valid even for pressurized air facilities such as the the Princeton Superpipe facility[85].

2.1.3 Statistically 1-D stationary flow in measurement volume

Turbulent channel flow was chosen for this experiment of its relative simplicity; the wall-normal direction in the only direction of inhomogeneity. We attempt to approach this ideal flow condition in our measurement volume by placing our measurement volume in the spanwise center of the channel and at an adequate distance from the channel inlet. Note that for the purposes of this experiment the flow can be considered stationary and 1-D if conditioning the Eulerian and Lagrangian statistics *only on y* (the wall-normal coordinate) does not bias the results, i. e. the flow in the measurement volume can be considered stationary and 1-D if for an arbitrary Eulerian statistic F and an arbitrary Lagrangian statistic χ if the following conditions are satisfied:

$$\mathrm{F}(x,y,z,t) = \mathrm{F}(y) \quad \text{where } (x,y,z) \text{ is the measurement position at time } t \tag{2.13}$$

$$\chi(x_0,y_0,z_0,t_0,\tau) = \chi(y_0,\tau) \quad \text{where } (x_0,y_0,z_0) \text{ is the initial position at the initial time } t_0 \tag{2.14}$$

Depending on the size and position of the measurement volume these conditions are less stringent than more typical definitions of fully developed channel flow, which are concerned with the channel flow on a macro scale. To eliminate the dependence on the spanwise coordinate z the channel must have a high aspect ratio (L/h), to eliminate the dependence on the streamwise coordinate x the channel must allow a long enough development length (L), and to eliminate the dependence on time the water tunnel must operate in a constant manner (minimal pressure fluctuations, etc.). These three conditions are discussed in turn below.

Aspect ratio

Sufficiently large aspect ratio that the flow is homogeneous in the spanwise direction in the measurement volume. The aspect ratio used in this study, AR = $w/2h = 8.9$, is greater AR ≈ 7, which was found by Dean[86] to be the minimum aspect ratio necessary for two-dimensional channel flow. A minimum aspect ratio of six was considered by Monty[87] to be necessary to approach homogeneity in the spanwise direction at the spanwise center of the channel. Eulerian LDV measurements were made in the measurement volume at at various spanwise and wall-normal locations, and velocity statistics were found to be homogeneous in the spanwise direction within the measurement volume.

Development length

A long test section allows the turbulent channel flow to become fully developed (i. e. homogeneous in the streamwise direction) upstream of the measurement volume. There are relatively few experimental studies in the literature that have systematically tested development length for high aspect ratio channel flow. Comte-Bellot reports measurements made in a high aspect ratio (AR=13) wind tunnel[88] for three Reynolds numbers, and tested systematically the dependence of velocity statistics on distance from the inlet of wind tunnel. She found for $Re = 1.2 \times 10^5$ (double that of the Reynolds number used for measurements reported here) the velocity statistics in the spanwise center of the channel become homogeneous in the streamwise direction by L/$h = 118$. A similar experimental study 50 years later was performed by Monty[87], and found that full development does not occur until L/$h = 260$. This discrepancy by noting that turbulent channel flow develops from two boundary layers which grow towards the channel center at increasing distances

from the inlet. Monty notes that at $L/h = 140$ the channel is fully developed excepted for the very close to the channel center, where the two boundary layers are not fully merged.

The turbulent channel flow used in these experiments allows PTV measurements to be taken at a maximum distance of $L/h = 155$ from the channel inlet. Boundary layer trips, consisting of a single strand of copper wire flat against the channel wall, were placed at the channel entrance to ensure the even development of the boundary layers on both sides of the channel.

Stationary flow

Idealized turbulent channel flow is driven by a perfectly constant streamwise pressure gradient. Fluctuations in the pressure gradient from the water tunnel/pump must therefore be minimized. These pressure fluctuations are minimized by the design of the water tunnel, which uses an elevated reservoir to create the pressure gradient in the channel and decouple the flow in the channel from pump fluctuations.

2.1.4 Water tunnel requirements

The recirculating water tunnel must fulfill several additional tasks required by the experiments described in this thesis, the most important of which are described below. The current experimental setup was adapted from a previously existing setup at LEGI constructed by C. Lindquist and J.P. Thibault [89] shown in figure 2.3. The principle differences are the test section and the corresponding inlet converging section and diverging outlet section.

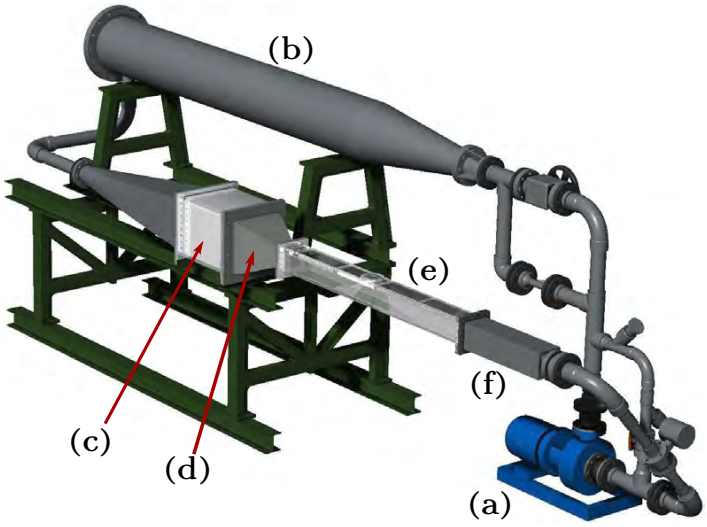

Figure 2.3: A CAD rendering of the water tunnel, reproduced from the thesis of C. Lindquist[89]. The various components of the water tunnel are labeled as (a) pump, (b) degassing chamber, (c) tranquilization chamber, (d) converging inlet section, (e) test section, and (f) convergent outlet section. Note that (d), (e), and (f) in this figure do not show the current configuration of the water tunnel.

Flow conditioning

Proper conditioning of the flow (with honeycomb grids, inlet contraction, etc.) is necessary to create uniform inlet conditions, and reduce large scale flow asymmetries.

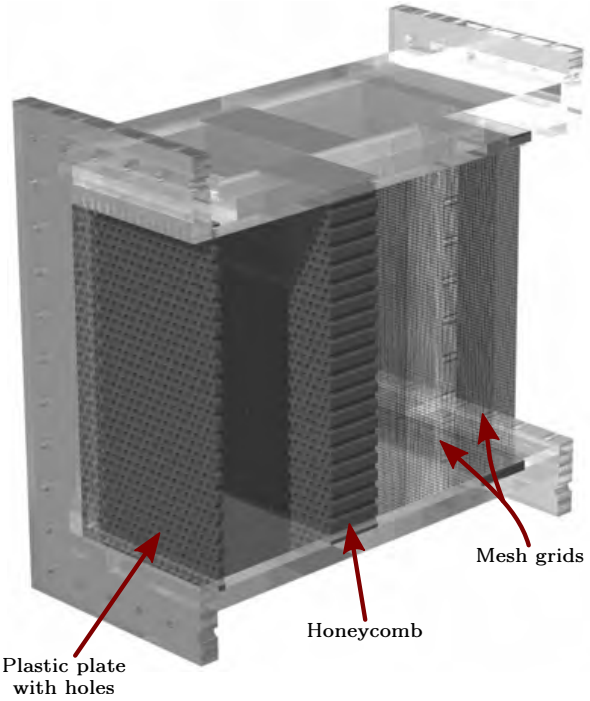

Figure 2.4: Detailed view of the tranquilization chamber, figure reproduced from the thesis of C. Lindquist[89]

Water temperature

Stability of water temperature is important because a change in temperature changes the kinematic viscosity of the water—a key parameter of the turbulence. Unregulated temperatures can range from 15 °C up to 40 °C after many hours of tunnel operation, which results in a range of kinematic viscosities between 1.14×10^{-6} m^2/s and 0.658×10^{-6} m^2/s. This variation in kinematic viscosity represents a significant change to the properties of the turbulence (see section 1.1.2). A cooling system was put in place to control the temperature of the water to between 16 °C and 20 °C, corresponding to a kinematic viscosity of 1.056×10^{-6} m^2/s ±5%. Results from measurements taken in this temperature are mixed together, and the 5% uncertainty in the value of the kinematic viscosity is taken into account in the error calculations of results.

The cooling system was realized with a closed circuit cooling loop, connected on one end to a large reservoir of cool water and on the other to a copper helix heat exchanger that was placed in the degassing chamber (labeled (b) in figure 2.3).

Vibration

The vibration of the turbulent channel, and crucially the vibration of the PTV cameras *relative* to the channel is an important potential source of PTV error that must be minimized. A heavy frame of 80 mm × 80 mm square aluminum tubing was used to stiffen the test section and provide mounting points for the PTV system (cameras, laser, etc.) such that the test section and the PTV system were fixed in relative position to each other as shown in figure 2.2. The efficacy of the frame in minimizing relative vibration was tested by an accelerometer affixed to the exterior of the test section, as well as direct imaging of the channel wall by the PTV system. Both of these tests showed showed minimal vibrations; the direct imaging test showed the wall moving relative to the camera ±30µm.

Optical access

Optical access to the tunnel is provided by the two windows shown in figure 2.2. The original design specified glass windows, but these proved too be to fragile to withstand the pressure fluctuations associated with the startup and shutdown of the water tunnel, and were replaced with thicker acrylic material. These thin windows allow the cameras and laser optical access the measurement volume with minimal distortion. The windows visible in figure 2.2 are longer than necessary for the PTV measurements because of the need to characterize and verify the flow development with the LDV as described in section 2.1.3.

2.1.5 Tracer particles

The tracer particles were chosen to approach the behavior of fluid particles as closely as experimental constraints allow. Lagrangian statistics, particularly of acceleration, require that a tracer particle be especially faithful to fluid particle trajectories [74]. This requirement is illustrated by considering the vortex trapping phenomenon, in which a fluid particle is entrained and trapped for a relatively long time in a vortex filament. If a tracer particle has even a slight tendency to exit the vortex (e. g. due to a slight inertia) there could be significant impact on the two-time Lagrangian statistics of acceleration, even if the particle inertia was low enough to be considered a good tracer particle for Eulerian PIV statistics in velocity.

Other than the requirement that the particle density be neutral [83, 74], and the Stokes number must be "small" there is not a consensus in the literature as to what constitutes a tracer particle suitable for Lagrangian acceleration measurement, especially in inhomogeneous turbulence. Recent work has suggested neutrally buoyant particles of $D_p/\eta < 5$[4] and $D_p/\eta < 2$[90] act as flow tracers in terms of acceleration variance in Von Karmen type flows, and that acceleration PDF shapes are preserved for particles even larger. The dependence of two-time Lagrangian statistics remains an open question.

In light of this uncertainty in the following criteria were used to select the tracer particles used in this study:

1. **Neutrally buoyant:** To avoid the spatial sampling bias [83, 91, 92, 93] which has been shown to exist for heavy particles even at quite low ($St = 0.1$) Stokes number.

2. $\mathbf{D_p/\eta < 2}$: To ensure tracer behavior with respect to acceleration variance.

3. $\mathbf{D_p/\delta_\nu \approx 1}$: To allow the unbiased Lagrangian measurement into the buffer layer ($5 < y^+ < 30$). Using tracer particles that allow measurement this close to the wall allows the unbiased measurement between the extremely inhomogeneous near wall zone that includes the peak of turbulent energy production ($y^+ = 11.8$)[94] and the almost homogeneous and isotropic zone near the channel centerline.

Based on the above criteria a fluorescent polystyrene particle with 10.2 µm diameter and $1.05\,\mathrm{g\,L^{-1}}$ density (Magsphere Inc, Pasadena California) was chosen as the tracer particle. Particle characteristics are examined in more depth in chapter 5, in the context of comparing tracer and non-tracer particles. The Stokes numbers of the tracer particles is seen to vary from 1.7×10^{-2} at $y^+ = 1$ to 9.8×10^{-4} at the channel centerline. These values of the Stokes number are similar to those from previous experimental PTV acceleration measurements[95]. The particle diameter is less than half of the Kolmogorov length scale η at the edge of the viscous sublayer ($y^+ = 5$), and smaller than the viscous wall scale δ_ν, which is smaller than the smaller structures known to exist in this flow.

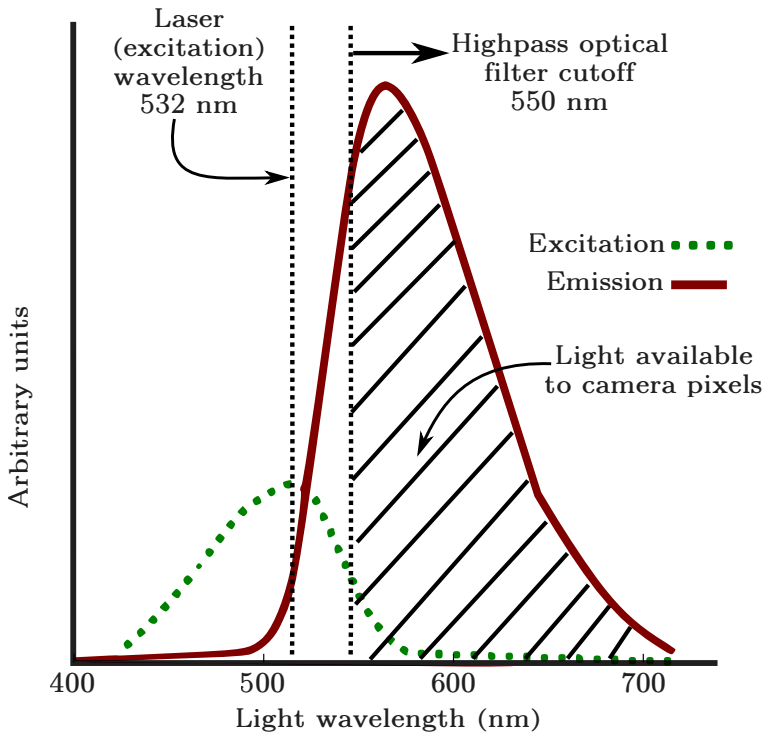

Figure 2.5: Excitation and emission spectra of the Magsphere 10 µm diameter fluorescent particles used as tracer particles in this study. This data was provide by Magsphere Inc., with annotations added by the author.

The use of fluorescent particles avoids two significant problems with measurements of this type:

1. It is difficult to avoid the presence of microbubbles in the channel, which are difficult to distinguish from the tracer particles in the PTV images. This problem will be further elaborated in the sections discussing the use of heavy particles (which are not fluorescent). Using fluorescent particles in conjunction with optical filters on the cameras ensures that only the fluorescent particles are seen in the images. An illustration of the separation between the laser wavelength and the emission wavelength is shown in figure 2.5. Microbubble contamination in PIV measurements may be considered acceptable for Eulerian velocity measurements, as microbubbles have fairly low Stokes numbers, but they pose a more serious problem to Lagrangian acceleration measurements, as discussed above.

2. Optical measurement techniques such as PIV and PTV are known to have problems near walls, where the reflection of the light source may obscure particle images[96]. Optical filters effectively suppress the wall reflections, allowing clear particle images to be seen in the images arbitrarily close to the wall.

2.2 Particle tracking velocimetry

Particle tracking velocimetry (PTV), sometimes also referred to as Lagrangian Particle Tracking, is a used to measure the position and displacement of particles in a system. In the context of fluid mechanics research PTV uses particles seeded in the flow and observed by one or more cameras. Multiple cameras allow reconstruction of particle trajectories in three dimensions, sometimes specified at 3-D PTV to distinguish it from single-camera systems that can only measure two components of the particle trajectory. Synchronized images from multiple cameras observing the same particle are used to reconstruct the position of the particle in real space at a given time. PTV algorithms are then used to trace the evolution of the particle position in real space over time, resulting in particle trajectories, i. e. direct Lagrangian measurements. The PTV measurements in the turbulent channel will be discussed as follows: The physical and optical aspects of the PTV system are detailed in section 2.2.1. Section 2.2.2 explains the image processing techniques used to find the centers of the particle images (including how overlapping particle images are handled). The calibration method used to obtain the transform function between image space and physical space is presented in section 2.2.3. The algorithms used to track the particles, including the reconstruction of "broken" trajectories is outlined in section 2.2.4. A discussion of the error and statistical bias associated with these PTV measurements is found in section 2.4. Finally a brief sketch of the challenges associated with the size of the raw datasets— over 80 terabytes in total—is found in section 2.3.1.

2.2.1 Physical and optical considerations

The PTV system used for these experiments was designed to resolve the smallest scales of the turbulent flow, which implies that the particles must be smaller than the smallest length scales we wish to measure, and the acquisition frequency must be fast enough to resolve[1] the smallest time scales we wish to measure. Given that these constraints are satisfied, the PTV system should be capable of measuring the largest measurement volume possible. A relatively large measurement volume is especially important in a turbulent flow with a non-zero mean velocity, because the mean velocity will sweep particles through the measurement volume and thus limit the residence time of the particles. Table 2.1 outlines the relevant PTV system design parameters and their effects.

The tracer particles were chosen based on the flow characteristics as discussed above. These particles are smaller than the particles typically used for PTV, and determine much of the design of this PTV system. Using table 2.1 as a guide, and noting that a large measurement volume and good small-scale resolution are conflicting design goals, the general strategy was to maximize the measurement volume while maintaining a particle image size and signal-to-noise ratio (SNR) at the lowest levels possible in order to adequately measure acceleration. In order to ameliorate the effects of small particle image size and low SNR the laser power and image acquisition frequency was pushed as high as was practically possible.

The tracer particles were found to have particle image diameters of approximately 2-3 pixels when a 1:1 magnification macro objective was used with the cameras. This

[1] Where fast enough here means at least as fast as the Nyquist frequency, i. e. twice as fast as the smallest timescale. In practice, higher sampling rates are necessary to well-resolve noisy signals, see section 2.4 for details.)

Table 2.1: Design parameters in PTV system

Design parameters:	Effect on small scale resolution:	Effect on large scale resolution:
Magnification:	Higher magnification ⇒ larger particle images ⇒ better SNR in centroid finding, up to ~ 10 pixel diameter of particle images	Lower magnification ⇒ larger measurement volume ⇒ longer particle residence time
Lens aperture:	More open ⇒ brighter and larger particle images ⇒ better SNR in centroid finding	More closed ⇒ greater depth of field ⇒ larger measurement volume
Acquisition frequency:	Faster acquisition ⇒ more particle positions ⇒ better SNR in filtered data, also less ambiguity in particle tracking. Slower acquisition ⇒ brighter particle images ⇒ better SNR in centroid	Higher acquisition frequency ⇒ shorter films ⇒ in principle shorter trajectories, although in practice the mean flow in the channel means particle residence times are much shorter than the length of the film
Laser power:	More laser power ⇒ brighter particle images ⇒ better SNR in centroid finding	Larger measurement volume ⇒ lower light power density ⇒ lower SNR in centroid finding

particle image diameter is the minimum necessary to achieve sub-pixel accuracy, thus 1:1 magnification was taken to be the minimum magnification required for this PTV system. The measurement volume is determined by the magnification and depths of field of the two objectives. Let L, W, and D, be the streamwise, wall-normal, and spanwise dimensions of the measurement volume, respectively. In the configuration of the two cameras shown in figure 2.2, the vertical camera observes the plane L x W, and D is the depth of field. The horizontal camera observes the plane L x D, and W is the depth of field. Thus L is directly observed by both cameras and determined uniquely by the magnification, but W and D are functions of the depths of field of the horizontal and vertical cameras, respectively. Depth of field is a function of the magnification and aperture setting of the objective, as well as level of "fuzziness" considered acceptable. In the camera configuration shown in 2.2, with 1:1 macro objectives with apertures closed to their maximum setting, we achieve a measurement volume of 34 mm × 20 mm × 12 mm. These dimensions represent the maximum volume in which particle images can be resolved, and includes zones in which the particle appear quite out-of-focus, and thus appear much larger and less bright than particles in the focal planes. This is especially true for the images from the horizontal camera, which is oriented such that the depth of field must be deep enough to encompass the distance from the wall to the channel center. Sample images illustrating this effect are shown and discussed in section 2.2.2.

PTV system hardware

The PTV system used in this experiment is comprised of the following hardware:

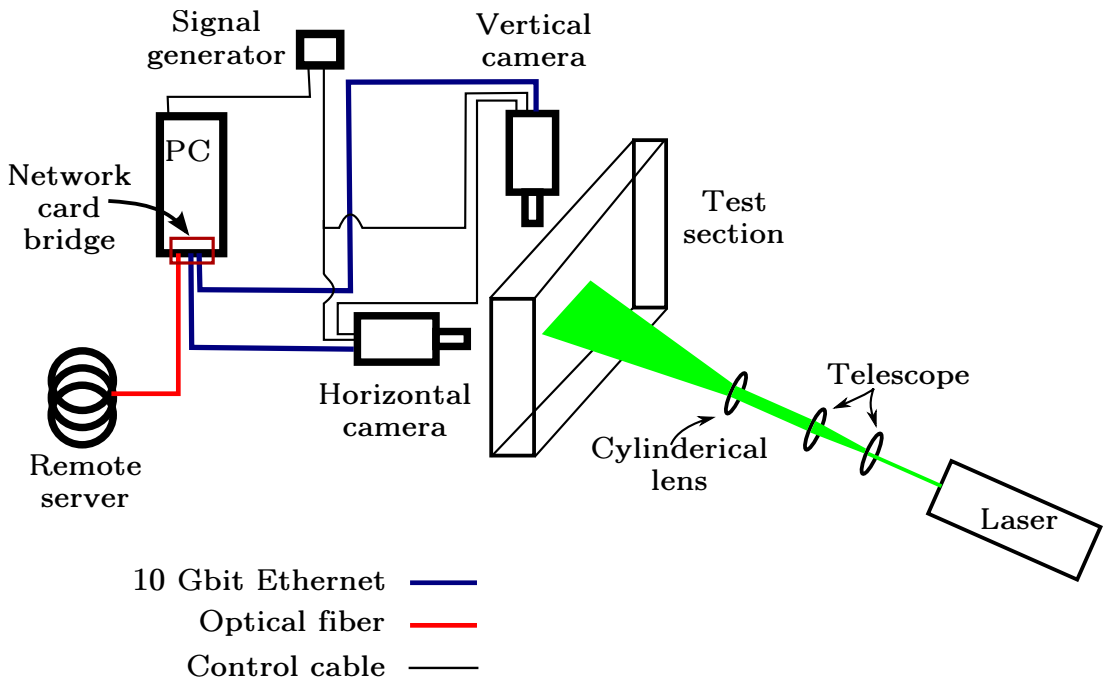

Figure 2.6: Schematic view of the PTV system, including the cameras and their data and control connections; the laser and associated optics.

- Two Phantom v2511 high speed digital cameras[2] recording 800 pixel × 1280 pixel 12bit grey scale images (16500 images per film). Maximum acquisition rate at full-resolution is 25 000 frames per second.
- Sigma 150 mm macro objective, 1:1 magnification
- Tamron 180 mm macro objective, 1:1 magnification
- High-pass optical filters OD4 550 nm cutoff frequency (Edmunds Optics) with 3-D printed objective adapter to block laser light from cameras
- 25 W continuous laser, 532 nm emission frequency
- Laser-line lenses and mirrors to shape and direct laser beam in to thick laser plane that illuminates the measurement volume in the test section
- PC with a high 10 Gbit ethernet network card with two ports to connect to cameras, and a network card with fiber optic connection to remote server
- Signal generator used to coordinate the two cameras

Data acquisition process

The data acquisition process is as follows:

1. The main water channel pump is brought up to operating speed, the cooling system and all of the PTV instruments are turned on, and the system is allowed to reach steady-state.

[2] A v2511 camera was kindly lent by P. Marmottant and by N. Plihon.

2. A script sends a prompt to the signal generator to send the go signal to the two cameras, starting the acquisition. The script then begins monitoring the saving of the films on the remote server.

3. After receiving the go signal from the signal generator the cameras start the acquisition, and each frame of the films are synced by the master/slave connection between the cameras.

4. When the acquisition of the films is finished (after 0.6 seconds) the cameras automatically begin saving the films in a custom binary format on the remote RAID server, using the local PC as a network bridge. Each film consists of 16541 images, and has a size on disk of 20 Gb.

5. After the films have finished saving (1.5 minutes) the cameras are reset to acquisition mode. The laser remains on while the films are being saved .

6. The script notes that the films have finished saving, and after a brief delay prompts the signal generator to send the go signal to the cameras, restarting the acquisition cycle.

2.2.2 Particle finding in images

The first step of the data processing used to transform the raw films into a usable dataset of Lagrangian trajectories is the extraction of the image coordinates of the particle centers. This is an image processing problem with an extensive literature, and many approaches have been proposed. The images taken with the PTV system described in section 2.2.1 have a few particularities that constrain the choice of an image process/particle finding strategy.

1. **Low SNR:** Closing the objective apertures as much as possible, using fluorescent particles, an acquisition rate of 25000 frames per second, and often out-of-focus particle images results in very dim particle images, despite the high laser power and the sensitive camera sensor. SNR is naturally defined for this PTV application as:

$$\mathrm{SNR} = \frac{\overline{\mathrm{S}} - \overline{\mathrm{N}}}{\sqrt{var(\mathrm{N})}} \tag{2.15}$$

   Where S and N are the pixel values associated with the tracked particles and all of the other pixels, respectively. This definition treats as noise all those pixels that are not associated with particle trajectories, which includes random sensor noise (typical length 1 pixel, uncorrelated in time), organized electronics noise (typical length of several pixels, correlated in time), and real particles that are not part of trajectories, such as particles on the boundaries of the measurement volume. SNR ratios are typically between 6 and 12 in these measurements, which is quite low. The implications of these levels of SNR on the measurement error is elaborated in section 2.4.

   Low SNR implies reduced effective dynamic range in the images. For example, the particle image in figure 2.7 shows a maximum pixel intesity value of 90 and a noise floor of approximately 20. The dynamic range of the particle image is compressed, i. e. the images are effectively 6-bit rather than the full 12-bit resolution of the camera. This increased discretization decreases particle center finding precision.

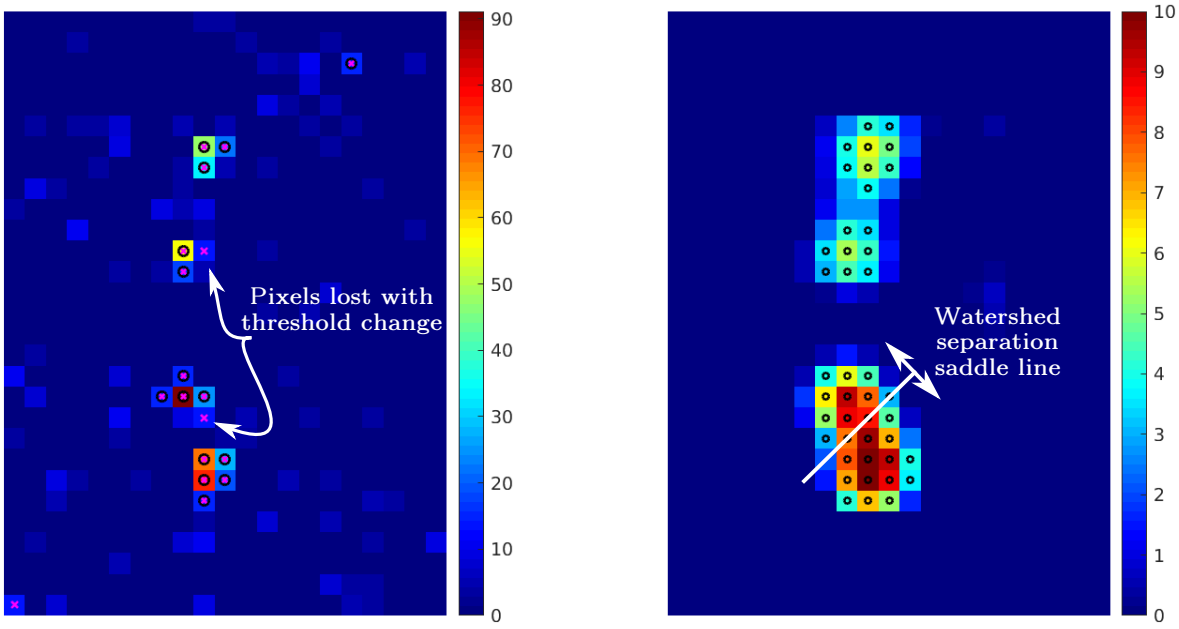

Figure 2.7: Four particle image examples: Unfiltered image on left, illustrating the pixels lost with a change in threshold from 13 (magenta x markers) to 14 (black circle markers), and the filtered image image on the right, illustrating the watershed line on overlapping particle images.

2. **Small particle images:** By design the particle images, especially those in or near the focal planes, are on the order of two pixels.

3. **Particle image distortion:** Geometrical constraints, especially the narrow optical access on the vertical camera, caused optical distortions of particle images that changed as a function of wall distance.

After testing several methods, the strategy chosen for this application was a image filter followed by thresholding and a simple weighted centroid algorithm. While this strategy is less accurate than others for synthetic PTV of good quality [97], it was found to be more robust for the low SNR data presented in this thesis, consistent with tests of particle finding methods on low SNR images by Cheezum et al [98].

Weighted centroid finding

The particle center locations in image-space using a weighted centroid method, which is a simple centroid calculation weighted by pixel intensities. This centroid $(\overline{x}, \overline{y})$ is calculated as follows:

$$\overline{x} = \frac{\sum_{i=1}^{n} \mathrm{I}_i x_i}{\sum_{i=1}^{n} \mathrm{I}_i} \qquad \overline{y} = \frac{\sum_{i=1}^{n} \mathrm{I}_i y_i}{\sum_{i=1}^{n} \mathrm{I}_i} \tag{2.16}$$

Where I is the pixel intensity, and n is the number of pixels in the particle images. For isolated particles the particle image has a simple definition: all those pixels that have a gray value above the threshold, that share an edge with at least one other pixel in the particle image, and have an overall number of pixels greater than a minimum particle image size. This definition is illustrated in figure 2.7, which also shows the more complicated definition of a particle image in the case of overlapping particle images.

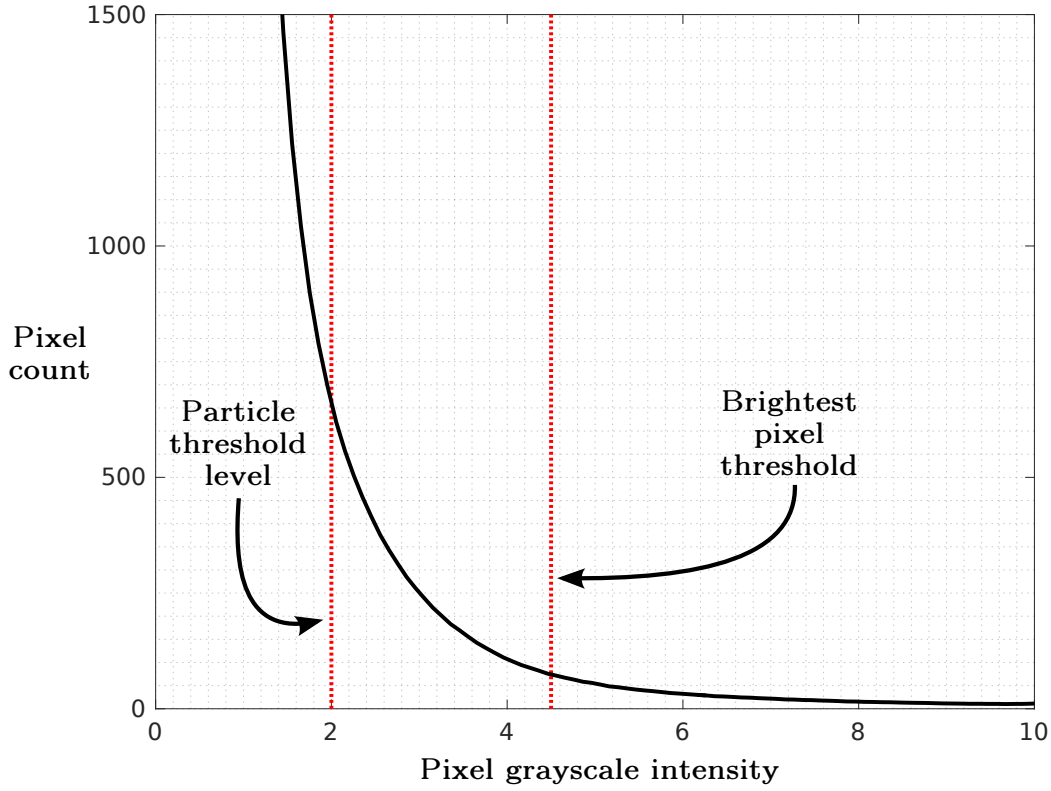

Figure 2.8: Histogram of pixel intensities (typical) from vertical camera

Image filtering

In principal a linear image filter has no effect on the weighted centroid computed from equation 2.16. However the low SNR of the images recording in these experiments requires the use of pixel intensity threshold values relatively close to the pixel intensity values of the particle images themselves. For small, dim particle images this is an unstable manner in which to calculate the particle center, as illustrated in 2.7, where a small subset of the raw image is shown on the left. Pixels above a threshold of 13 are marked with magenta x's, and pixels above a threshold of 14 are marked with black circles. This small change in threshold results in a lost pixel from two of the particle images shown in this example, which can change significantly the weighted centroid calculated from equation 2.16, especially for small particle images. In order to ameliorate this problem a bandpass image filter[99] is applied to the raw images (the filtered image is shown on the right in figure 2.7) which suppresses the single pixel noise and enlarges and smooths the particle images. Small changes in threshold will still result in the loss of pixels from particle images, but the effect of this pixel loss (or gain) on the weighted centroid results is lessened. Other image filters were considered and tested, such as the Wiener image filter [100], but no significant improvement over the bandpass filter was found for this application.

Image thresholding

Image thresholding, or segmentation, is a common procedure in many image processing applications, and is typically based on the histogram of pixel values. If there is a separation between the pixels of interest and background pixels there are robust methods[101]of choosing a threshold.

Overlapping particle images

If particle images overlap, as illustrated in figure 2.7, then using equation 2.16 to calculate the particle centers will give the centroid of the combined particle image instead of the two (or more) particle center locations. Here we follow the algorithm outlined by Dracos[102], which splits a particle image into as many parts as there are local maxima with a watershed algorithm, then assigns border pixels (those pixels on the saddle line between local maxima, marked with a black line in figure 2.7) to one side or the other based on the brightest neighboring pixel.

Parameter optimization

The parameters in the particle center finding algorithm outlined in the foregoing sections, the basic threshold, the threshold for the brightest pixel in a particle image, the image filter parameters, and the minimum particle image size, are tuned in order to maximize accuracy and the overall efficiency of the data processing, while minimizing bias. Accuracy is maximized by avoiding particles with a low SNR (low maximum brightness, small size, etc.). Efficiency is maximized by avoiding particles that will not become part of trajectories (either because they are a result of noise or because the are moving in and out of the measurement volume). Bias is minimized by not discriminating too much based on particle image size and power, as these quantities change as a function of position in the measurement volume (see section 2.2.1). This is a multi-objective optimization with conflicting objectives, which is solved in this case by placing the preference on maximizing the lack of bias, while maintaining sufficient accuracy to allow the calculation of acceleration, and permitting quite inefficient processing. Practically speaking this means that thresholds are set quite low and thus many more particle centers are calculated than are tracked. 3-D correspondences must be calculated for all particle centers found, and so having many untracked particles limits the particle seeding density (and thus ultimately the number of trajectories per film), which is discussed in more detail in section 2.2.4.

2.2.3 Calibration and stereo matching

The calibration of a 3-D PTV system consists of calculating a transform function that calculates real-space coordinates from a set of arbitrary image coordinates from multiple cameras:

$$\mathrm{X,Y,Z} = \mathrm{T}\left([x^1, y^1], [x^2, y^2] \ldots [x^n, y^n]\right) \tag{2.17}$$

Where X, Y, Z are real-space coordinates, x, y are image-space coordinates, and n is the total number of cameras. The application of the resulting transform is called stereo matching. The calibration/stereo matching is composed of three steps: the measurement of points throughout the measurement volume for which real-space coordinates are known a priori, the selection and calculation of the transformation function T, and the application of this transformation function to particle positions in images coordinates obtained from the particle center finding procedure described in section 2.2.2; these three steps are described in detail here.

The measurement of known points for calibration.

In order to calculate the transform T a set of points of known position must be measured by the cameras. These known points should be distributed in the measurement volume and must be of known distance to the wall (which is equivalent to saying that the streamwise

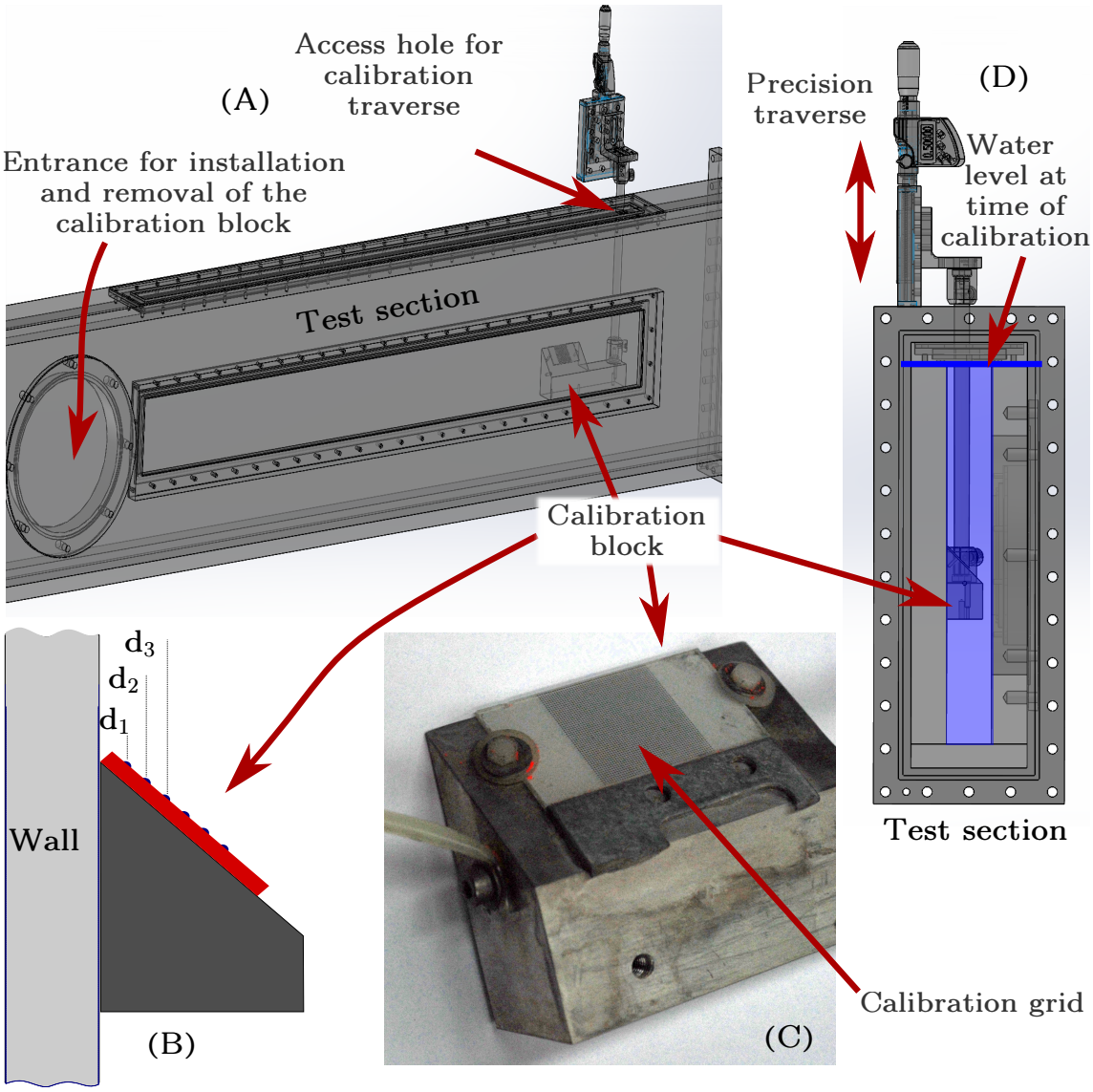

Figure 2.9: The calibration block shown in the test section in the position used during the calibration (A), a sketch of the calibration grid and the distances from the grid points to the wall (B), a close-up photograph showing the calibration grid mounted on the calibration block (C), and an end view of the calibration block and traverse system in-situ (D).

and spanwise coordinate of the world origin point is relatively arbitrary, but the wall-normal coordinate must be at a known distance to the wall). The realization of these calibration points was achieved by the use of a calibration grid of known dot spacing mounted of a block, as shown in figure 2.9. The calibration block was carefully made such there are two precision-machined surfaces—one that touches the wall, and the other at 45° to the first and on which the calibration grid is mounted. The calibration grid (Max Levy Autograph, Philadelphia, USA) is a regular array of 0.25 mm diameter dots etched on glass at 0.5 mm spacing (overall array size is 25 mm × 25 mm). The calibration grid was custom modified by the manufacturer such that the edge of the calibration grid substrate is of known distance to the first row of grid points. This edge is carefully aligned with the edge of the calibration block, such that when the surface of the calibration block is touching the wall distance between all grid points and the wall is known.

One of the difficulties inherent in this experimental setup in the lack of access to the interior of the test section. For example, the calibration must occur when the test section is

full of water (due to the difference in the optical properties of air and water), but in order to fill the test section with water all of the access ports in the test section must be closed. The calibration procedure must allow the precision movement of the calibration block *while the test section is full of water and the access ports closed.* This was achieved by the following procedure: An access hole slightly larger than the post used to displace the calibration block was machined into the top access port. When the tunnel is running this hole is plugged such that the inner surface is smooth and flush with the rest of the test section. The post is attached to the calibration block, and a semi-rigid tube is threaded through the access hole and attached to the post. The block-post assembly is then introduced into the test section by the round access port noted in figure 2.9 (A), and the semi-rigid tube is used to pull the calibration block-post assembly into place, and pull the post up though the access hole where it can then be attached to the precision traverse. The traverse is then carefully adjusted until the back surface of the calibration block is parallel to and in contact with the wall of the test section. The round access port may then be closed, and the test section filled with water up to the point where the top window is wetted, put water is just beginning to overflow the access hole in the top window. The system is then ready for calibration, and images from both cameras are taken of the calibration grid, the calibration is shifted up or down by a fixed distance with the precision traverse, new images are taken with the cameras, and the process is continued until the entire measurement volume is traversed and several image pairs are recorded. The calibration block is then removed in the reverse process by which it was installed. While complicated, this procedure has the advantage of leaving the top window in place, and thus avoiding potential changes in the optical path associated with a slight change in the seating of the top window after its re-installation.

The calculation of the calibration transform

There are several strategies commonly used for 3-D PTV calibration; three common strategies were tested by Joshi et al[103] with real and synthetic PTV and PIV images. Another technique was recently published[104] that uses physical arguments (light rays do not bend except at material interfaces) to simplify and improve the accuracy of traditional calibration methods. One of the key findings of Joshi and coworkers was that a linear transformation (i. e. the Hall method) has comparable error and accuracy to non-linear transformations (specifically the Tsai and Soloff methods) for cases in which there is little optical distortion. The experimental setup used in this thesis consisted of two cameras, each perpendicular to the interface, and each using a long-focal-length macro lens with a relatively shallow depth of field. This setup allows the use of a simple linear, projective transformation with minimal error.

A linear transform function is of the form

$$\mathbf{x}^i = \mathrm{P}_i \mathbf{X} \tag{2.18}$$

Where P_i is the camera matrix for camera i, and $\mathbf{x}^i$ are the associated image coordinates in the image of the ith camera. The camera matrix P may be interpreted as the product of linear transforms, for example

$$\mathrm{P} = \mathrm{RT}... \tag{2.19}$$

Where R is the rotation matrix, T is the translation matrix, etc. In the literature the camera matrix is often considered to be the sum of a matrix composed of extrinsic parameters (translation, rotation, etc.) and intrinsic camera parameters . As a practical matter this decomposition is not necessary, and the camera matrices may be considered to an arbitrary

projective transformation. Projective transformations preserve direction, so for each camera

$$\mathbf{x} = \mathrm{P}\mathbf{X} \tag{2.20}$$

$$\mathbf{x} \times \mathrm{P}\mathbf{X} = \mathbf{0} \tag{2.21}$$

The above is a system of equations with the number of equations equal to the number of grid points and 12 unknowns (the 12 elements of the camera matrix P). Due to the presence of non-projective optical distortions, error in the placement of the calibration grid, and error in the localization of the grid points in the calibration image equation 2.21 is properly written as

$$\mathbf{x} \times \mathrm{P}\mathbf{X} = \epsilon \tag{2.22}$$

The strategy is to minimize the calibration error by minimizing ϵ in the system of equations 2.22, which is achieved by a non-linear least squares solver. Further details of this calculation may be found in reference [105].

Stereo-matching

Stereo-matching is the process of finding the same particle in two (or more) images. The real position of a particle is at the intersection of the lines of sight for that particle in all of the cameras. The error in both the particle center finding in each image and the calculation of the calibration transform means that in general these lines of sight to not intersect. The task of stereo-matching is for each particle in a given image, find the particle in the other image (or images) that minimize the minimum distance between their lines of sight, rejecting those matches that have a minimum distance above a given threshold. Stereo-matching is typically quite computationally expensive, as the minimum distance between two lines must be calculated p^n times per time-step, where p is the number of particles per image and n is the number of cameras.

The use of a simple projective calibration such as that described in section 2.2.3 allows a very efficient matricial calculation for stereo-matching. Briefly, a purely projective transformation admits a direct linear mapping from one image coordinate to the other

$$\mathbf{x}_1 \mathrm{F} \mathbf{x}_2 = 0 \tag{2.23}$$

where $\mathbf{x}_1$ and $\mathbf{x}_2$ are image coordinates from the first and second cameras, respectively, and F is the mapping function (often referred to as the fundamental matrix in the context of computer vision). The relationship shown in equation 2.23 may also be written in terms of epipolar lines, i. e. if $\mathbf{l}$ is the epipolar line corresponding image coordinate $\mathbf{x}$, then

$$\mathbf{l}_1 = \mathrm{F}\mathbf{x}_1 \tag{2.24}$$

$$\mathbf{l}_2 = \mathrm{F}\mathbf{x}_2 \tag{2.25}$$

These epipolar lines are the projection of the possible positions of the particle in image space 2 given the particle position in image space 1 (or vice versa). This relationship is illustrated in figure 2.10. Because of the error associated with the particle center finding and the calculation of F the epipolar lines do not intersect the particle in image space, and there is a distance d associated with the minimum distance between the particle image and the epipolar line. Projective geometry allows the calculation of F from the two camera matrices P_1 and P_2:

$$\mathrm{F} = [\mathrm{P}_2\mathrm{C}] \times \mathrm{P}_2\mathrm{P}_1^{+} \quad \text{where} \quad \mathrm{P}_1\mathrm{P}_1^{+} = \mathrm{I} \quad \text{and} \quad \mathrm{P}_1\mathrm{C} = \mathbf{0} \tag{2.26}$$

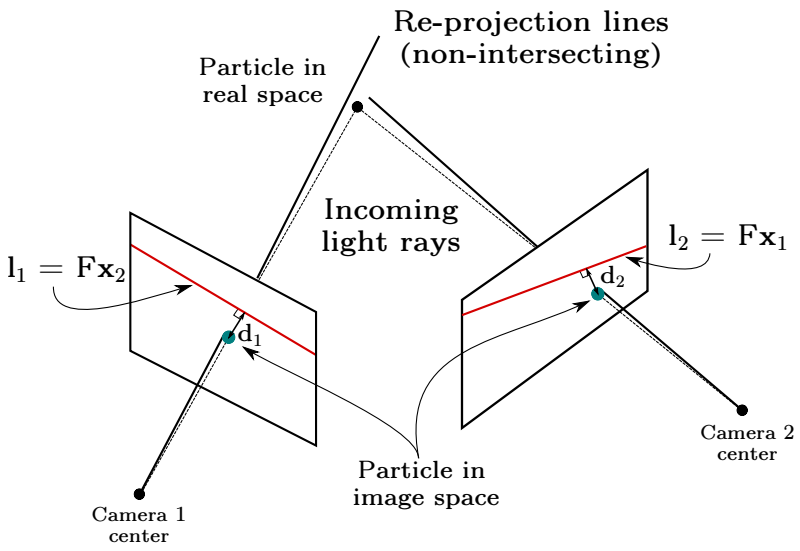

Figure 2.10: Schematic of a real particle which projects its light on the two camera planes, the re-projection lines (which have some error from the particle center finding and the calibration), and the corresponding epipolar lines $l = Fx$. The distances d_1 and d_2, the minimum distance between the epipolar line and the particle position in image coordinates, are also shown.

The proof of equation 2.26 is found in reference [105]. Note that one could calculate F directly from the calibration images in a way similar to the calculations for the camera matrices, but the camera matrices P_1, P_2 are in any case necessary for the final triangulation step described below, and so equation 2.26 may be used directly.

The relationship in equation 2.23 is used to determine particle correspondences. The $\mathbf{x}_1 F \mathbf{x}_2$ is calculated at each time-step, yielding a matrix of size $n_1 \times n_2$, where n_1, n_2 are the number of particles found by camera 1 and camera 2, respectively. All elements in this correspondence matrix below a certain threshold represent a pair of particle images that correspond to one real particle. If this threshold is set too low real correspondences may be missed, and if it is set too high there will me many false matches. In practice this threshold is adjusted to be high enough such that all of the real correspondences are captured, even if many false correspondences are generated. The tracking algorithm attempts to track the particles from these false correspondences and generally fails, as particles arising from false correspondences are not part of trajectories that are coherent over time.

Once the stereo-matching has been completed it is a simple matter to use the camera matrices P_1, P_2 to solve the combined equations

$$\mathbf{x}_1 = P_1 \mathbf{X} \tag{2.27}$$

$$\mathbf{x}_2 = P_2 \mathbf{X} \tag{2.28}$$

where $\mathbf{x}_1$ and $\mathbf{x}_2$ are *corresponding* image coordinates and $\mathbf{X}$ is the real-space coordinate.

2.2.4 Particle tracking

After the particle centers have been found in image space as described in section 2.2.2, and these image space coordinates have been mapped into real space as described in section 2.2.3 we are left with a list of four dimensional points $\mathbf{X}^i(x, y, z, t)$ for $i = 1, 2, \ldots n$ where n is the total number of particles found. This set of particles is transformed into a set of particle trajectories by the particle tracking algorithm shown in figure 2.11. This algorithm was implemented in Matlab, using an code initially based on a 2D tracking code written by Nicholas Ouellette, which was quite substantially modified from the original.

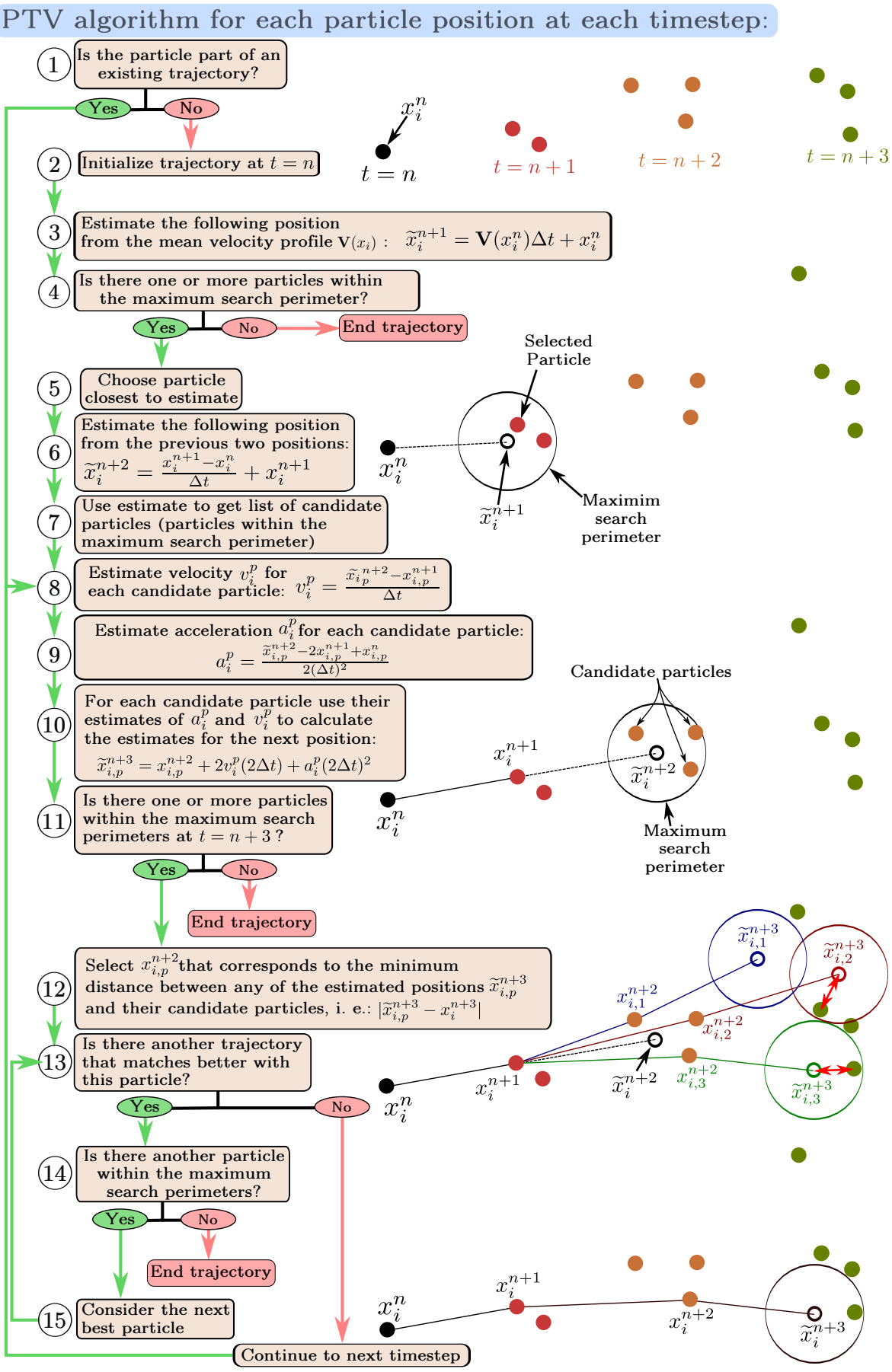

Figure 2.11: Particle tracking algorithm

Particle tracking algorithms have multiple parameters that need to be tuned depending on the measurement system. The overall strategy and balance between the potentially competing objectives of the algorithm is explained here, and the step-by-step details of the algorithm implementation is detailed in figure 2.11. This task can be intuitively understood by watching a PTV film following the same particle from one frame to the next. If the frequency of the image acquisition is high the particle moves relatively little between frames, and thus following a particle is easier. Conversely, if there are many particles close together in the image it becomes more difficult to be certain that a given particle is the same particle that was seen in the previous frame. Based on this intuitive notion of "ease of following" there are few key parameters that determine the level of difficulty of the particle tracking, which are shown in table 2.2.

Of the parameters listed in table 2.2 only particle density is easily adjusted for a given experimental set-up. This project does not attempt to measure two-particle statistics (e.g. pair dispersion or fluctuating spatial gradients), so particle density may be set rather arbitrarily, only recalling that lower particle density means that fewer particle trajectories are measured per film. The global strategy is then to balance the particle density (and thus the "efficiency" of the data collection) against the complexity and computational cost of the tracking algorithm.

Table 2.2: Key parameter affecting ease of particle tracking

PTV parameters	**Effect on tracking**	
Particle density	Lower particle density	$\Longrightarrow$ easier to track
Number of cameras	More cameras	$\Longrightarrow$ easier to track
Acquisition frequency	Higher acquisition frequency	$\Longrightarrow$ easier to track
Mean flow	Greater mean flow-to-turbulence ratio	$\Longrightarrow$ easier to track

The algorithm chosen was based on the 4 frame best estimate method of Ouellette *et al*[97]. Velocity and acceleration for each trajectory are estimated from past particle positions in order to estimate future particle positions, then the particle closest to this estimate is considered to be part of the trajectory. More complicated methods using more than three points, and therefore less sensitive to particle position noise, could be considered, but adequate performance was found using this algorithm at particle densities of up to 500 particles per image. The algorithm described in figure 2.11 was applied to the data using a rather large value for the maximum search parameter, which often results in spurious positions at the beginning and endings of the trajectory. These spurious extreme values, along with the fact that trajectories are often artificially broken when the view of a particle is temporarily obstructed in one or both of the cameras, required the use of a post-processing step to repair and reconnect the trajectories.

Trajectory reconnection and repair

Trajectories may be broken or may contain spurious positions for many reasons: the view of a particle is temporarily obstructed, the particle moves into and out of the volume of measure, or the tracking algorithm may have included a particle position that is not part of

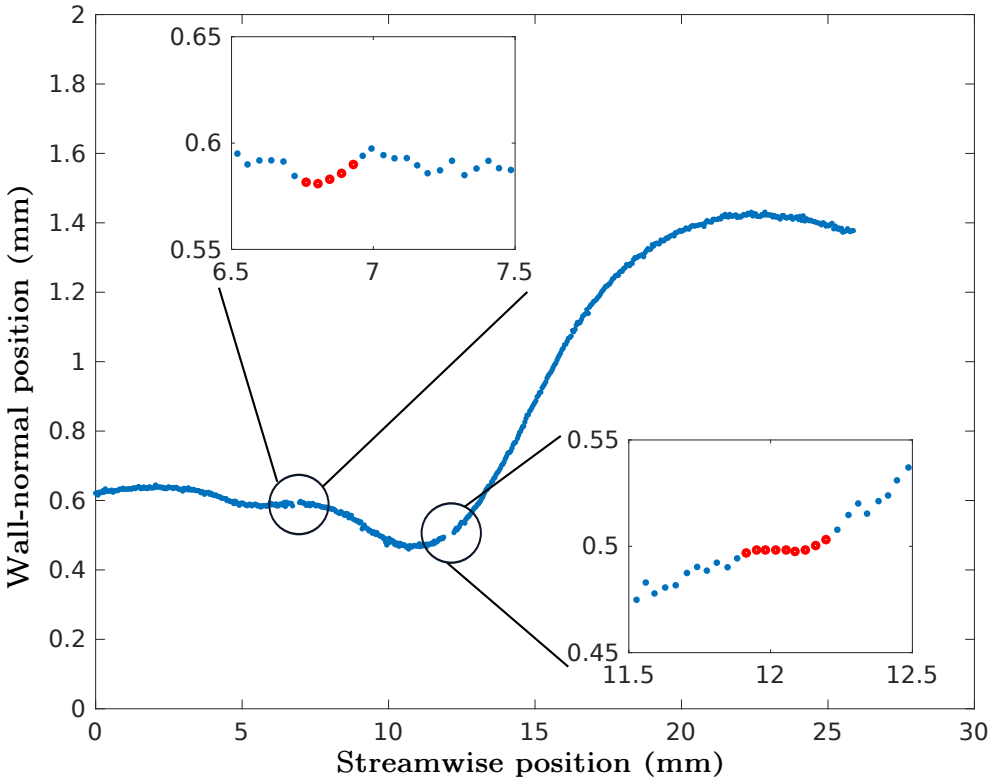

Figure 2.12: Three tracer particle trajectories (shown in the 2-D x-y projection) that were reconnected. The two gaps in the trajectory are highlighted, with the interpolated points shown in red.

the real particle trajectory. The repair and especially reconnection of these trajectories is important because longer trajectories permit a greater convergence of Lagrangian statistics at longer times. A two-camera PTV system has no redundancy, and so a temporary occlusion of one particle image is sufficient to break the trajectory. An attempt was made to reconnect and repair the trajectories within the limits of reasonable interpolation, based on the physics of the particle dynamics.

Trajectories are repaired by removing points that are non-physical, usually at the beginning or ending of the trajectory, but occasionally also in the middle, when the tracking algorithm confuses two real particle trajectories and create a "jump" from one to the other. In the case of spurious extreme values the ends of the trajectory are simple trimmed to remove them. In the case of spurious values in the middle of a trajectory the trajectory is split in two, and the extreme value removed. What constitutes a spurious extreme value was determined empirically by regarding the histograms of $x_i^{n+1} - x_i^n$, where $i = 1,2,3$ and n is the time-step. One could also use the fact that real high acceleration events are correlated in time but spurious extreme values are generally delta correlated , but this was not found to be necessary in this case.

Trajectories are reconnected by identifying the ends of trajectories that are "close" in $[x, y, z, t]$- space, deciding if they are two pieces of the same real trajectory, and interpolating between them. This task was accomplished for each trajectory by the following steps:

1. Estimate the velocity v_i at the end of the trajectory

2. For a given trajectory that has a final position at time t_n, find all trajectories that have beginning points t such that $t_n < t < t_n + t_{limit}$, where t_{limit} is some time limit beyond which trajectories are not reconnected.

3. For all candidate trajectories that meet the above condition, use the time difference between the first point of the candidate trajectory and t_N and the estimated velocity to calculate an estimated position, shown schematically in figure 2.13 as colored hollow points corresponding to the three candidate tracks.

4. The candidate trajectory corresponding with the smallest three-dimensional distance between the beginning point of the candidate trajectory and the estimated position is chosen to be reconnected, as long as this minimum distance is below a given threshold.

5. The missing positions are interpolated using a penalized least-squares method[106] individually in all three dimensions, and example of which is shown in 2.12.

The parameters in this process, the limits in time (t_{limit}) and distance in x, y, z beyond which trajectory reconnection is not permitted, are chosen to minimize false connections. Despite this conservative approach, this reconnection step significantly increased the mean trajectory length and the convergence of Lagrangian statistics at longer times.

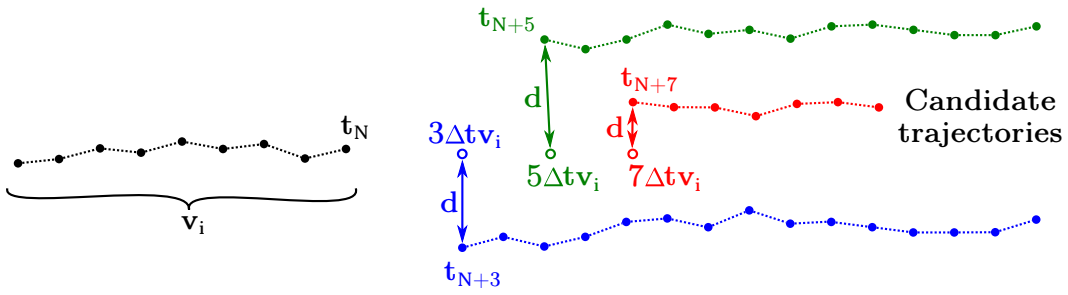

Figure 2.13: Schematic of the reconnection algorithm.

2.3 Data processing

Three dimensional calibrated particle trajectories are the elemental form of data collected in this study. However the primary results of this thesis are Lagrangian statistics in acceleration and velocity which require significant post-processing, which is the subject of this section.

2.3.1 "Big data" considerations

An important aspect of this project was the management of the large quantity of raw data that was necessary to collect. Lagrangian statistics in the context of turbulent channel flow must be conditioned on initial distance to the wall, which is a layer of conditioning not typically found in similar experiments in HIT. Trajectories are binned by initial distance to the wall, which effectively divides the dataset by the number of bins. This fact, plus the relatively low particle density that was necessary because of the two-camera PTV system, means that a large number of movies needed to be recorded to have reasonable convergence of the statistics. A brief summary of the size of the tracer particle raw dataset is shown in table 2.3.

Table 2.3: Tracer particle raw dataset description

Film pairs	Total films	Images per film	Total images	Image size on disk	Raw dataset size on disk
2606	5212	16541	86.2×10^6	1.28 MB	110.5 TB

The size of this dataset required the use of a processing cluster with associated RAID storage, high-speed optical fiber network connections, and a reasonably efficient storage and data processing strategy, which is outlined in figure 2.14. The large volume of raw data is made manageable with the direct 10 Gbit connect between the cameras and network raid storage, the details of which are shown in figure 2.6. This connection, along with the efficient 10-bit binary video format, allow a 10-fold increase the rate of data collection and avoids having to transfer the data from local to network storage for further processing. Once the films are on the network RAID the processing tasks are embarrassingly parallel (to borrow a term of art from computer science), i. e. the processing tasks are independent and easily divisible into parallel processes that may be performed concurrently. In practice, this means that individual images can be processed independently, and the resulting lists of particle centers from two synchronized films can also be processed independently. A custom job manager was developed to assign computing resources to the processing tasks. Unlike CFD, these experimental data processing tasks are typically limited by memory and file I/O resources, and the job manager was designed to allocate resources on the basis of required/available memory. The parallel tasks are then processed individually using matlab scripts compiled into stand-alone programs. If all of the trajectories were of the same length than a matrix would be the logical form in which to store the processed data, e. g. columns being time steps and the rows being independent trajectories. The experimental dataset contains trajectories of varying lengths which does not allow a matricial data structure to be efficiently used. As a compromise a flattened data structure was developed to stock the trajectories, as illustrated in figure 2.15.

2.3.2 Differentiation and filtering

The trajectories obtained from the methods described above are discrete (one position per time step) and include a certain amount of noise. A common strategy for filtering such data [107, 31] is the convolution of the signal (here the taken to be a single component of the 3-D trajectory) with a simple function, defined as

$$f * g = \int_{-\infty}^{\infty} f(\tau) g(t-\tau) \quad \text{where } f \text{ is the signal and } g \text{ is some smoothing kernel} \tag{2.29}$$

Equation 2.29 may be thought of as a weighted running average filter, for which g defines the weighting scheme. The weighting function g used in this work the Gaussian function, which has several properties of interest to this application. First, a Gaussian low-pass filter has a reasonably good frequency response; figure 2.16 contrasts the strong suppression of high frequencies by the Gaussian filter to the poorer performance of the moving average filter. Second, by using the fact that derivatives are commutative in a convolution, i. e. $\frac{df}{dt} * g = \frac{dg}{dt} * f$ the trajectories can be smoothed and the time derivatives calculated in the

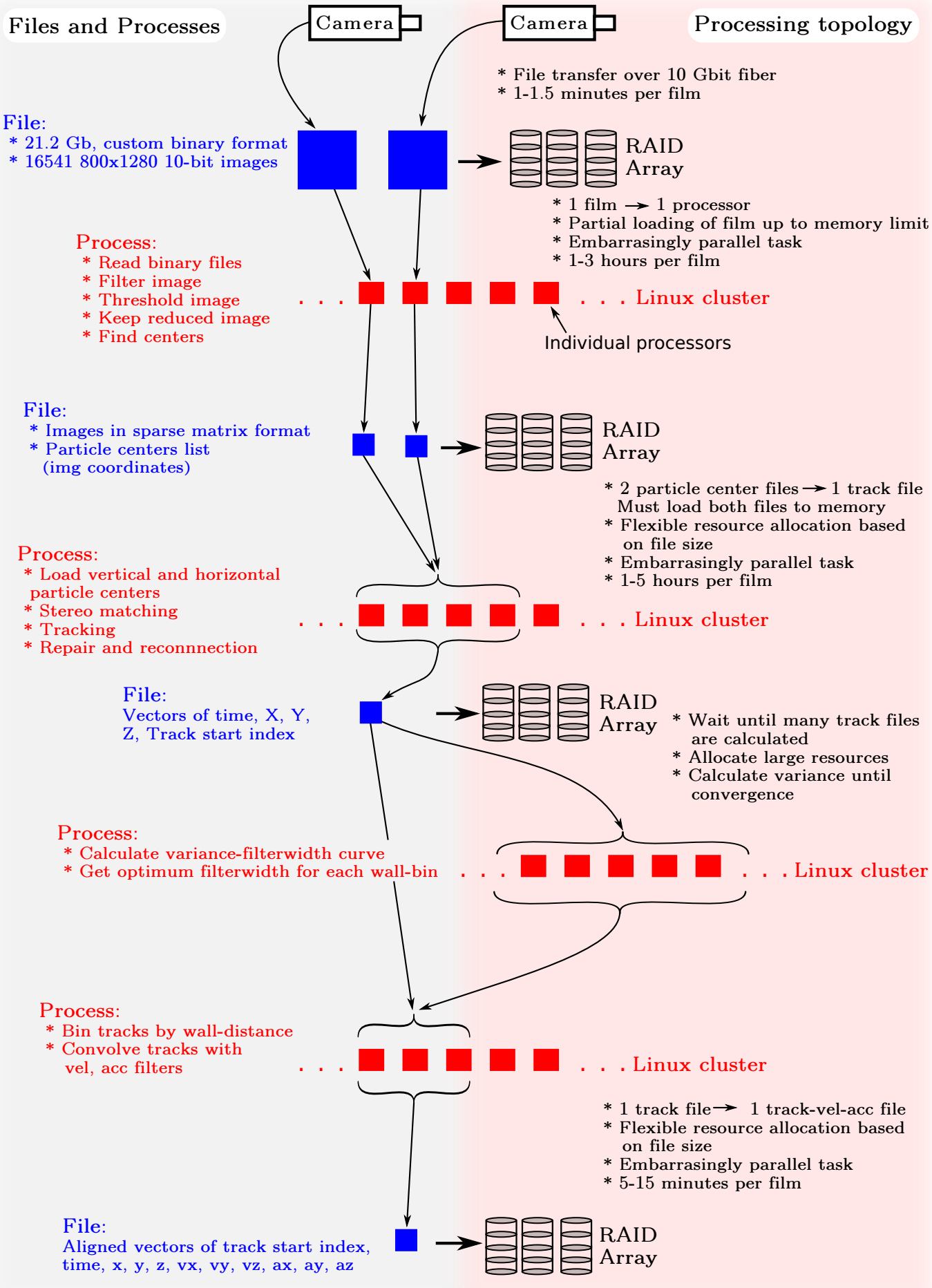

Figure 2.14: Data processing schematic showing processes, files, and processing topology.

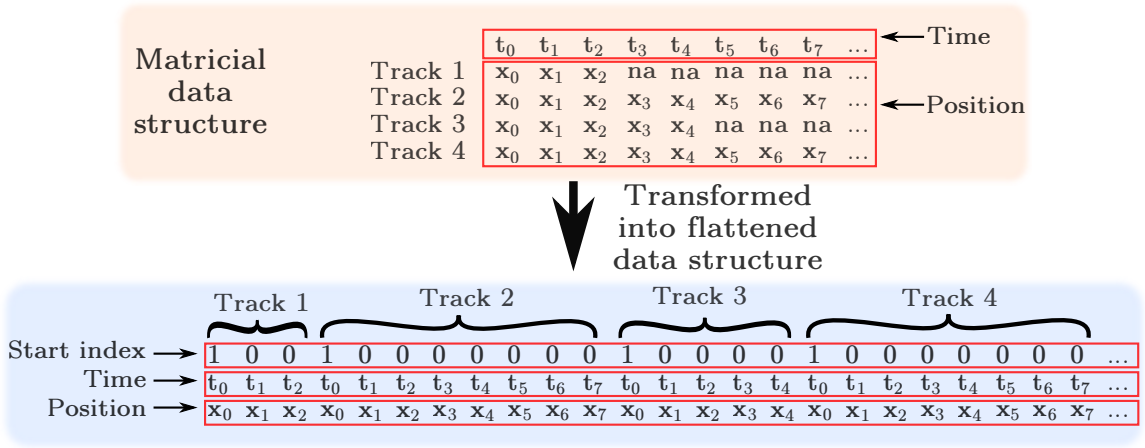

Figure 2.15: A time-aligned matricial data structure with trajectories of uneven length (top) transformed into the efficient flattened data structure used for this project. Note that this data structure requires the addition of the variable "Start index", which is true at the beginning of each trajectory and false otherwise. Independent variables are outlined in red. Variables not shown are the position variables y and z, and the 6 variables that are the components of velocity and acceleration.

same operation, simply by convolving the trajectories by the derivatives of the Gaussian function, which are the analytical functions shown in equation 2.30.

$$
\begin{aligned}
g(\tau) &= \frac{1}{\sqrt{\pi w^2}} \exp\left(\frac{-\tau^2}{w^2}\right) \\
\frac{dg}{d\tau}(\tau) &= \frac{-2\tau}{\sqrt{\pi} w^3} \exp\left(\frac{-\tau^2}{w^2}\right) \\
\frac{d^2 g}{d\tau^2}(\tau) &= \frac{2}{\sqrt{\pi} w^3} \left(\frac{2\tau^2}{w^2} - 1\right) \exp\left(\frac{-\tau^2}{w^2}\right)
\end{aligned}
\tag{2.30}
$$

Finally, scale-space analysis has proven that, uniquely, the Gaussian kernel guarantees that no new signal structure is created as the scale of the smoothing is increased[107]. The Gaussian kernels defined in equations 2.30 have infinite support, which in clearly impractical for a convolution kernel, so they must be truncated and discretized in a manner that preserves their properties as much as possible. If equations 2.30 are simply sampled then the resulting kernel will not perform as expected, e.g. if G is the discrete Gaussian kernel with values samples from g then $\overline{G * s} > \overline{s}$, where s is some arbitrary signal. The truncated and discretized versions of equations 2.30 are

$$
G(n) = A_1 \exp\left(\frac{-n^2}{w^2}\right) \approx g(\tau) \tag{2.31}
$$

$$
V(n) = A_2 n \exp\left(\frac{-n^2}{w^2}\right) + B_2 \approx \frac{dg}{d\tau}(\tau) \tag{2.32}
$$

$$
A(n) = A_3 \left(n^2 - 1\right) \exp\left(\frac{-n^2}{w^2}\right) + B_3 \approx \frac{d^2 g}{d\tau^2}(\tau) \tag{2.33}
$$

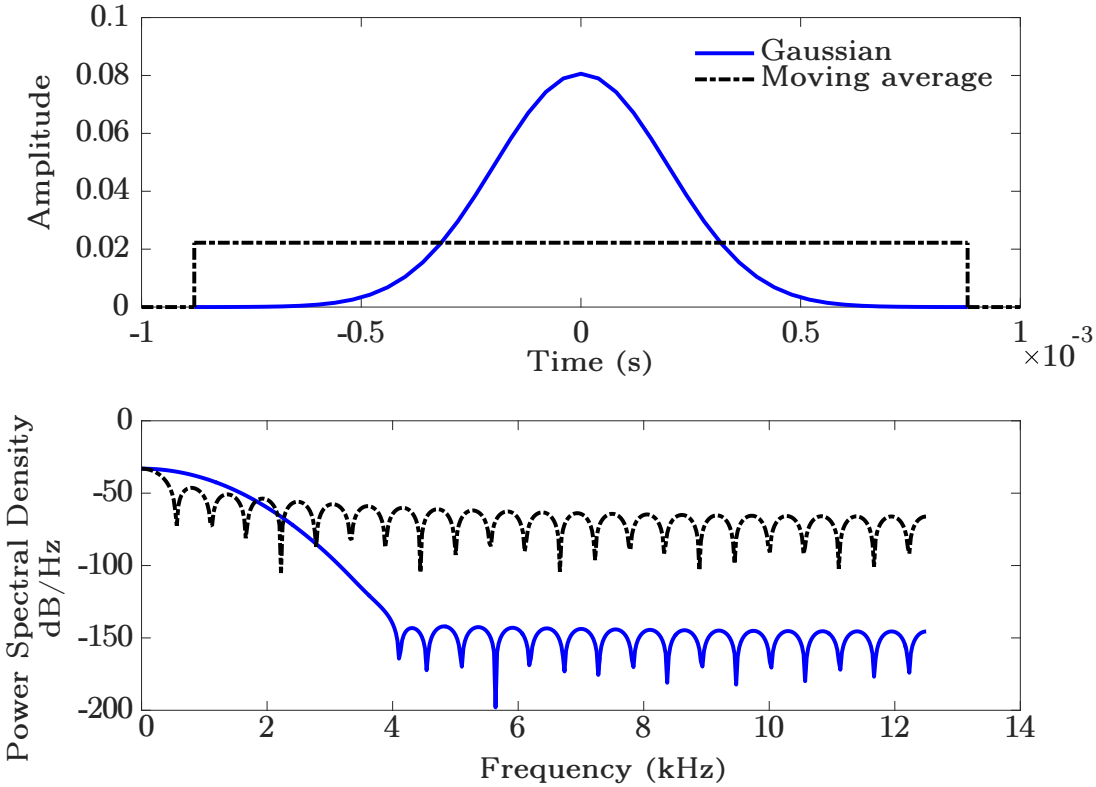

Figure 2.16: Two possible choices of weighting schemes for a moving average filter (top) and their frequency responses (bottom)

and are calibrated such that the following conditions are met:

$$\mathrm{G}(n) * k = k \quad \text{where } k \text{ is a constant} \tag{2.34}$$
$$\mathrm{V}(n) * k = 0 \tag{2.35}$$
$$\mathrm{V}(n) * kn^2 = 2kn \tag{2.36}$$
$$\mathrm{A}(n) * k = 0 \tag{2.37}$$
$$\mathrm{A}(n) * kn^2 = 2k \tag{2.38}$$
$$\tag{2.39}$$

These truncated, discretized kernels and their continuous function equivalents are plotted in figure 2.17. Figure 2.18 shows an example of a trajectory and the results of its convolution with the Gaussian kernel, and the first and second derivative of the Gaussian kernel to calculate velocity and acceleration, respectively.

The degree to which the signal should be smoothed, i. e. the length of the filters shown in figure 2.17, is a key question in the data analysis. The question becomes especially important when considering particle acceleration, as the second time derivative of the raw position data amplifies the noise considerably. Ideally, the filter should eliminate the noise without distorting the signal. The degree to which this ideal is approached depends on the time scale separation of the signal and the noise and their relative strengths (the SNR). The acceleration noise can be assumed to be delta-correlated, but the acceleration time scale and variance is dependent on position in the channel, so in general the ideal filter length will be position dependent.

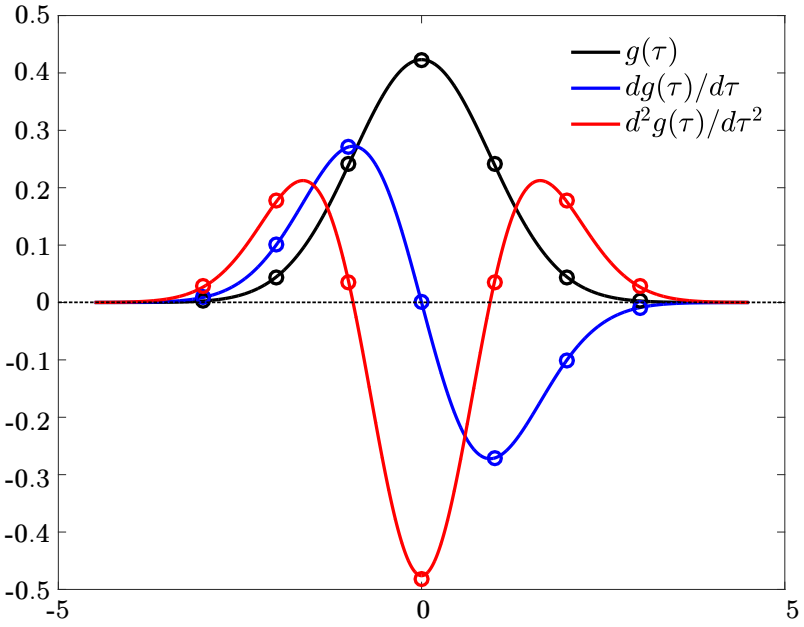

Figure 2.17: A Gaussian kernel, and the first and second time derivatives (continuous lines), as well as their discretized versions (circles)

The effect of filter length on acceleration variance is explored as follows. The trajectories are placed into bins determined by their distance to the wall at $t = t_0$, the trajectories in each wall-bin are filtered using a range of filter widths, and the acceleration variance is calculated for each filter width. The results of these calculations for the wall-normal component of acceleration in selected wall-bins is shown in 2.19(a). Also plotted is the variance of the convolution of Gaussian white noise and acceleration kernels over a range of kernel widths. For very short kernel widths very little difference is observed between the pure noise and the real signals, indicating that the noise in the signals is not adequately filtered at these filter widths. The acceleration variance of the real signals is seen to have a second regime, in which the variance is less dependent on the filter length. These two regimes have been previously observed [30, 108] as well as simulated from DNS data[30]. The optimal filter length is often taken to be the intersection of these two regimes. As previously mentioned the level of noise and time scale is a function of distance to the wall, there is also a difference between individual components due to small-scale anisotropy as well as technical details of the PTV setup (e.g. the span-wise component has greater position noise due to how the horizontal camera was positioned) . The optimal kernel widths for each component of acceleration and velocity found by the method described above are shown in figure 2.19 (b).

2.3.3 Wall scaling variables

The results presented in this thesis are often scaled by viscous quantities, otherwise known as wall-scaling variables. These variables are derived from the physical properties of the

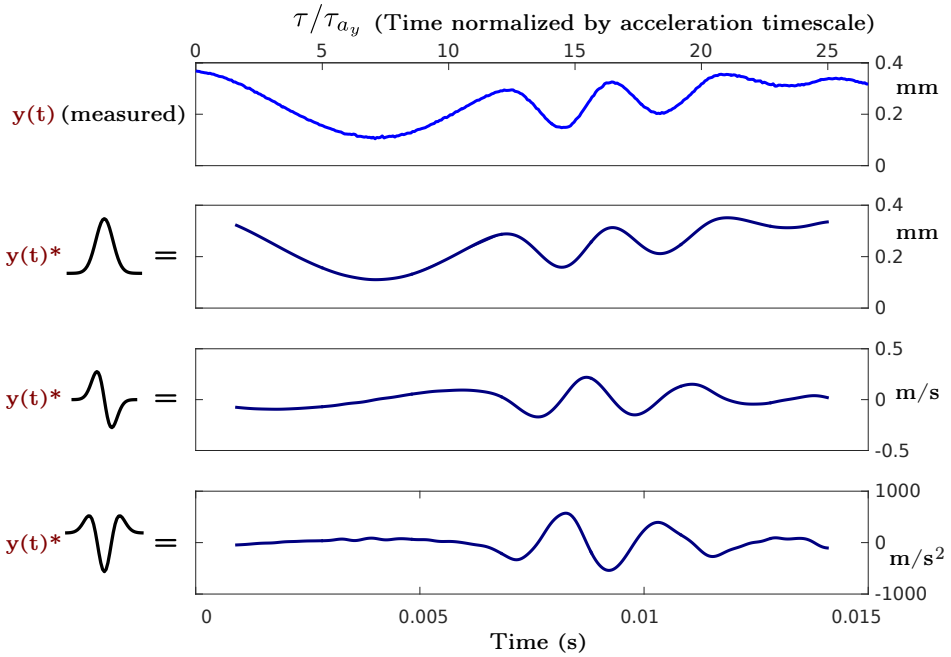

Figure 2.18: The time history of the wall-normal position of a sample trajectory. From top to bottom: the directly measured wall-normal position, the wall-normal position convolved with the Gaussian kernel to smooth the trajectory, the wall-normal position convolved with the derivative of the Gaussian kernel to yield the smoothed wall-normal velocity history, and wall-normal position convolved with the second time derivative of the Gaussian kernel to yield the smoothed acceleration history.

fluid, the density ρ and kinematic viscosity ν, and the shear stress at the wall τ_w:

$$u_\tau = \sqrt{\frac{\tau_w}{\rho}} \tag{2.40}$$

$$\delta_\nu = \frac{\nu}{u_\tau} \tag{2.41}$$

This scaling, instead of the so-called outer-variable scaling based on the channel width, the bulk mean velocity, etc., was chosen in order allow direct comparison with DNS and other channel flow and boundary layer results. However, the fundamental quantity on which this wall scaling is based, the shear stress at the wall τ_w, is not a directly measured quantity in these experiments, and must therefore be estimated. The scaling variable u_τ was estimated from the log law of the wall (discussed in detail in section 1.2) which may be written as

$$\frac{U_0}{u_\tau} = \frac{1}{\kappa} ln\left[\frac{u_\tau Re_0}{U_0}\right] + B + B_1 \tag{2.42}$$

where κ, B, and B_1 are empirical constants. For the purposes of this calculation the values of these constants were taken from Pope[10]: $\kappa = 0.41$, $B = 5.2$, and $B_1 = 0.2$. Equation 2.42 is solved with these values and the measured value of the mean velocity at the center of the channel (U_0) to estimate the friction velocity $u_\tau = 0.081\,\mathrm{m\,s^{-1}}$. The uncertainty of this result will be discussed in the next section (2.4), and all of the scales derived from this result are tabulated in table 2.4.

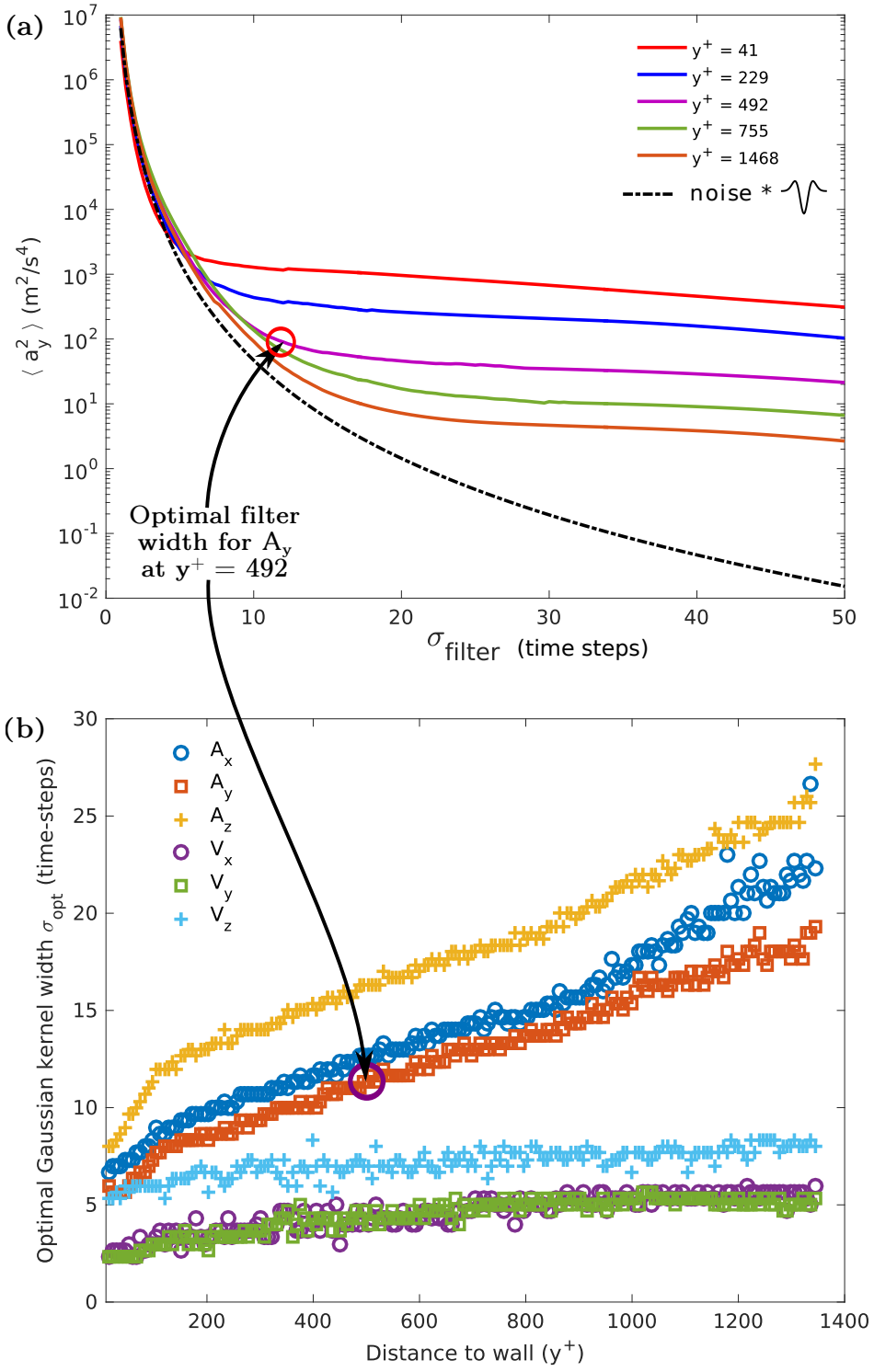

Figure 2.19: **Subfigure (a):** The variance of acceleration as a function of the filter width (in times steps) for trajectories from five wall-normal bins. Also shown is Gaussian white noise convoluted with the acceleration kernels. **Subfigure (b):** The corresponding optimized filter widths used for filtering each component of the velocity and acceleration.

2.4 Error and bias

There are many sources of error and bias in the results reported in this study, and the propagation of error and bias though the chain of measurement and processing is complex. Statistical tools, such as the bootstrap method[109], may be used to quantify the uncertainty associated with random error without an *a priori* knowledge of the sources of error. However, these methods are not a replacement for an accounting of the precision of key experimental parameters, nor are they capable of accounting for systematic uncertainty, or bias. How best to quantify uncertainty in turbulence PTV measurements is still an open question, nevertheless the following analysis illuminates the sources of error, and quantifies them as much as possible. First, the uncertainties associated with the scaling variables used in the data reduction is presented. Next, a treatment of the error associated with the a single measured trajectory and the calculation if the velocity and acceleration. Finally, the errors and biases related to the statistics that are formed from ensembles of these trajectories are discussed.

2.4.1 Uncertainty in scaling variables

Physical properties of the fluid, Eulerian mean quantities, and estimates of wall-scale variables are used in the data reduction of the results presented in this study, and all of these quantities have associated uncertainty. These scaling variables are listed below, with a discussion of how their uncertainties are estimated. These results are summarized in table 2.4.

1. **Physical properties of the fluid**: The density ρ and viscosity ν of the fluid were not measured directly, but taken to be that of fresh water at a given temperature. The range of temperatures observed in the experiment was used to estimate the range of these values. No attempt was made to use a time history of the changes in temperature, instead a global range of temperature was used to estimate the global uncertainty in ρ and ν for all the measurements performed.

2. **Eulerian velocity profile**: The Eulerian velocity profile was used to estimate the centerline velocity U_0 and the bulk velocity $\overline{U}$. This profile was measured by LDV and PTV; each measurement method has associated random and systematic errors. U_0 and $\overline{U}$ are calculated from multiple independent realizations with each measurement system, then the results of these two measurement methods used together to estimate the mean and uncertainty:

$$U_0 = \frac{U_{0,\mathrm{PTV}} + U_{0,\mathrm{LDV}}}{2} \qquad \epsilon_{U_0} = \frac{\epsilon_{U_{0,\mathrm{PTV}}} + \epsilon_{U_{0,\mathrm{LDV}}}}{2} \tag{2.43}$$

3. **Wall-scaling variables**: The wall-scaling variables δ_ν, and Re_τ are based on the shear stress at the wall, which was not directly measured. The wall scaling variables were instead estimated using equation 2.42, which assumes a log profile in the channel. The uncertainty resulting from this estimation is difficult to quantify, as it is unclear how deviations from the assumed log profile affect the calculation of u_τ. Instead, the uncertainty of the skin friction coefficient $\tau_w/(\frac{1}{2}\rho U_0^2)$ was estimated from a compilation of previously published experimental data[110] that found skin friction as a function of Reynolds number. This uncertainty is then propagated in the calculation of the other wall-scaling variables (e.g. $u_\tau = \sqrt{\tau_w/\rho}$) in the usual way[111].

Table 2.4: Scaling variables mean and uncertainty

Variable	Mean	Uncertainty (%)	Note
ρ	$(998.5 \pm 3.9)\,\mathrm{kg\,m^{-3}}$	0.4%	due to temp. range $(18 \pm 2)\,^{\circ}\mathrm{C}$
ν	$(1.054 \pm 0.529) \times 10^{-6}\,\mathrm{m^2\,s^{-1}}$	5%	due to temp. range $(18 \pm 2)\,^{\circ}\mathrm{C}$
h	$(0.018\,75 \pm 0.001\,00)\,\mathrm{m}$	5%	Construction tolerance
U_0	$(1.75 \pm 0.05)\,\mathrm{m\,s^{-1}}$	2.9%	Centerline velocity
Re_0	6.23×10^4	8%	$Re_0 \equiv \frac{2hU_0}{\nu}$
u_τ	$(0.076 \pm 0.006)\,\mathrm{m\,s^{-1}}$	7.5%	From eq. 2.42
δ_ν	$(1.38 \pm 0.18) \times 10^{-5}\,\mathrm{m}$	13%	$\delta_\nu \equiv \nu / u_\tau$
Re_τ	1350 ± 190	14%	$Re_\tau \equiv h/\delta_\nu$

2.4.2 Uncertainty in a single trajectory

The error associated with a single trajectory is illustrated in figure 2.20, which shows schematically the measured position of the tracer particle, the error associated with this measurement (which in general form is not centered nor symmetric, and is time and position dependent), and the true positions of the fluid particle that is the object of the measurement. These error can be divided according to their sources

$$\widetilde{\mathrm{X}}_i(t) = \mathrm{X}_i(t) + \sum_j^{\mathrm{N}} \epsilon_i^j(t) \quad \text{for } i = x, y, z \quad \mathrm{N} = \text{Number of sources of error} \tag{2.44}$$

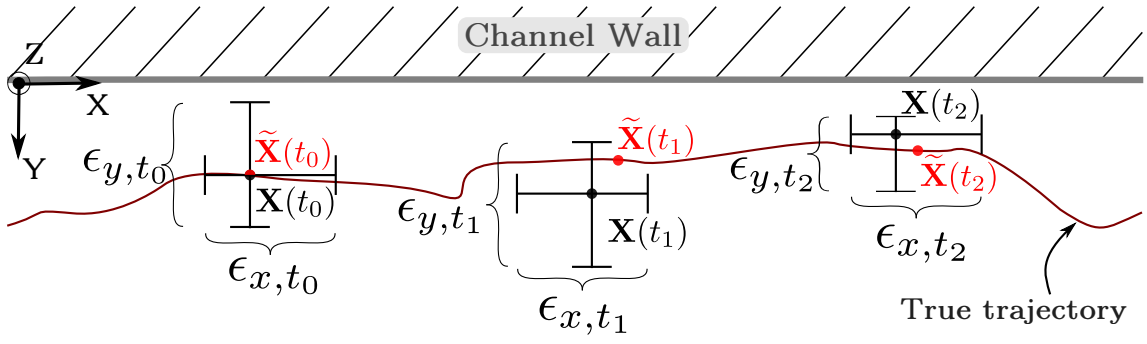

Figure 2.20: An example of the first three measured positions $\mathbf{X}(t)$ of a trajectory, with associated errors $\epsilon_i(t)$, and the true (unknown) positions $\widetilde{\mathbf{X}}(t)$.

1. **Tracer particle fidelity**: This is a time dependent error, as by definition $\mathrm{X}_i(t_0) = \widetilde{\mathrm{X}}_i(t_0)$. The tracer particles used in this flow are considered to be highly faithful to the fluid particle trajectories, as discussed in section 2.1.5, but this source of error is particularly delicate in inhomogeneous turbulent flow, as diverging particle paths

explore flow regions with different statistical properties. In this study the error associated with tracer particle fidelity is neglected.

2. **Camera and tunnel vibration**: Relative motion of the fields of view of the cameras and the test section results in an error in the measurement of particle position. Care was taken in the design of the experimental setup to minimize this vibration, but it is impossible to totally eliminate. This relative motion due to vibration is considered Gaussian and non-time dependent. The magnitude of this error was estimated to be ±30 μm using the position of the wall, which was visible to one of the cameras in some of the experiments.

3. **Center finding error** : The particle image can be modeled as the discretization of a Gaussian light source centered on the particle with the addition of image noise. This model can be simulated by creating synthetic images in which the true particle centers are known, which allows the quantification of the precision of particle center finding methods as a function of noise and particle image size[97]. An example of this analysis is shown in figure 2.21, which shows a Gaussian particle image that has been added to a real PTV image. The real particle center is known, allowing a quantification of the error associated with the image processing/center finding procedure. A systematic investigation of this error was performed by varying the size and brightness of the synthetic particles. Figure 2.22 shows the results of this investigation of error for synthetic particles on noise-free backgrounds and inserted into real PTV images[3]. Results of this analysis show particle center position error of approximately 0.1 pixel (2.7 μm) for synthetic particles of size $\sigma \gtrapprox 1$ pixel. Systematic analysis of the Gaussianity of the real particle images was not performed, but estimates indicate that 0.1 pixel is a reasonable estimate for particle position error in these measurements. This error is similar to that found by Ouellette *et al*[97] in a study of synthetic particles on a noisy background.

4. **Calibration error**: The error associated with calibration may be decomposed into two contributions: the error associated with the absolute position of the calibration grid, and the error associated with the calibration model. The error associated with the absolute position of the calibration grid is quite difficult to estimate, as it relates to the degree to which the block was in good contact with the channel wall, the accuracy with which the calibration block was displaced in the transverse direction by the positioning stage, etc. The error associated with the absolute position of the grid points is taken to be very small relative the errors in the calibration model.

   The calibration model is a linear transform that does not take into account optical aberrations and other non-linearities. The error associated with this model is quantified by considering the difference between the known absolute position of the grid points and the position of the grid points in real space as given by the calibration. These errors were found to vary by component, from approximately ±10 μm in the wall-normal direction to approximately ±30 μm (≈ ±1 pixel) in the transverse direction. It is important to note that this error is an error of *absolute* position. Because the source of this error is optical aberrations we expect that this error is spatially smooth, i. e. a straight line across the measurement volume would be seen as a smoothly curved line that shows a maximum deviation from linearity of 30 μm. The

[3] Adding synthetic particles to real PTV images allows a more realistic quantification of error than simple adding Gaussian noise to the synthetic particle image, as the true image noise is not necessarily Gaussian.

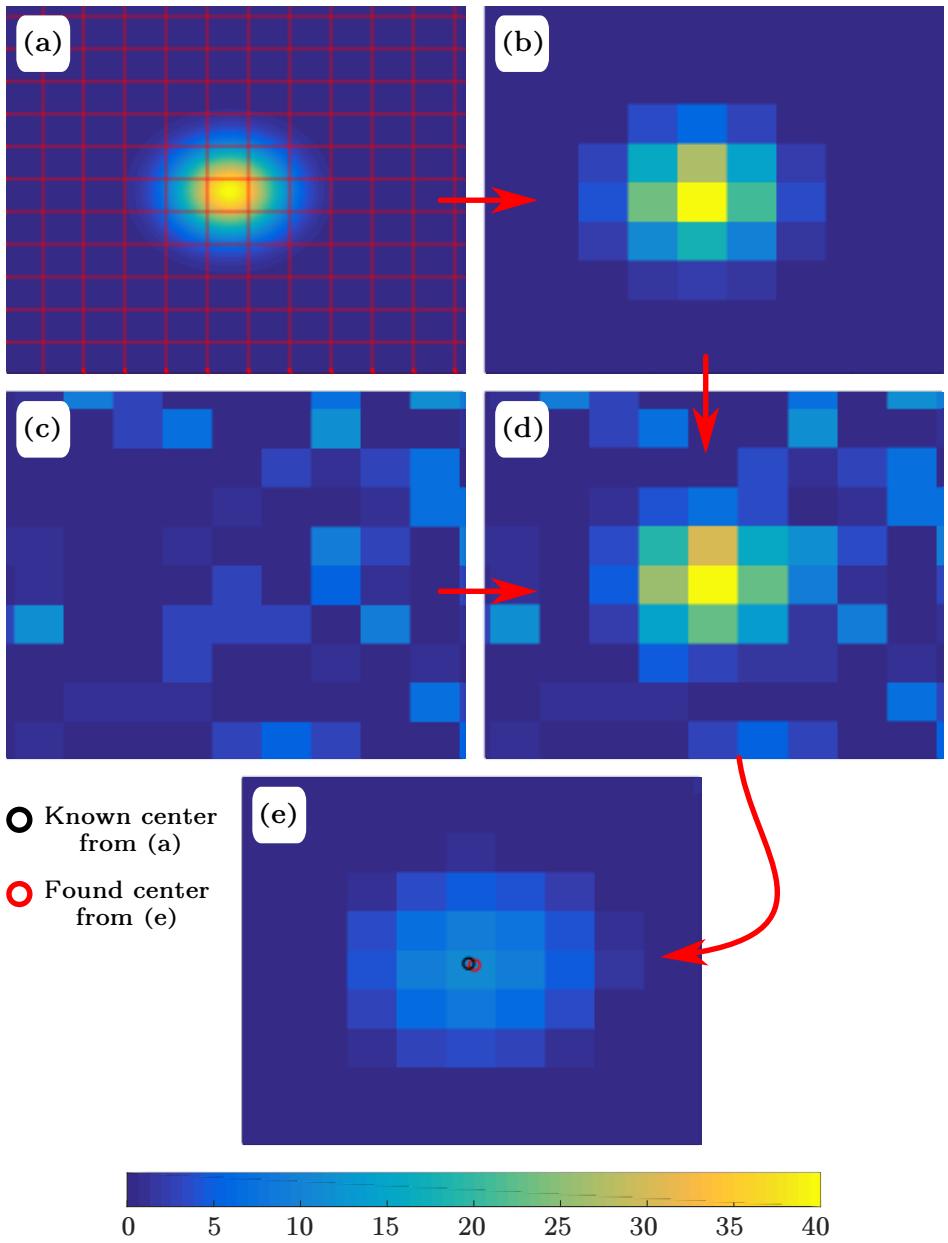

Figure 2.21: An example of how the particle finding error analysis is performed. (a) A fine-grained 2-D Gaussian synthetic particle is created, with a known center point relative to a coarse-grained grid. (b) The synthetic particle is discretized by integrating the fine-grained image with respect to the coarse pixel grid. (c) An image from the acquisition series , with the real levels of noise visible. (d) The discretized synthetic image (b) is summed with the real image (c), i. e. (d) = (b)+(c). (e) The real image with added discretized synthetic particles passed through the typical processing, including image filtering and particle center finding, the result of which is marked with the red circle, and compared to the known center location (marked with a black circle).

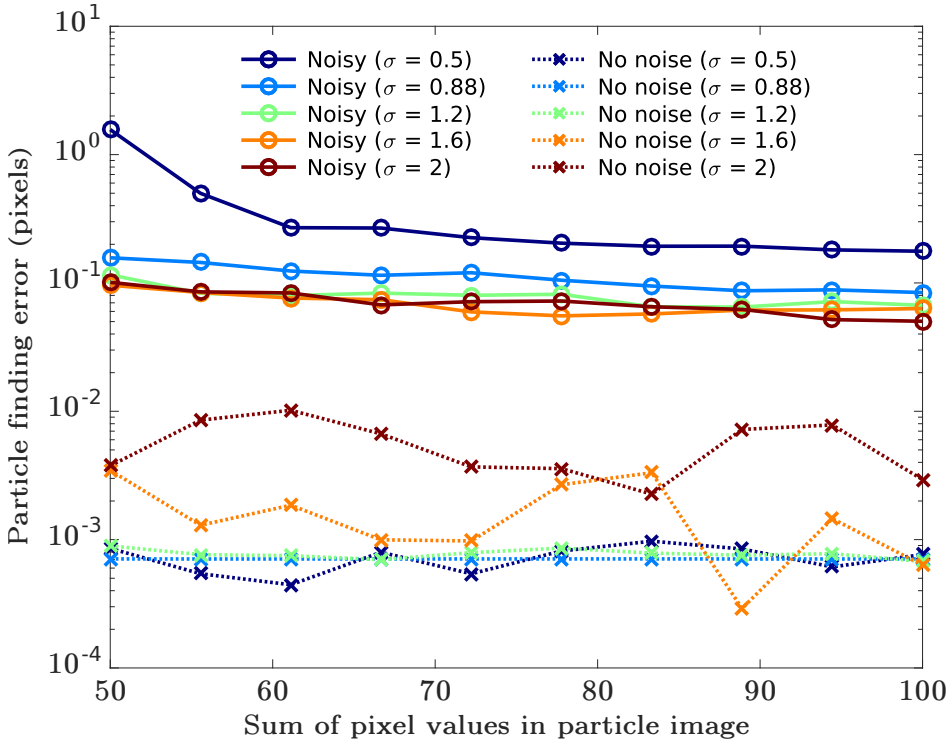

Figure 2.22: Particle finding error in the finding of synthetic particles. Synthetic particles of different sizes (a range of standard deviation from 0.5 to 2 pixels), and brightness (horizontal axis). The particle center finding algorithm is applied to the discretized synthetic particles for no noise (dotted lines) and the discretized synthetic particles placed in the real, noisy images (solid lines).

errors in velocity and acceleration statistics from this error may be thought of as the slope and curvature of this line, which are very small.

5. **Tracking error**: Errors due to failures in the tracking procedure are possible, though difficult to quantify. False matches, in which the tracking algorithm assigns a particle position to the trajectory that is not truly part of the trajectory, tend to occur at the beginning and end of the particle trajectories, where the clipping associated with the convolution of Gaussian kernels discards the ends of the trajectory. False matches in the middle of the trajectories are possible, resulting in a "jump" in the trajectory over a single time step. Track repair and reconnection algorithms were designed to find these "jumps", and break the trajectories at these points. Low particle seeding density and careful tuning of these algorithms minimized these tracking errors.

The velocity and acceleration of the trajectory is calculated by convolving the position time series (component-wise) with the first and second derivative of the finite Gaussian kernel, as discussed in section 2.3.2. The effect of the measurement uncertainty and noise can be explored by separating the signal and noise in these calculations.

$$\widetilde{a}_i(t) = a(t) + \epsilon_{i,a}^{diff} + \epsilon_{i,a}^{pos} \tag{2.45}$$

$$\widetilde{a}_i(t) = \mathrm{A}[n] * (x_i(t) + \epsilon_{i,x}) \tag{2.46}$$

$$a_i(t) + \epsilon_{i,a}^{diff} = \mathrm{A}[n] * x_i(t) \quad \text{and} \quad \epsilon_{i,a}^{pos} = \mathrm{A}[n] * \epsilon_{i,x} \tag{2.47}$$

The error in the acceleration due to the error in position $\epsilon_{i,a}^{pos}$ is the consequence of the convolution of the position error with the acceleration kernel $\mathrm{A}[n]$. If the position error is

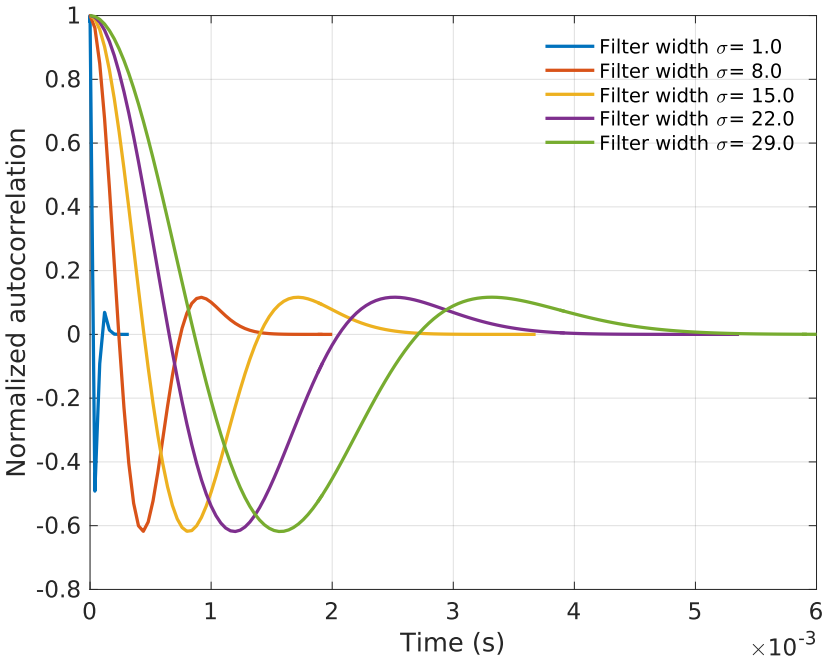

Figure 2.23: The normalized autocorrelation of the acceleration of delta-correlated noise for various filter widths of acceleration kernels, up to the longest acceleration kernel ($\sigma = 29$ time-steps) used.

taken to be time independent and normally distributed then

$$\epsilon^{pos}_{i,a} = \sum_{n=-l}^{l} p_n \epsilon_{i,x} \quad \text{where } p_n \text{ are the coefficients of the acceleration kernel} \tag{2.48}$$

$$\Rightarrow \epsilon^{pos}_{i,a} \sim \mathrm{N}(\mu^{pos}_{i,a}, \sigma^{pos}_{i,a}) \quad \text{where:} \tag{2.49}$$

$$\mu^{pos}_{i,a} = \sum_{n=-l}^{l} p_n \mu^{pos}_{i,x} = 0 \tag{2.50}$$

$$\sigma^{pos}_{i,a} = \sqrt{\left(\sum_{n=-l}^{l} p_n \sigma^{pos}_{i,x} \right)^2} \tag{2.51}$$

It is important to note that the time-independent position noise becomes correlated after the convolution, which may be seen by considering the autocorrelation:

$$\epsilon^{pos}_{i,a}(t)\epsilon^{pos}_{i,a}(t+\tau) = \left(\epsilon^{pos}_{i,x}(t) * \mathrm{A}[n]\right) * \left(\epsilon^{pos}_{i,x}(t+\tau) * \mathrm{A}[n]\right) \tag{2.52}$$

$$\epsilon^{pos}_{i,a}(t)\epsilon^{pos}_{i,a}(t+\tau) = \left(\epsilon^{pos}_{i,x}(t) * \epsilon^{pos}_{i,x}(t+\tau)\right) * (\mathrm{A}[n] * \mathrm{A}[n]) \tag{2.53}$$

$$\epsilon^{pos}_{i,a}(t)\epsilon^{pos}_{i,a}(t+\tau) = var\left(\epsilon^{pos}_{i,x}(t)\right) \delta(t) * (\mathrm{A}[n] * \mathrm{A}[n]) \tag{2.54}$$

$$\epsilon^{pos}_{i,a}(t)\epsilon^{pos}_{i,a}(t+\tau) = var\left(\epsilon^{pos}_{i,x}(t)\right) (\mathrm{A}[n] * \mathrm{A}[n]) \tag{2.55}$$

This correlation of delta-correlated noise after convolution is shown in figure 2.23.

2.4.3 Statistical bias

Statistical results have uncertainties as a result of the error associated with individual trajectories, but also due to statistical bias in which particle trajectories are measured,

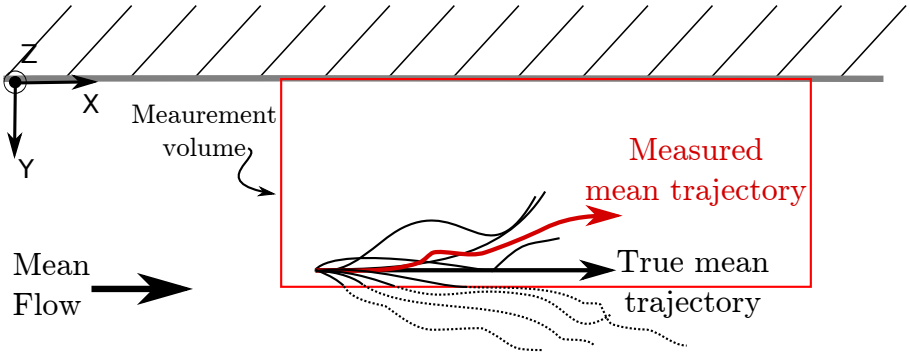

Figure 2.24: Illustration of statistical bias due to the finite measurement volume.

and how they are measured. An example of a statistical bias is illustrated in figure 2.24, which shows a schematic view of trajectories conditioned on a wall-normal location near the outer edge of the measurement volume. As these particles disperse from their initial location y_0 at t_0, some of them leave the measurement volume, and their trajectories cease to be measured. Trajectories that move towards the wall are measured and contribute to the statistics, but trajectories that leave the measurement volume do not, resulting in a statistical bias.

Assuming that the tracer particles have an unbiased distribution in the flow[4] statistical biases arise from the particles arriving or leaving the measurement volume in a manner that biases the statistics. Statistical bias has previously been observed in similar measurements in HIT [30, 112] for which the mean flow in the measurement volume was zero. In this case the finite-measurement-volume effect is increasingly seen in two-time Lagrangian statistics for increasing time-lags.

The significant mean flow, relatively low turbulence intensity[5], and the fact that the measurement volume is bounded by the channel wall on one side, all act to reduce the statistical bias of the measurements in the present study. Tracer particles have a limited residence time in the measurement volume, as they are being swept through the measurement volume by the mean flow. This imposes an effective maximum time-lag on the measured statistics, and thus avoids the case of some trajectories staying in the measurement volume for long times, as occurs in HIT. Weak velocity fluctuations relative to the mean flow results in tracer particle trajectories that are swept into and out of the measurement volume in a statistically unbiased manner.

In this system statistical biases occur because of the measurement volume boundary in the wall-normal direction, as illustrated by figure 2.24. This effect is ameliorated ignoring trajectories that start too close to the outer boundary of the measurement volume, i. e. trajectories for which $y_0 > y_{limit}$ at $t = t_0$ were ignored. This allows trajectories that are located at y_{limit} at $t = t_0$ to disperse towards the channel and still be within the measurement volume. This y_{limit} was determined empirically, and found to be $y^+ \approx 1200$.

The procedure described above to reduce the statistical bias at the measurement volume boundary near the channel centerline is particularly important because the wall-normal direction in the only direction of inhomogeneity in this system. Measurement volume boundaries also exist in the transverse direction. The turbulence is statistically homogeneous in the transverse direction, but statistical bias can nonetheless results from these measurement volume boundaries. For example, one can imagine a streamwise

[4] Which is a reasonable assumption, given their small size, density ratio very close to unity, and the intense mixing throughout the water tunnel.

[5] The turbulence intensity TI $\equiv \sqrt{\langle u'^2 \rangle}/\langle \mathrm{U} \rangle < 20\%$ over most of the channel $\left(y^+ > 30\right)$

helical vortex with its axis of rotation at this boundary. As the tracer particle is swept around the helix it moves in and out of the measurement volume resulting in several short, discrete trajectories. By contrast, a less energetic particle with a more ballistic motion would stay in the measurement volume and result in a long, continuously-measured trajectory. Ideally a similar procedure would be implemented in the transverse direction, and any particles that are not at $-z_{limit} < z < z_{limit}$ at $t = t_0$ would be ignored. Some investigations regarding trajectory lengths and acceleration statistics indicate that the measurement volume boundaries in the transverse direction has a minimal statistical bias, but a though analysis, perhaps with DNS results, is recommended for future work.

Error bars

The foregoing was a discussion of the sources and magnitudes of the uncertainty and bias. A rigorous calculation of uncertainty, in which all of these errors are propagated through the chain of measurement and calculation, was not performed. How such an error propagation should be calculated for PTV results remains an active area of research[113, 96]. Error bars, where they are presented in this thesis, are calculated from the statistical uncertainty directly (using the bootstrap method[109]), as well as the uncertainty of the scaling variables(u_τ, δ_ν, etc.) shown in table 2.4.

2.5 Direct numerical simulation

The direct numerical simulation (DNS) of a turbulent channel at a Reynolds number matched to that of the experiment was performed by J. I. Polanco and I. Vinkovic at the Laboratoire de Méchanicques des Fluids et d'Acoustique (LMFA) in Lyon, France. Their work is the numerical component of a larger collaborative project; the work described in this thesis is the experimental component. These results are reported in this thesis when their inclusion serves to deepen the understanding of experimental results, with the gracious permission of J. I. Polanco and I. Vinkovic. A brief description of the details of these simulations has been published[42]. A sketch of the numerical setup is provided here for convenience. These simulations are performed between two parallel walls, using periodic boundary conditions on the streamwise and spanwise boundaries. The details of the pseudo-spectral method is described by Buffat[114]. The computational domain is sketched to scale in figure 2.25, including the key dimensions. The grid spacing is uniform except in the wall-normal direction, where the spacing varies from $y^+ = 0.04$ near the wall to $y^+ = 10.5$ at the center of the channel. An initial population of 2×10^6 point particles are initialized at random positions in the computational domain, and are advanced in time using the Eulerian velocity at the particle position. Third-order Hermite polynomials were used to interpolate the Eulerian velocity field at particle locations between grid points, which is important as Lagrangian acceleration statistics are sensitive to interpolation schemes.

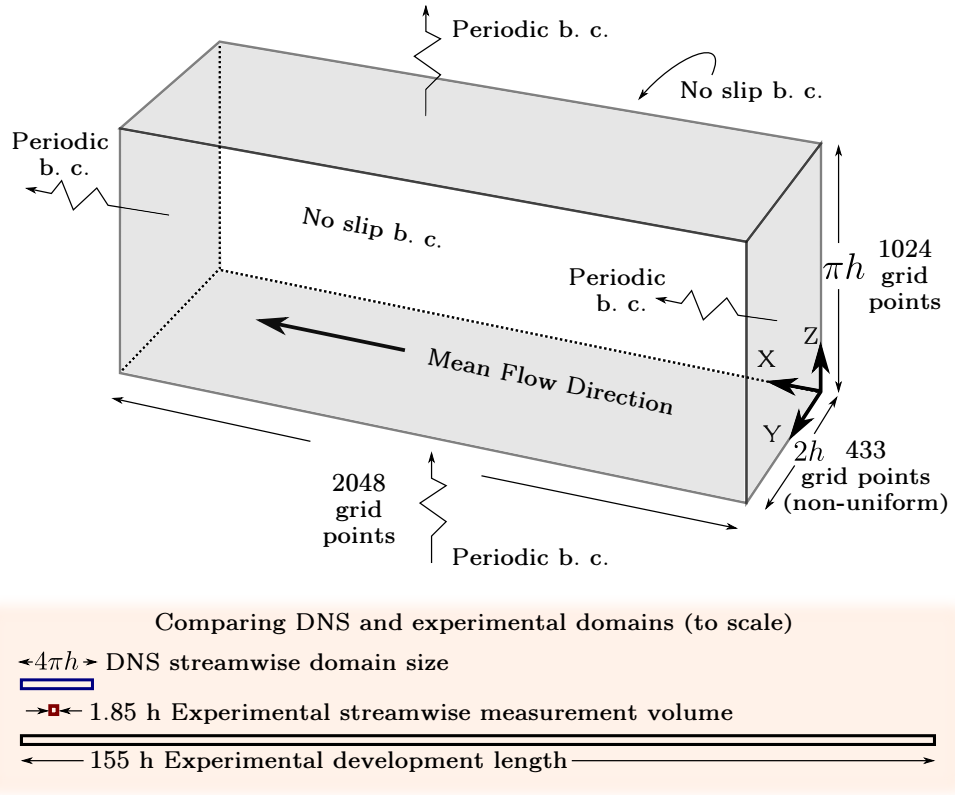

Figure 2.25: Sketch of the DNS domain, with key dimensions.

2.6 Conclusion

This chapter has presented the techniques used to make high-resolution measurements of tracer particle trajectories in a turbulent channel. While high-resolution 3-D PTV with high-speed cameras is an increasingly well-established technique, its application to a turbulent channel flow presents unique challenges. A detailed look at the many competing parameters (tracer particle diameter, measurement volume size, etc.) revealed a fairly small parameter space in which such measurements are possible given current technology. Specifically, Lagrangian measurements close to the wall require very small particles, which require high magnification, which limit the size of the measurement volume. Unlike in HIT, the measurement volume must be relatively large to allow reasonable particle residence time and limit statistical bias. Cameras with 25K frames-per-second acquisition speeds at full resolution and high sensitivities were used in conjunction with a 25 W continuous laser. This technology allowed the use of high magnifications, relatively large measurement volumes, and small particles that were necessary to make these measurements.

The data processing steps are explained, from the raw data consisting of synchronized movies to the wall-scaled Eulerian and Lagrangian statistics. The large volume of raw data, low-SNR images, and lack of redundancy in 3-D stereo reconstruction all require carefully optimized PTV algorithms. Sources and magnitudes of measurement uncertainty and bias are estimated and discussed.

This chapter focuses on the methods and materials relevant to the measurement of tracer particles. Non-tracer particle were also measured, and although most the techniques used were similar to those described here there were some changes necessary to realize these non-tracer particle measurements. The details of these measurement techniques are given in chapter 5.

Chapter 3

Eulerian statistics in the turbulent channel

> I am writing all this down in blue ink, so as to remember that all words, not just some, are written in water
>
> Bluets, *Maggie Nelson*

Contents

3.1 Introduction

This chapter concerns the Eulerian single-point statistics of turbulent channel flow. Eulerian statistics of velocity in turbulent channels have been extensively studied, both numerically and experimentally, but Eulerian statistics in acceleration are much less well known. These statistics are necessary to the development of Lagrangian stochastic models, as well as Eulerian stochastic models such as the one proposed by Zamansky *et al*[3]. All of the Eulerian statistics presented in this chapter have been extracted from the Lagrangian particle trajectories. This manner of measuring Eulerian quantities introduces some statistical bias, which is discussed in the sections below.

This chapter is divided into three sections, which present Eulerian statistics in velocity, in acceleration, and mixed velocity- acceleration statistics.

3.2 Velocity statistics

The Eulerian statistics of velocity in a turbulent channel flow have been extensively studied. The velocity statistics are presented here to confirm that they are consistent with previously published results. Mixed acceleration-velocity statistics, both Eulerian and Lagrangian will be discussed in later sections, and so confidence in relatively simple velocity statistics should first be established. Even in this well-understood area there are subtle questions involving bias and the conditioning of statistics, questions which arise directly from the simplest statistical result: the mean streamwise velocity profile across the channel.

3.2.1 Profiles of mean velocity and Reynolds stress tensor

The mean streamwise velocity profile across the half-width of the channel may be calculated from the measured Lagrangian trajectories in the following way: points on the tracer particle trajectories are considered to be independent points, these points are sorted into bins based of their wall-normal position, and the mean of all of the streamwise velocities in each bin is calculated, i. e.

$$y_k = \frac{1}{n}\sum_i^n y|_{\mathrm{Y}_k<y<\mathrm{Y}_{k+1}} \qquad \langle \mathrm{U}_x(y_k)\rangle = \frac{1}{n}\sum_i^n u_x(y)|_{\mathrm{Y}_k<y<\mathrm{Y}_{k+1}} \tag{3.1}$$

where Y_k are the edges of the conditioning bins and n is the number of points that fall into a given bin. The mean streamwise velocity profile calculated with all of the measured points is plotted in figure 3.1(top), along with results from DNS at the same Reynolds number[42] and experimental hot-wire measurements from Monty *et al*[115] in a channel at $\mathrm{Re}_\tau = 1040$. Figure 3.1 shows good agreement between these three data sets in the log layer and outer layer ($y^+ > 50$), but our experimental measurements are significantly different from the DNS and the Eulerian experimental measurements of Monty *et al* in the near wall region. This discrepancy was explored by plotting the histograms of the streamwise velocity at three selected wall-normal positions (illustrated by red circles in figure 3.1). These three histograms are plotted in the middle row of figure 3.1, and show a bimodal distribution of streamwise velocity. This bimodal distribution is visible from the wall up to $y^+ \approx 25$, with the high velocity lobe becoming greater as distance to the wall increases, up to $y^+ = 24.7 - 28.4$, where the low-speed lobe is shown to be vanishingly small. This bimodal distribution of streamwise velocity is not seen in channel flow DNS[116, 94],

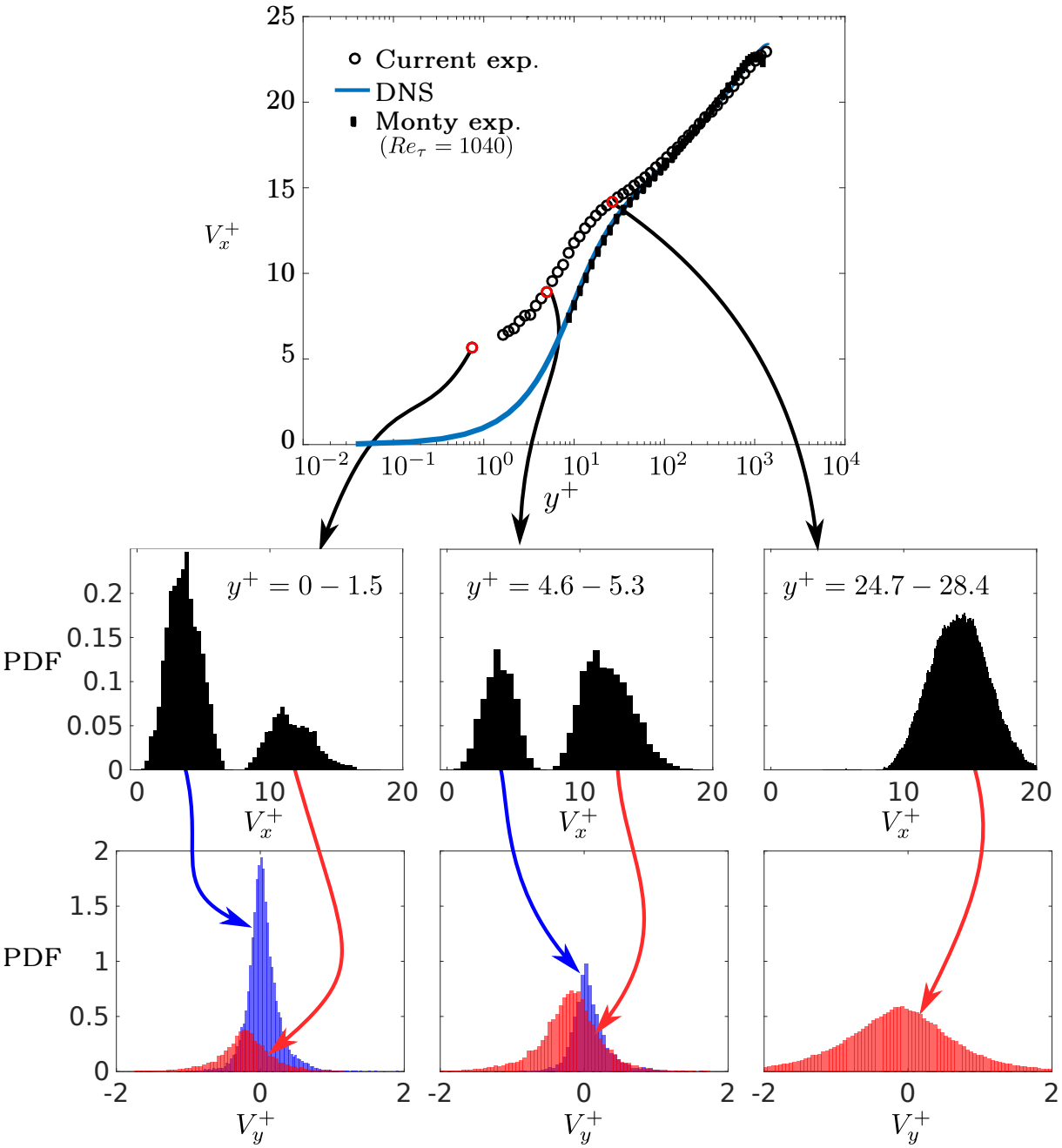

Figure 3.1: Top: Wall scaled mean streamwise velocity as measured (uncorrected) in the experiment (markers) and from the DNS at the same Reynolds number. Three wall normal locations are highlighted in red: $y^+ = 0 - 1.5$, $y^+ = 4.6 - 5.3$, and $y^+ = 24.7 - 28.4$. Middle: PDF's of the full streamwise velocity at these locations, showing strong bimodal distributions up $y^+ \approx 25$. Bottom: PDF's of the wall-normal velocity *for each "lobe"* is shown, i.e. the PDF of the wall-normal velocity of corresponding to the low-streamwise velocity "lobe" are shown in blue, and the those corresponding to the high streamwise velocities are shown in red.

and appears to be a measurement artifact[1] . The nature of this measurement artifact is further explored by looking at the low-speed and high-speed lobes of the streamwise velocity individually. The bottom row of figure 3.1 plots the histograms of the wall-normal

[1]Although a similar bimodal distribution has been reported at least once in PTV measurements of a viscous sublayer from Popovich and Hummel[117] from 1967, although this measurement included relatively few observations (by modern standards), and may very well represent a similar bias.

velocity associated with each lobe of the streamwise velocity histogram (middle row). A clear trend is observed, in which high streamwise velocities are associated with negative wall-normal velocity (towards the wall), and low streamwise velocities are associated with slightly positive wall-normal velocities. These distributions seem to suggest a non-homogeneous distribution of the tracer particles and/or a preferential sampling of the flow by the tracer particles in the near-wall region. Specifically, fast particles moving toward the wall seem to be oversampled in these results. The small particle size ($D_p/y^+ \approx 0.8$) , density ratio close to unity (ρ_p/ρ_f =1.05) , and good agreement in acceleration statistics between the experimental and DNS results all suggest the tracer particles follow the flow faithfully. This seeming contradiction—particles that act as good flow tracers but give anomalous mean velocity results—is known to the users of Laser Doppler Velocimetry (LDV), which measures the velocity of tracer particles as they traverse a small measurement volume[118]. This bias is easily understood in the context of a small spherical measurement volume in HIT—particles moving faster are statistically more likely to be sampled than particles moving more slowly. A correction method used for LDV measurements may be written as

$$\langle u \rangle = \frac{\sum_i u^i w^i}{\sum_i w^i} \tag{3.2}$$

where w^i is the correction factor, with $w^i = 1$ in the uncorrected case. The simplest correction factor is simply the inverse of the magnitude of velocity, i. e.

$$\langle \mathrm{U}_x \rangle = \frac{\sum_i \mathrm{U}_x^i / |\mathbf{U^i}|}{\sum_i 1/|\mathbf{U^i}|} \tag{3.3}$$

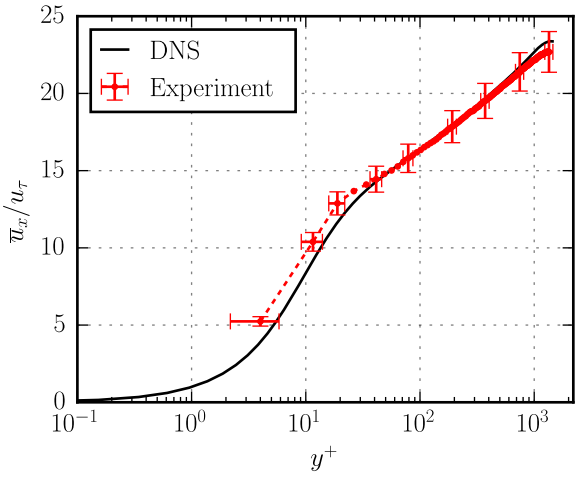

Figure 3.2: Mean streamwise velocity profile with velocity magnitude correction, plotted with the DNS of equal Reynolds number.

The mean streamwise velocity profile using the correction shown in equation 3.3 is plotted in figure 3.2, and shows a much better agreement with the DNS than the uncorrected profile in figure 3.1. This result supports the conclusion that there is a measurement volume bias associated with these Eulerian statistics. Many such corrections have been proposed for LDV results[118], but it is unclear how these corrections, typically developed in the context of an ovoid measurement volume, should be adapted to a wall-bin type measurement volume, in which the streamwise and transverse dimensions are very large, and the wall-normal dimension is small. The systematic investigation of velocity corrections has not been published, and is beyond the scope of this project[2]. Due to the lack of certainty with regard to the bias correction factor the Eulerian statistics presented in the following will not be corrected.

The experimentally measured Eulerian velocity variance is plotted in figure 3.3 by component, along results from DNS. Large deviations from the DNS near the wall are

[2]DNS, having access to simultaneous Eulerian and Lagrangian measurements, is ideally suited to such a study, and would eliminate any effect due to the use of a real "tracer" particle.

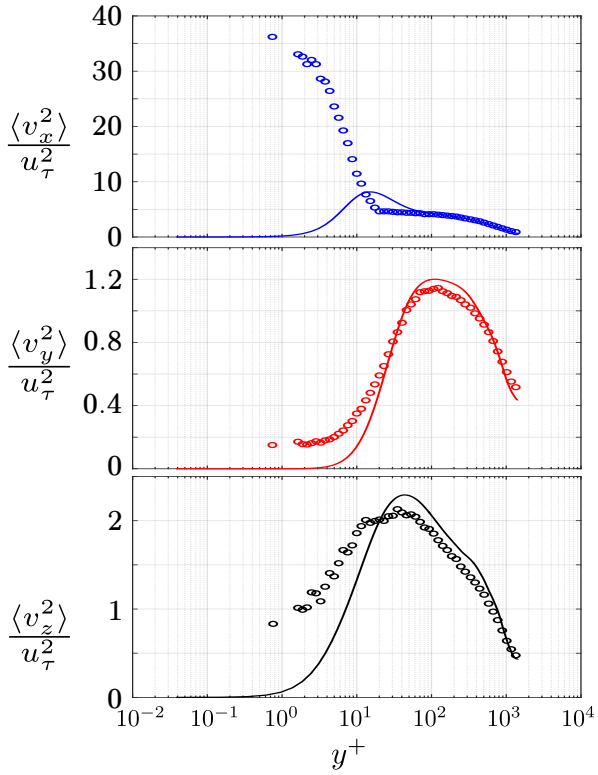

Figure 3.3: Variance of the streamwise (top) wall-normal (middle) and transverse (bottom) components of Eulerian velocity from experimental measurements (symbols) and matched-Reynolds-number DNS (lines).

seen in the streamwise component, with much better agreement closer to the wall for the wall-normal and transverse components. This large variance of the streamwise velocity close to the wall is not surprising, given the wide, bimodal histograms seen in figure 3.1. The bias observed in the mean and variance of the streamwise velocity is less visible in the other components, which follow the DNS up to $y^+ \approx 10$, and capture the location of the maximum of the variance. The variance in the wall-normal velocity appears to plateau very near the wall, which is almost certainly an effect of the bias discussed above. Notice the maximum variance in the streamwise velocity component is much greater than the other two maxima, and thus dominates the turbulent kinetic energy.

The Eulerian velocity one-point correlation tensor, also called the Reynolds tensor, is written in terms of fluctuating velocity components u_i as follows

$$\left\langle \begin{array}{ccc} u_x u_x & u_x u_y & u_x u_z \\ u_y u_x & u_y u_y & u_y u_z \\ u_z u_x & u_z u_y & u_z u_z \end{array} \right\rangle \tag{3.4}$$

The trace of this symmetric matrix is plotted in figure 3.3, and the off-diagonal components containing the transverse velocity component u_z are zero by symmetry (which was also confirmed experimentally). The remaining component, the Reynolds stress $\langle u_x u_y \rangle$, is plotted in figure 3.4 (a), with two series of DNS results for comparison. The same experimental data is plotted on a linear scale (b) to see clearly the linear total stress across the channel and the relative contribution of the Reynolds stress.

$$\tau_{total} = \frac{d\langle u_x^+ \rangle}{dy^+} - \langle u_x^+ u_y^+ \rangle = 1 - \frac{y}{h} \tag{3.5}$$

The experimental Reynolds stress results between $y^+ = 0-20$ are clearly anomalous, and are certainly a result of the bimodal distribution error discussed above. Notice that although experimental results increases close to the wall, this increase is less dramatic than the variance of u_x^+ (shown in figure 3.3), further evidence for the conditional probability with respect to the two lobes of the streamwise velocity histogram discussed above.

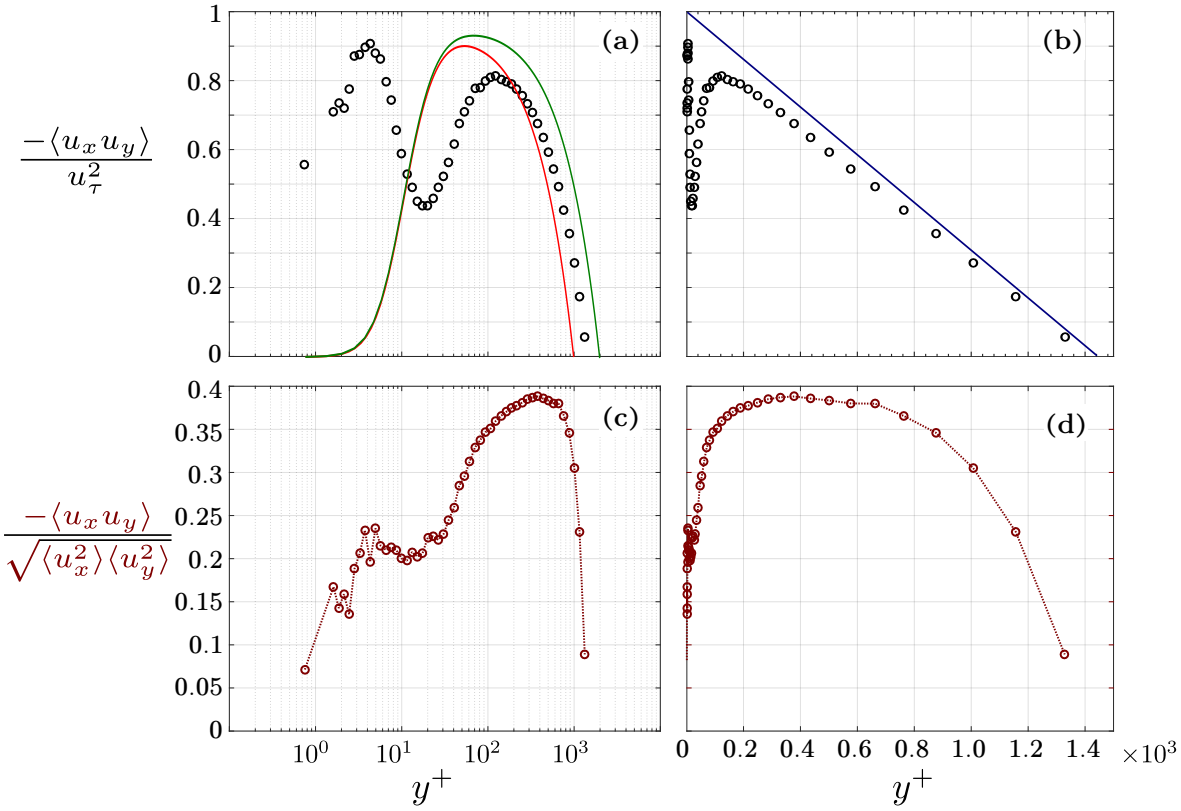

Figure 3.4: **a:** Negative Reynolds stress $-\langle u_x^+ u_y^+ \rangle$ profile measured experimentally (symbols) and from DNS at $Re_\tau = 1000$ (red line) and DNS at $Re_\tau = 2003$ (green line) as reported by Lee and Moser[119]. **b:** The same experimental data shown on a linear scale (b) to emphasis the linear relationship in equation 3.5. **c-d:** The normalized velocity correlations on log and linear horizontal axes.

Figure 3.4 (c-d) also shows the normalized Reynolds stress. The velocity components are weakly correlated near the wall, with increasing correlation throughout the log layer and a persistent plateau throughout much of the channel. The velocity correlation is expected to be zero at the channel centerline, by symmetry.

3.2.2 Velocity distribution

The distributions and higher order statistics of velocity across the width of the channel are briefly presented. In HIT the components of velocity have been found to be approximately Gaussian[10]. Velocity distributions reflect the larger scale forcing and boundary conditions of the turbulent flow, and so deviations from Gaussianity across the channel are expected. Figure 3.5 shows the normalized PDF's of the three components of fluctuating velocity at four representative distances from the wall: in the viscous layer, the buffer layer, the log layer, and in the outer layer. Notice that the distances are given by a range, and that this range (or bin) is not constant—the bin near the wall is quite thin (width of $y^+ < 1$) compared to the bin in the outer layer (width of $y^+ = 131$). The width of

the bin is approximately proportional to the number of observations in the bin, and the statistical convergence is worse for the thin bins close to the wall. The bins were chosen as a compromise between the spatial resolution, which is especially important near the wall where the statistics change rapidly with wall distance, and having an adequate number of observations.

The streamwise velocity PDF shows the bimodal distribution in the viscous layer previously seen for the full streamwise velocity in figure 3.1. By the location in the buffer layer ($y^+ = 15 - 17$) this bimodal distribution almost completely disappears, although a small trace of a low speed lobe may still be seen. The pdf in the log layer is very close to being Gaussian, in contrast to the PDF in the outer layer which has a prominent negative skew.

The PDFs of the wall-normal component of velocity are also quite varied in form with respect to wall distance. The transverse component appears more Gaussian than the other components, except in the viscous layer.

The profiles of the third and fourth order moments of the velocity components are useful to quantify the departure from Gaussianity of the pdfs; these quantities are shown in figure 3.6. The skewness reported here agree qualitatively with the results of Kim *et al*[94], including the positive skewness of the wall-normal velocity very close to the wall, negative skewness in the buffer layer, then positive skewness throughout the log and outer layers[3]. Also notable is the large change in skewness of the streamwise component within the log layer.

[3]For a discussion of this dynamic with respect to quadrant analysis see the paper of Kim *et al*[94]

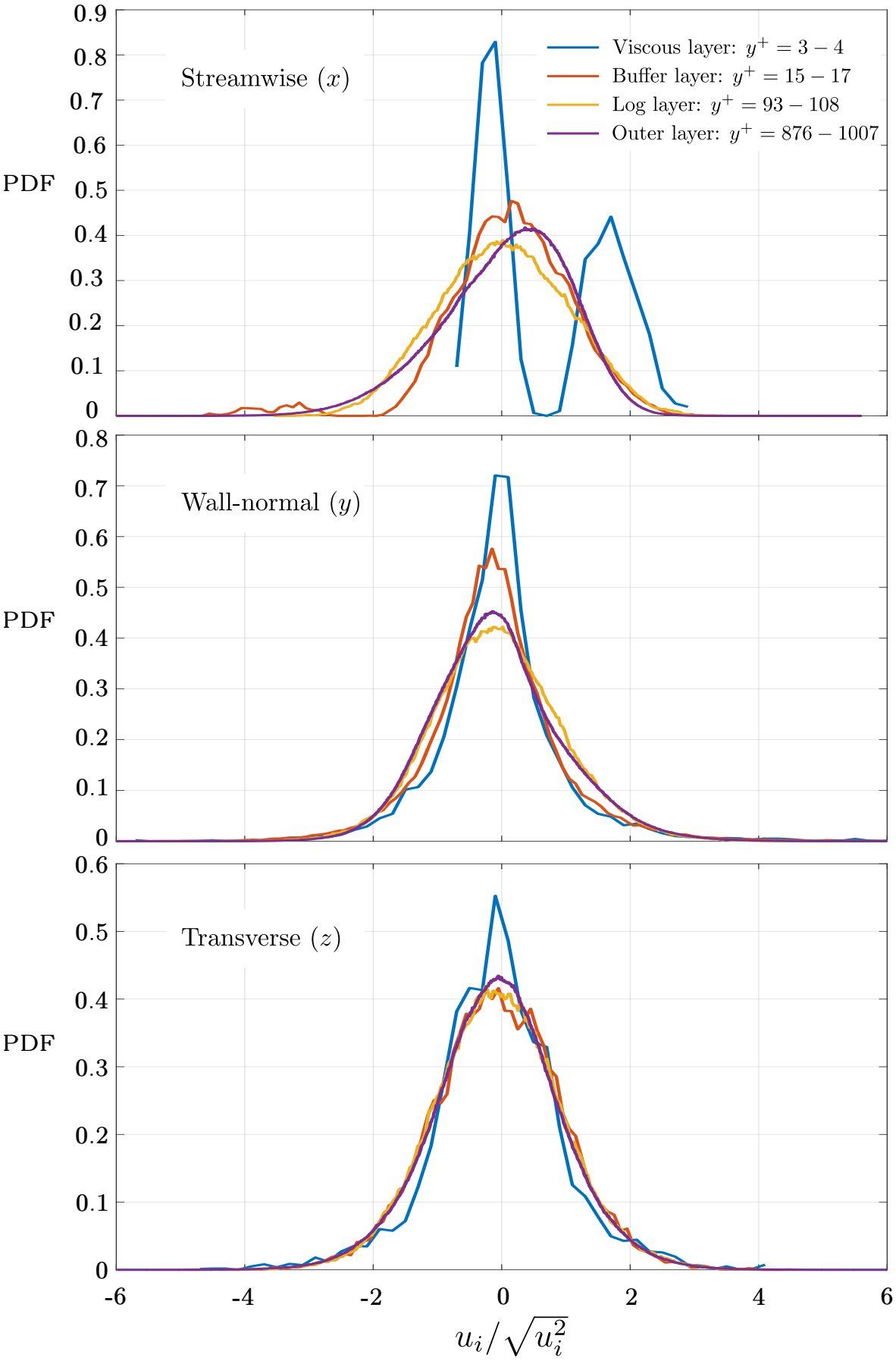

Figure 3.5: Probability density functions of the components of velocity at four representative locations in the turbulent channel. Each PDF is normalized by the rms of velocity at that location.

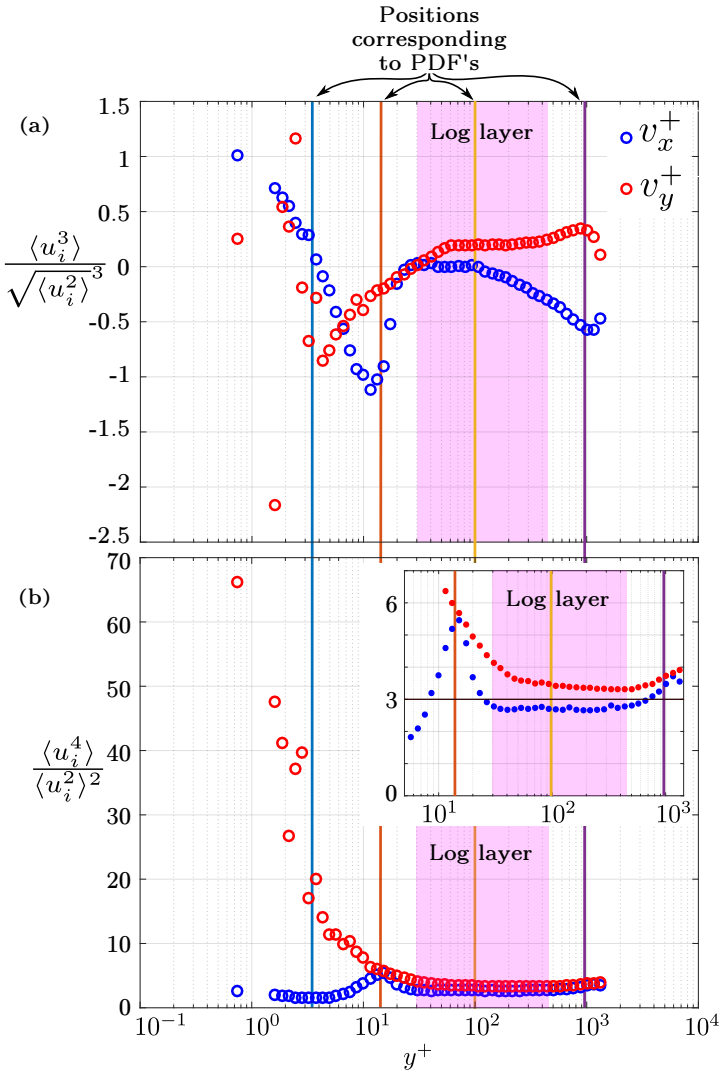

Figure 3.6: The skewness (a) and flatness (b) of the streamwise and wall-normal components of velocity. The inset in (b) provides a zoomed-in view of the flatness, and highlights the Gaussian flatness value of 3 Colored lines mark the four distances from the wall corresponding to the PDF's shown in figure 3.5.

Skewness and flatness results were compared to experimental measurements of Comte-Bellot[88], performed for similar Reynolds numbers. Overall good agreement was found, with some exceptions in the near-wall region ($y^+ < 20$).

The foregoing statistics describe the components of velocity individually. In order to see dependence between velocity components the conditional means were calculated; the mean streamwise velocity conditioned on the wall-normal velocity is plotted in figure 3.7. The profile of the Reynolds stress $\langle u_x u_y \rangle$ was found to be negative across the channel (fig. 3.4), implying that opposite signed velocity components are more probable than equally signed components. The conditional means in figure 3.7 reflect this, except at the location in the viscous layer. Notice that in the buffer layer large wall-normal velocities away from the wall are only weakly correlated with streamwise velocity fluctuations, but large wall-normal velocities towards the wall ($-v_y$) are more correlated with faster streamwise fluctuations. The inverse is true in the outer layer, where positive v_y and negative v_x fluctuations are more likely than negative v_y and positive v_x fluctuations. In the log layer these correlations are approximately symmetric.

The Eulerian velocity statistics shown here illustrate the complex inhomogeneity of turbulent channel flow[4]. Turbulence statistics have large spatial gradients, especially near the wall, and are only approximately self-similar in the log layer. The statistics of velocity components were shown to be highly anisotropic and correlated to each other throughout the channel. The phenomenology of Kolmogorov suggests that at large Reynolds numbers this large scale inhomogeneity and anisotropy should be forgotten at smaller scales, and the small scales should be homogeneous and isotropic, at least locally. The next section examines Eulerian statistics in acceleration, a fundamentally small-scale quantity, and explores where, and to what extent, this phenomenology holds in the turbulent channel.

[4]This was an extremely brief overview of Eulerian statistics in channel flow; the interested reader is refered to the the pioneering measurements of Comte-Bellot[88], the more recent experimental work of Monty[87], and the ever increasing DNS results from Kim[94] to Lee[119].

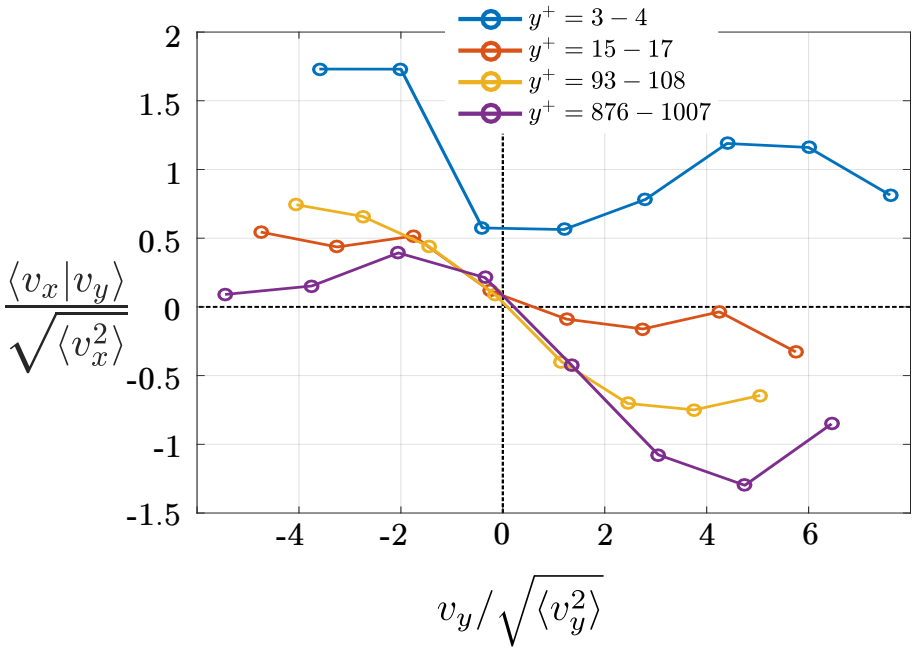

Figure 3.7: The mean fluctuating streamwise velocity conditioned on the instantaneous value of the wall-normal velocity at four distances from the wall. The widely spaced symbols reflect the large velocity bin size, which was necessary due to the difficulty of converging statistics conditioned once on position and once again on velocity.

3.3 Acceleration statistics

Acceleration is a fundamentally Lagrangian quantity, and as such has typically been studied in a Lagrangian frame of reference. Eulerian statistics, such as the PDF of acceleration and its moments, may be extracted from the Lagrangian data, and have been used to explore the intermittency of fluid particle accelerations. The primary focus of research efforts has been HIT, in which these statistics are not dependent on position. In a turbulent channel these statistics are dependent on distance to the wall, and it is therefore important to understand their Eulerian profiles as a prerequisite to the understanding of Lagrangian statistics in a turbulent channel.

3.3.1 Profiles of acceleration mean and variance

Eulerian statistics in acceleration are presented in this section, beginning with the profiles of the mean and the variance in figure 3.8. Mean acceleration in a turbulent channel may be understood directly from the N-S equations, using the averaged N-S equation introduced in chapter 1 (equation 1.17).

$$\text{Averaged N-S:} \quad \langle \mathrm{A}_i \rangle = -\frac{1}{\rho}\frac{\partial \langle \mathrm{P} \rangle}{\partial x_i} + \nu \frac{\partial^2 \langle \mathrm{U}_i \rangle}{\partial x_j \partial x_j} \tag{3.6}$$

$$\text{Streamwise component:} \quad \langle \mathrm{A}_x \rangle = -\frac{1}{\rho}\frac{\partial \langle \mathrm{P} \rangle}{\partial x} + \nu \frac{d^2 \langle \mathrm{U}_x \rangle}{dy^2} \tag{3.7}$$

$$\text{Wall-normal component:} \quad \langle \mathrm{A}_y \rangle = -\frac{1}{\rho}\frac{\partial \langle \mathrm{P} \rangle}{\partial y} \tag{3.8}$$

Previous discussion in section 1.2 discussed why the streamwise pressure gradient is constant across the channel, so the mean streamwise acceleration profile is the sum of a

constant and the curvature of the mean velocity profile. Careful examination of figure 3.8 shows that at the channel center the mean streamwise acceleration is slightly negative. At the channel center $d^2\langle U_x\rangle/dy^2$ is very small (and negative), and thus most of the mean streamwise acceleration is due to the mean streamwise pressure gradient. The contribution of the curvature of the mean velocity profile to the mean streamwise acceleration is clearly much greater (up to ≈ 95 times at $y^+ \approx 8$) than the contribution of the mean streamwise pressure gradient.

Equation 3.8 shows the mean wall-normal acceleration is directly proportional to the mean pressure gradient in the wall-normal direction. Figure 3.8 shows the profile of the mean wall-normal acceleration, which is approximately equal in magnitude to the mean streamwise acceleration profile. This implies that the mean wall-normal pressure gradient near the wall is much larger (up to ≈ 95 times larger) than the mean streamwise pressure gradient driving the flow.

The variances of the acceleration components are shown in figure 3.8 to be approximately equal in magnitude at their peak values, although the peak values occur at different distances to the wall; $y^+ = 5$, 28,20, for the streamwise, wall-normal, and spanwise components, respectively. Note that unlike the components of velocity where the ratio between root-mean-square (rms) and mean is quite low, the components of acceleration have a large ratio of rms to mean over most of the channel width. Near the peaks of the mean acceleration this ratio is at a minimum: $\sqrt{\langle a_x^2\rangle/\langle A_x\rangle^2} \approx 2.25$ for the streamwise component, and $\sqrt{\langle a_y^2\rangle/\langle A_y\rangle^2} \approx 3.13$ for the wall-normal component. Good agreement is seen between experimental results and DNS results for the mean and variance of acceleration, especially for $y^+ \gtrapprox 10$. Note that the large error bars in figure 3.8 are mostly due to the uncertainty in the scaling variables. The acceleration variance is normalized by u_τ^6/ν^2, which magnifies the uncertainty from u_τ.

3.3.2 Decomposition of acceleration

Higher order single point Eulerian statistics are presented below in the typical inertial reference frame x,y,z that has been used up to this point, as well as in a non-inertial reference frame attached the the particle trajectory. In this reference frame, the acceleration may be decomposed into the component parallel to the velocity, $a_\parallel$, and a component normal to the velocity, $a_\perp$. Exact definitions are given in equation 3.9. This decomposition is linked directly to the change in energy of the fluid particle ($\mathbf{A}\cdot\mathbf{V}$) and the geometry of the particle trajectory, e. g. a helical particle trajectory has a constant magnitude $a_\perp$ related to the curvature of the helix. This decomposition of the acceleration has been used by Mordant *et al*[112], Toschi *et al*[37], and Biferale *et al*[120] to explore the connection between acceleration, vorticity, and vortex filaments in HIT. These researchers showed that fluid particles trapped in vortex filaments, characterized by a helical particle paths and large centripetal accelerations that change sign quickly (as a particle moves in a helical path $a_\perp$ points towards the axis of the helix and rotates with the particle). In homogeneous isotropic turbulence, a flow in which the statistics of the three inertial-reference-frame components are equal by definition, the parallel and perpendicular components of acceleration are statistically distinct.

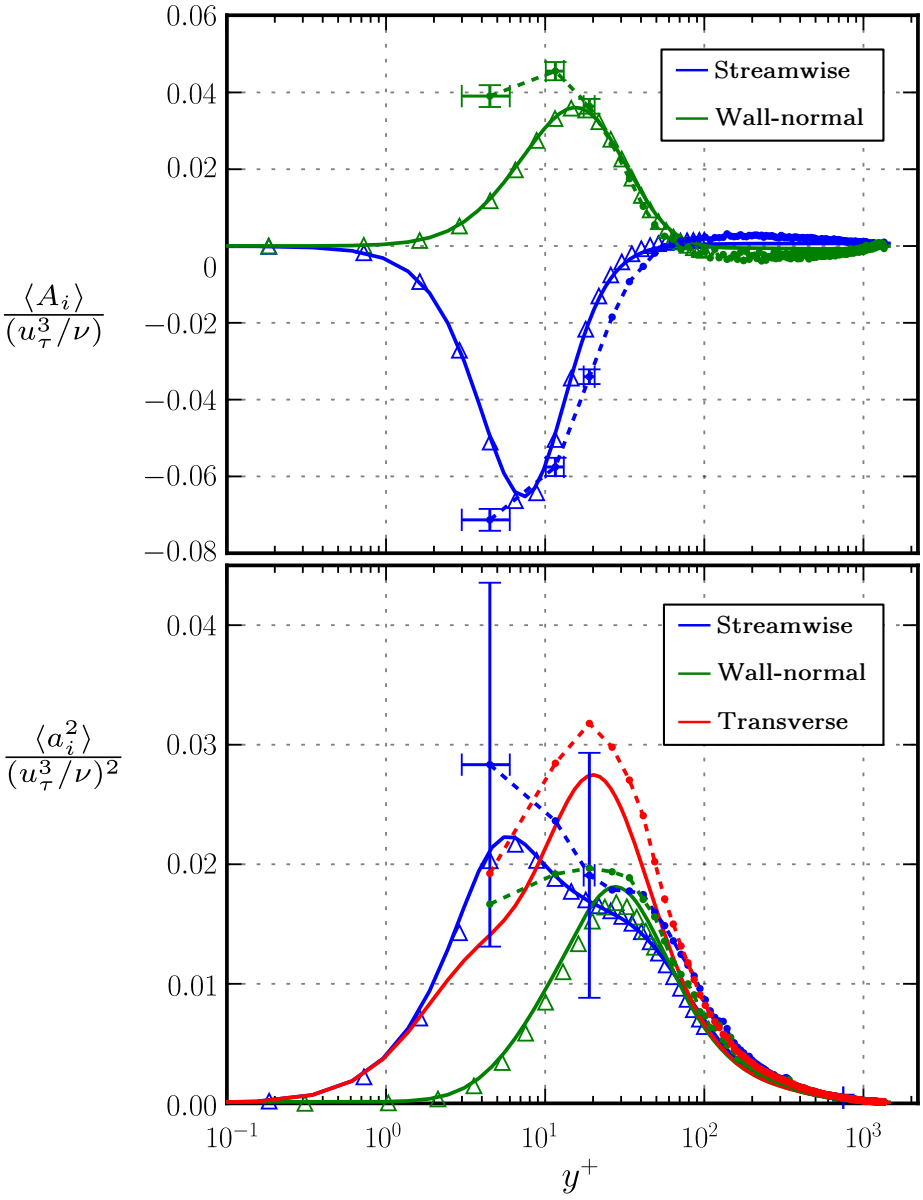

Figure 3.8: Mean acceleration profiles (top) and acceleration variance profiles (bottom) from experimental measurements at $Re_\tau = 1440$ (Symbols connected with dashed lines), DNS at $Re_\tau = 1440$ from Polanco and Vinkovic[42] (solid lines), and another DNS at $Re_\tau = 600$ (triangles) from Yeo *et al*[78]. Figure adapted from Stelzenmuller *et al*[42].

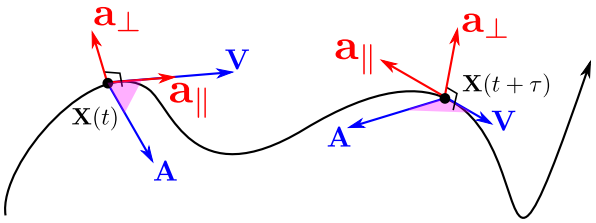

$$\begin{aligned} \hat{\mathbf{t}} &\equiv \mathbf{V}/|\mathbf{V}| \\ \mathbf{a}_\parallel &\equiv (\mathbf{A}\cdot\mathbf{V})\,\hat{\mathbf{t}} \\ \mathbf{a}_\perp &\equiv \mathbf{A}\times\hat{\mathbf{t}} \end{aligned} \tag{3.9}$$

An explicit connection between velocity, acceleration and the differential geometry of the particle path given by the Frenet-Serret formulas was considered by Braun *et al*[121]. Choi *et al*[122], Scagliarini[123]and Xu *et al*[124] studied the the Lagrangian statistics in velocity, helicity, and acceleration in terms of the curvature $\kappa \equiv a_\perp/u^2$ and torsion $\tau \equiv \mathbf{u}\cdot(\mathbf{a}\times\dot{\mathbf{a}})/u^6\kappa^2$ used in the Frenet apparatus. Bos *et al*[125] looked at the dynamics

of the change in angle of a particle trajectory, which at short times relates directly to the curvature and the normal acceleration.

This geometrical approach to particle trajectories in turbulence is based on the decomposition of acceleration given in equation 3.9. Statistics in these acceleration components are presented below along with the usual components (x, y, z). The turbulence is quasi-isotropic and quasi-homogeneous at the channel center and increasingly organized and populated with coherent structures near the wall. The decomposition of the acceleration into parallel and perpendicular components has a direct connection to the geometry of particle trajectories, and as such is an effective tool to describe the complex, wall-distance-dependent topology of the turbulence. A more complete effort to present statistics in the geometrical quantities such as curvature and torsion directly await a future work.

3.3.3 PDFs of acceleration

Probability density functions of the components and magnitude of acceleration at four distances from the wall are plotted in figure 3.9. At all four locations and for all components long-tailed, highly non-Gaussian distributions are observed, consistent with observations in HIT. In the viscous and buffer layers significant differences between the acceleration components are seen, is contrast to the log layer and outer layer location which show approximate similarity between components. Note that acceleration statistics vary strongly with distance from the wall in the viscous and buffer layers, and combining data from the wall-bins as given in figure 3.9 results in an averaging effect that reduces resolution of the PDFs, e.g. the pdf at $y^+ = 5 \pm 1$ has a different form than the PDF at $y^+ = 30 \pm 1$, but these differences are mixed together in the results shown in figure 3.9 for the wall bin $y^+ = 5 - 30$. Thinner wall-bins are more sensitive to these difference, but are unable to resolve the low-probability tails of the PDF due to limited data. In the viscous and buffer layers the parallel component of the acceleration is highly congruent with the streamwise component of acceleration, which is consistent with idea that near the wall the turbulence is dominated by structures parallel to the wall, and the turbulence is quasi-bidimensional. Throughout the channel the perpendicular component of acceleration has a sharp cusp around zero that appears qualitatively different from the other components, indicating the high probability of low-curvature, straight-line trajectories.

The joint PDFs of Cartesian components show that negative streamwise accelerations are correlated with positive wall-normal accelerations in the viscous and buffer layers; farther from the wall the joint PDFs appear approximately isotropic. Particles advected towards the wall decelerate in the streamwise direction ($a_x < 0$, i. e. opposing the mean flow direction) due to the slower mean velocity, and accelerate towards the channel center when approaching the wall. These joint PDFs show that particles advected towards the wall in this manner have higher acceleration events than particles advected away from the wall.

Joint PDFs of the parallel and perpendicular components of acceleration show a distinctive cross shape at all four locations in the channel, indicating that intense acceleration events in one component are correlated with low acceleration in the other component. Recall from the definition of these components (equation 3.9) that this result means rapid changes in velocity magnitude (high values of $a_\parallel$) are more likely when the velocity direction is not changing rapidly (small values of $a_\perp$), and vice-versa. Rapid changes in the direction of velocity may be associated with high-vorticity regions of the flow, and rapid changes in velocity magnitude with high-strain regions of the flow[126].

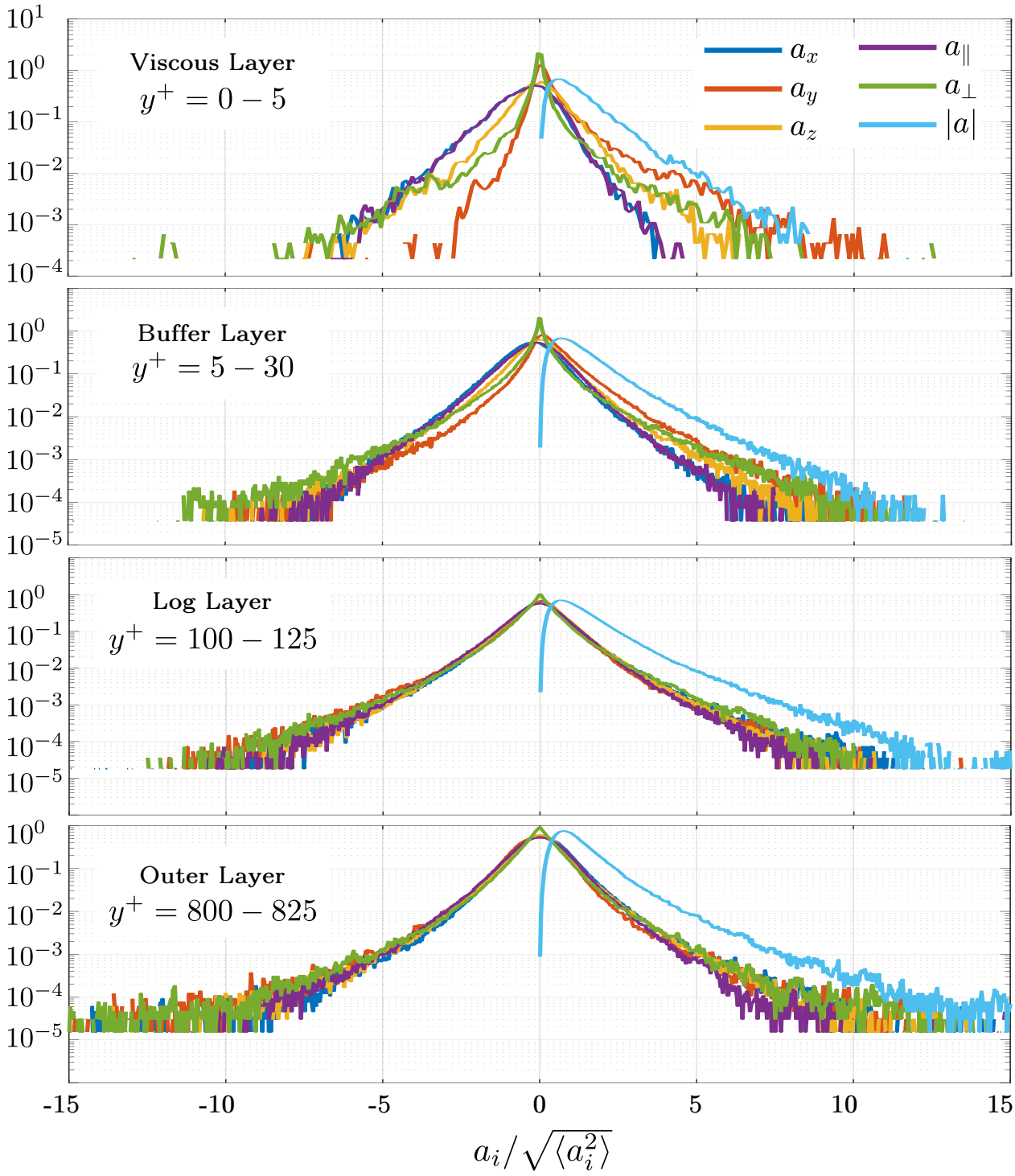

Figure 3.9: PDFs of the components of acceleration in the streamwise (a_x), wall-normal (a_y) , and transverse (a_z) directions. Also plotted are the components of acceleration parallel to the local instantaneous velocity ($a_\parallel$), perpendicular to the instantaneous velocity ($a_\perp$), and the magnitude of acceleration. These PDFs are taken from measurements in four wall-bins at four distances from the wall, distances that correspond to four characteristic layers. The wall-bin closest to the wall, in the viscous layer, is 5 wall-units wide (corresponding to the entire width of the viscous layer), the other wall-bins are 25 wall-units wide, and are consequently have better statistical convergence.

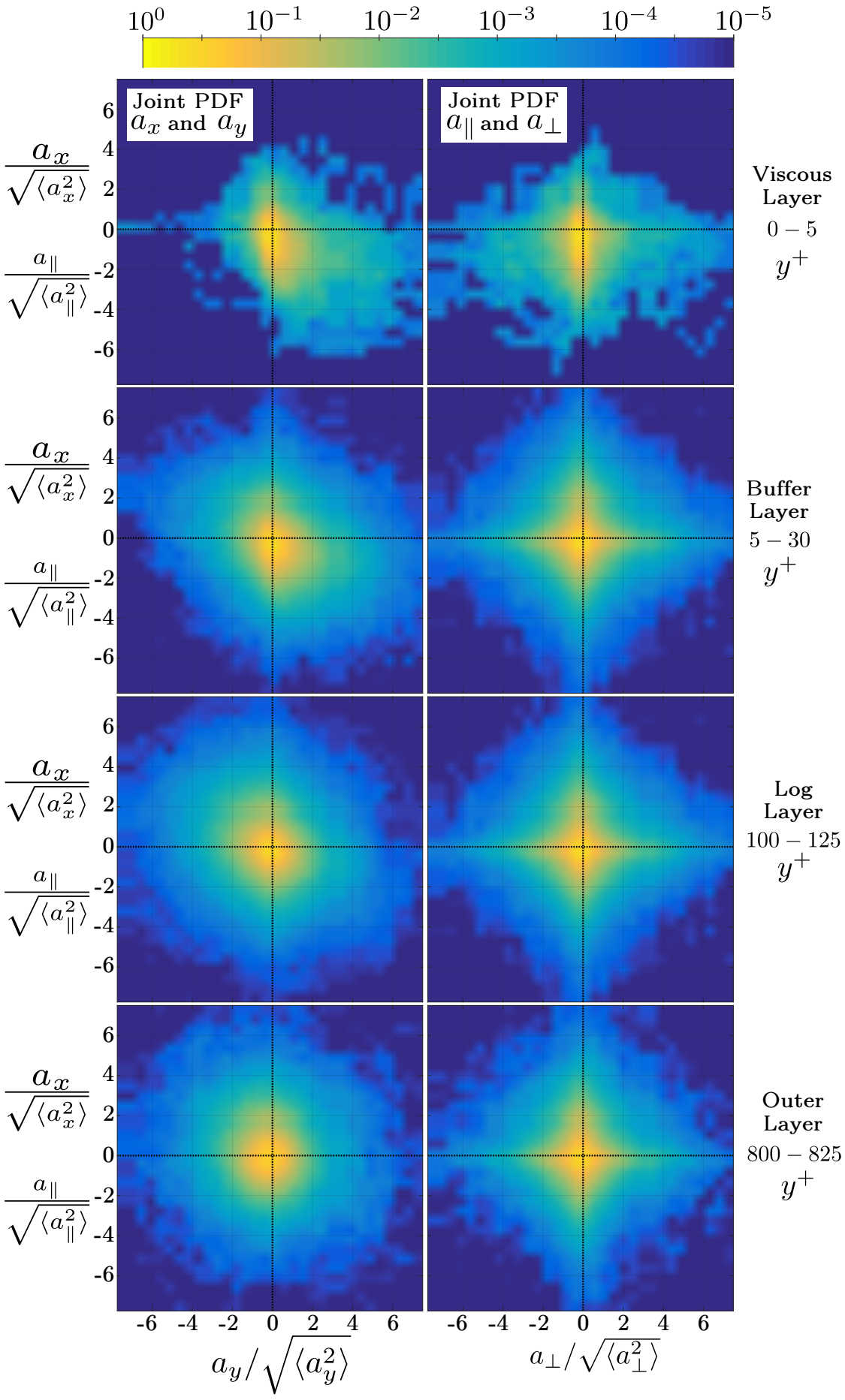

Figure 3.10: Joint PDFs of the components of acceleration at four distances from the wall.

The asymmetry of the PDFs shown in figure 3.9—especially visible in the wall-normal and perpendicular components of acceleration near the wall—is quantified by taking the third moment of the acceleration components, with the appropriate normalization: $\langle a_i^3 \rangle / \langle a_i^2 \rangle^{3/2}$. This quantity, also called the skewness, is plotted in figure 3.11 (a). The skewness across the channel for streamwise, wall-normal, parallel and perpendicular components of acceleration is shown in figure 3.11 (a, top), and a zoomed in view in shown directly below. The skewness of the transverse z component of acceleration is zero by symmetry.

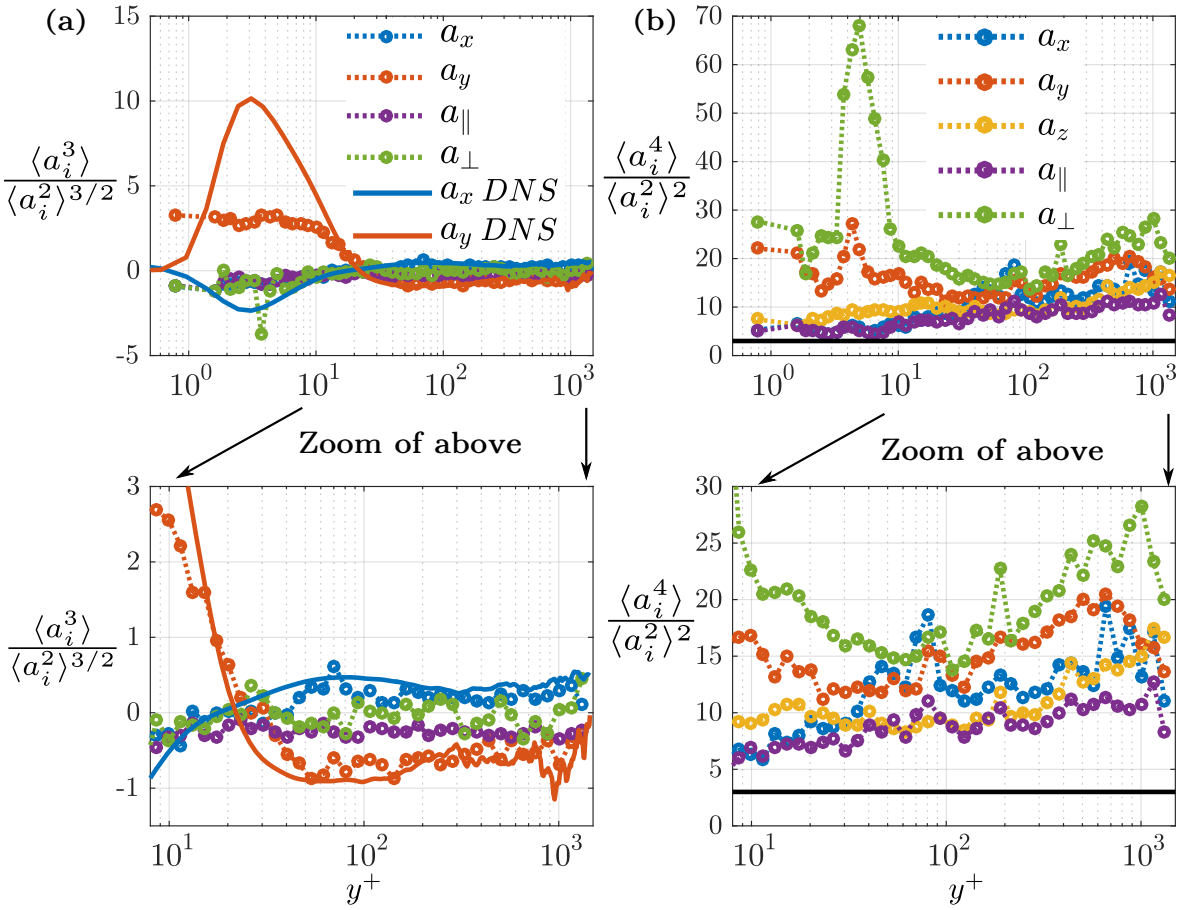

Figure 3.11: Skewness (a) and flatness (b) of acceleration components across the channel. DNS results from equal Reynolds number channel simulations. Bottom row subfigures are simply zoomed in views of the sub-figures above.

DNS results show extremely large skewness values[5] for the wall-normal component of acceleration, peaking at $y^+ \approx 3$. Experimental results agree quite well to DNS results except close the the wall ($y^+ < 15$), a lack of agreement probably due to increasingly poor statistical convergence in the experimental data in this region. The skewness of the wall-normal and streamwise components of acceleration changes sign at $y^+ \approx 25$, and non-zero skewness continues to be observed up the the channel center. This persistence of non-zero skewness in acceleration, which is a measure of small scale anisotropy, has been previously observed in channel flow DNS[78]. Also of note is the difference between the skewness in a_x, a_y and the lesser skewness of both the parallel and the perpendicular components of acceleration throughout the channel width.

[5]Positive skewness is interpreted as a higher probability of extreme positive events than extreme negative events. In this case large accelerations away from the wall are more probable than large accelerations towards the wall.

The normalized fourth moment of the acceleration PDF, $\langle a_i^4 \rangle / \langle a_i^2 \rangle^2$, is a symmetric measure of the importance of the extreme events relative to the events close to the mean. A Gaussian distribution has a flatness of 3, and larger flatness values indicate "fatter tails"—i. e. a higher probability of extreme events—and/or a "thinner core"—i. e. a lower probability of events close to the mean. The flatness for the streamwise, wall-normal, transverse, parallel, and perpendicular components of acceleration is plotted in figure 3.11 (b) and the zoomed in view of the same results directly below. All components show higher values of flatness than the Gaussian value of 3 (shown in the thick black line), as expected. This results are in qualitative agreement with previously published DNS results[75, 78], except in the near-wall region ($y^+ < 10$) where flatness values in excess of 400 have been reported. Although higher than the other components, the flatness values of the wall-normal component of the acceleration in the experimental data does not show an very large peak near the wall, again probably due to a lack of statistical convergence. The parallel component has the smallest flatness value across the channel, and the parallel component the largest, although from the pdf in figure 3.9 the large flatness values are a consequence of a thinner core region of the PDF; the tails of the pdf's are similar to the other components. A similar trend was observed by Kim *et al*[82] for the parallel component of acceleration in a turbulent jet, where the flatness of this component was found to be large compared to the streamwise and radial components.

These results may be compared to findings for the parallel and perpendicular components of acceleration in HIT ($Re_\lambda = 300$) from Lévêque and Naso[126]. In HIT a Cartesian component of acceleration has zero skewness and high flatness[6]. Lévêque and Naso found that the parallel component of acceleration is negatively skewed, and the perpendicular component is not skewed. This is similar to the result shown in figure 3.11 across most of the channel ($y^+ > 20$), even as the Cartesian components show non-zero skew. The trends in acceleration flatness also follow those found in HIT: the flatness of the parallel component is less than the flatness of the Cartesian component, whereas the perpendicular component has a slightly higher flatness than the Cartesian component. The agreement between HIT and the channel flow results regarding the flatness and skewness of parallel and perpendicular acceleration components is notable, considering the significant differences observed between these two systems vis-à-vis the Cartesian components of acceleration.

3.3.4 Correlation of acceleration components

The mean correlation between the streamwise and the wall-normal components of acceleration across the channel is shown in figure 3.12. This quantity $\langle a_x a_y \rangle$ is analogous to the Reynolds stress, and like the Reynolds stress is zero in homogeneous isotropic turbulence. The top two sub-figures show this quantity with appropriate wall-scaling, plotted on a log-linear scale (left), and a linear-linear scale (right). This correlation approaches zero approximately midway between the wall and the channel center. If the data closer to the wall than $y^+ \approx 10$ is neglected[7] then a maximum correlation of 0.25 appears a $y^+ \approx 40$. This peak appears in the same location for both the absolute correlation and the correlation normalized by the product of the rms of the two components. At this location the normalized velocity correlation is also approximately 0.25. The correlation is expected to be zero at the channel center by symmetry, and the trend observed in the normalized sub-figures at

[6] The level of flatness depends on Re_λ

[7] The uncertainty around this experimental data is quite high, and the experimental and DNS acceleration results begin to diverge at approximately $y^+ \approx 10$

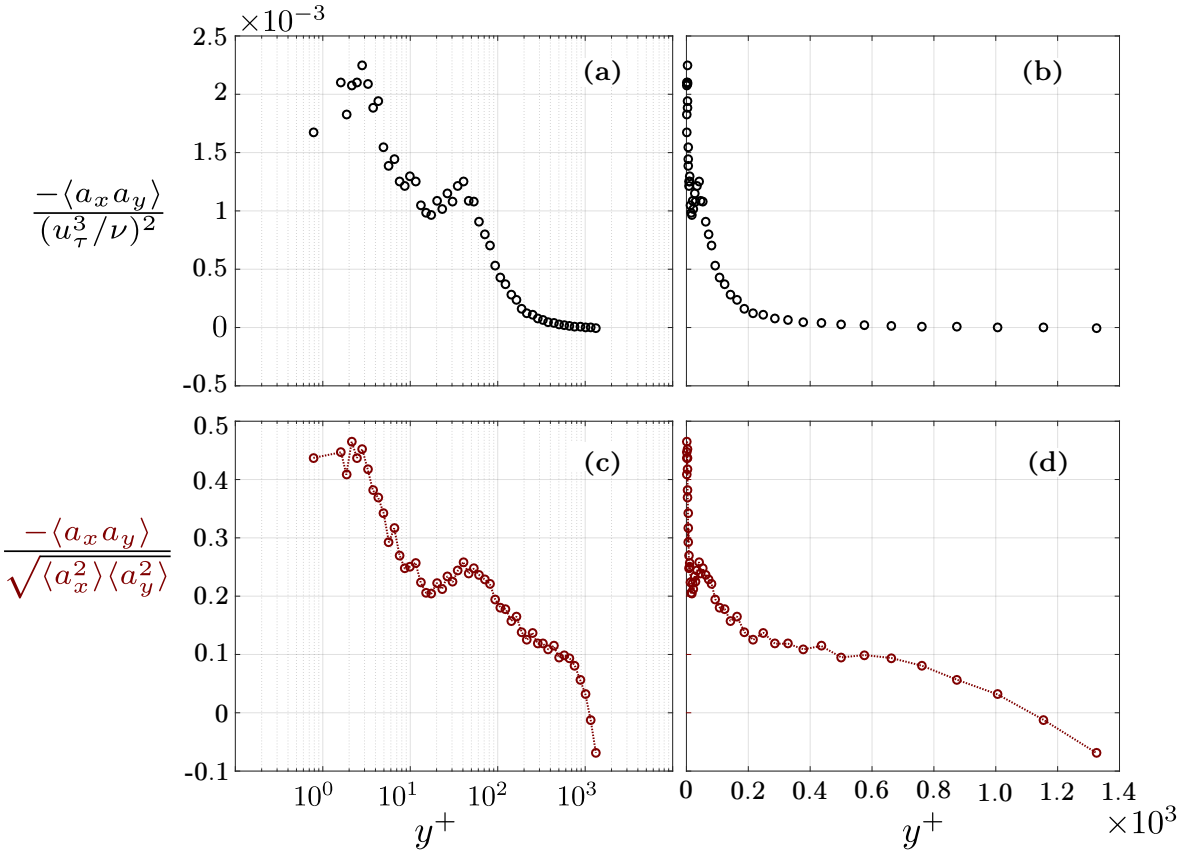

Figure 3.12: The mean correlation of streamwise and wall-normal components of acceleration across the channel, plotted in wall scaled variables in linear-log scale(a) and linear-linear scale (b). The mean correlation of streamwise and wall-normal components of acceleration across the channel, normalized by the product of the standard deviations in linear-log scale (c) and linear-linear scale (d).

$y^+ \gtrsim 800$ is probably a result of the uncertainty with respect the ratio of two values, $\langle a_x a_y \rangle$ and $\sqrt{\langle a_x^2 \rangle \langle a_y^2 \rangle}$ that are simultaneously approaching zero.

3.3.5 Contributions of the parallel and perpendicular components of acceleration

The magnitude of the acceleration is given as

$$|\mathbf{a}| \equiv \sqrt{a_x^2 + a_y^2 + a_z^2} \tag{3.10}$$

As discussed above in section 3.3.2, the acceleration may be decomposed into two orthogonal components: $a_\parallel$ and $a_\perp$, such that

$$|\mathbf{a}| \equiv \sqrt{a_\parallel^2 + a_\perp^2} \tag{3.11}$$

For isotropic turbulence the components on the r.h.s. of equation 3.10 are statistically equal, and the acceleration magnitude may be written as

$$\langle |\mathbf{a}| \rangle = \left\langle \sqrt{3 a_i^2} \right\rangle \quad i \in 1,2,3 \tag{3.12}$$

for any 3-D orthonormal coordinate system. The perpendicular component of acceleration has two degrees of freedom, so in an isotropic system the acceleration magnitude may be written as

$$\langle |\mathbf{a}| \rangle = \left\langle \sqrt{3a_{\parallel}^2} \right\rangle = \left\langle \sqrt{\frac{3}{2}a_{\parallel}^2} \right\rangle \tag{3.13}$$

The mean square of the parallel and perpendicular components of acceleration are plotted in figure 3.13 (top), along with the square of the total magnitude. The relative contribution to the square of the total magnitude by the parallel and perpendicular components is shown in the middle sub-figure. This ratio is corrected according to equation 3.13, and re-plotted in the bottom sub-figure.

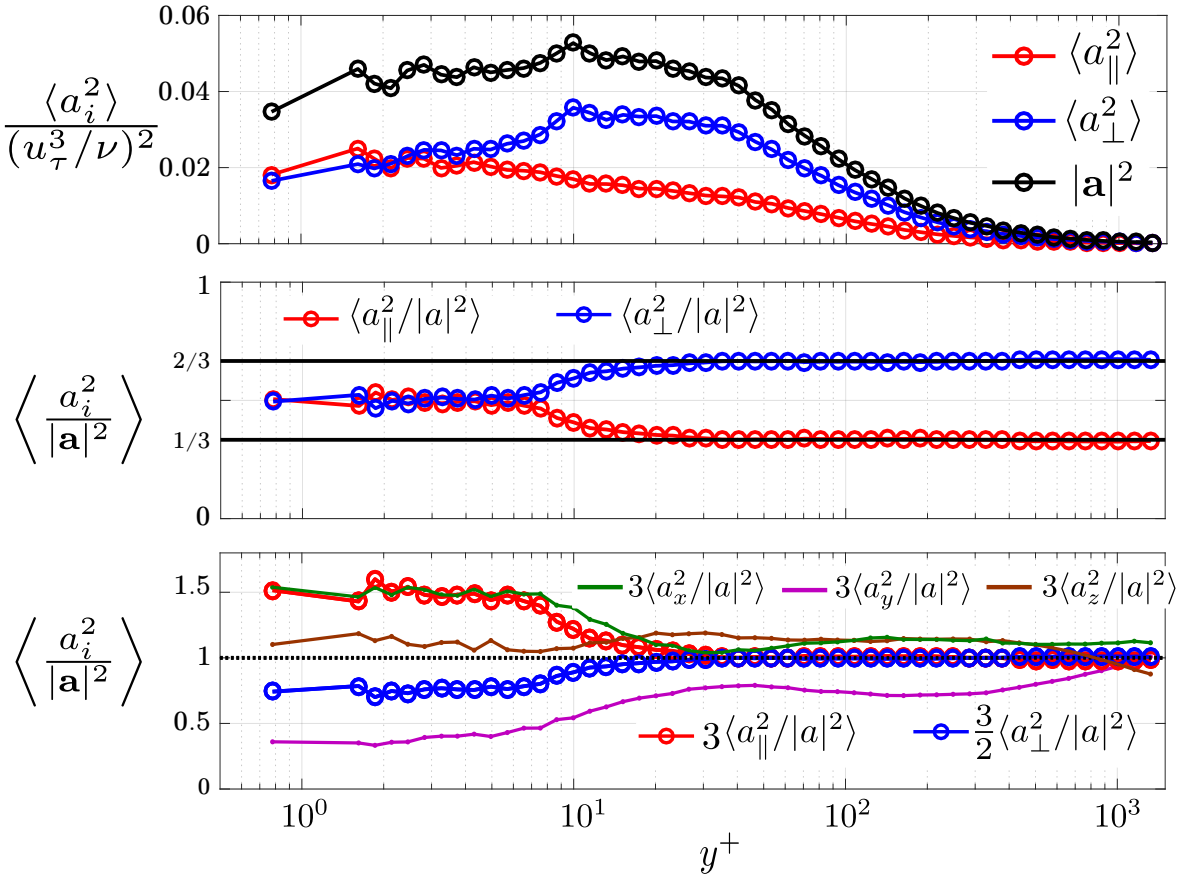

Figure 3.13: **Top:** The mean square of the parallel (red) and perpendicular (blue) components of acceleration according to the definition given in equation 3.9. Also plotted in the mean square acceleration magnitude (black). **Middle**: The mean square parallel and perpendicular components of the acceleration normalized by the mean square magnitude of acceleration are plotted across the channel. Note that the mean is taken *after* the normalization. **Bottom**: The same ratios plotted in the middle sub-figure normalized such that 1 is the ratio corresponding to isotropy. This ratio is also plotted with the x, y, z components of acceleration for comparison.

Figure 3.13 shows a broader peak in the mean square magnitude and perpendicular component at $y^+ \approx 10-20$. The location and width of these peaks are consistent with the results for the acceleration variance in x, y, and z seen in figure 3.8. The parallel component of acceleration increase monotonically towards the wall. The ratios of the square of both the perpendicular and parallel acceleration components with square of the acceleration magnitude indicate a return to isotropy at $y^+ \approx 20-30$. Closer to the wall the parallel acceleration component contributes more to the magnitude of acceleration than

the perpendicular component, relative to the expected isotropic contribution. This is further illustrated by the bottom sub-figure in figure 3.13, where the the correct normalization factor[8] allows the direct comparison of components. None of the x, y, or z components of acceleration converge to the isotropic value of 1, in contrast to the parallel and perpendicular components of acceleration, which converge to isotropy at approximately the same distance from the wall.

The parallel-perpendicular decomposition of acceleration defined in equation 3.9 may be written as follows

$$\hat{t} = \mathbf{v}/|\mathbf{v}| \tag{3.14}$$

$$\hat{b} = \frac{\mathbf{a}\times\mathbf{v}}{|\mathbf{a}\times\mathbf{v}|} \tag{3.15}$$

where $\hat{t}$ and $\hat{b}$ are the unit vectors for the parallel and perpendicular components[9] of acceleration. These projection of these components on the x, y, z reference frame, written as

$$\mathbf{a}_\parallel = |\mathbf{a}_\parallel|\hat{t} = |\mathbf{a}_\parallel| t_x + |\mathbf{a}_\parallel| t_y + |\mathbf{a}_\parallel| t_z \tag{3.16}$$

$$\mathbf{a}_\perp = |\mathbf{a}_\perp|\hat{b} = |\mathbf{a}_\perp| b_x + |\mathbf{a}_\perp| b_y + |\mathbf{a}_\perp| b_z \tag{3.17}$$

where for example t_x is the projection of the unit vector $\hat{t}$ in the direction $\hat{x}$. Plotting the projections of the parallel component of acceleration (the last three terms in equation 3.16) and the projections of the perpendicular component of acceleration (the last three terms in equation 3.17) shows the organization of these components of acceleration relative the the geometry of the channel.

Figure 3.14 shows the relative importance of the contributions from the x, y, and z components of acceleration to the parallel and perpendicular components of acceleration. In isotropic turbulence these contributions would be statistically equal, i. e. the blue, red, and black curves for each symbol would collapse onto one curve in figure 3.14. The parallel component of acceleration (shown in figure 3.14 with the cross symbols) is dominated by contributions from the streamwise component along the width of the channel, and the wall-normal contribution is relatively low, consistent with the increasing alignment of the acceleration with the wall in the near-wall region.

The perpendicular component of acceleration is dominated by the contribution from the wall-normal component in the near-wall region, and continues to be the largest contribution far from the wall. In other words, on average, the accelerations responsible for bending the particle trajectory are strongest in the wall-normal direction, significantly stronger than the these accelerations in the streamwise direction, which is in turn stronger that these accelerations in the transverse direction. Recall that in the case of the highly simplified vision of a quasi-streamwise vortex—a helical particle path in which the axis of the helix is parallel to x, and located at $y^+ \approx 20$—the perpendicular component of acceleration is constant, and is composed of equal contributions of the a_y and a_z. The results in figure 3.14 show that while quasi-streamwise vortices similar to this simplified model may exist they are not dominant in the statistics.

[8] The normalization factor is 3 for all components except $a_\perp$, where the normalization factor is 3/2.

[9] This notation was chosen to be consistent with the Frenet apparatus, in which the direction $\mathbf{a}\times\mathbf{v}$ is called binormal.

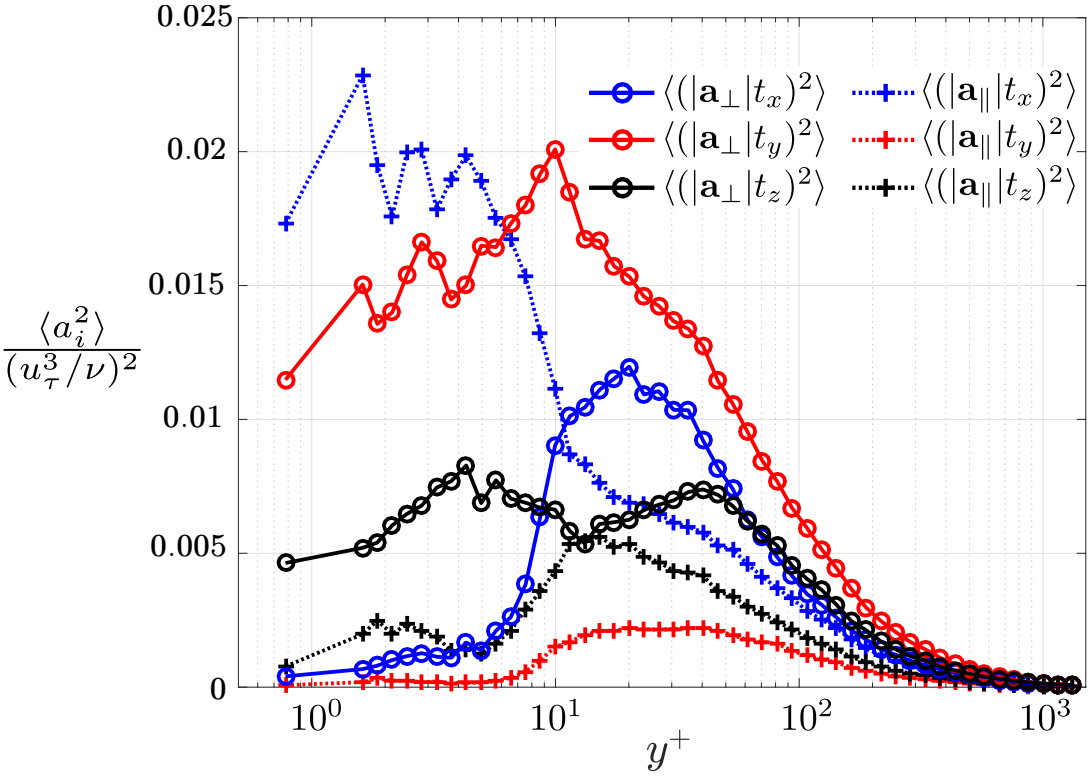

Figure 3.14: The absolute values of the parallel (crosses) and perpendicular (circles) components of acceleration are shown, decomposed into their projections on the $\hat{x}$, $\hat{y}$, and $\hat{z}$ unit vectors.

3.3.6 Acceleration angles

The decomposition of the total acceleration into the magnitude and direction, $a_i = |a|e_i$, has been considered may many researchers in the context of HIT, and forms the basis of some Lagrangian stochastic models. In HIT the orientation of acceleration is definition isotropically distributed, but DNS results from a turbulent channel simulation by Zamansky *et al*[3] show significant, wall-distance dependent, deviations from isotropy. Two angles are

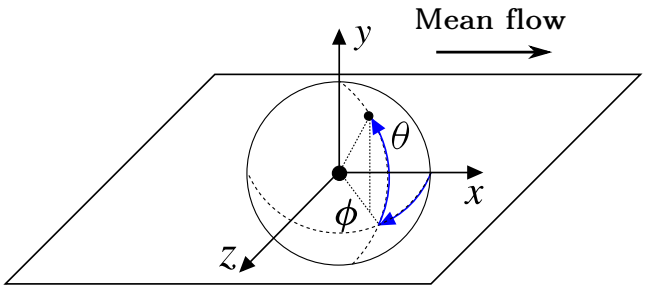

Figure 3.15: Definition of the longitudinal (ϕ) and wall-normal (θ) angles; figure adapted from Zamansky *et al* [3].

necessary to determine 3-D orientation; these two angles are defined following Zamansky *et al*, and are illustrated in figure 3.15.

The wall-normal angle θ is defined between $\pi/2$ (acceleration is oriented perpendicular to, and pointing away from, the wall) to $-\pi/2$ (acceleration is oriented perpendicular to, and pointing towards, the wall). The PDF of this angle at a variety of distances to wall is plotted in figure 3.16, which shows strong anisotropy in the orientation of acceleration near the wall. The experimental data does not show a return to isotropy until $y^+ = 1000$,

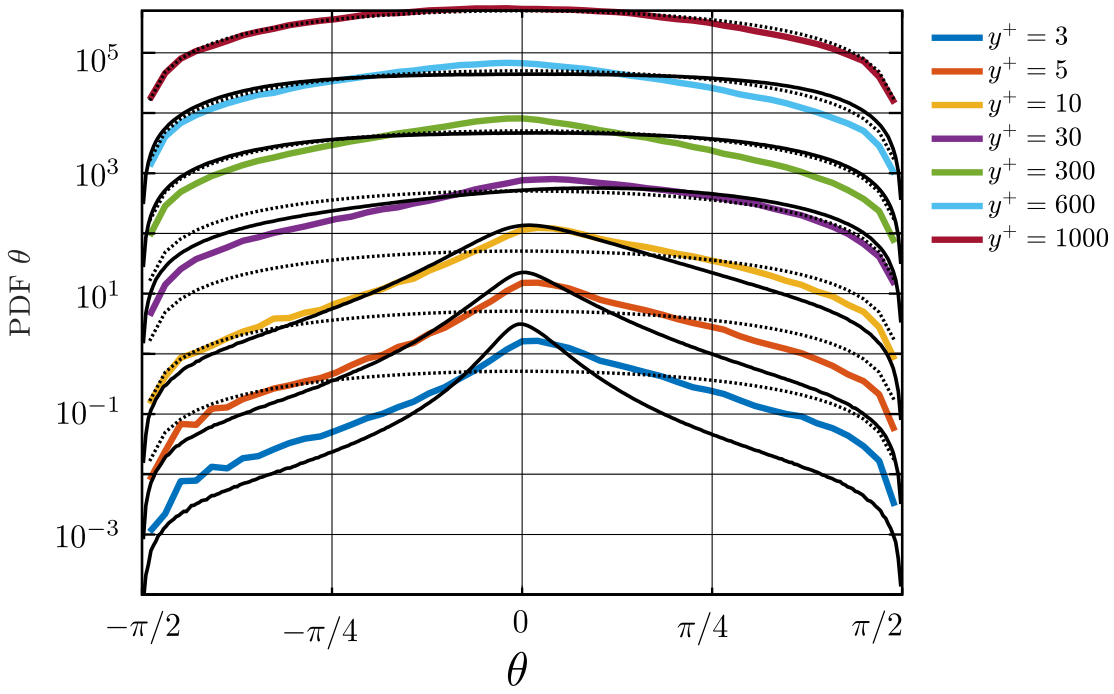

Figure 3.16: PDF of the wall-normal (θ) orientation of acceleration at various distances from the wall. Colored lines represent experimental data, solid black line the Re_τ = 1000 DNS results of Zamansky *et al*[3], and dotted lines represent the isotropic distribution. Curves are shifted up by one decade for clarity.

although the DNS data appears approximately isotropic at $y^+ = 300$. Near the wall the probability of a small wall-normal angle is significantly elevated relative to isotropy, i. e. near the wall the acceleration is more often parallel to the wall ($\theta \approx 0$) than perpendicular ($\theta \approx \pm\pi/2$). The peak values of the mean acceleration profiles (shown in figure 3.8) are of approximately equal magnitude, implying that the accelerations approximately parallel to the wall that are observed more frequently have lower magnitudes (on average) than the accelerations perpendicular to the wall.

The experimental data is also significantly more positively skewed than the DNS near the wall. Positive skewness in the PDF of wall-normal angle is interpreted as a higher probability of acceleration away from the wall, which is consistent with the idea that fast particles moving towards the wall are being oversampled, as discussed in the previous section in the context of a bimodal streamwise velocity histogram. These fast particles having a decreasing wall-normal velocity as they approach the wall, and therefore a a positive wall-normal component of acceleration.

The longitudinal angle ϕ measures the relative contributions of the streamwise and transverse components of the acceleration orientation, and is defined from $-\pi$ to π, where $\phi = 0 \Rightarrow e_x = 1$ (acceleration in the direction of the flow). The channel is homogeneous in the transverse (z) direction, so the statistics are expected to be symmetric about $\phi = 0$. The PDF of the longitudinal angle ϕ is plotted in figure 3.17 at various locations in the channel. The longitudinal angle is observed to be more isotropic than the wall-normal angle, with an approximate return to isotropy at $y^+ \approx 300$. There is good agreement between the DNS and experiments, although the return to isotropy appear to be slightly more pronounced in the experimental results than in the DNS (e. g. at $y^+ = 300, 600$), which is the inverse of what was found for the wall-normal angle θ.

These trends are further examined by plotting the second moments of these PDF's, which (again following Zamansky *et al*) are plotted in figure 3.18 as the variance of the sine

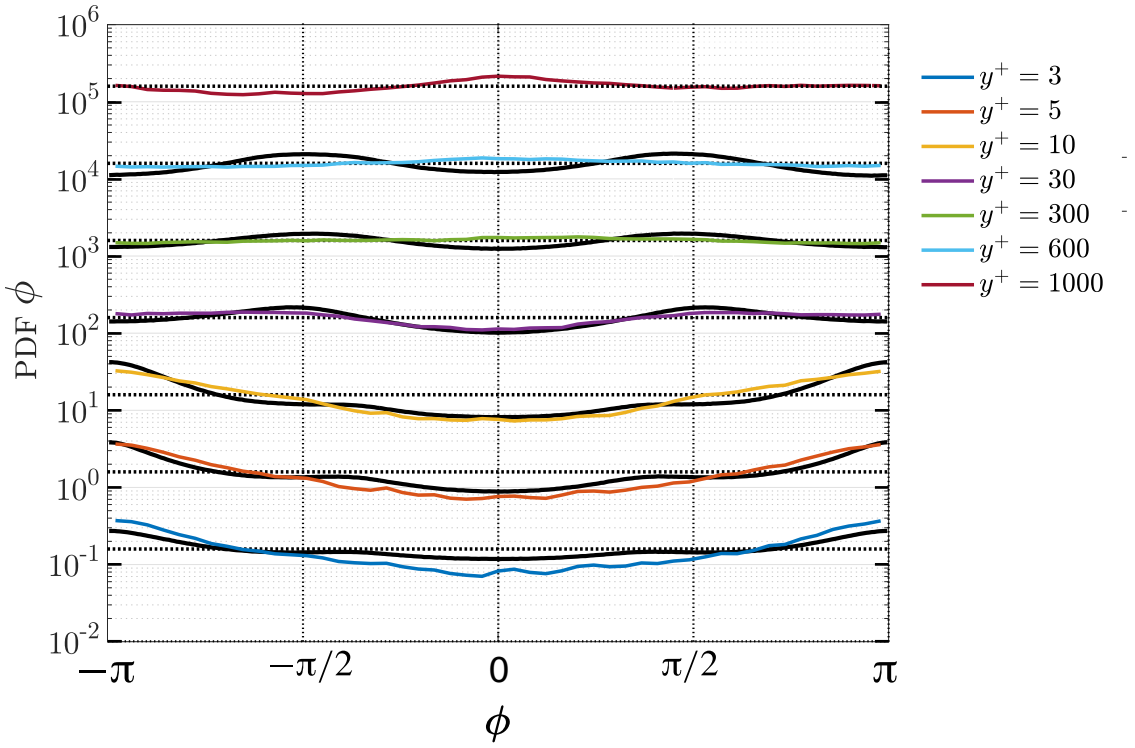

Figure 3.17: PDF of the longitudinal (ϕ) orientation of acceleration at various distances from the wall. Colored lines represent experimental data, solid black line the Re_τ = 1000 DNS results of Zamansky *et al*[3], and dotted lines represent the isotropic distribution. Curves are shifted up by one decade for clarity.

of the two angles θ and ϕ, normalized by the variance of the isotropic distribution. The results in figure 3.18 are somewhat puzzling, as a return to isotropy is expected, especially towards the center of the channel. Approximate isotropy is seen in the DNS results after $y^+ \approx 50$, but there is a general drift *away* from isotropy towards the center of the channel. Similarly, the experimental results for the longitudinal angle ϕ show approximate isotropy after $y^+ \approx 50$, but in the outer layer a slight drift away from anisotropy. The wall-normal angle θ remains anisotropic up to the channel center, although a plateau is observed at approximately the same location as the plateau in ϕ. This lack of isotropy may be due to a statistical bias related to binning the Lagrangian data , a bias to which the wall-normal angle is especially sensitive.

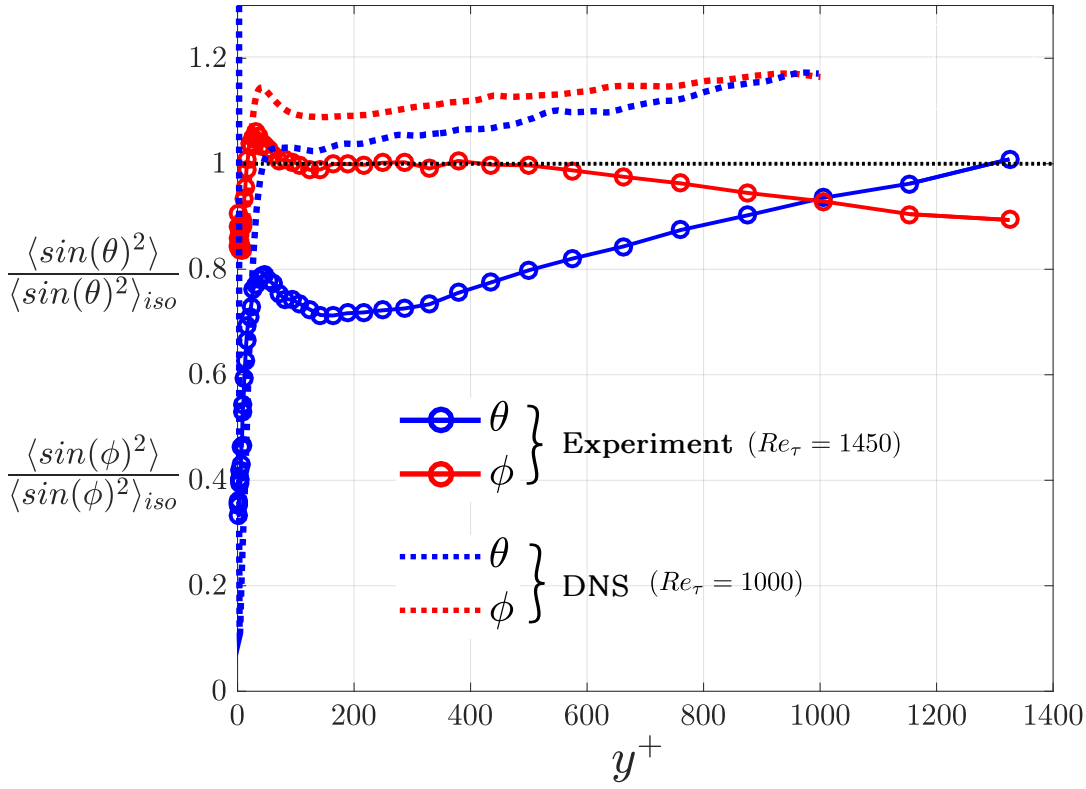

Figure 3.18: Variances of the sine of the longitudinal (ϕ) and wall-normal (θ) angles, normalized by the variance in the isotropic case. DNS at $Re_\tau = 1000$ taken from Zamansky *et al*[3].

3.4 Mixed acceleration-velocity statistics

The time-resolved 3-D measurements of tracer particle trajectories give simultaneous velocity and acceleration measurements; the mixed statistics in acceleration and velocity are briefly presented in this section.

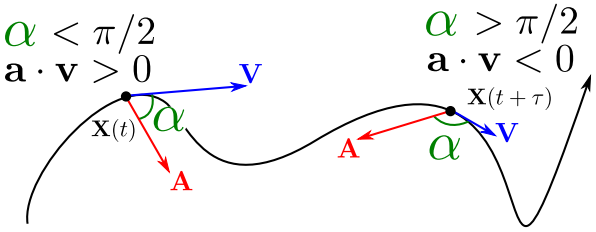

The inner product of the acceleration and velocity $\mathbf{A} \cdot \mathbf{V}$ is intuitively understood as the work done on a fluid particle by the system: a positive value ($\mathbf{A} \cdot \mathbf{V} > 0$) means the turbulent system adds kinetic energy to the fluid particle, and a negative value ($\mathbf{A} \cdot \mathbf{V} < 0$) means that the fluid particle loses kinetic energy to the system, either by increasing the kinetic energy of other fluid particles or transforming the kinetic energy into heat. The quantity $\mathbf{A} \cdot \mathbf{V}$ is an intrinsically Lagrangian quantity, and care must be taken in the extraction of Eulerian statistics and, perhaps especially, their interpretation.

The directly measured mean power $\langle A \cdot V \rangle$ across the channel is plotted in figure 3.19. The total power (black points) is shown to be local equilibrium at $y^+ \gtrapprox 50$. This location is consistent with the results of Kim *et al*[94] that showed the ratio of production to dissipation is greater than unity near the wall, and achieves equilibrium at $y^+ \gtrapprox 50$. The positive and negative contributions to this mean are also plotted individually on figure 3.19, and show a peak of the mean positive power at this location, unlike the mean negative power which is shown to approximately constant in the near wall region.

These single-particle statistics are not enough to fully elucidate the connection between this Lagrangian power and inherently Eulerian quantities based on spatial velocity

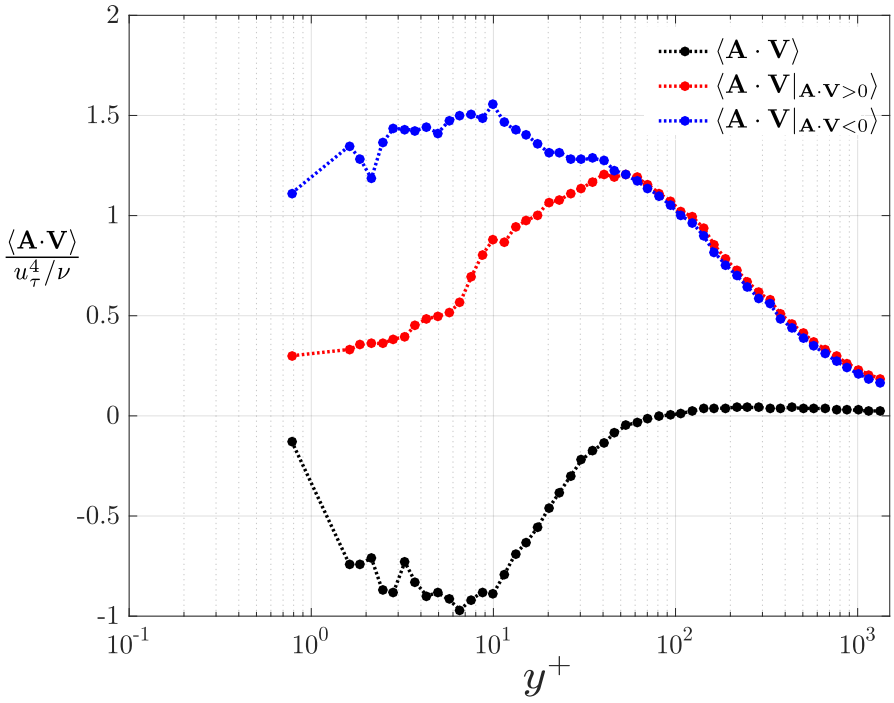

Figure 3.19: The mean of $\mathbf{A}\cdot\mathbf{V}$ across the channel. Also plotted are the mean of the positive values of $\mathbf{A}\cdot\mathbf{V}$ and the mean of the negative values of $\mathbf{A}\cdot\mathbf{V}$.

gradients, such as dissipation. Nevertheless, some insight into the connection between the measurable single point velocity statistics and the Lagrangian power may be had by considering the kinematic relation[10]:

$$\mathbf{A}(\mathbf{x}_0,t|t_0)\cdot\mathbf{V}(\mathbf{x}_0,t|t_0) = \left[\left(\frac{\partial\mathbf{U}(\mathbf{x},t)}{\partial\mathbf{x}}\frac{\partial\mathbf{X}(\mathbf{x}_0,t|t_0)}{\partial t}+\frac{\partial\mathbf{U}(\mathbf{x},t)}{\partial t}\right)\cdot\mathbf{U}(\mathbf{x},t)\right]_{\mathbf{x}=\mathbf{X}(\mathbf{x}_0,t|t_0)} \tag{3.18}$$

$$= \left[\left(\frac{\partial\mathbf{U}(\mathbf{x},t)}{\partial\mathbf{x}}\mathbf{U}(\mathbf{x},t)\right)\cdot\mathbf{U}(\mathbf{x},t)+\left(\frac{1}{2}\frac{\partial\mathrm{U}^2(\mathbf{x},t)}{\partial t}\right)\right]_{\mathbf{x}=\mathbf{X}(\mathbf{x}_0,t|t_0)} \tag{3.19}$$

$$= \left[\underbrace{[(\mathbf{U}(\mathbf{x},t)\cdot\nabla)\,\mathbf{U}(\mathbf{x},t)]\cdot\mathbf{U}(\mathbf{x},t)}_{\text{Convective term}}+\underbrace{\left(\frac{1}{2}\frac{\partial\mathrm{U}^2(\mathbf{x},t)}{\partial t}\right)}_{\text{Local term}}\right]_{\mathbf{x}=\mathbf{X}(\mathbf{x}_0,t|t_0)} \tag{3.20}$$

Taking the local term first, using the Reynolds decomposition

$$\frac{1}{2}\frac{\partial\mathrm{U}^2(\mathbf{x},t)}{\partial t} = \frac{1}{2}\frac{\partial}{\partial t}\left(\langle\mathrm{U}\rangle+u\right)^2(\mathbf{x},t) \tag{3.21}$$

$$= \frac{1}{2}\frac{\partial}{\partial t}\left(\langle\mathrm{U}\rangle+u\right)^2(\mathbf{x},t) \tag{3.22}$$

$$= \frac{\partial}{\partial t}\langle\mathrm{U}(\mathbf{x})\rangle u(\mathbf{x},t)+\frac{1}{2}\frac{\partial u^2(\mathbf{x},t)}{\partial t} \tag{3.23}$$

In the Eulerian frame, i. e. at a fixed point $\mathbf{x}$ this local term averages to zero in stationary turbulence. It is important to note that in the Lagrangian frame this local term does not necessarily average to zero if $t\neq t_0$. The convective term is similarly developed with the

[10] Following the development shown in equation 1.9

Reynolds decomposition, shown more clearly using index notation

$$\mathrm{U}_i(\mathbf{x},t)\mathrm{U}_j(\mathbf{x},t)\frac{\partial \mathrm{U}_i(\mathbf{x},t)}{\partial x_j} = (\langle \mathrm{U}_i\rangle + u_i)(\mathbf{x},t)(\langle \mathrm{U}_j\rangle + u_j)(\mathbf{x},t)\frac{\partial(\langle \mathrm{U}_i\rangle + u_i)(\mathbf{x},t)}{\partial x_j} \tag{3.24}$$

Expanding the r.h.s of equation 3.24 yields eight terms. After the mean is taken some terms vanish, and the mean of equation 3.24 is expanded to

$$\left\langle \mathrm{U}_i(\mathbf{x},t)\mathrm{U}_j(\mathbf{x},t)\frac{\partial \mathrm{U}_i(\mathbf{x},t)}{\partial x_j}\right\rangle = \left\langle \frac{\partial\langle \mathrm{U}_i\rangle}{\partial x_j}\left(\langle \mathrm{U}_i\rangle\langle \mathrm{U}_j\rangle + u_i u_j\right)\right\rangle + \left\langle \frac{\partial u_i}{\partial x_j}\left(\langle \mathrm{U}_i\rangle u_j + u_i\langle \mathrm{U}_j\rangle + u_i u_j\right)\right\rangle \tag{3.25}$$

Using the symmetries of the channel this general equation is further simplified to

$$\left\langle \mathrm{U}_i(\mathbf{x},t)\mathrm{U}_j(\mathbf{x},t)\frac{\partial \mathrm{U}_i(\mathbf{x},t)}{\partial x_j}\right\rangle = \left\langle \frac{\partial\langle \mathrm{U}_x\rangle}{\partial y}\left(\langle \mathrm{U}_x\rangle\langle \mathrm{U}_x\rangle + u_x u_y\right)\right\rangle + \left\langle \langle \mathrm{U}_x\rangle\frac{\partial u_x}{\partial x_j}u_j + \langle \mathrm{U}_x\rangle\frac{\partial u_i}{\partial x}u_i + u_i u_j\frac{\partial u_i}{\partial x_j}\right\rangle \tag{3.26}$$

The foregoing development leads to an expression for the mean Lagrangian quantity $\mathbf{A}\cdot\mathbf{V}$ at $\mathbf{x}=\mathbf{x_0}$, $t=t_0$ in terms of Eulerian quantities as

$$\langle \mathbf{A}(\mathbf{x}_0,t_0)\cdot\mathbf{V}(\mathbf{x}_0,t_0)\rangle = \overbrace{\langle \mathrm{U}_x\rangle^2\left\langle\frac{\partial\langle \mathrm{U}_x\rangle}{\partial y}\right\rangle}^{\text{Mean component}} + \overbrace{\langle u_x u_y\rangle\left\langle\frac{\partial\langle \mathrm{U}_x\rangle}{\partial y}\right\rangle}^{\text{Production}} + \underbrace{\left\langle \langle \mathrm{U}_x\rangle\frac{\partial u_x}{\partial x_j}u_j + \langle \mathrm{U}_x\rangle\frac{\partial u_i}{\partial x}u_i + u_i u_j\frac{\partial u_i}{\partial x_j}\right\rangle}_{\text{Turbulent shear component}} \tag{3.27}$$

Three of the six terms in equation 3.27 are measurable in the present study: the direct measure of $\langle\mathbf{A}\cdot\mathbf{V}\rangle$ and the mean shear component terms. The measurement of the turbulent shear component terms, specifically the instantaneous spatial gradients, require different measurement techniques. However, the turbulent shear component as a whole may be inferred from equation 3.27 and knowledge of the other components. The contribution of the mean and turbulent components as defined in equation 3.27 are plotted in figure 3.20, which shows very large, opposite signed contributions of the mean component and the (inferred) turbulent shear component. Comparatively, the production term is very close to zero. The relative importance of the mean component and production term is unsurprising, given the profiles of Reynolds stress (figure 3.4) and mean velocity (figure3.20) seen in section 3.2. F

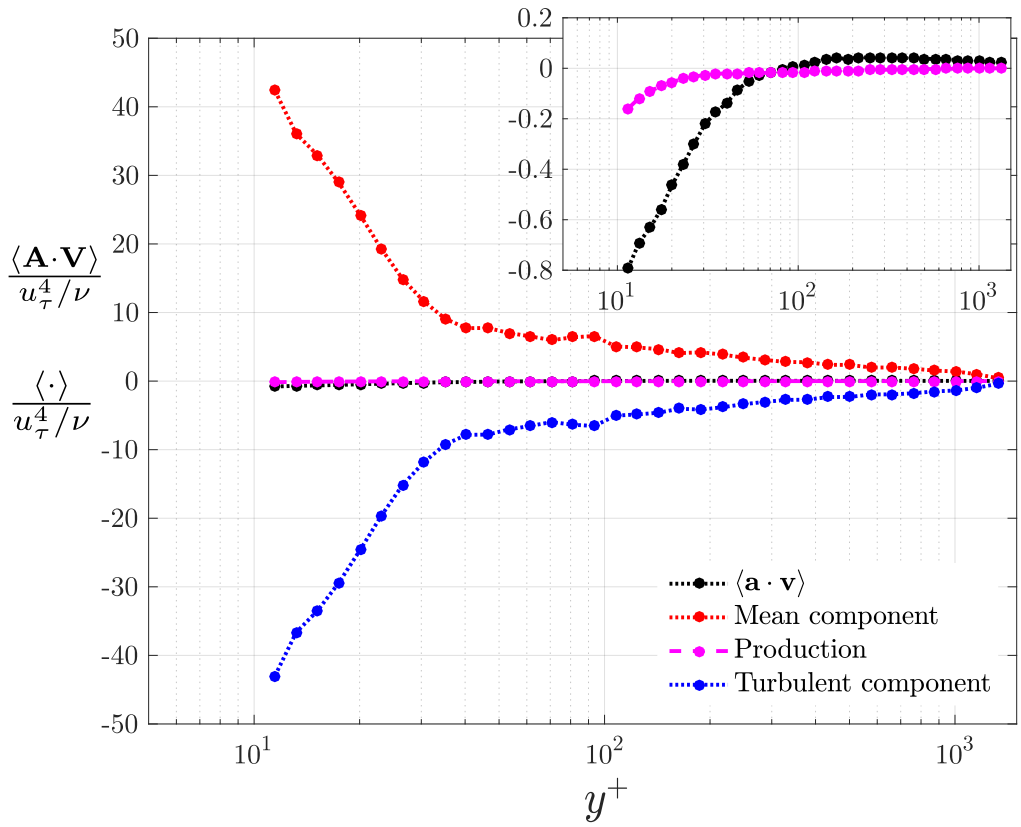

Figure 3.20: Mean Lagrangian power across the channel, and the individual components of equation 3.27. **Inset:** Zoomed in view of same.

3.5 Conclusion

This chapter provides a statistical description of the turbulent channel in a Eulerian framework. Eulerian statistics in velocity, acceleration, and combined velocity-acceleration were extracted from the database of particle trajectories, and their evolution across the channel width examined.

A discrepancy between the the mean streamwise velocity profile measured in this study and other groups was discussed, and considered to be a statistical bias similar to those seen in LDV measurements. A correction based on the magnitude of the velocity was applied that provided agreement between the corrected mean velocity profile and previous measurements. A systematic study to characterize the statistical bias of the binning procedure should be done, which would allow more precise calculation of error as well as explicitly justify correction schemes. Apart from this anomaly in the near wall region, velocity statistics are in agreement with previous work. Of particular interest is the significant correlation (~ 0.35) between the streamwise and wall-normal components of velocity over most of the channel width, and the non-Gaussianity of the higher order velocity statistics over most of the channel width. Velocity statistics in the turbulent channel are quite dissimilar from those of HIT, even far from the wall.

Acceleration statistics across the channel are described, both in the typical Cartesian coordinates and the components parallel and perpendicular to the local instantaneous velocity. Profiles of the first through fourth moments of acceleration across the channel show significant anisotropy near the wall. The first and third moments for example, differ significantly from zero (as expected in HIT) near wall, and even far from the wall continue to be non-zero. The streamwise and wall-normal components of acceleration are found

to be non-negligibly correlated across most of the channel (e. g. ~ 0.1 in the outer layer). This correlation was also observed in the joint PDFs of these two acceleration components. A return to isotropy from the near wall region towards the channel center was found for the Cartesian components of acceleration and the perpendicular/parallel components of acceleration. The contribution to the acceleration magnitude of each component was considered in figure 3.13, and was found to be isotropic much closer to the wall ($y^+ \approx 30$) for the perpendicular/parallel components than the Cartesian components. The angles formed by the acceleration vector, were found to be in fairly close agreement with the results of Zamansky *et al*[3].

Finally, the inner product of acceleration and velocity, or the Lagrangian power is briefly considered. This power was shown to be non-zero (i. e. out of local equilibrium) close to the wall ($y^+ < 50$); closer to the wall the average positive contributions to the power decrease, while the negative contributions stay relatively constant. Further analysis of this quantity is left to future work. Of particular interest to the author is the Lagrangian power conditioned on velocity as suggested by Pumir *et al*[127], who found that fast particles are accelerated preferentially. How this redistribution of energy between fluid particles occurs in the near wall region is an interesting unanswered question. The connection between the third moment of the Lagrangian power and time-irreversibility was suggested by Mordant and Xu *et al*[128]. The degree to which the "more organized" turbulence in the near wall region has more or less of this measure of time-irreversibility is also an intriguing question.

Chapter 4

Lagrangian statistics in the turbulent channel

I counted till they danced so
Their slippers leaped the town –
And then I took a pencil
To note the rebels down –
And then they grew so jolly
I did resign the prig –
And ten of my once stately toes
Are marshalled for a jig!

Snowflakes, *Emily Dickinson*

Contents

4.1 Introduction

Lagrangian statistics of fluid particles in inhomogeneous turbulence are important to many research areas, from the modeling dispersion from point sources to a fundamental understanding of the turbulent boundary layers. This chapter presents the one and two-time Lagrangian statistics of tracer particles measured in the turbulent channel. The conditioning of Lagrangian statistics on initial position in inhomogeneous turbulence produces unintuitive results, for example there is a mean tendency for fluid particle to drift towards the center of the channel, which at first glance seems to violate mass conservation. Details regarding how these Lagrangian statistics are calculated is given in section 4.2. Lagrangian mean positions and velocities are discussed in section 4.3, along with some predictions from kinematic arguments and Eulerian statistics. Single particle dispersion in the framework of Taylor, and the limits of these predictions from HIT, is presented in section 4.4. Finally, the Lagrangian acceleration statistics and Lagrangian timescales were the subject of an article previously published in *Physical Review Fluids*, which is reproduced in section 4.6.

4.2 Conditioning and convergence of Lagrangian statistics

The Lagrangian framework in turbulence contains subtleties that are easily hidden when discussing stationary homogeneous isotropic turbulence. It is therefore important to develop explicitly the definitions, assumptions, and methods used in the extraction of Lagrangian statistics from the measurements of inhomogeneous turbulence. Following the notation of Monin and Yaglom[12] with slight modifications, the fluid particle trajectory is given by

$$\mathbf{X}(\mathbf{x}_0, t|t_0) \tag{4.1}$$

where $\mathbf{x}_0$ is in principle an arbitrary label, but is most usefully taken to be the position of the fluid particle at a given time t_0. The expression 4.1 is the position of the fluid particle at time t that was located at $\mathbf{x}_0$ at t_0. This may be thought of as condition: $\mathbf{X}(\mathbf{x}_0, t|t_0)$ is the position of the particle at t *conditioned by* the initial position $\mathbf{x}_0$ at time t_0. The Lagrangian velocity is defined simply the time derivative of this position

$$\mathbf{V}(\mathbf{x}_0, t|t_0) \equiv \frac{\partial \mathbf{X}(\mathbf{x}_0, t|t_0)}{\partial t} \tag{4.2}$$

which is equivalent to the Eulerian velocity *at the same position and time*, i. e.

$$\frac{\partial \mathbf{X}(\mathbf{x}_0, t|t_0)}{\partial t} = \mathbf{U}\left(\mathbf{X}(\mathbf{x}_0, t|t_0), t\right) \quad \text{where } \mathbf{U} \text{ is the Eulerian velocity} \tag{4.3}$$

Statistical homogeneity in the context of turbulence may be defined as the independence of the expected value of a variable on position, which is quite simple in the Eulerian framework, e.g.

$$\frac{\partial \langle \mathbf{U}(\mathbf{x}, t) \rangle}{\partial \mathbf{x}} = 0 \tag{4.4}$$

and similarly for stationarity

$$\frac{\partial \langle \mathbf{U}(\mathbf{x}, t) \rangle}{\partial t} = 0 \tag{4.5}$$

Eulerian and Lagrangian quantities coincide at $t = t_0$, so Eulerian stationarity implies that explicit dependence on t_0 may be dropped, and the time in Lagrangian statistics may be represented simply as the time lag $\tau = t - t_0$.

These properties of homogeneity and stationarity may be translated directly to the Lagrangian velocity using the relationship between the Lagrangian velocity and Eulerian velocity shown in equation 4.3:

$$\frac{\partial \langle \mathbf{U}(\mathbf{x}, t) \rangle}{\partial \mathbf{x}} = \partial \left\langle \frac{\partial \mathbf{X}(\mathbf{x}_0, t | t_0}{\partial t} \right\rangle / \partial \mathbf{x} = 0 \tag{4.6}$$

$$\frac{\partial \langle \mathbf{U}(\mathbf{x}, t) \rangle}{\partial t} = \partial \left\langle \frac{\partial \mathbf{X}(\mathbf{x}_0, t | t_0)}{\partial t} \right\rangle / \partial t = 0 \tag{4.7}$$

i. e. in Lagrangian statistics in stationary homogeneous turbulence are independent of initial position and initial time. This explanation glosses over the finer points of this proof, which was carefully worked out by Lumley[129]. One of the practical consequences of equations 4.6-4.7 is that if a turbulent flow is stationary and homogeneous in the Eulerian sense, then all Lagrangian measurements may be used in the calculations of Lagrangian statistics without reference to their initial position or their starting time.

In the context of idealized channel flow (which is achieved experimentally to good approximation, as discussed in section 2.1.3) there is stationarity and a single dimension of statistical inhomogeneity:

$$\frac{\partial \langle \mathbf{U}(\mathbf{x}, t) \rangle}{\partial t} = \frac{\partial \langle \mathbf{U}(\mathbf{x}, t) \rangle}{\partial x} = \frac{\partial \langle \mathbf{U}(\mathbf{x}, t) \rangle}{\partial z} = 0, \quad \frac{\partial \langle \mathbf{U}(\mathbf{x}, t) \rangle}{\partial y} \neq 0 \tag{4.8}$$

Equation 4.8 has two relevant consequences: 1) Lagrangian statistics must be conditioned by y, the distance to the wall, and 2) Lagrangian statistics are not stationary, despite the stationarity of the flow in the Eulerian sense. These two consequences are discussed below in detail.

Spatial dependence of Lagrangian statistics

The symmetries of channel flow allow the reduction of the conditioning by initial position, e. g.,

$$\langle \mathbf{V}(\mathbf{x}_0, \tau) \rangle \rightarrow \langle \mathbf{V}(y_0, \tau) \rangle \tag{4.9}$$

In practice this condition must be approximate, i. e., trajectories may be included in the calculation of a given statistic if their initial wall-normal positions are approximately equal:

$$\langle \mathbf{V}(y_0, \tau) \rangle \rightarrow \langle \mathbf{V}(y_0 \pm \Delta \mathrm{Y}/2, \tau) \rangle \tag{4.10}$$

The above results in a binning of trajectories based on their distance from the wall at an arbitrary time t_0, which is illustrated in figure 4.1. These wall-distance bins impose spatial averaging over spatially inhomogeneous results, and only justified in the limit of small spatial inhomogeneities on the scale of the ΔY. The width and distribution of these wall-distance bins is a choice: large wall-distance bins include more trajectories and are thus more statistically converged, but at the expense of increasingly unjustified spatial "smoothing". For the results presented in this thesis the wall-distance bins were typically taken to be $\Delta \mathrm{Y} = 25$ wall-units near the wall (the area in which spatial gradient are high) and $\Delta \mathrm{Y} = 75$ wall-units in the bulk flow. Some results, such as the PDFs of acceleration shown in figure which changes significantly between $0-25$ wall-units, were obtained using thinner wall-distance bins—trading statistical convergence for spatial resolution.

Another practical consideration is the manner in which the trajectories are binned. There are several possible strategies, all of which attempt to find a balance between statistical convergence and statistical bias. In one of the few experimental Lagrangian studies of

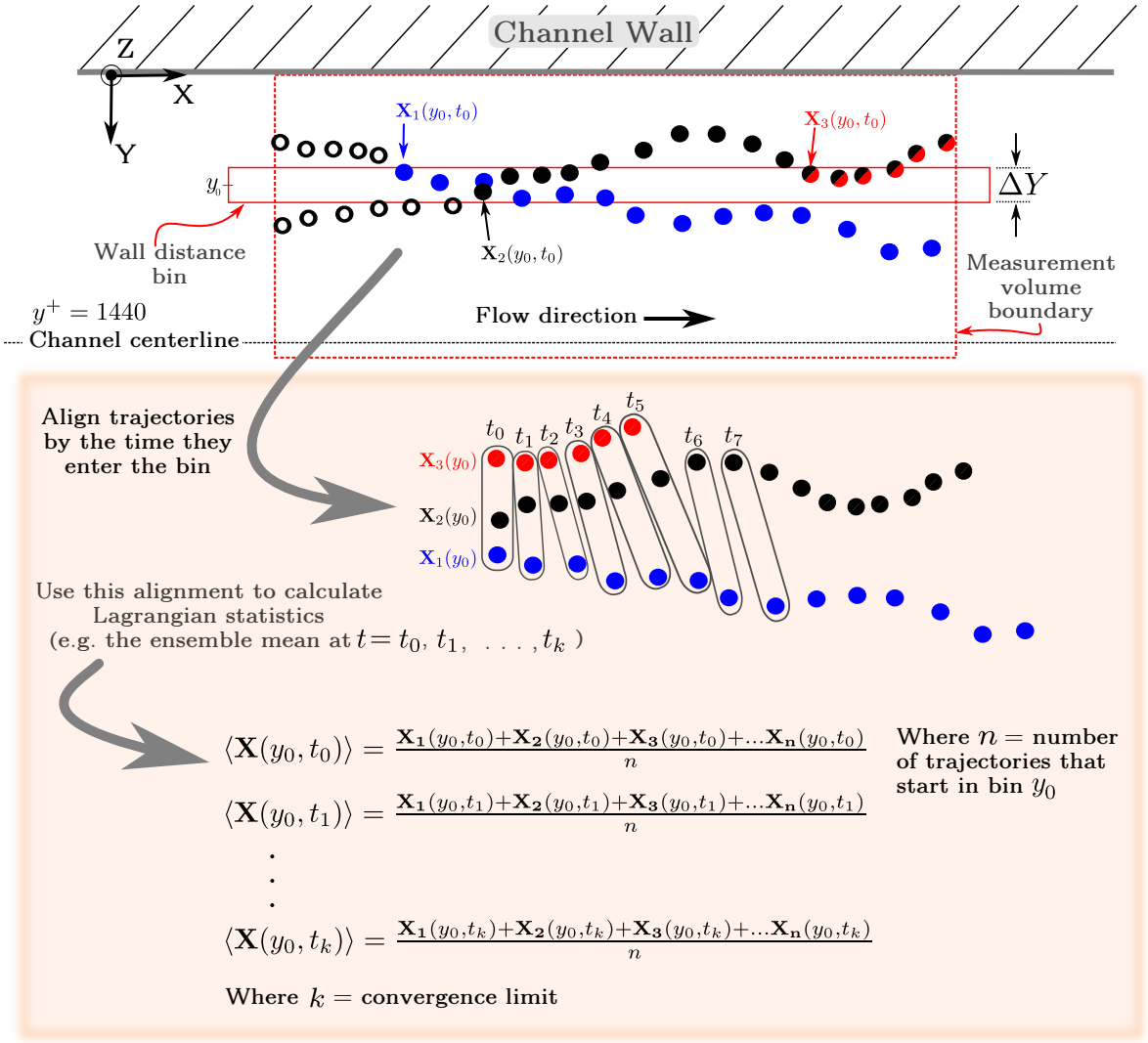

Figure 4.1: Illustration of trajectory binning procedure and the calculation of Lagrangian statistics

inhomogeneous turbulence[79] Walpot and coworkers use a binning strategy similar to that illustrated in figure 4.1, which is to start considering a trajectory to be in a given bin at the first position within the bin, and allow counting of the trajectory more than once if the trajectory leaves and then re-enters the bin. This method as described favors the calculation of Lagrangian statistics in positive time ($t = t_0 + \tau$) , but may be easily reversed in time to calculate Lagrangian statistics at negative times ($t = t_0 - \tau$). This method was found to produce a bias in Lagrangian statistics at short times, especially in the bins near the wall. This bias is illustrated in figure 4.2; briefly, a bias occurs because if we consider t_0 to be the first point in which a particle trajectory enters a bin, and particles *entering the bin are statistically different* from those that have been in the bin for a longer time, then the statistics will be biased by the history of the trajectory before t_0. For example, in the bin closest to the wall particles arrive in the bin with a negative wall-normal velocity. We set t_0 at the time the particles cross the edge of the bin, these particles then continue to move toward the wall. This is strategy is illustrated by the blue line in figure 4.2, and the resulting negative dip at short positive times is an artifact of the binning strategy.

A more conservative approach from the perspective of minimizing bias is to bin the trajectory based on a central position, use the same t_0 for positive and negative time calculation. This strategy is illustrated in figure 4.2 by the green line (positive time-lag)

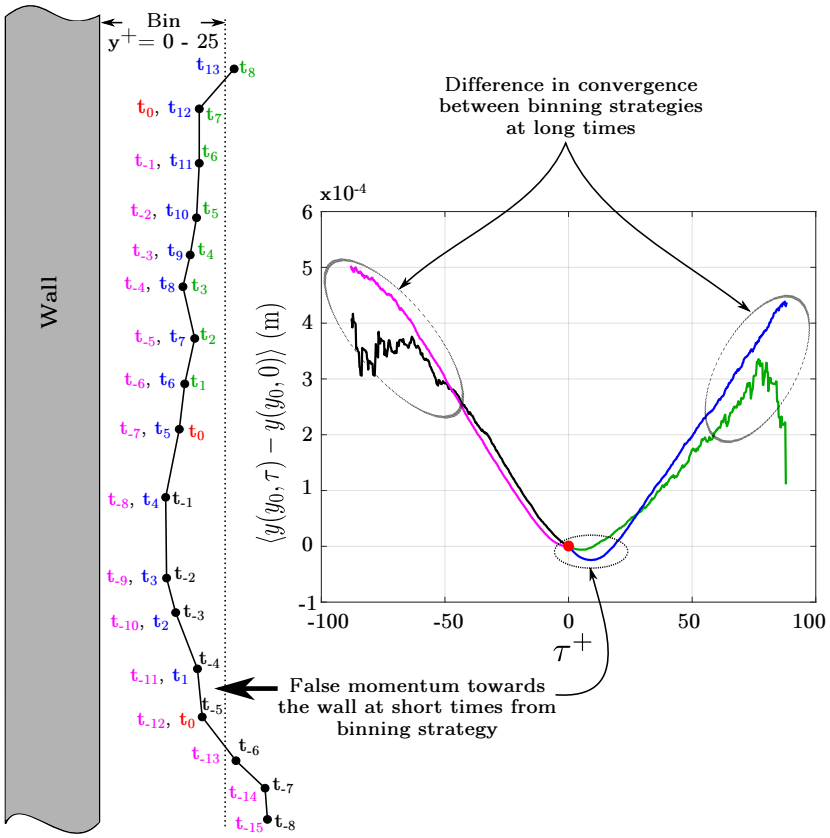

Figure 4.2: Lagrangian mean wall-normal position for two different binning strategies. Lines on the plot at right are color-coded with the corresponding binning strategy illustrated to the left.

and the black line (negative time-lag). The bias at small positive times is not seen with this strategy. There is little difference between the two strategies for negative times, reinforcing the idea that the bias comes from high momentum particles coming into the measurement volume.

While the more conservative approach minimizes bias, it also effectively cuts in half the effective trajectory. Lagrangian statistics in the channel flow are already quite limited in terms of maximum time-lag due to the limited residence time of the particle. The number of trajectories up to a given time-lag τ for the two strategies, using a typical distribution of wall bins, is shown in figure 4.3. The steep roll-off of the number of trajectories at a given time-leg is an effect of the limited residence time, which is shorter in the areas of the channel with high mean flow ($y^+ > 100$). The optimal binning strategy depends on the statistics being considered and the size and distribution of the bins (for example large bins makes the crossing of a bin boundary less probable). Binning strategies will be discussed further in the context of specific results.

Non-stationarity of Lagrangian statistics

Non-stationarity is concisely stated for an arbitrary Lagrangian statistic χ as

$$\chi(y_0, \tau_1) \neq \chi(y_0, \tau_2) \quad \text{unless } \tau_1 = \tau_2 \tag{4.11}$$

Lagrangian correlations in HIT are typically normalized by the variance, e. g. the autocorrelation of acceleration is given as

$$\frac{\langle a(0)a(\tau)\rangle}{\langle a^2\rangle} \quad \text{where } a \text{ is a component of the acceleration vector } \mathbf{a} \tag{4.12}$$

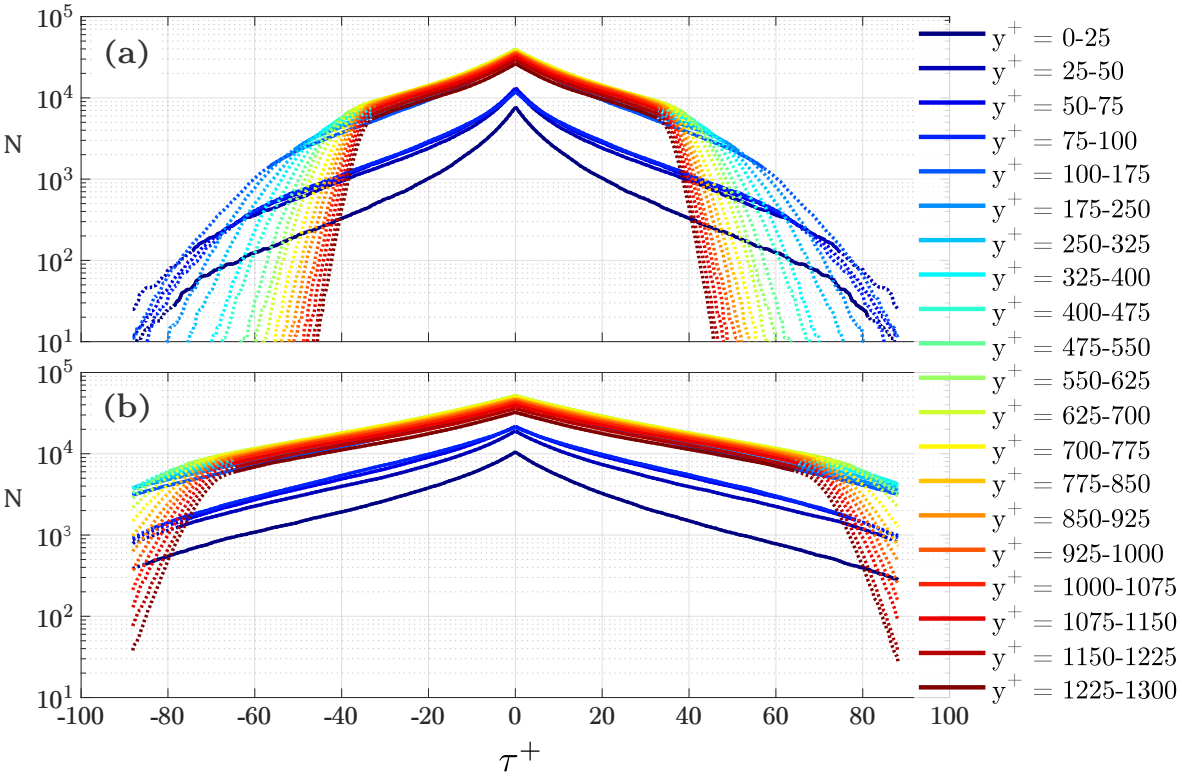

Figure 4.3: Number of tracer particle trajectories of length τ^+. **Subfigure (a):** Number of trajectories using conservative binning strategy (t_0 in the middle of the trajectory) . **Subplot (b):** Number of trajectories using the less conservative strategy (t_0 is the first position in the bin).

which implicitly assumes that that the acceleration variance does not change between $t = 0$ and $t = \tau$. If there is a mean displacement in the wall-normal direction, then this is no longer a valid assumption: in general the mean particle position $\langle y(0)\rangle \neq \langle y(\tau)\rangle$, so the particle samples a different region of the flow where $\langle a(0)\rangle \neq \langle a(\tau)\rangle$. Equation 4.12 is properly adapted for the turbulent channel is

$$\frac{\langle a(y_0,0)a(y_0,\tau)\rangle}{\sqrt{\langle a(y_0,0)^2\rangle}\sqrt{\langle a(y_0,\tau)^2\rangle}} \tag{4.13}$$

A broader consequence is that Lagrangian single-time statistics do not equal Eulerian statistics, for example in the channel

$$\langle U_y(y_0,t)\rangle = 0 \quad \text{but in general} \quad \langle V(y_0,\tau)\rangle \neq 0 \quad \text{except in the case where } \tau = 0 \tag{4.14}$$

These single-time Lagrangian statistics are discussed in depth in the following section.

4.3 Short-time models of Lagrangian statistics from Eulerian statistics

What is the consequence of Eulerian statistical inhomogeneity on the Lagrangian statistics? As discussed by Tennekes[14], even in stationary turbulence the Lagrangian statistics of a fluid particle wandering in inhomogeneous turbulence are not stationary. An intuitive example of this phenomenon can be had by making the following thought experiment: In a turbulent channel flow dye is injected very close to the wall. This dye plume grows

as it is being swept down the channel, eventually filling the entire channel width. If the dye is considered to approximately follow fluid particles[1], the plume can be considered to be an ensemble of fluid particle trajectories acted on by turbulent diffusion. If the mean trajectory is calculated (e. g., by methods like that illustrated in figure 4.1) the result is a mean path from the wall toward the channel center, implying a non-zero mean wall-normal Lagrangian velocity and non-stationarity of Lagrangian statistics.

This intuitive result can expressed mathematically using the labeling theorem, which gives

$$\mathrm{V}_i(\mathbf{x},t) - \mathrm{U}_i(\mathbf{x},t) = \int_{t_0}^{t} \mathrm{U}_i(\mathbf{x},t') \frac{\partial}{\partial a_i} \mathrm{V}_i(\mathbf{x},t')\, dt' \tag{4.15}$$

where $\mathbf{x}$ is the particle position at time t_0 and $\partial/\partial a_i$ is a spatial derivative of the starting point $\mathbf{x}$ at t_0. The derivation of equation 4.15 is presented by Bennett[130] and is not reproduced here. Equation 4.15 is true for individual trajectories and instantaneous Eulerian velocities, and if the ensemble average is taken the r.h.s does not generally equal zero in inhomogeneous turbulence.

For incompressible flow ($\partial u_k/\partial x_k = 0$) , equation 4.15 may be written as

$$\mathrm{V}_i(\mathbf{x},t) - \mathrm{U}_i(\mathbf{x},t) = \frac{\partial}{\partial a_k} \mathrm{K}_{ik}(\mathbf{x},t) \tag{4.16}$$

$$\mathrm{K}_{ik}(\mathbf{x},t) = \int_{t_0}^{t} \mathrm{U}_k(\mathbf{x},t') \mathrm{V}_i(\mathbf{x},t')\, dt' \tag{4.17}$$

Using equation 4.3 K_{ik} may be written in terms of the Eulerian velocity along the particle path

$$\mathrm{K}_{ik}(\mathbf{x},t) = \int_{t_0}^{t} \mathrm{U}_k(\mathbf{x},t') \mathrm{U}_i[\mathbf{X}(\mathbf{x},t'),t']\, dt' \tag{4.18}$$

Looking at the component $i = y$ and using the Reynolds decomposition, recalling that $\overline{\mathrm{U}}_y = \overline{\mathrm{U}}_z = 0$ over the whole channel:

$$\begin{aligned}\langle \mathrm{V}_y(\mathbf{x},t)\rangle = \overline{\mathrm{U}}_x(\mathbf{x},t) &\left\langle \frac{\partial}{\partial a_x} \int_{t_0}^{t} u_y[\mathbf{X}(\mathbf{x},t'),t']\, dt' \right\rangle + \left\langle \frac{\partial}{\partial a_x} \int_{t_0}^{t} u_x(\mathbf{x},t)\, u_y[\mathbf{X}(\mathbf{x},t'),t']\, dt' \right\rangle \\ &+ \left\langle \frac{\partial}{\partial a_y} \int_{t_0}^{t} u_y(\mathbf{x},t')\, u_y[\mathbf{X}(\mathbf{x},t'),t']\, dt' \right\rangle \\ &+ \left\langle \frac{\partial}{\partial a_z} \int_{t_0}^{t} u_z(\mathbf{x},t')\, u_y[\mathbf{X}(\mathbf{x},t'),t']\, dt' \right\rangle \end{aligned} \tag{4.19}$$

The spatial gradients in the starting point must be zero on average in the streamwise and spanwise directions (see discussion above), so equation 4.19 is simplified to

$$\langle \mathrm{V}_y(\mathbf{x},t)\rangle = \left\langle \frac{d}{d a_y} \int_{t_0}^{t} u_y(\mathbf{x},t')\, u_y[\mathbf{X}(\mathbf{x},t'),t']\, dt' \right\rangle \tag{4.20}$$

Equation 4.20 is difficult to interpret, but we can observe that the integrand resembles an Eulerian velocity correlation at a distance $\mathbf{r}(t) = \mathbf{X}(\mathbf{x},t) - \mathbf{x}$. Inhomogeneous turbulence implies inhomogeneous Eulerian velocity correlations, for example let $\mathbf{r} = y_0$ where y_0 is some arbitrary distance in the inertial range $\eta < y_0 < l$ in the wall-normal direction, then in general

$$\langle u_y(y)\, u_y(y+y_0)\rangle \neq \langle u_y(y)\, u_y(y-y_0)\rangle \tag{4.21}$$

[1] In high Reynolds number flow where the where the fluid viscosity is large compared to the diffusivity of the dye ($Sc \gg 1$) molecular transport is small compared to turbulent transport.

Taking an approximation of equation 4.20 at some short time $\Delta t = t - t_0$

$$\langle V_y(\mathbf{x}, t)\rangle = \left\langle \frac{d}{da_y}[u_y(\mathbf{x}, t_0+\Delta t)\, u_y(\mathbf{x}+\Delta\mathbf{x}, t_0+\Delta t)]\Delta t \right\rangle \quad \text{where } \Delta\mathbf{x} = \mathbf{X}(\mathbf{x}, t+\Delta t) - \mathbf{x} \tag{4.22}$$

In the limit of $\Delta t = 0$ the mean Lagrangian velocity also goes to zero (as expected), but at short times such that the Eulerian velocities at the two positions $\mathbf{x}$ and $\mathbf{x}+\Delta\mathbf{x}$ remain highly correlated one can approximate the Lagrangian velocity as the mean Eulerian gradient[2] of the variance of the wall-normal component of the Eulerian velocity

$$\langle V_y(\mathbf{x}, t)\rangle \approx \frac{d}{dy}\langle u_y^2(\mathbf{x})\rangle \Delta t \quad \text{for} \quad 0 < \Delta t < t_{lim} \tag{4.23}$$

where t_{lim} is a short time with respect to the correlation of $u_y(\mathbf{x}, t_0+\Delta t)$ and $u_y[\mathbf{X}(\mathbf{x}, t_0+\Delta t), t_0+\Delta t]$.

Figure 4.4 applies the approximation shown in equation 4.23 for the Lagrangian mean wall-normal velocity $\langle V_y(\tau)\rangle$ to experimental results. Also shown is the Eulerian profile of the variance of the wall-normal component of velocity that used to make the approximation. The short-time kinematic approximation works well for short negative times, slightly less well for positive times, and diverges significantly at longer times, especially for those mean velocities with initial positions close to the wall.

The same logic used in the derivation of equation 4.23 may be applied to the streamwise component of equation 4.17, giving the approximation

$$\langle V_x(\mathbf{x}, t)\rangle - \langle U_x(\mathbf{x})\rangle \approx \frac{d}{dy}\langle u_x(\mathbf{x})\, u_y(\mathbf{x})\rangle \Delta t \quad \text{for} \quad 0 < \Delta t < t_{lim} \tag{4.24}$$

This estimate is compared to the measured Lagrangian mean streamwise velocity in figure 4.5. The estimate is found to be a poor match for the data close to the wall, although the trend is approximately correct. This lack of agreement is not surprising given the large change in the Eulerian mean streamwise velocity profile close to the wall, which has a tendency to magnify small errors in $\langle V_x - U_x\rangle$. The difference between estimate and data in the outer layer (green line) is seen to be asymmetric in time, for reasons unknown.

The foregoing development was purely kinematic, as the equation 4.15 derives from Lagrangian kinematics. Dynamical insight into the difference between mean Lagrangian and Eulerian velocities (sometimes called *generalized Stokes drift*[130]) is found by taking the mean of the incompressible Navier-Stokes equation 1.2, which may be written as

$$\left\langle \frac{DU_i}{Dt} \right\rangle = \left\langle \frac{-1}{\rho}\frac{dp}{dx_i} + \nu \frac{d^2 U_i}{dx_j dx_j} \right\rangle \tag{4.25}$$

The l.h.s of the above equation is the material derivative, which is identically the mean Lagrangian acceleration dV_i/dt at $\tau = 0$.

$$\left\langle \frac{dV_i(\mathbf{x}, \tau)}{dt} \right\rangle \Bigg|_{\tau=0} = \frac{-1}{\rho}\frac{d\langle p(\mathbf{x})\rangle}{dx_i} + \nu \frac{d^2\langle U_i(\mathbf{x})\rangle}{dx_j dx_j} \tag{4.26}$$

Considering the wall-normal component $i = y$ where $\langle U_y\rangle = 0$, equation 4.26 reduces to

$$\left\langle \frac{dV_i(\mathbf{x}, \tau)}{dt} \right\rangle \Bigg|_{\tau=0} = \frac{-1}{\rho}\frac{d\langle p(\mathbf{x})\rangle}{dx_i} \tag{4.27}$$

[2] Assuming here that $\nabla\langle f\rangle = \langle \nabla f\rangle$, see Pope[10] p. 72

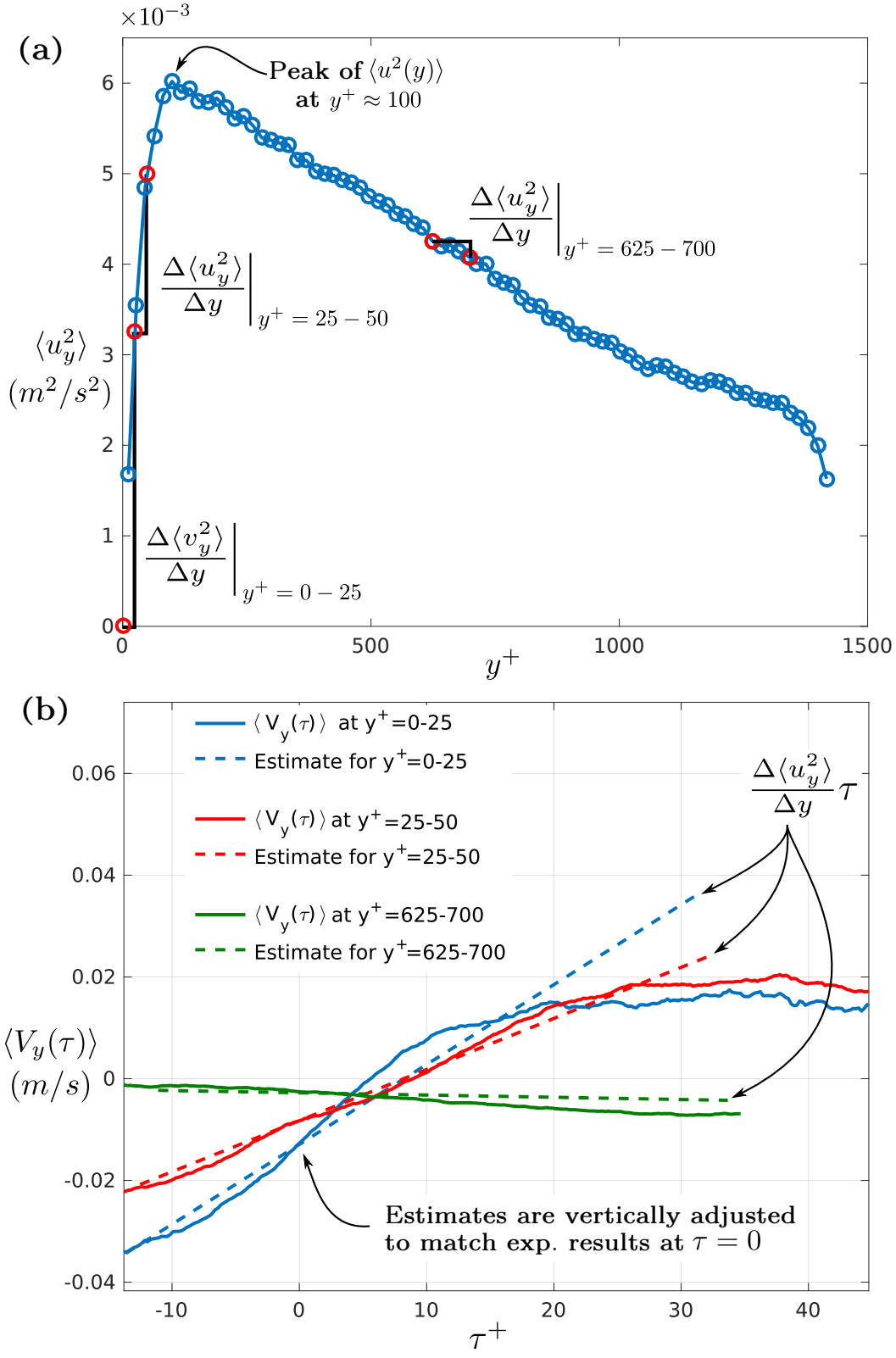

Figure 4.4: **Subfigure (a):** The Eulerian profile of the mean wall-normal velocity variance $\langle u_y^2(y)\rangle$ across the width of the channel. The slope of this profile $\Delta\langle u_y^2\rangle/\Delta y \approx d\langle u_y^2\rangle/dy$ for three selected wall-bin locations is also shown—two between the wall and the peak of $\langle u_y^2\rangle$ and the third on the other side of the peak. **Subfigure (b):** Shows the Lagrangian mean wall-normal velocities $\langle V_y(y_0,\tau)\rangle$ from these three selected wall-bins as a function of the time lag τ. The estimates of $d\langle u_y^2\rangle/dy$ taken from (a) are used to calculated the estimations $\langle V_y(y_0,\tau)\rangle \approx \tau d\langle u_y^2\rangle/dy$ for small τ. Small but non-zero values of $\langle V_y(y_0,0)\rangle$ (i.e. Eulerian velocity) is seen for bins close to the wall. These velocities are likely due to binning biases, as the are greater near the wall. The estimates shown here were adjusted such that they match the experimental results at $\tau = 0$.

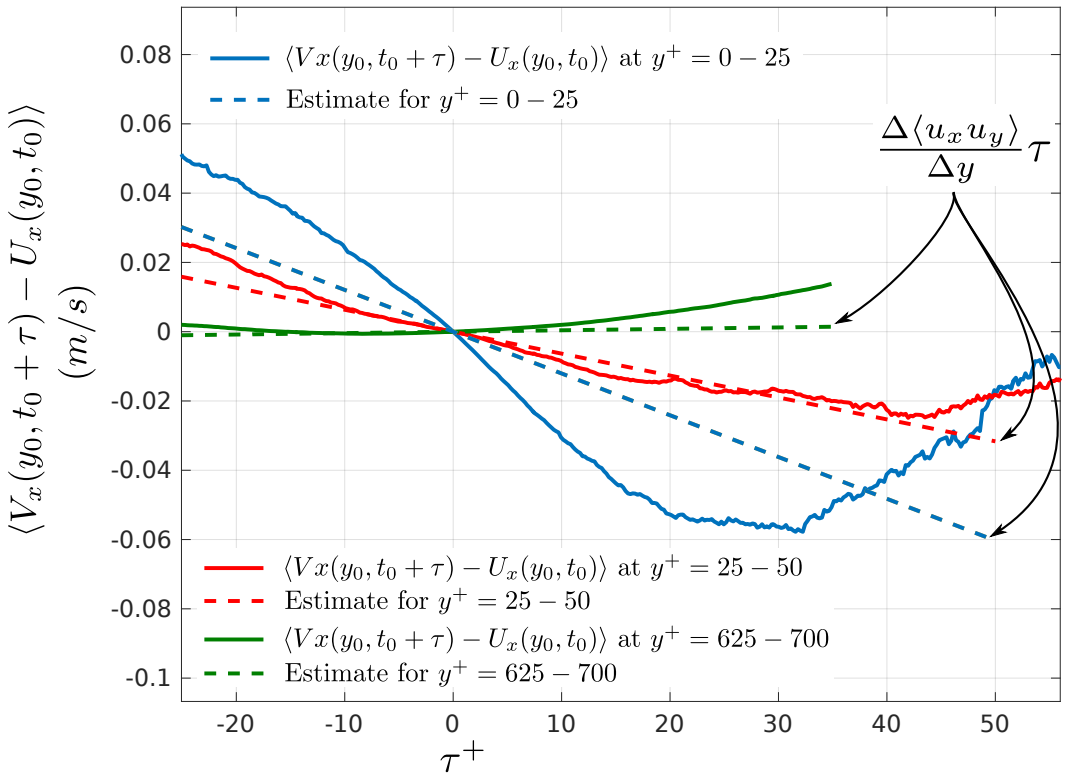

Figure 4.5: Mean difference between Lagrangian and Eulerian streamwise velocity at three locations in the channel. Estimates from equation 4.24 are also shown.

Equation 4.27 shows that in a channel flow the mean acceleration is inversely proportional to the wall-normal pressure gradient. This pressure gradient may be related to other Eulerian quantities by the Reynolds stress equation which, following the derivation and notation of Pope[10](pp.83-86) may be written as

$$\rho\frac{\partial\langle U_i\rangle}{\partial t}+\rho\langle U_j\rangle\frac{\partial\langle U_i\rangle}{\partial x_j}=\frac{\partial}{\partial x_j}\left[\mu\left(\frac{\partial\langle U_j\rangle}{\partial x_i}+\frac{\partial\langle U_i\rangle}{\partial x_j}\right)-\langle p\rangle\delta_{ij}-\rho\langle u_i u_j\rangle\right] \tag{4.28}$$

Regarding the wall-normal component, again in the context of channel flow where $\langle U_y\rangle = 0$, equation 4.28 reduces to mean force balance between the pressure-gradient force and the Reynolds-stress-gradient force

$$\frac{-1}{\rho}\frac{\partial\langle p\rangle}{\partial y}=\frac{d\langle u_y u_y\rangle}{dy} \tag{4.29}$$

The force balance(or more properly *acceleration* balance) in equation 4.29 is in average equilibrium at all positions in the channel; the mean Eulerian wall-normal component of velocity is zero $\left(\langle U_y\rangle = 0\right)$. Equations 4.29 and 4.27 may be combined, where the dependencies of these terms are reintroduced

$$\left\langle\frac{dV_y(\mathbf{x},\tau)}{dt}\right\rangle\Bigg|_{\tau=0}=\frac{d\langle u_y u_y\rangle}{dy}(\mathbf{x}) \tag{4.30}$$

This Eulerian acceleration balance may be written as

$$\langle V_y(y_0,\tau)\rangle-\langle V_y(y_0,0)\rangle=\lim_{\tau\to 0}\tau\frac{d\langle u_y u_y\rangle}{dy}(\mathbf{x}) \tag{4.31}$$

Equation 4.31 suggests an iterative approach that may be solved numerically for the mean Lagrangian wall-normal velocity $\langle \mathrm{V}(y_0, t-t_0)\rangle$ at a given time $t = \mathrm{N}\Delta t$ using a given Eulerian wall-normal-velocity-variance profile as

$$\left\langle \mathrm{V}[y_0, \mathrm{N}] \right\rangle = \frac{y_{\mathrm{N}+1} - y_{\mathrm{N}}}{\Delta t} = \sum_{i=0}^{\mathrm{N}} \Delta t \frac{d\langle u_y u_y \rangle}{dy}(y_i) \tag{4.32}$$

The above equation is more powerful than the estimation derived from purely kinematic arguments, $\langle \mathrm{V}_y(\mathbf{x}, t)\rangle \approx \frac{d}{dy}\langle u_y^2(\mathbf{x})\rangle \Delta t$ (equation 4.23), which is only valid for small values of Δt. Mean Lagrangian positions and velocities calculated with equations 4.32 are presented in figure 4.6, along with measured results. Equation 4.32 is strictly justified only at the first

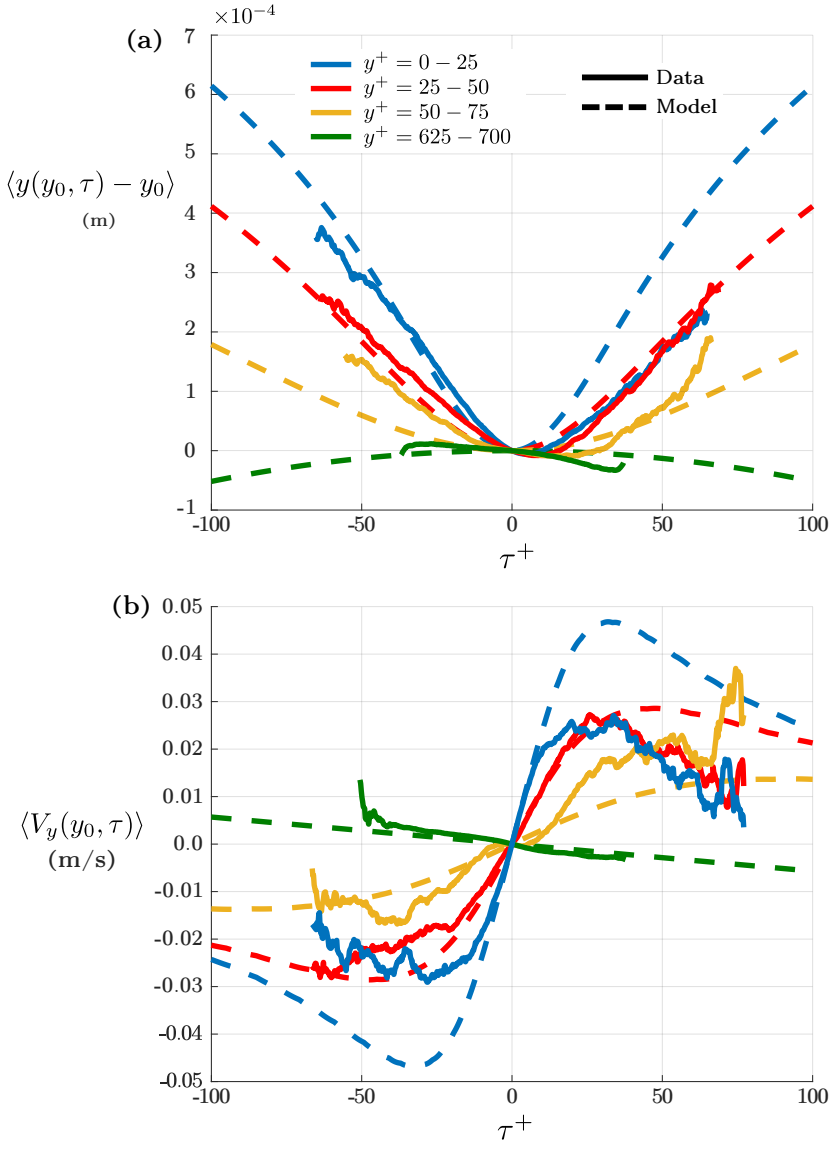

Figure 4.6: **Subfigure (a):** Mean Lagrangian wall-normal positions $\left(\langle y(t_0, \tau)\rangle\right) - y_0$ for four initial positions. **Subfigure (b):** Mean Lagrangian wall-normal velocity $\left(\langle \mathrm{V}_y(y_0, \tau)\rangle\right)$ for four initial positions. Shown in dotted lines in both **(a)** and **(b)** are predictions calculated from equation 4.32 using the measured Eulerian profile of wall-normal velocity variance.

time step. For the following time steps errors accumulate. The reason for these errors is that the mean Eulerian acceleration field at the mean particle position y_i is, in general, not equal to the mean acceleration *seen by the particles*: $\langle a(y_0, \tau)\rangle = \langle d\mathrm{V}(y_0, \tau)/dt\rangle$. The mean

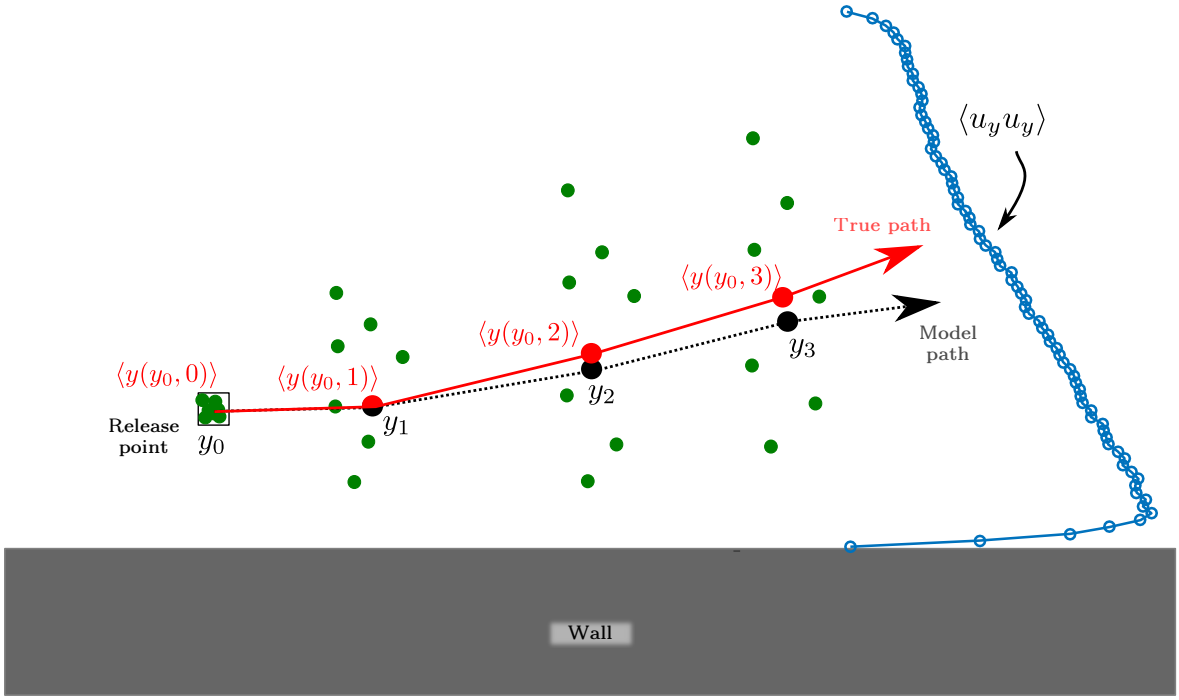

Figure 4.7: Illustration of the limits of the model shown in equation 4.32.

Lagrangian position is the the double integral in time of the mean acceleration seen by the particles

$$\langle y(y_0,\tau)\rangle = \int_0^\tau \int_0^\tau \langle a(y_0,\tau')\rangle d\tau' d\tau'' + y_0 \tag{4.33}$$

The model in Equation 4.32 is accurate as long as

$$\langle a(y_0,\tau)\rangle = \langle a(y_{model}(\tau))\rangle \tag{4.34}$$

the mean Lagrangian acceleration is the mean of the accelerations seen be the all of the particles at time τ

$$\langle a(y_0,i)\rangle = \frac{1}{N}\sum_j^N a(y_i^j) \tag{4.35}$$

If the distribution of the particles is such that the mean acceleration seen by the particles at time τ is equal to the mean acceleration at the mean location at time τ than the model is accurate. This condition holds for example when the acceleration field is constant over the region in which the particles are distributed.

Equation 4.32 is in good agreement with the measurements of Lagrangian mean wall-normal position and velocity. Limits in the resolution of the the spatial gradient of velocity create errors which are compounded in time, which explains the error increasing for larger time-lags. There is error related to the spatial smoothing as well: the spatial gradient of velocity variance is large near the wall, and wall-bins encompass significantly different values of this gradient.

4.4 Single-particle dispersion

Single-particle dispersion is defined as

$$\Delta X_i(y_0,\tau) \equiv \langle [X_i(y_0,\tau) - X_i(y_0,t_0)]^2 \rangle \tag{4.36}$$

and is a measure of the dispersion of particles from a common release point y_0 after a time-lag τ. The residence time of the particles in the measurement volume is small, so only the short-time dispersion is available from the present study. Only the wall-normal dispersion statistics are presented here. Figure 4.8 shows wall-normal dispersion as a function of time for six locations in the channel. Two locations are in the buffer layer ($y^+ = 0-10$, $y^+ = 10-20$), two are in the log layer($y^+ = 50-100$, $y^+ = 150-200$), and two are in the outer layer, or central region ($y^+ = 500-550$, $y^+ = 950-1000$). The wall-normal

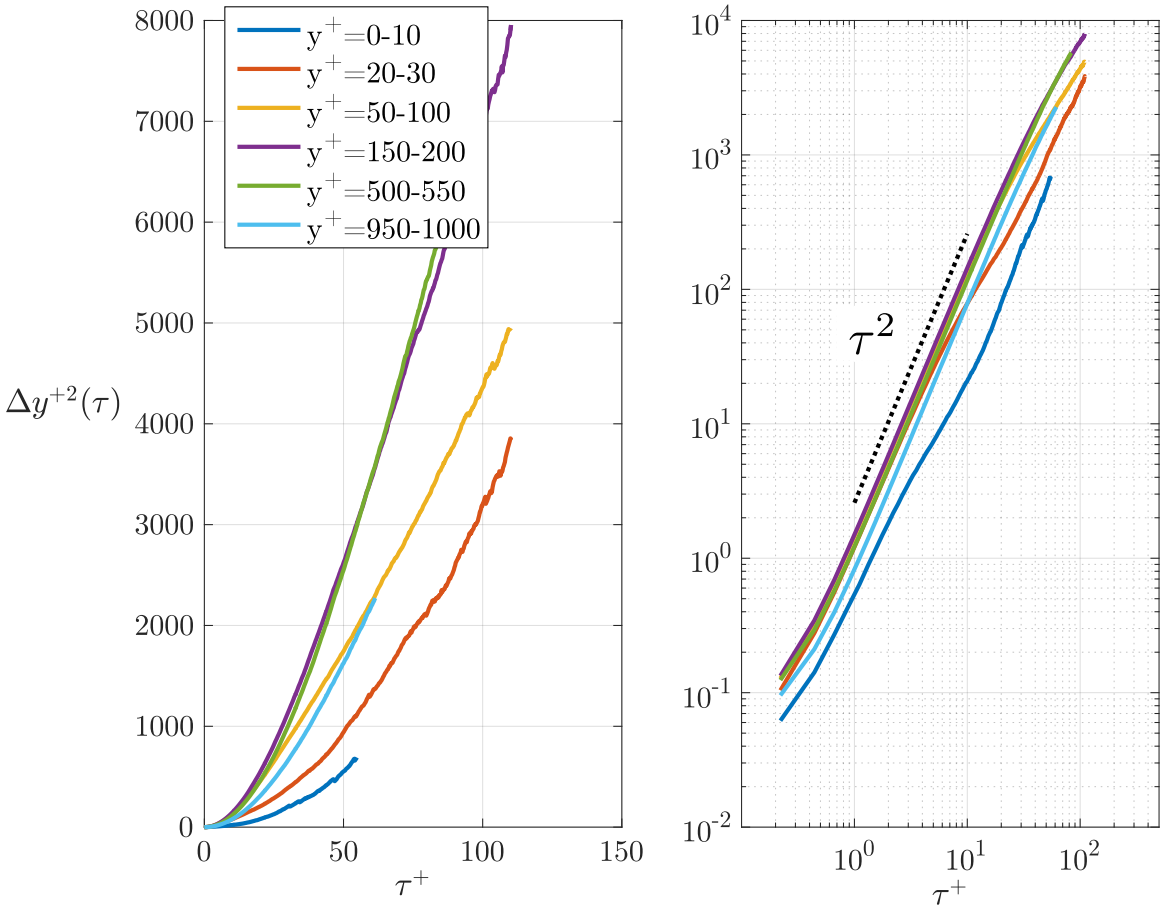

Figure 4.8: Mean square dispersion in the wall-normal direction from six locations in the channel.

dispersion is not monotonic with wall distance: the dispersion is greatest for the release points $y^+ = 150-200$ and $y^+ = 500-550$ (which are very similar over all measured time-lags). The wall normal dispersion plotted in log scale seems to show a quadratic scaling, except perhaps for the release point closest to the wall. This quadratic scaling is expected at short time-lags in HIT from Taylor's prediction of single-particle dispersion, as discussed in section 1.3. The main result is rewritten here for convenience:

$$\langle \mathrm{X}_i(\mathbf{x}_0, t|t_0)\mathrm{X}_j(\mathbf{x}_0, t|t_0)\rangle = 2(t-t_0)\int_{t_0}^{t} \sigma_{ij}(\tau)\rho_{ij}(\tau)d\tau - 2\int_{t_0}^{t} \tau\sigma_{ij}(\tau)\rho_{ij}(\tau)d\tau \tag{4.37}$$

where

$$\sigma_{ij}(\tau) \equiv \langle \mathrm{V}_i(\mathbf{x}_0, t_0|t_0)\rangle\langle \mathrm{V}_j(\mathbf{x}_0, t_0+\tau|t_0)\rangle \tag{4.38}$$

For short time lags $\tau \ll \mathrm{T}_{\mathrm{L},ij}$ the velocity is highly correlated so $\rho_{ij} \approx 1$, also $\sigma_{ij}(\tau) \approx \sigma_{ij}(0)$. Using these approximations in equation 4.37 gives

$$\langle \mathrm{X}_i(\mathbf{x}_0, t|t_0)\mathrm{X}_j(\mathbf{x}_0, t|t_0)\rangle \approx \tau^2\sigma_{ij}(0) \quad \text{for } \tau \ll \mathrm{T}_{\mathrm{L},ij} \tag{4.39}$$

This Taylor scaling is examined in more detail in figure 4.9, which plots the the wall-normal dispersion normalized by the variance of the wall-normal component of velocity and the time-lag squared. In HIT $\sigma_{yy}(\tau) = \langle u_y^2 \rangle$, which would result in a normalized dispersion equal to one at short time-lags. A short plateau at ≈ 1.3 is seen in figure 4.9

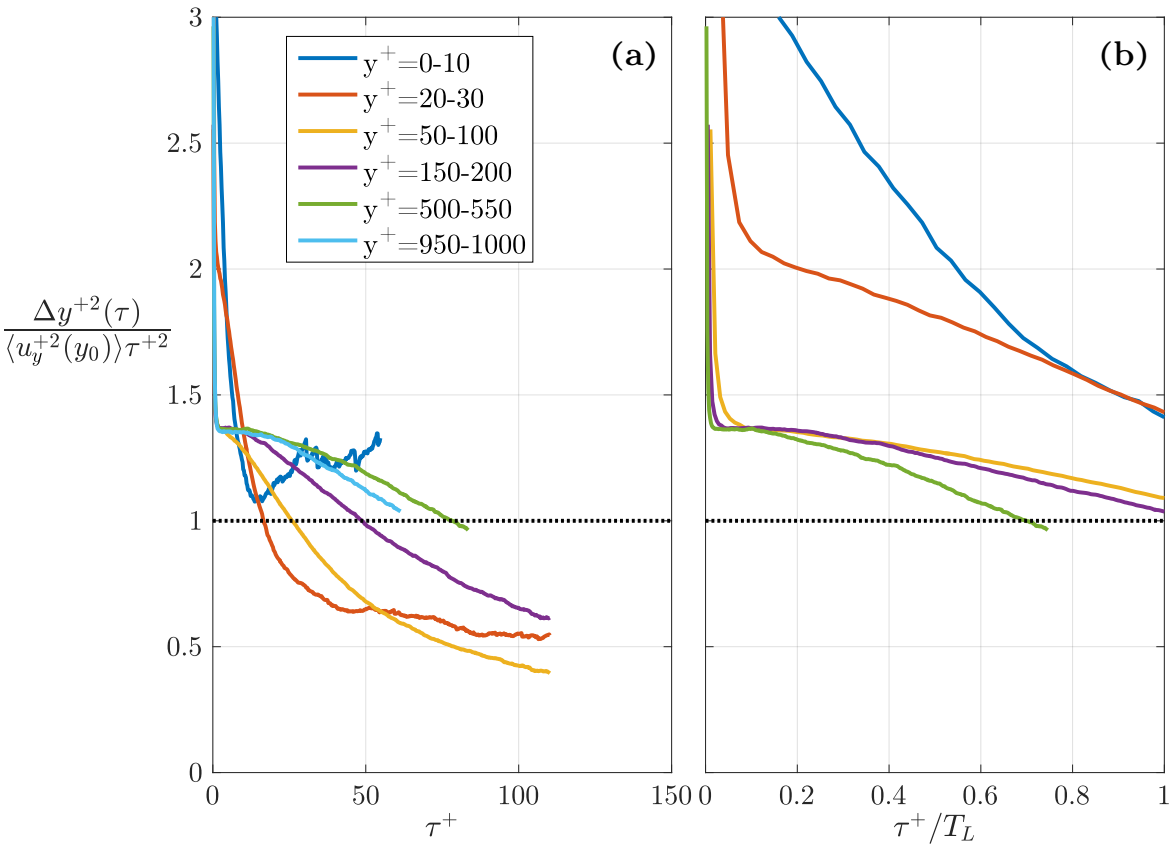

Figure 4.9: **Subfigure (a):** Mean square dispersion in the wall-normal direction from six locations in the channel, normalized by the velocity variance and the time-lag squared. This quantity should be unity at short time-lags ($\tau \ll T_L$) in HIT according to Taylor dispersion. **Subfigure (a):** The same normalized dispersion shown in **(b)**, but the horizontal axis is rescaled such that each curve is plotted against the fraction of the Lagrangian velocity integral scale at the release location. T_L was not available for $y^+ = 950 - 1000$, so the dispersion for that release point is not shown.

(a) at short times for the three release positions farthest from the wall, after which the normalized dispersion decreases with time. Recall that this scaling holds (in HIT) in the limit of $\tau \ll T_L$, but the Lagrangian velocity scale is not equal at all release positions. As will be shown later in this chapter (section 4.10) T_L increases monotonically with distance to the wall. In order to have a fair comparison of the dispersion from various release points, the normalized dispersion is plotted in τ/T_L, shown in subplot (b) of figure 4.9. A plateau is observed at short time-lags ($\tau/T_L \lessapprox 0.25$) for the three release points in the log and outer layers. The dispersion from the release points in the buffer layer show no such plateau. Such behavior may be explained by noting that for release points very close to the wall there is significant mean displacement away from the wall, even at short time-lags (see figure 4.6). The velocity variance also changes significantly between $y^+ = 0 - 50$ (see figure 4.4). These observations suggest that $\sigma_{yy}(0)$ (i. e. $\langle u_y^2 \rangle$) is *not* a good estimate for $\sigma_{yy}(\tau)$ even at short times, and the full integrals in equation 4.37 must be considered.

The time derivative of the dispersion, also called the diffusivity, is directly modeled in

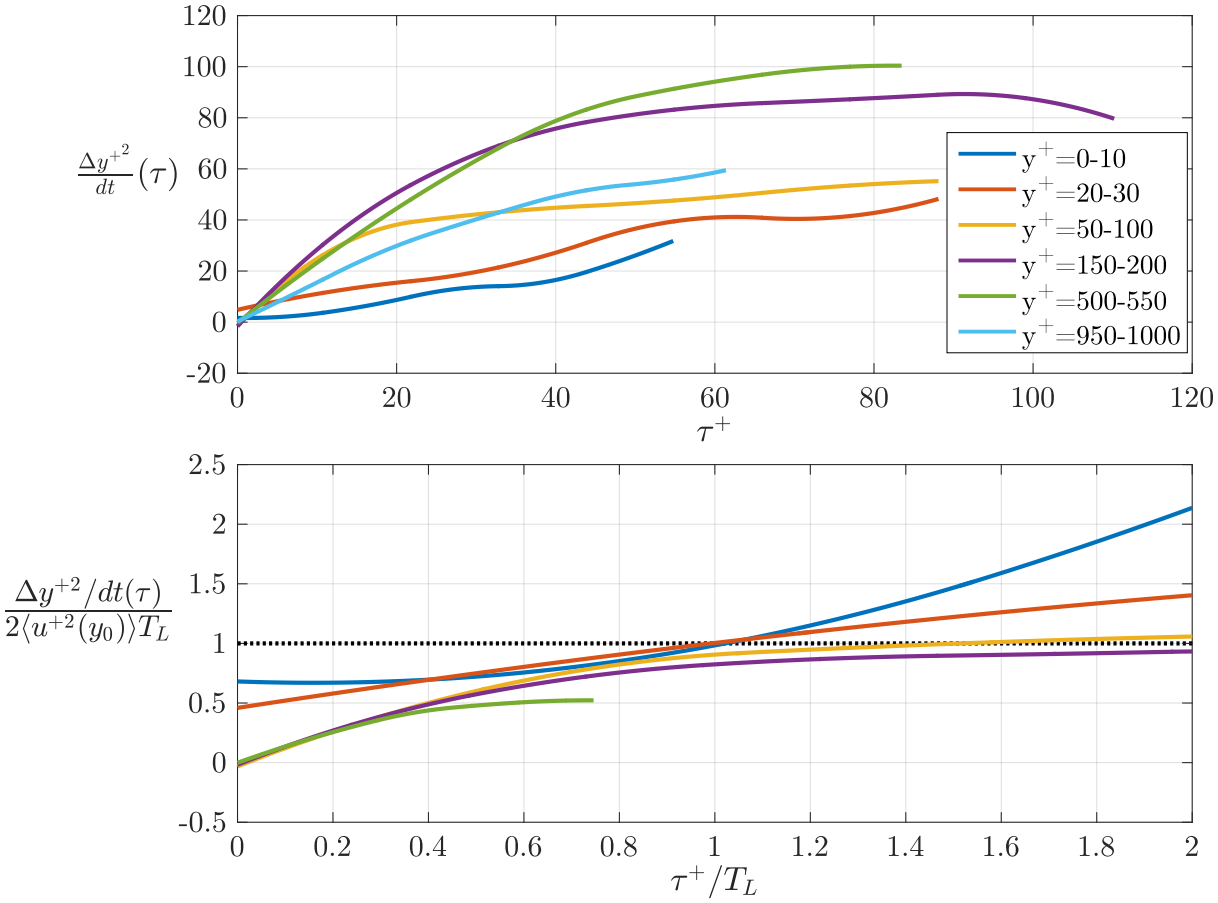

Figure 4.10: **Subfigure (a):** Rate of dispersion in the wall-normal direction for six locations in the channel. **Subfigure (b):** Rate of dispersion in the wall-normal direction for six locations in the channel normalized by the velocity variance at the release location and the Lagrangian velocity timescale.

Langevin-type models (see section 1.3). Taylor theory gives

$$\frac{d}{dt}\langle X_i(\mathbf{x}_0, t|t_0)X_j(\mathbf{x}_0, t|t_0)\rangle = 2\int_{t_0}^{t} \sigma_{ij}(\tau)\rho_{ij}(\tau)d\tau \tag{4.40}$$

Again, the velocity variance may be taken out of this integral in HIT. Figure 4.10 (a) shows this dispersion rate plotted against the time-lag. The wall-normal diffusivity increases with time-lag for all locations. Also shown is the diffusivity normalized by the Lagrangian velocity timescale and the velocity variance at the release point, and rescaled with T_L in the manner described above. Scaled in this manner the diffusivity is expected to approach unity after $\tau > T_L$, as the integrand in equation 4.40 is the velocity autocorrelation. This plateau behavior is seen for the release points in log layer ($y^+ = 50-100$, $y^+ = 150-200$), but the residence time of the particles in the measurement volume is insufficient to see this plateau for the release points in the outer layer.

4.4.1 Time-evolution of the PDF of particle position

The mean square particle displacement over time considered above is the variance of the particle position PDF. The variance of this PDF was characterized above, in the framework developed by Taylor. Unlike in HIT the dispersion of particles from a point source in the channel flow results in highly non-Gaussian PDFs of particle position. This non-Gaussianity is not captured by the variance, so it is instructive to consider the PDFs of

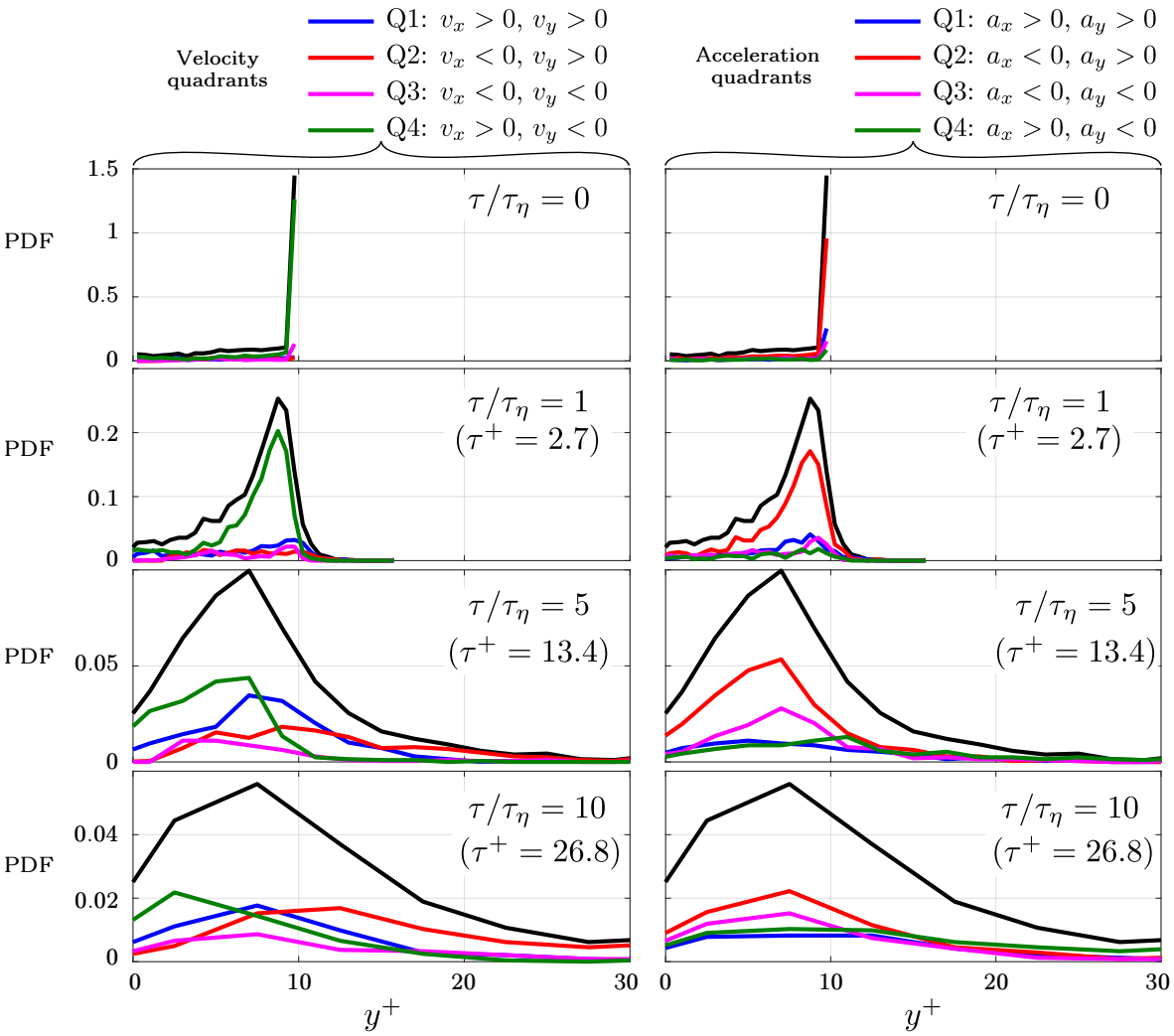

Figure 4.11: PDFs of wall-normal tracer particle position at $t = t_0$, and three subsequent times (black lines). The particle "release point" is y^+0-10. **Left column:** PDF of the wall-normal position of tracer particles conditioned on having *velocities* in one of the four quadrants defined in the legend. **Right column:** PDF of the wall-normal position of tracer particles conditioned on having *accelerations* in one of the four quadrants defined in the legend.

particle position directly. The time evolution of the PDFs of wall-normal position are presented below for two locations: one in the buffer layer and one in the log layer. Also shown are the PDFs conditioned on the quadrants of velocity and acceleration, i. e.

$$\mathrm{PDF}(y(y_0,\tau)|\mathrm{Q}^v) \quad \text{and} \quad \mathrm{PDF}(y(y_0,\tau)|\mathrm{Q}^a) \tag{4.41}$$

where the quadrants Q^v and Q^a are defined in figures 4.11-4.12.

Figure 4.11 shows the PDF of wall-normal position at the "release time" $t = t_0$ and three subsequent times: 1, 5, and 10 times the local Kolmogorov timescale τ_η. Notice that this is not dispersion from a point-source: the finite width of the initial release point ($y^+ = 0-10$) is seen in the PDF of wall position at $t = t_0$. Homogeneous distribution of the particle position at $t = t_0$ is not observed; the particles are seen to be clustered close to the $y^+ = 10$ edge of the bin. This is in part a consequence of the bias found in the discussion of Eulerian velocity statistics in section 3.2. After one Kolmogorov time the particles have dispersed very little towards the center of the channel, but have dispersed significantly towards the wall. This dispersion towards the wall seems to be related to particles arriving in the bin with momentum towards the wall; most of the particles in

the PDF at $t/\tau_\eta = 0$ and $t/\tau_\eta = 1$ are in the velocity quadrant 4, i. e. they have a velocity towards the wall and in the streamwise direction. Most of these particle are in acceleration quadrant 2 (i. e. they are slowing down in the streamwise direction and slowing down as they approach the wall) which is also supports the idea that these faster particles are arriving with momentum in the bin and slowing as they approach the wall. At later times,

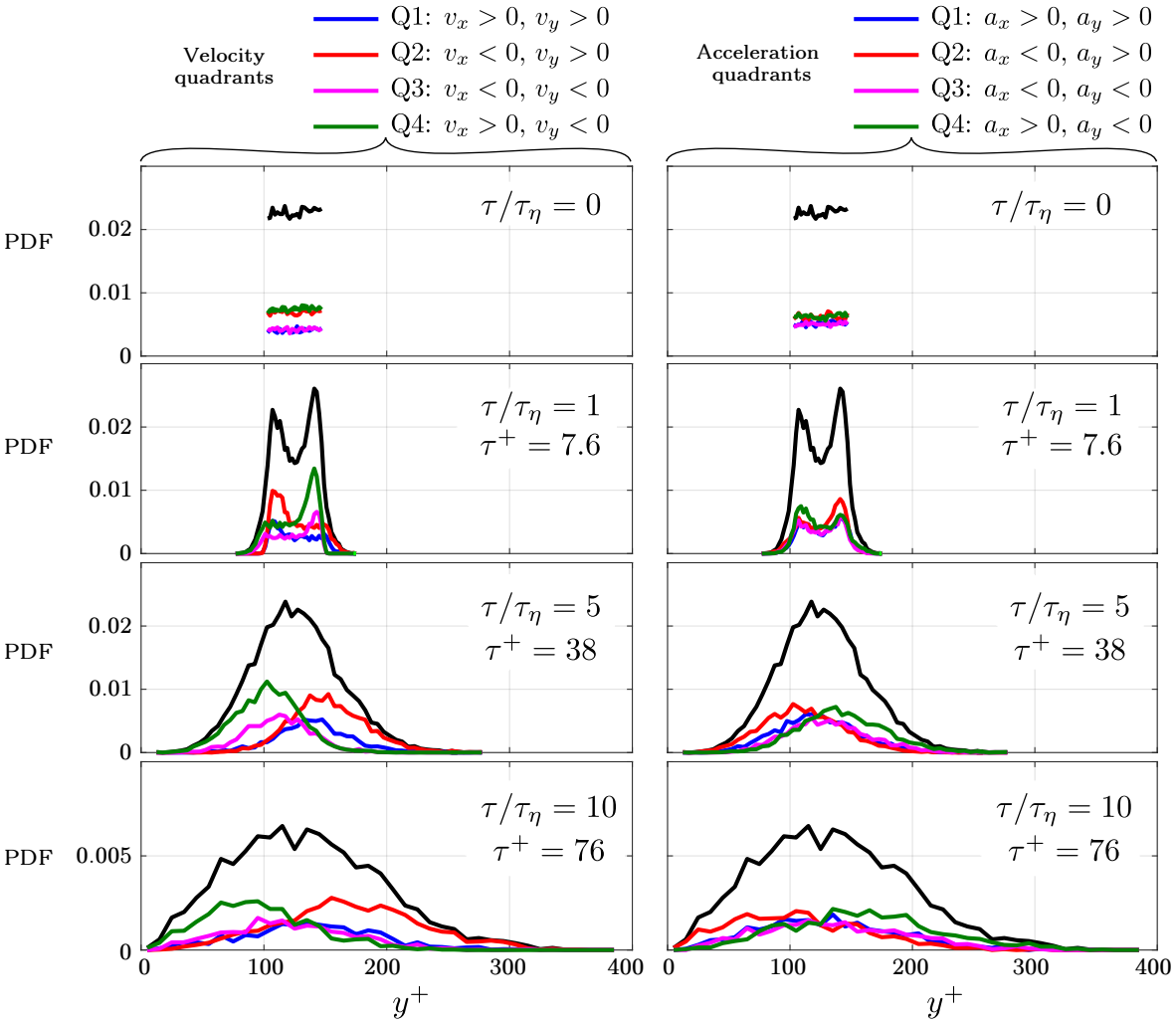

Figure 4.12: PDFs of wall-normal tracer particle position at $t = t_0$, and three subsequent times (black lines). The particle "release point" is $y^+ 100 - 150$. The Lagrangian velocity timescale at this location is $T_L^+ = 33$. **Left column:** PDF of the wall-normal position of tracer particles conditioned on having *velocities* in one of the four quadrants defined in the legend. **Right column:** PDF of the wall-normal position of tracer particles conditioned on having *accelerations* in one of the four quadrants defined in the legend.

$\tau/\tau_\eta = 5 - 10$ the distribution shape stabilizes, with a long tail growing towards the channel center. The Kolmogorov velocity scale is small at this location in the channel, $T_L^+ \approx 7$, so these PDFs are at times in which the diffusivity is constant in HIT. The PDFs conditioned on the quadrants of acceleration show that this initlal dominance of the PDF by those particles with accelerations in Q_2^a is weakened over time, as it approaches equilibrium with Q_3^a. The mean streamwise component of acceleration is negative in this location, so the second and third quadrants of acceleration are expected to dominate in the PDF.

The time evolution of the PDF of wall-normal position from a release point in the log layer ($y^+ = 100 - 150$) is shown in figure 4.12. At the release time the particles are approximately homogeneously distributed, as expected. One Kolmogorov timescale after

the release time, particles with negative wall-normal velocities are more probable on the right edge of the bin, and particles with positive wall-normal velocities are more probable on the left edge of the bin. This behavior is consistent with the bias illustrated in figure 4.2: setting the initial time t_0 when the particle enters the bin creates a bias near the edges of the bin. After five Kolmogorov timescales, which at this location is slightly more than one Lagrangian velocity timescale, the PDF appears close to Gaussian, and the particles have not yet reached the wall. The PDFs conditioned on velocity quadrants show that the particles that have dispersed towards the wall have negative wall-normal velocities, and the particles that have dispersed towards the center have positive wall-normal velocities, which is expected. Less intuitive is why the opposite signed quadrants ($Q2^{\nu}$ and $Q4^{\nu}$) are more represented in the PDF than same-signed quadrants ($Q1^{\nu}$ and $Q3^{\nu}$). This is an effect of the Reynolds stress: figure 3.4 shows that the fluctuating streamwise and wall-normal components of the velocity are negatively correlated to ≈ 0.3 in this location in the channel.

4.5 Conclusion

Lagrangian statistics in inhomogeneous turbulence must be conditioned on initial position and is non-stationary. Consequences of two different binning strategies were seen in mean Lagrangian trajectories and the the conditional PDFs of particle position. Statistical bias at short times must be balanced with statistical convergence at long times. Inhomogeneity creates differences between mean Eulerian velocity and mean Lagrangian velocity. Kinematic development allowed the estimation of mean Lagrangian velocity at short times, and a simple dynamical argument allow a similar prediction. Measurement of the wall-normal dispersion was reported for several locations in the channel. Taylor scaling of τ^2 and a HIT predictions for the diffusivity were found to hold approximately even very close ($y^+ = 50 - 100$, the beginning of the log layer) to the wall. PDFs of wall-normal particle position at three time-lags after the "release time" were considered in the buffer layer and in the log layer. In the log layer the PDF is approximately Gaussian after one Lagrangian timescale and particles have not reached the wall. This suggests the dispersion acts in a manner similar to that of HIT until the presence of the wall is felt. These PDFs were conditioned on the quadrants of velocity and acceleration, which clearly show the negatively correlated components of velocity.

4.6 Physical Review Fluids article

Some of the results described in this thesis regarding Lagrangian correlations of acceleration and their associated time scales were previously published in the journal Physical Review Fluids, in an article written in collaboration with Juan Ignacio Polanco, Ivana Vinkovic, and Nicolas Mordant. Instead of rewriting this article it is reproduced here as it appeared in the journal. The section, figure, and reference numbering have been adapted to the format of this thesis, specifically the references in the paper are found in the main reference section of this thesis. Complementary results, especially Lagrangian correlations of acceleration and velocity that were not included in this paper may be found in appendix A.2.

4.7 Introduction

The Lagrangian study of fluid particle trajectories is a natural first step in predicting the transport of components that are passively entrained by the flow such as chemical/radioactive pollution (passive scalars), aerosols (with small inertia) or the mixing of components prior to combustion. Indeed, in many cases the Péclet number is very large so that most of the statistical properties of scalar dispersion are directly related to that of the dispersion of fluid particles (except of course at the smallest scales at which molecular diffusion plays an ultimate role that depends on the Schmidt number). Despite advances in computational power and resources, direct numerical simulations (DNS) are still out of reach in practical situations. Thus, an efficient modeling is required to obtain reliable predictions. Due to the random nature of turbulence, it is tempting to develop stochastic models that could be used for simulations with an average or large-scale knowledge of the flow. A growingly popular method is Large Eddy Simulation (LES) in which only the largest scales of the turbulence are resolved whereas the small scales of the turbulent spectra are modeled [131]. Various classes of models can be used for the unresolved part of the flow, and Lagrangian stochastic subgrid models can be developed for such simulations as used in combustion for instance [132, 3]. An efficient model would also be useful to forecast the dispersion of pollution from localized sources (e.g. industrial accident) using coarse grid meteorological predictions.

In the context of homogeneous and isotropic turbulence (HIT), 1D Lagrangian stochastic models have been developed as variations of the Langevin equation, i.e. modeling the velocity v of a fluid particle as a Markovian process [54]:

$$dv = -\frac{v}{T_L}dt + \left(\frac{2\sigma^2}{T_L}\right)^{1/2} dW(t) \tag{4.42}$$

with T_L the Lagrangian integral time scale, $W(t)$ a Wiener process and σ^2 the velocity variance. Due to the absence of correlations between velocity components this equation is 1D. It is so strongly constrained by symmetries and the input from the Kolmogorov 1941 theory that it involves only one parameter $T_L = \frac{2\sigma^2}{C_0\epsilon}$ (with ϵ the average turbulent energy dissipation rate per unit mass and C_0 a universal constant). This approach incorporates naturally Taylor's classic result [50] of long term turbulent diffusion of a single particle. This equation includes neither the dependency on the Reynolds number nor intermittency. Concerning the former point, this simple framework (equation 4.42) has been extended by [38] to include finite Reynolds number effects. The model is now a second order stochastic equation that models the acceleration and no longer the velocity:

$$da = -\alpha_1 a dt - \alpha_2 \int_0^t a(s) ds dt + \sqrt{2\alpha_1\alpha_2\sigma^2} dW(t). \tag{4.43}$$

Parameters α_1 and α_2 are two inverse time scales related to the Kolmogorov time scale $\tau_\eta = \sqrt{\nu/\epsilon}$ and the integral Lagrangian time scale T_L. The Reynolds number thus appears as the ratio of the two time scales. At very high Reynolds number, the Kolmogorov 1941 theory predicts that the ratio $\frac{T_L}{\tau_\eta} = \frac{2Re_\lambda}{C_0\sqrt{15}}$ (with Re_λ the usual Taylor-scale Reynolds number). Sawford [38] suggested an empirical formula estimated from DNS at moderate Re_λ given by:

$$\frac{T_L}{\tau_\eta} = \frac{2Re_\lambda}{C_0\sqrt{15}}(1 + 7.5C_0^2 Re_\lambda^{-1.64}). \tag{4.44}$$

This model remains Gaussian at all scales and thus does not include any intermittency effect. Moreover, it remains unidimensional with no interdependency between acceleration

(or velocity) components. Real flows as encountered in nature (atmospheric boundary layer) or in industrial applications (pipes, mixers, combustion chambers...) can rarely be considered as homogeneous and isotropic, notably due to non-zero average shear and wall-confinement. [55] showed that a homogeneous, anisotropic Langevin-type stochastic model should include the time scales associated with the auto- and cross-correlations of the acceleration and velocity components.

The last twenty years have seen the development of experimental techniques and DNS capabilities that have allowed the direct simultaneous observation of the acceleration, velocity, and position of fluid particles, mostly focused on HIT. They showed that acceleration statistics are strongly non-Gaussian (intermittent) [68]. Modelling such features requires to further increase the dimensionality of the stochastic models in the framework of the non extensive statistical mechanics [67, 133, 134] or to use a non-Markovian model [70]. In both cases, inspired by the Kolmogorov-Obukhov 1962 theory, dissipation (that appears in the magnitude of the noise in the stochastic equations) is assumed to be itself a stochastic variable and fluctuates with a long time scale comparable to T_L. Thus, the stochastic equations involve multiplicative noise that make their developments much more involved.

Data concerning more realistic flows are scarce [75, 135, 63, 136, 73, 64, 77]. Complex models of inhomogeneous and anisotropic turbulence are weakly constrained by symmetries or scaling considerations and thus require significant experimental or numerical input. Del Castello & Clercx [136] studied anisotropic turbulence affected by rotation which remains quite far from realistic flows. Walpot *et al.* reported some Lagrangian statistics of velocity in the circular pipe flow and their incorporation in stochastic modeling but no acceleration data [63]. Gerashenko *et al.* [73] studied the case of inertial (heavy) particles in a boundary layer but not the case of the Lagrangian tracers. Chen *et al.* [135] provided Eulerian information on the acceleration in a turbulent channel flow but did not discuss the Lagrangian dynamics. Choi et al. [75] report a numerical analysis of the Lagrangian dynamics of acceleration in a turbulent channel flow but their Reynolds number is relatively low and they discuss neither the coupling between acceleration components nor the time scales. This article reports small scale-resolved Lagrangian experimental measurements in a statistically stationary, high aspect ratio turbulent channel flow, as well as DNS results with parameters matching those of the experiment. Such a flow represents a relatively simple academic framework that incorporates the basic ingredients of real flows: average shear (anisotropy) and confinement (inhomogeneity). In the fully developed part of the flow, the Eulerian statistics of the turbulence are stationary in time and translation-invariant in the streamwise and transverse direction. Thanks to these symmetries, the statistics can be conditioned on a single parameter, the wall distance y. This relative simplicity makes this flow a privileged framework to develop and benchmark advanced Lagrangian stochastic models applicable to realistic flows.

It is well known that near-wall turbulence is characterized by multiscale coherent structures with preferential orientations [46]. These structures include intense vortices elongated in the mean flow direction, that strongly affect the near-wall flow dynamics. These streamwise vortices induce strong centripetal accelerations, being the main source of acceleration intermittency near the walls [76], as illustrated on Fig. 4.13. On the other hand, large-scale inhomogeneity implies that velocity and acceleration statistics depend on wall distance. Thus, it is also of interest to investigate the far-wall behavior, where a return to isotropy may be expected, and stochastic models based on isotropic turbulence may be applied.

We first present the experimental and numerical setups that allow us to measure the acceleration of particles along their trajectories. In part 4.9 we show the statistical analysis

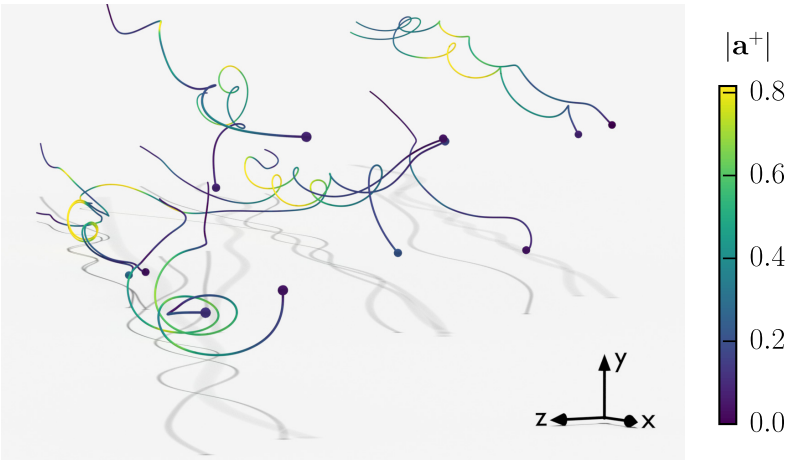

Figure 4.13: Sample high-acceleration particle tracks obtained from DNS. Particles are located in the near-wall region ($y^+ \lesssim 200$). Trajectories are shown over $\Delta t^+ = 120$. The shadow is projected on the wall. Colors represent the norm of particle acceleration. $|\mathbf{a}^+| = 1$ corresponds roughly to 430 m/s^2 in the experiments.

of the temporal dynamics through the computation of time correlation functions of both acceleration and velocity components. This analysis provides estimates of the relevant time scales that are discussed in part 4.10. In part 4.11 we focus on the acceleration probability distributions and compare them to the case of HIT.

4.8 Experimental and numerical setups

We study the turbulent flow in a channel between two parallel walls separated by a distance $2h$ using the same Reynolds number ($Re = U_0 h/\nu = 34\,000$) in both experiments and DNS. This corresponds to a friction Reynolds number $Re_\tau = u_\tau h/\nu \approx 1440$, where $u_\tau = \sqrt{\tau_w/\rho}$ is the friction velocity associated to the shear stress τ_w at the wall and ν the kinematic viscosity. In the following, the superscript + indicates quantities expressed in wall units, nondimensionalized by u_τ and ν.

The experiment consists of measurements made in a closed-loop water tunnel, shown in Fig. 4.14, with a centerline velocity $U_0 = 1.75\,\mathrm{m\,s^{-1}}$. We chose water as a working fluid in order to have neutrally buoyant and small enough tracer particles, which is very difficult to achieve in air. The experimental test section is 3.2 m long with a cross-section of 37.5 mm × 316 mm, with tripped boundary layers at the entrance. The development length is $155h$ and the channel height is $16.9h$, ensuring statistical homogeneity in the streamwise and spanwise directions.

The wall unit is $\delta = \nu/u_\tau = 13\,\mu$m in our experimental conditions, thus we chose to seed the flow with 10 µm polystyrene spheres that are small enough to accurately trace the flow down to the viscous layer. The Stokes number of these particles ranges from $St = 0.02$ at $y^+ = 0.5$ to $St = 9 \times 10^{-4}$ at the center of the channel. Fluorescent particles are used in order to improve the contrast in the vicinity of the wall by eliminating reflections of the illumination laser near the wall. This choice makes the measurement conditions quite challenging due to the weak amount of light emitted by the particles. Three dimensional particle trajectories are measured by particle tracking velocimetry [97] in a 35 mm × 20 mm × 8 mm measurement volume illuminated by a 8 mm-thick 25W CW laser sheet, using two highly sensitive very high speed Phantom v2511 cameras running at a sampling rate of 25 000 frames/s (with one 180 mm and one 150 mm macro lenses with

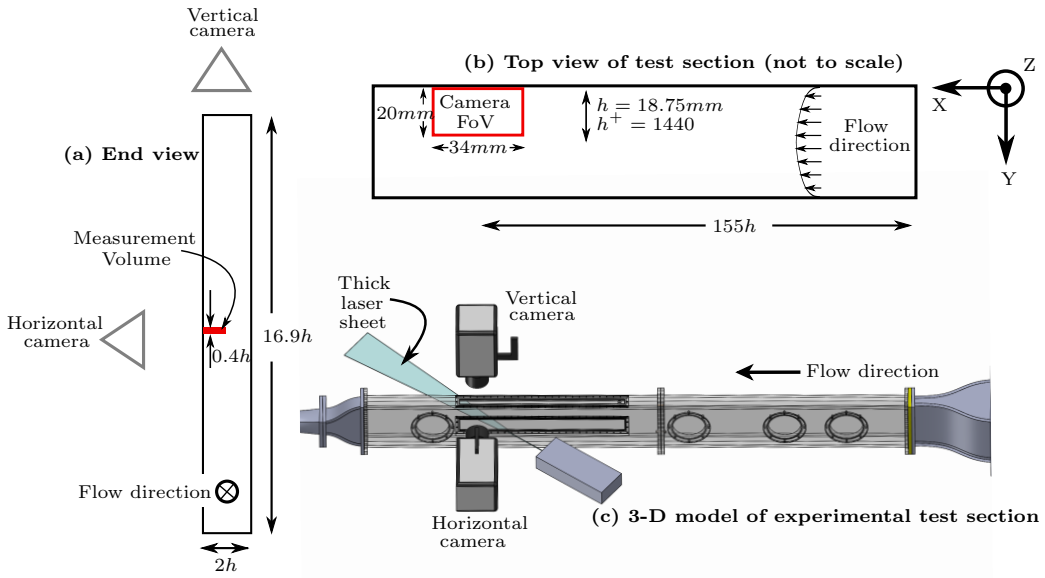

Figure 4.14: Sketch of the turbulent channel used in the experiment. Subfigure (a) is a sketch of the end view of the channel showing the aspect ratio of the channel (the spanwise distance is $16.9h$) and the end view of the measurement volume, as well as the position of the two cameras. Subfigure (b) shows a top view of the channel, with the field of view (FoV) of the vertical camera highlighted. Subfigure (c) shows a 3-D rendering of the experimental setup, including the relative positions of the two high speed cameras and the thick laser sheet used to illuminate the measurement volume.

optical filters tuned to the emission frequency of the fluorescent particles). The measurement volume covers half the width of the channel and is long enough in the downstream direction for a sufficiently long time of particle tracking. This allows us to observe the full decorrelation of the acceleration and (close to the wall) the velocity. Such a high sampling rate is required in order to have enough time resolution to differentiate twice the trajectories and compute the acceleration. Particle velocity and acceleration are obtained by convolution of the trajectories with Gaussian differentiating kernels, which also serves to filter out noise from the measurements [31]. The pixel size corresponds to 27 µm in physical space, but thanks to the diffraction of their emitted light, the fluorescent particles cover about three pixels in the images, which has been shown to be a good condition for subpixel position accuracy. Indeed, the estimated accuracy is 1/10th of a pixel (i.e. 3 µm) after filtering. Although this allows us to have a fairly precise estimation of the position of the particles in the bulk of the flow, the apparent size of the particle and the existence of images reflected in the wall prevents us from measuring the position of the particles very near the wall. The closest distance at which accurate detection of the particle was possible is $y^+ = 4$, i.e. about 50 µm. Thus, our range of measurement spans the interval $y^+ \in [4, 1400]$ i.e. more than two orders of magnitude in wall distance.

Direct numerical simulations are performed using a pseudo-spectral method for the resolution of the velocity field between two parallel walls, coupled with Lagrangian tracking of passive tracers advected by the resolved fluid velocity. The pseudo-spectral method, described in detail by [137], assumes periodicity in the streamwise (x) and spanwise (z) directions, where a Fourier decomposition of the velocity field is applied. In the wall-normal (y) direction, a Chebyshev expansion is performed in order to enforce no-slip boundary conditions at the walls. The size of the computational domain is $L_x \times L_y \times L_z = 4\pi h \times 2h \times \pi h$ (in wall units, $L_x^+ \times L_y^+ \times L_z^+ = 18166 \times 2891 \times 4541$) in the streamwise, wall-normal and spanwise directions, respectively. The velocity field is decomposed into $2048 \times 433 \times 1024$ spectral modes. In physical space, this corresponds to a uniform grid

spacing $\Delta x^+ = 8.9$ and $\Delta z^+ = 4.4$ in the streamwise and spanwise directions, respectively. In the wall-normal direction, the grid spacing Δy^+ varies between 0.04 (wall region) and 10.5 (channel center). An explicit second-order Adams-Bashforth scheme is used to advance the resolved equations in time, with a simulation time step $\Delta t^+ = 0.03$. The total simulation time in channel units is $\mathrm{TU}/h = 217$, which corresponds to about 17 turnover times of the centerline flow.

Once the instantaneous velocity field $\vec{u}$ is known, the acceleration field is computed in the Eulerian frame according to $\vec{a} = \partial\vec{u}/\partial t + \nabla\left(\vec{u}^2/2\right) + (\nabla \times \vec{u}) \times \vec{u}$. Orzag's 2/3 rule [138] is applied in the x and z directions to the velocity and acceleration fields to filter out aliasing noise resulting from evaluation of non-linear terms.

The simulation is started with a fully-developed, statistically stationary turbulent channel flow containing 2×10^6 randomly distributed fluid particles. Velocity and acceleration of fluid particles are determined from interpolation of the respective Eulerian fields at each particle location using third-order Hermite polynomials. The choice of the interpolation scheme is critical, particularly for the evaluation of Lagrangian acceleration statistics. Lower-order schemes such as trilinear or Lagrange interpolation lead to spurious oscillations which are clearly visible in the temporal spectrum of particle acceleration [75, 139]. Particle positions are advanced in time using a second-order Adams-Bashforth scheme, as for the Eulerian velocity field. Sample trajectories obtained from this procedure are shown in Figs. 4.13 and 4.17.

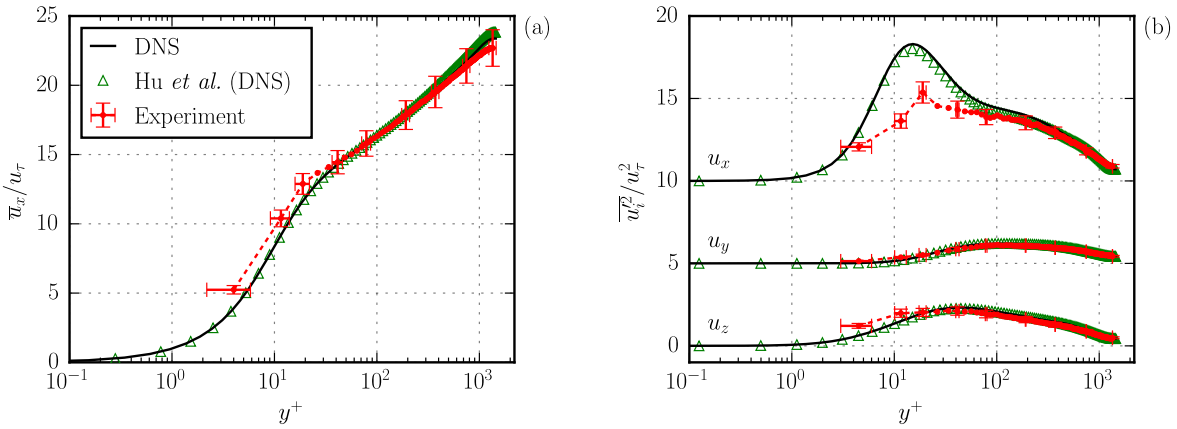

Figure 4.15: Mean and variance velocity profiles. Comparison between experiments (dashed lines), DNS (solid lines) and [140] DNS at $Re_\tau = 1440$ (triangles). Velocity variance profiles are shifted vertically for clarity. All quantities are normalized in wall units.

In Fig. 4.15, mean and variance velocity profiles from experiments and simulations are compared with the channel flow DNS of [140] at roughly the same Reynolds number $Re_\tau = 1440$. Experimental profiles are obtained by sampling the instantaneous velocity of particles conditioned by their wall distance y^+. In the three cases, the mean streamwise velocity profile presents a clear logarithmic behavior over $40 \lesssim y^+ \lesssim 1200$. Results from both simulations are consistent with each other, while slight departures in the mean profile are observed for the experiments. These differences are more pronounced near the wall ($y^+ < 30$) and towards the channel center ($y^+ > 500$). Similar remarks can be made for the streamwise velocity variance, where an important difference is found at $y^+ < 50$ relative to the simulations. On the other hand, wall-normal and transverse velocity variances from experiments are in agreement with the simulations at all measured wall distances.

Error bars shown on the experimental results in Fig. 4.15 and the following experimental results reported in this paper (with the exception of the probability density function

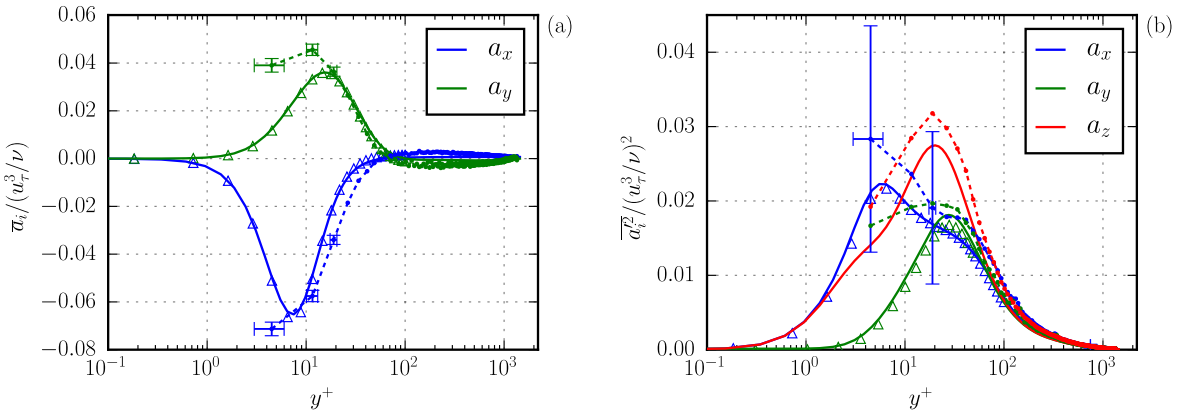

Figure 4.16: Mean and variance acceleration profiles. Comparison between experiments (dashed lines), DNS (solid lines) and [78] DNS at $Re_\tau = 600$ (triangles).

results discussed in Section 4.11) are calculated statistically for a 95% confidence interval [141]. Error bars also take into account the experimental precision associated with the parameters used to report normalized results, u_τ, ν, etc., which is incorporated into the error calculation in the standard way [142], and in some cases is responsible for a large part of the error, as in the plot of $\overline{a'^2}/(u_\tau^3/\nu)^2$ shown in Fig. 4.16.

Figure 4.16 shows the mean and variance acceleration profiles obtained by our experiments and DNS. The profiles are consistent with the DNS results of [78] (also presented in the figure) even though their simulations were performed at a considerably lower Reynolds number $Re_\tau = 600$. As shown by [78], the mean streamwise acceleration can be decomposed into an irrotational and a solenoidal contribution, associated with the mean streamwise pressure gradient and the viscous stress, respectively. In wall units, this is expressed as $\overline{a}_x^+ = \overline{a}_x^{I+} + \overline{a}_x^{S+} = \frac{1}{Re_\tau} + \frac{d^2\overline{u}_x^+}{dy^{+2}}$. Near the wall, the solenoidal term $\overline{a}_x^S$ dominates and is negative, which shows that the negative peak of mean streamwise acceleration at $y^+ \approx 7$ is a consequence of a viscous contribution. For the mean wall-normal acceleration, the solenoidal term $\overline{a}_y^S$ is zero. Therefore, its profile is entirely determined by the mean wall-normal pressure gradient [78].

Profiles of acceleration variance (Fig. 4.16b) reveal qualitative agreement between both sets of data, although large uncertainty is seen in the experimental results near the wall. It is worth noting that, at their respective peaks, the standard deviation of acceleration is larger than the magnitude of the mean acceleration, indicating that dynamics near the wall are strongly influenced by acceleration fluctuations. As shown by [76], these dynamics are dominated by the presence of near-wall streamwise vortices inducing high-magnitude, oscillating centripetal accelerations mainly oriented in the spanwise and wall-normal directions.

4.9 Lagrangian correlations

The Lagrangian description deals with particle trajectories that are parameterized by their initial position $\vec{r}_0$ and by the time delay τ relative to the initial time t_0. In stationary HIT, Lagrangian statistics do not depend on $\vec{r}_0$ due to translational invariance, nor on t_0 due to statistical stationarity. Statistics are thus parametrized only by the time delay τ. Furthermore, single-point single-time statistics such as moments of acceleration components $\langle a_i^p(\tau)\rangle$ are constant in τ. In inhomogeneous turbulence, things are more complex. Indeed the initial position $\vec{r}_0$ must be retained. The symmetries of the channel flow are such that

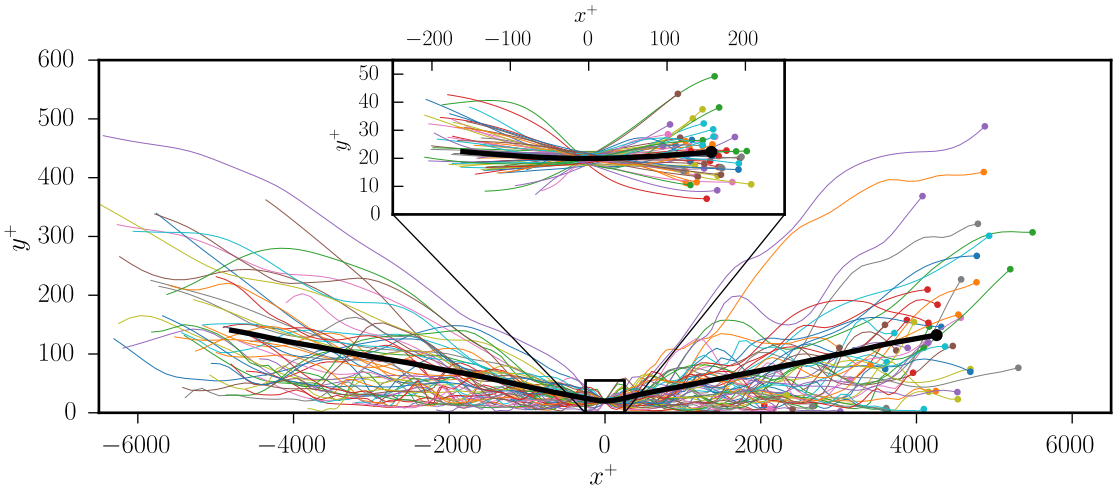

Figure 4.17: Illustration of the Lagrangian averaging procedure. Thin curves represent trajectories of particles located at $y^+ = y_0^+ \pm 0.5\,\delta y^+$ at a reference time t_0 (here, $y_0^+ = 20$ and $\delta y^+ = 5$). Trajectories are shifted in the streamwise direction so that $x(t_0) = 0$. The thick curve represents the Lagrangian average of particle position $\langle \vec{r}(\tau, y_0) \rangle$. The channel center is at $y^+ = 1440$. Trajectories $\vec{r}(t_0 + \tau, y_0)$ are shown for time lags $\tau^+ \in [-338, 338]$. The zoomed-up inset represents time lags $\tau^+ \in [-13.5, 13.5]$.

the dependency of the statistics on $\vec{r}_0$ reduces to a dependency on the initial distance from the wall, y_0. Moreover, single-time Lagrangian statistics now vary with the time delay τ. For instance, the Lagrangian average of the streamwise velocity component, $\langle v_x(t_0 + \tau, y_0) \rangle$, depends on τ because particles move away from their initial distance (toward the center on average, see Fig. 4.17) and thus experience regions of higher average velocity.

In inhomogeneous flows, the Lagrangian and Eulerian averages coincide only for $\tau = 0$. Stationarity of Eulerian statistics implies that Lagrangian statistics depend only on τ and y_0 and not on t_0. Inhomogeneity also implies that Lagrangian statistics for negative values of τ are *a priori* different from those at positive τ. Practically, estimators of Lagrangian statistics are the following. A small interval of width δy around a given initial value of y_0 is chosen. As soon as a trajectory has a value $y(t)$ that belongs to this interval, the initial time t_0 is set. Statistics are then accumulated as a function of τ. This procedure is illustrated in Fig. 4.17 for the average particle position $\langle \vec{r}(\tau, y_0) \rangle$.

An adequate tool to obtain time scales and coupling between components is the Lagrangian correlation coefficient of fluid particle acceleration, defined as

$$\rho_{ij}(\tau, y_0) = \frac{\langle a_i'(t_0, y_0)\, a_j'(t_0 + \tau, y_0) \rangle}{\langle a_i'^2(t_0, y_0) \rangle^{1/2} \langle a_j'^2(t_0 + \tau, y_0) \rangle^{1/2}}, \tag{4.45}$$

where $a_i'(t_0 + \tau, y_0) = a_i(t_0 + \tau, y_0) - \langle a_i(t_0 + \tau, y_0) \rangle$ is the fluid particle acceleration fluctuation relative to the Lagrangian average, with $i = x, y$ or z. The estimators thus correlate the initial acceleration with that at a time lag τ along the trajectory of fluid particles initially at y_0.

Figures 4.18 and 4.19 show various components of the acceleration correlation tensor ρ_{ij} calculated at different initial wall distances y_0^+. Time lags equal to the local Kolmogorov time scale $\tau_\eta(y) = \sqrt{\nu/\epsilon(y)}$ are also represented in the figures, with the local mean turbulent energy dissipation rate estimated from DNS as $\epsilon = \nu \overline{(\partial_j u_i')(\partial_j u_i')}$.

The inhomogeneity of the flow is visible in the fact that the typical decorrelation time varies significantly over the width of the channel. The anisotropy is visible in the fact that the streamwise and wall-normal components display some non zero correlation

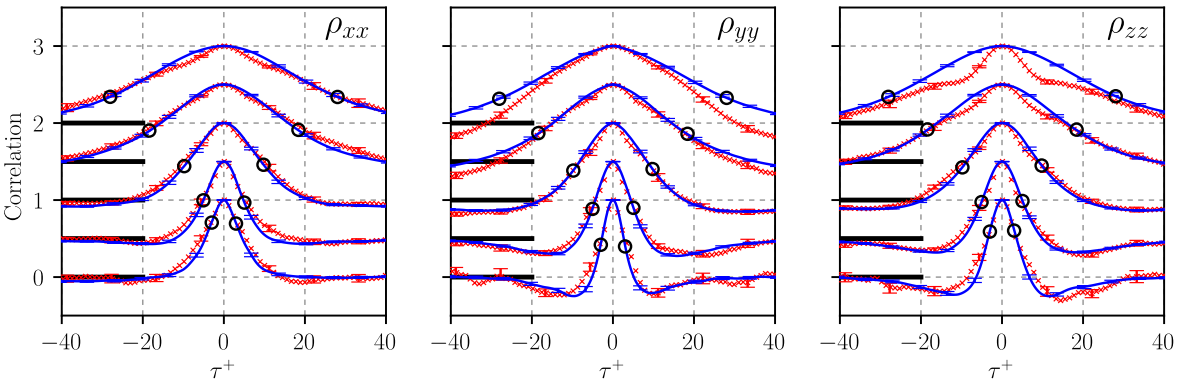

Figure 4.18: From left to right, Lagrangian auto-correlations of streamwise (ρ_{xx}), wall-normal (ρ_{yy}) and spanwise (ρ_{zz}) particle acceleration. Experiments - crosses. DNS - lines. Circles indicate time lags $\tau = \pm\tau_\eta$. Curves are shifted vertically by increments of 0.5 for clarity. From bottom to top, the curves correspond to particles located initially at $y_0^+ = 20$, 60, 200, 600 and 1000. Horizontal black lines show the zero-correlation level for each y_0^+. In the experiment, $\tau^+ = 1$ corresponds to 0.175 milliseconds.

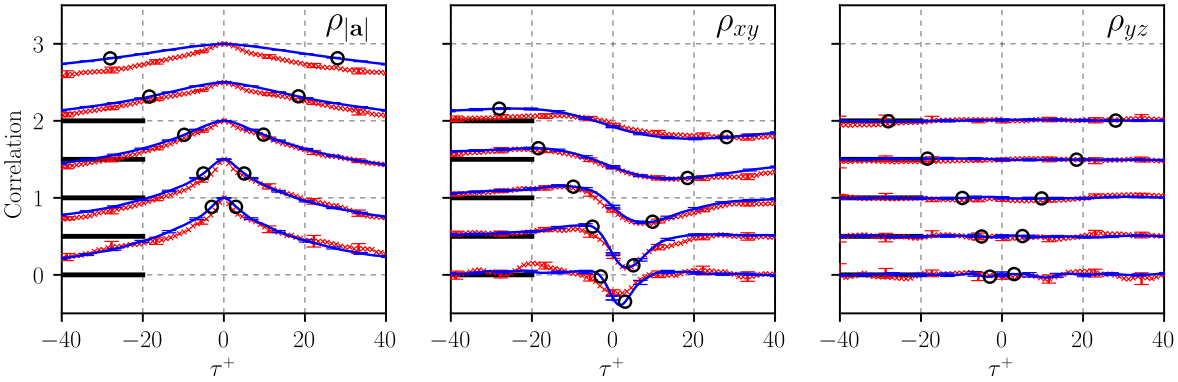

Figure 4.19: From left to right, Lagrangian auto-correlation of acceleration magnitude ($\rho_{|\vec{a}|}$) and acceleration cross-correlations ρ_{xy} and ρ_{yz}. From bottom to top, the curves correspond to particles located initially at $y_0^+ = 20$, 60, 200, 600 and 1000. (For details, see Fig. 4.18.)

(in contrast with HIT), as shown on Fig 4.19(b). Cross-correlations with the transverse component remain zero due to the statistical symmetry $z \leftrightarrow -z$, as shown on Fig. 4.19(c).

In the vicinity of the wall the decorrelation time is close to one in wall units, showing that this is the adequate characteristic time for rescaling of small-scale quantities such as the acceleration in this region. This will be discussed further in the analysis of the characteristic Lagrangian time scales. A very good agreement is observed between experimental and DNS results, with the exception of the long time behavior of ρ_{yy} at $y^+ = 1000$, and the short time behavior of ρ_{zz} at $y^+ = 1000$. While the former remains unexplained, the latter is due to the higher level of noise in the measurement of the z-component, which is a technical consequence of the way the PTV is performed. Namely, near the center of the channel, the signal-to-noise ratio for the z-component of acceleration comes close to the limits of the data processing methods described in Section 4.8 and in previous work [31], and the correlation of noise is seen in the short time behavior of ρ_{zz} at $y^+ = 1000$.

Previous studies in HIT [112, 37] have associated fluid particle acceleration and vortex dynamics by observing that high acceleration events often correspond to centripetal accelerations in vortex filaments, and the auto-correlation of the centripetal component of these accelerations become negative to a much greater degree than the auto-correlation of

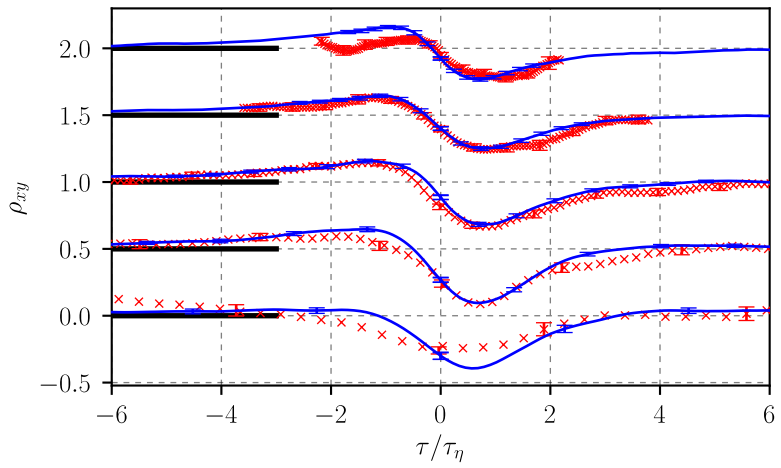

Figure 4.20: Lagrangian correlation between streamwise and wall-normal acceleration components. Time delay τ is normalized with the local Kolmogorov time scale τ_η. From bottom to top, the curves correspond to particles located initially at $y_0^+ = 20$, 60, 200, 600 and 1000. (For details, see Fig. 4.18.)

the component of the acceleration parallel to the vortex filament. Contrary to HIT where there are no preferential directions, in the near-wall region of a wall-bounded turbulent flow the preferential orientation of vortices in the streamwise direction is expected. As shown on Fig. 4.18, near the wall the auto-correlations of a_y and a_z become negative at approximately $\tau = 2\tau_\eta$ (similarly to the case of HIT), while the correlation of a_x remains positive with a significantly longer initial decorrelation time. The negative ρ_{yy} and ρ_{zz} correlations can be associated with the effect of near-wall streamwise vortices. A fluid particle trapped in one such vortex experiences strong centripetal accelerations towards the vortex rotation axis [76]. This strong form of anisotropy of the acceleration is only observed near the walls ($y^+ < 50$) and becomes negligible towards the channel center, as confirmed below by the acceleration time scales associated to these correlations.

The auto-correlations ρ_{xx} and ρ_{yy} are almost symmetric in time, e.g. $\rho_{xx}(-\tau, y_0) \approx \rho_{xx}(\tau, y_0)$. This symmetry can be explained by the nearly time-symmetric average trajectories in the near-wall region as illustrated in Fig. 4.17, i.e. $\langle \vec{r}(\tau, y_0) \rangle \approx \langle \vec{r}(-\tau, y_0) \rangle$. In contrast, the cross-correlation ρ_{xy} is strongly time-asymmetric close to the wall. This asymmetry, along with the non-zero time lag at which the peak is observed, suggests the idea of causality between acceleration components. That is, a streamwise acceleration fluctuation is followed on average by an opposite-sign wall-normal acceleration fluctuation. Towards the channel center, this effect persists and the correlation becomes antisymmetric with time, $\rho_{xy}(-\tau) \approx -\rho_{xy}(\tau)$, due to the decreasing influence of wall confinement.

The correlation between a_x and a_y (Fig. 4.19(b)) is most important near the walls. In that region, the zero-time cross-correlation (equivalent to an Eulerian single-point single-time correlation) is negative due to increased viscous effects combined with confinement by the wall (see the joint PDFs in Section 4.11 for more details). Moreover, the cross-correlation peak is always found at a non-zero time lag. Far from the wall, the correlation is close to zero at $\tau^+ = 0$, while it increases in absolute value for non-zero time lags. The influence of the boundary layer remains visible even in the bulk of the channel where the correlation is still non-zero, indicating that small-scale anisotropy is still present in that region. In Fig. 4.20, the ρ_{xy} cross-correlation is displayed as function of the normalized time lag τ/τ_η. The time lag of the negative correlation peak is shown to scale with τ_η, with a value τ/τ_η fluctuating between 0.5 and 0.7 with the wall distance y_0^+.

The $\rho_{xy}(\tau, y_0)$ correlation describes the changes of orientation of the acceleration

fluctuation vector $\vec{a}'(t_0+\tau, y_0)$ projected on the x-y plane. Its behavior implies that there is a preferential direction of rotation of $\vec{a}'$ along a particle trajectory. Moreover, such changes of orientation happen over times of the order of the Kolmogorov time scale. Thus, this anisotropy is associated with the smallest scales of turbulence, and is observed for all wall distances. The preferential direction of rotation implied by the cross-correlation is consistent with the direction of mean shear, represented by an average vorticity $\overline{\omega}_z = -d\bar{u}/dy$ which is negative in the lower half of the channel, where the presented statistics are obtained. This result is consistent with evidence of small-scale anisotropy found in other turbulent flows governed by large-scale anisotropy. For instance, from DNS of homogeneous shear flow, Pumir and Shraiman [143] found signs of small-scale anisotropy which did not decrease at increasing Reynolds number, in contradiction with Kolmogorov's local isotropy hypothesis [144]. In their work, small-scale anisotropy was quantified by the skewness of the spanwise vorticity ω_z, which was shown to be of the same sign as the large-scale average vorticity. More recently, and using a similar approach, Pumir *et al*[45] showed the presence of small-scale anisotropy from DNS of turbulent channel flow at $Re_\tau \approx 1000$ all along the log-layer. Our results show that such small-scale anisotropy is also observed by the Lagrangian acceleration statistics. Therefore, a stochastic model for the Lagrangian acceleration which includes elements derived from the ρ_{xy} correlation would be able to reproduce the presence of small-scale anisotropy in shear flows.

In Fig. 4.19(a) we plot the auto-correlation of the acceleration magnitude $|\vec{a}|$, showing that this quantity stays correlated for far longer than each acceleration component. This behavior is observed at all wall distances and is consistent with results in HIT [16, 35]. It is explained by the fact that changes in the orientation of the acceleration vector are much more sudden than changes in its magnitude. In near-wall turbulence, this observation is again explained by centripetal acceleration induced by streamwise vortices, which preserve the acceleration magnitude for a longer time than the acceleration orientation [76].

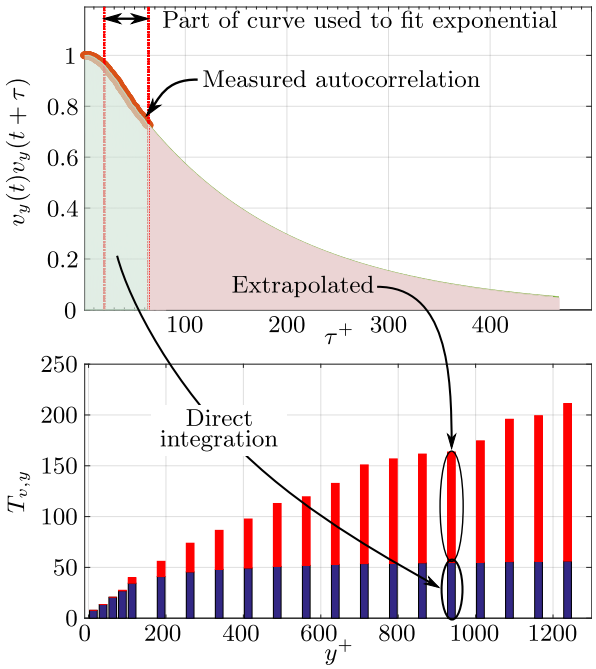

Figure 4.21: An example of how Lagrangian velocity time scales are calculated. The auto-correlation of the wall-normal component of velocity from $y^+ = 925$ is shown (top plot) in red, where the part of the measured auto-correlation used to fit the exponential extrapolation is also shown. The bottom plot shows the Lagrangian wall-normal velocity time scale across the channel, where the portion of the time scale that is directly measured is shown in blue and the portion of the time scale that comes from the extrapolation is shown in red.

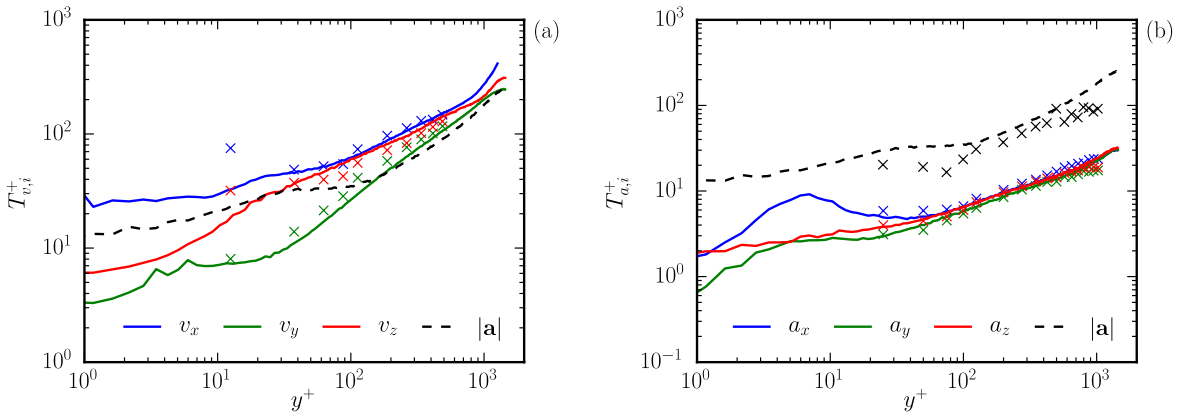

Figure 4.22: Lagrangian velocity and acceleration time scales in wall units. Experiments - crosses. DNS - solid lines. The acceleration magnitude time scale $T_{|\vec{a}|}$ is represented by dashed lines.

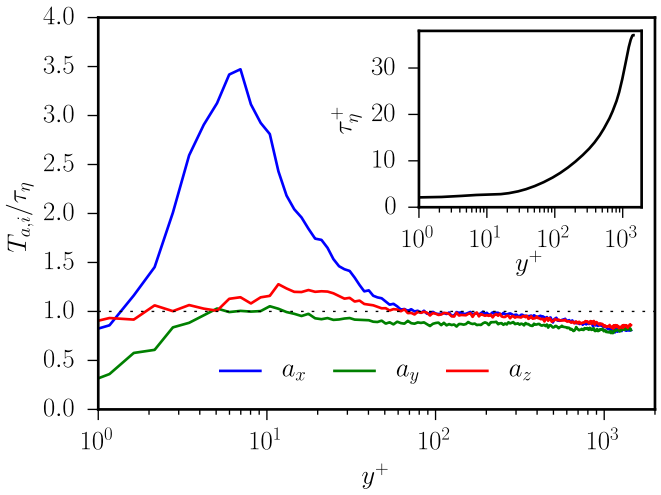

Figure 4.23: Lagrangian acceleration time scales normalized by the local Kolmogorov time scale (DNS results only). Inset: local Kolmogorov time scale in wall units.

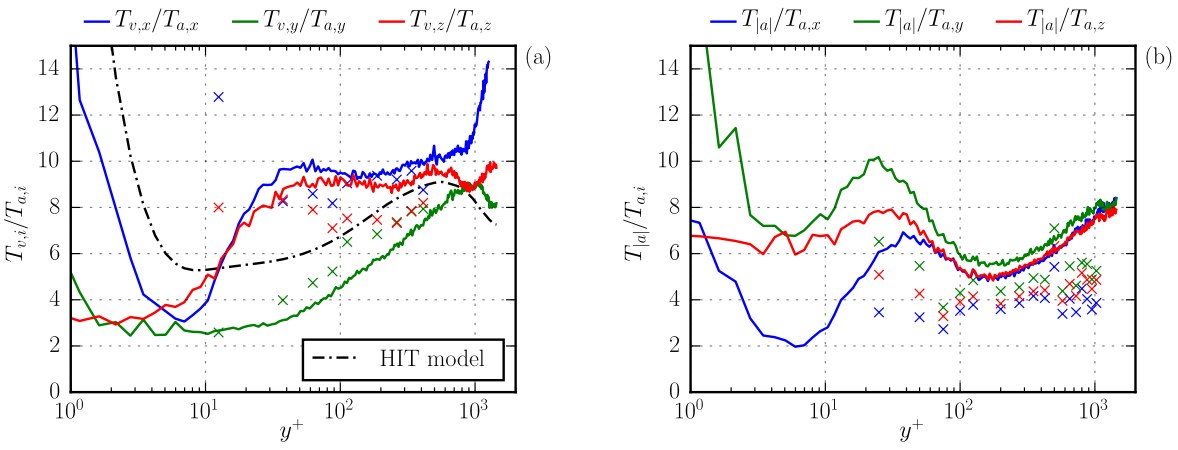

Figure 4.24: Lagrangian time scale ratios. Experiments - crosses. DNS - solid lines. (a) Ratio between the Lagrangian velocity and acceleration time scales, by component. Also shown is the HIT model [38] for the ratio of Lagrangian velocity and acceleration time scales. (b) Ratio between the time scales of acceleration magnitude and the components of acceleration.

4.10 Lagrangian time scales

The characteristic time scale associated to each acceleration component is estimated according to

$$\mathrm{T}_{a,i}(y_0) = \int_0^{\tau_c} \rho_{ii}(\tau, y_0)\,\mathrm{d}\tau, \tag{4.46}$$

where τ_c is the time lag at which the auto-correlation first crosses 0.05. This definition is chosen because the classical definition with the integration going to infinite time cannot be applied to all acceleration components since some correlations become negative. This is also the case for HIT for which the integral of the acceleration correlations is actually zero because of the stationarity of the velocity. The usual zero-crossing time as in [16] can neither be used here because some correlations (near the center of the channel) do not cross zero during the observation time. Our definition is a convenient mix between these two usual definitions of the typical time scale.

Lagrangian velocity (integral) time scales $\mathrm{T}_{v,i}$, as well as the acceleration norm time scale $\mathrm{T}_{|\vec{a}|}$, are defined equivalently. Due to the limited measurement volume in the experiment, the full decorrelation of the auto-correlations of velocity and the norm of the acceleration is not achieved at all wall distances in the channel. These auto-correlations have been extrapolated as illustrated by Fig. 4.21, and the uncertainty of these results increases with increased extrapolation. This extrapolation is not necessary for the acceleration auto-correlations shown in Fig. 4.18 (which decay much faster) and thus for the computation of the time scales $\mathrm{T}_{a,i}$.

The evolution of all time scales with wall distance is shown in Fig. 4.22. As can be deduced from the auto-correlation curves, the acceleration time scales $\mathrm{T}_{a,i}$ and $\mathrm{T}_{|\vec{a}|}$ generally increase with wall distance. The same is observed for the Lagrangian velocity time scales. The acceleration norm time scale $\mathrm{T}_{|\vec{a}|}$ is about one order of magnitude larger than the time scale of the acceleration components. It is of the order of the integral time scales $\mathrm{T}_{v,i}$.

In Fig. 4.23, the Lagrangian acceleration time scales are normalized with the local Kolmogorov time scale. Both ϵ and τ_η vary with wall distance. The acceleration time scales are of the order of τ_η all along the channel. The normalized time scales only weakly change for $y^+ > 80$, reaching a value between 0.8 and 0.9 in the bulk of the channel. However, in that region, small differences persist between $\mathrm{T}_{a,y}$ and the time scales obtained for the other two components, suggesting once more that anisotropy is still present far from the wall. Close to the wall ($y^+ \lesssim 40$), the longer correlation time of the streamwise acceleration is reflected in a larger time scale $\mathrm{T}_{a,x}$ compared to the other components.

Fig. 4.24(a) shows the ratio of Lagrangian time scales of velocity and acceleration for each component. Also shown in Fig. 4.24(a) is eq. (4.44), the empirical fit to the DNS data of Yeung and Pope [16] proposed1 by Sawford [38], using the profile of Re_λ calculated from the DNS and $\mathrm{C}_0 = 7$ as suggested by Sawford. The HIT model follows the trend of the data. However there is significant anisotropy in these ratio of time scales that extends far away from the wall. First-order Lagrangian stochastic models in velocity such as given by eq. (4.42) are based implicitly on the scale separation between the velocity and the acceleration time scales. Here, a small separation is seen between these two time scales near the wall. Significantly, the time scale ratio for the wall-normal component (y) is approximately half of that predicted by the local Reynolds number (the HIT model plotted in the figure) near the wall. Even farther from the wall, this time scale ratio is significantly over-predicted by the HIT model.

The long time scales of the acceleration norm previously reported have inspired the development of a Lagrangian subgrid stochastic model that models the acceleration norm

and acceleration direction as two independent stochastic processes [72, 3]. Fig. 4.24(b) shows that the ratio of Lagrangian time scales of acceleration norm to acceleration components are only weakly varying for $y^+ > 50$ and comparable in magnitude to the ratios of Lagrangian velocity and acceleration time scales. 1

4.11 Distributions

Fig. 4.25 shows the probability distribution function (PDF) of the three acceleration components obtained at different wall distances. All curves present very long tails corresponding to extremely high acceleration events associated to intermittency [68]. Once again, good agreement is achieved between the experiments and the DNS. The acceleration PDFs are also compared with the functional shape proposed by [35] for HIT, which assumes that the acceleration magnitude follows a log-normal probability distribution and that the acceleration vector is isotropic. According to those assumptions, the PDF of an acceleration component is given by

$$\mathrm{P}(a_i) = \frac{e^{s^2/2}}{4m}\left[1 - \mathrm{erf}\left(\frac{\ln\frac{|a_i|}{m} + s^2}{\sqrt{2}s}\right)\right], \tag{4.47}$$

where m determines the variance of a_i ($m = \sqrt{3/e^{2s^2}}$ for variance 1), while s determines the shape of the PDF. A value $s = 1$ is used in the comparisons. Towards the channel center, the PDFs of the three acceleration components match this prediction, suggesting that the instantaneous behavior of acceleration becomes close to isotropic. More strikingly, the spanwise acceleration seems to match the prediction very close to the wall, suggesting that this component is not affected by anisotropy as in the other two directions. The general agreement with the shape of the HIT PDF suggests that intermittency is extremely strong in the boundary layer although the Reynolds number is moderate: $Re_\lambda \sim 60$ to 100 in our flow whereas it was close to 1000 in [35]. It implies also that this shape of the PDF presents some universality.

The PDFs of the streamwise and wall-normal acceleration components become quite asymmetric near the wall. This asymmetry is quantified by their skewness $\mathrm{S}_i = \langle a_i'^3\rangle / \langle a_i'^2\rangle^{3/2}$ shown in Fig. 4.26. Due to flow symmetry, the skewness of a_z is zero. Very close to the wall, S_x and S_y are strongly negative and positive, respectively, indicating that their PDFs are very asymmetric due to wall-induced anisotropy. The signs of S_x and S_y are both inverted after $y^+ \approx 20$. Their respective values remain different from zero and change little for $y^+ > 80$. This reinforces the idea that turbulence anisotropy is still present in the channel center.

The dependency between the acceleration components is analyzed by the joint PDF, $\mathrm{P}(a_x, a_y)$. Fig. 4.27 shows the results obtained at two wall distances, $y^+ = 15$ and 59. Close to the wall (Fig. 4.27a), the joint PDF has a stretched shape, showing a preference for events given by $a_x < 0$ and $a_y > 0$. These events can be associated to fluid particles advected towards the wall. These particles move towards regions of decreasing mean streamwise velocity, leading on average to a streamwise deceleration of their motion ($a_x < 0$). Simultaneously, their negative wall-normal velocity goes to zero due to confinement by the wall, resulting in a positive wall-normal acceleration ($a_y > 0$). This dependency between both acceleration components is confirmed by the conditional means $\langle a_x | a_y \rangle$ and $\langle a_y | a_x \rangle$, which are superposed to the joint PDF contours. Particles advected away from the wall are less affected by wall confinement, and thus the impact on their wall-normal acceleration is less visible in the joint PDF. Nonetheless, on average, those particles also

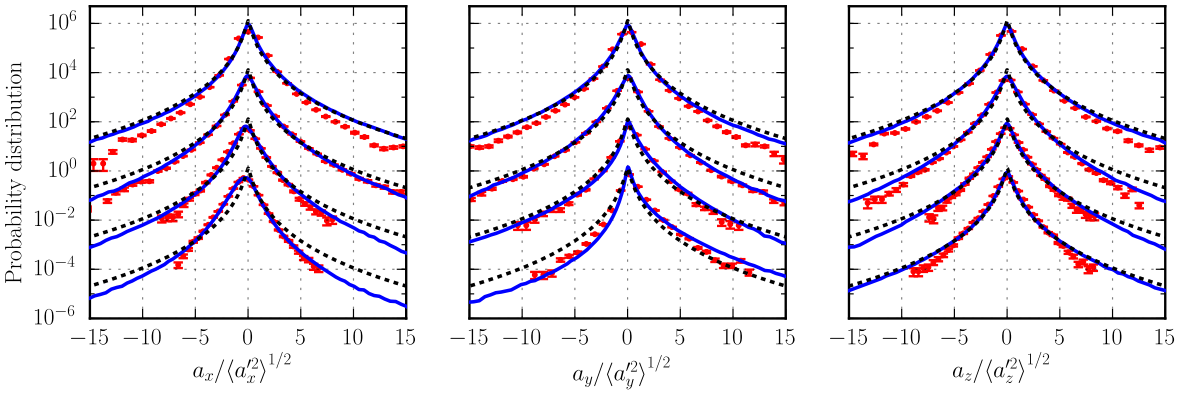

Figure 4.25: PDF of streamwise, wall-normal and spanwise particle acceleration. Experiments - symbols with error bars. DNS - lines. The dashed lines represent the theoretical prediction for the acceleration PDF in HIT [35]. The PDFs are normalized by the root-mean-square value of acceleration. From bottom to top, the curves correspond to particles located at $y^+ = 10$, 20, 200 and 1200. The statistical convergence of the experimental data is shown by error bars equal to $1/\sqrt{n_i}$ where n_i is the number of events in bin i.

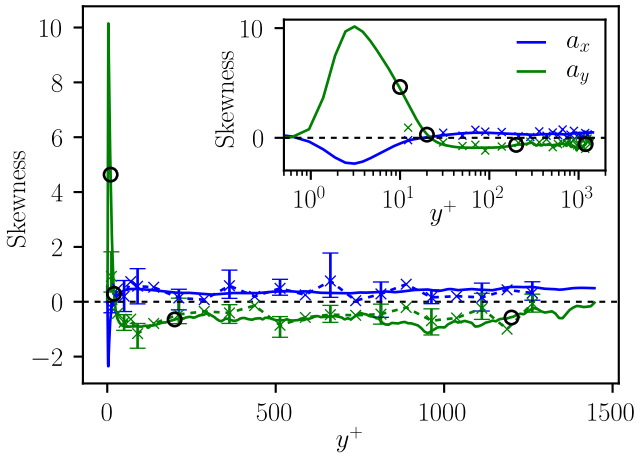

Figure 4.26: Skewness of streamwise and wall-normal acceleration components. Experiments - crosses. DNS - lines. Circles indicate skewness of a_y at $y^+ = 10$, 20, 200 and 1200. Inset: skewness profiles with y^+ in logarithmic scale.

experience the effect of the mean velocity gradient, which results in this case in a positive streamwise acceleration.

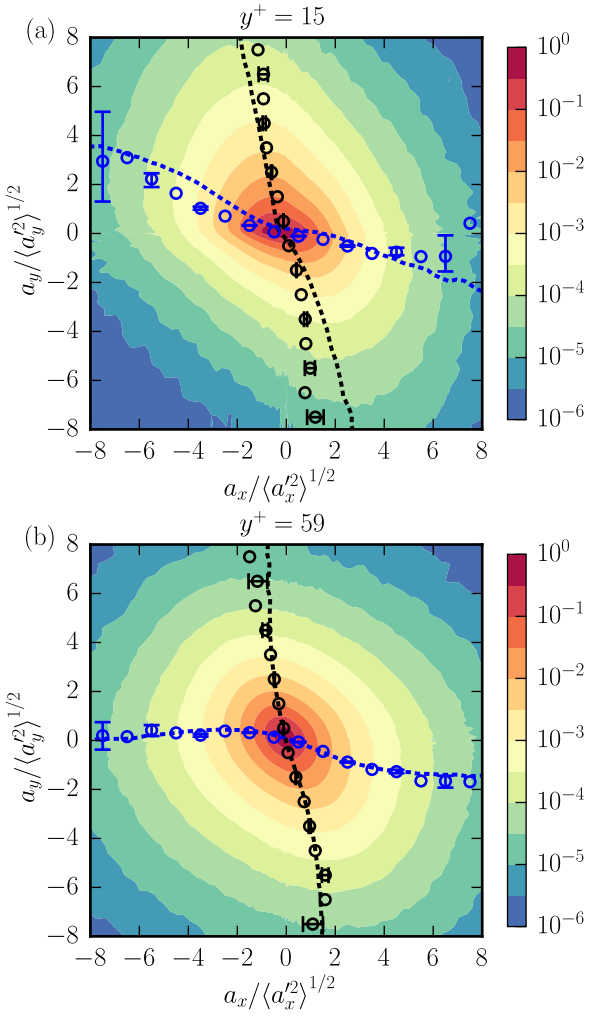

Figure 4.27: Joint PDF of streamwise and wall-normal acceleration at $y^+ = 15$ and 59. Conditional means $\langle a_x|a_y\rangle/\langle a_x'^2\rangle^{1/2}$ and $\langle a_y|a_x\rangle/\langle a_y'^2\rangle^{1/2}$ are superposed to the contours using black and blue markers, respectively. Experiments - circles. DNS - dashed lines.

4.12 Concluding remarks

By performing both DNS and experiments, the highly anisotropic turbulent flow in the vicinity of channel walls is described in terms of Lagrangian statistics. Near-wall vortical structures are clearly identified by their influence on the acceleration auto-correlations. Viscous effects and wall-confinement have also a strong impact on acceleration statistics as evidenced by the joint PDFs. Less expectedly, signs of small-scale anisotropy are present across the channel. The observed behavior of the Lagrangian time scales can be a basis for the formulation of Lagrangian stochastic models of acceleration applied to wall-bounded turbulent flows. These models must also take into account the dependency among acceleration components, which is apparent in the presented cross-correlations and joint PDFs of acceleration. Acceleration models based on the presented results should be able to capture the effects of (i) the near-wall dynamics associated with confinement and coherent structures and (ii) the small-scale anisotropy present in the whole channel.

This work is supported by Agence Nationale de la Recherche (grant #ANR-13-BS09-0009) and by the LabEx Tec 21 (Investissements d'Avenir grant #ANR-11-LABX-0030). Simulations have been performed on the P2CHPD cluster. J.I.P. is grateful to CONICYT Becas Chile grant No. 72160511 for supporting his work. NM is supported by Institut

Universitaire de France. We thank Laboratoire de Physique at ENS de Lyon and CNRS for providing one of the high speed cameras. We thank M. Kusulja for the design of the water tunnel, J. Virone and V. Govart for technical assistance.

Chapter 5

Lagrangian statistics of non-tracer particles in the turbulent channel

One goes in straightforward ways,
One in a circle roams:
Waits for a girl of his gone days,
Or for returning home.

But I do go – and woe is there –
By a way nor straight, nor broad,
But into never and nowhere,
Like trains – off the railroad.

My way, *Anna Akhmatova*

Contents

5.1 Introduction

The dynamics of particles in turbulent flow is of considerable interest in a range of applications, from rain formation in clouds to deposition of sediment on the walls of pipes. Previous chapters considered the case in which particles were small enough, and of similar density to the fluid, such that they could be considered proxies for fluid particles, i. e. tracer particles. This chapter is concerned with non-tracer particles: particles that have sufficiently different density from the fluid and/or are sufficiently larger than the smallest scales of fluid motion such that their dynamics no longer closely follow the dynamics of the fluid.

Multi-phase systems of fluid turbulence and non-tracer particles are typically characterized by four parameters, in addition to those used to characterize the fluid turbulence (e. g. Re):

1. **Stokes number:** The ratio between the particle response time t_p and the Kolmogorov time scale t_η, $\mathrm{S}t \equiv t_p / t_\eta$
2. **Length scale ratio:** The ratio between the particle diameter D_p and the Kolmogorov length scale η
3. **Characterization of the role of gravity, e. g. Froude number:**[1] a_η / g
4. **Particle diameter distribution:** The distribution F of D_p.
5. **Particle volume fraction ϕ:** The ratio between the volume the fluid and the volume occupied by the particles

The first four parameters concern the dynamics of individual particles, while the fifth indicates to what extent collective effects, particle collisions, and the effects of the particles on the turbulence are important. The results presented in this chapter come from the regime in which the particles are all of the same diameter, and the particle volume fraction is sufficiently small such that the dynamics of a multi-particle system is equivalent to the dynamics of a single particle.

Non-tracer particles by definition do not faithfully follow the flow, i. e. non-tracer fluid particle trajectories located at $\mathbf{x_0}$ at time t_0 will diverge from fluid particle trajectories located located at $\mathbf{x_0}$ at time t_0. An equation for this divergence for small particles[2] was rigorously derived by Maxey and Riley[145], and contemporaneously by Gatignol[146]. While exact, this equation is complex, and it is common to simplify it to the leading order term: drag force proportional to the Stokes number (see e. g. Balkovsky *et al*[147]). This simplification, commonly used in DNS of particles in turbulence, is valid for in the limit of point-particles ($\mathrm{D}_p \to 0$); for larger particles the sub-dominant terms of the Maxey-Riley-Gatignol equation are increasingly important. For even larger particles the assumptions of this equation are no longer met[148], and the particle diameter is of similar extent to the smallest spatial gradients in the turbulence.

Non-tracer particle divergence from the fluid particle trajectory affects the particle statistics in a complex manner. Three mechanisms are commonly encountered in the literature, and are summarized here.

[1] Properly speaking this a characteristic of the fluid phase, and not related to the particle phase. In order to characterize the role of gravity in particle dynamics this Froude number should be combined with the density ratio of the particle, or $\mathrm{S}t/\mathrm{F}r$ as in Mathai *et al*[83].

[2] Small is more precisely defined as the limit of $\mathrm{R}e_p \ll 1$, where $\mathrm{R}e_p$ is the particle Reynolds number.

1. **Biased sampling:** Biased sampling occurs when the non-tracer particle trajectories sample the flow field in a manner systematically different from that of the tracer particles. A simple example of biased sampling was described by Maxey[149] as the centrifugal expulsion of small, heavy particles from vortices. As these heavy particles are preferentially found in low-vorticity regions of the turbulence, statistics such as the variance of particle acceleration are biased. Indeed, Bec *et al* studied inertial particles in DNS and found that even for particles with quite low Stokes numbers, i. e. particles with very little divergence from fluid particle trajectories, the acceleration variance was significantly lower that the fluid acceleration variance due to the bias sampling effect. Many experimental results (see e.g. Aliseda *et al*[150]) have observed heavy particle clustering in HIT, which is a result of this preferential concentration.

2. **Temporal filtering:** Temporal filtering is conceptually simple: the particle response time acts as a low-pass filter which attenuates the high frequency perturbations of particle motion. This filtering was considered by Ayyalasomayajula *et al*[92] in the context of a simple sinusoidal forcing example, in which case the filtering is only dependent on the forcing frequency. Salazar and Collins[93] performed DNS with small inertial particles to determined the relative effects of biased sampling and temporal filtering, and found the impact of the temporal filtering on acceleration statistics increasingly important for larger Stokes numbers. For both acceleration pdf's and autocorrelations of acceleration, bias sampling is responsible for most of the difference between inertial particles and tracer particles for Stokes numbers up to 0.5.

3. **Spatial filtering:** Sufficiently large particles are subject to forcing that varies over the surface of the particle. In this way the particle may be thought of as a spatial filter that integrates small scale forcing over its surface. This filtering is discussed in the context of the Faxén correction to the point-particle equation by Calzavarini *et al*[151], and in the context of the development of an exact equation for larger particles in turbulence by Loth and Dorgan[148]. A simpler treatment was first given by Voth *et al*[30], in which the acceleration variance of a neutrally-buoyant particle was affected only by flow structures larger than the particle, i. e. the particle diameter acted as a spatial filter cut-off length. Kolmogorov scaling then predicts $\langle a_p^2 \rangle \sim \mathrm{D}_p^{-2/3}$ where a_p is the particle acceleration and D_p is the particle diameter.

Although there has been a large amount of work published regarding the dynamics of particles in turbulence, it is only relatively recently that technological advances have allowed experimental measurements that fully resolve particle acceleration. Similarly, while some truncated version of the Maxey-Riley-Gatignol may be used to model small particles in DNS, fully resolved "real" particles in DNS has proved to be quite expensive, an only feasible with recently available computing resources. What follows is a very brief review of these recent studies, particularly focused on the measurement of acceleration and other Lagrangian statistics for particles similar to those used in the present study: heavy particles and large, neutrally-buoyant particles.

5.1.1 Heavy particles

Particularly relevant to this study are results reported by Gerashchenko *et al*[73] regarding Lagrangian acceleration statistics in a turbulent boundary layer. Poly-dispersed water droplets were measured using a two-component particle tracking system in a wind tunnel.

Some of these droplets were of similar Stokes numbers and diameters to those in the present study, but although the use of air as the carrier fluid results in density ratios much larger and length scale ratios that are much smaller. These particles were sufficiently small to be considered "point-like", with negligible finite-size effects. The wall-normal component of the mean acceleration was found to be of much lesser magnitude than that of the streamwise component, which was explained by the gravitational effects acting with the high density ratio. Similarly, the acceleration rms was observed to be much greater in the streamwise direction than in the wall-normal direction, the reason for which remains unclear. Further, the acceleration rms was shown to be higher for particles with larger Stokes number, contrary to the results from HIT. Following this work Lavezzo *et al*[152] performed channel flow DNS with goal of elucidating the results presented by Gerashchenko *et al.* The DNS was able to reproduce the results of the experiment, and when the effect of gravity is removed from the DNS the streamwise rms of acceleration was found to decrease significantly. Gerashchenko *et al*[73] use an alternative definition of the Froude number: $\mathrm{F}r = g\mathrm{S}t/a_{rms}$ (greater values indicate a larger role of gravity in the dynamics), and reports particle Froude numbers of $\mathrm{F}r \approx 0.75-1$. Using a similar definition, the particle Froude numbers of the heavy particles tested in the presents study are $\mathrm{F}r \approx 0.2-0.27$

Volk *et al*[153] experimentally measured acceleration statistics of moderately heavy particles ($\rho_p/\rho_f = 1.4$, $\mathrm{S}t = 0.58$) in HIT, and made comparisons with DNS results for point-particles. The authors found that even though the numerical simulations were qualitatively able to reproduce the experimental results there were quantitative differences, which were attributed to the the finite size of the particles in the experiment (1.2η). Specifically, the experiments showed higher thicker tails on the pdf of acceleration than the numerics, and the experimentally measured autocorrelation of acceleration showed a more rapid decorrelation than in the numerics. Even the normalized acceleration variance a_0 was 67% of the tracer value in the experiment, but 92% of the tracer value in the numerics.

Xu and Bodenschatz[154] similarly measured heavy particle ($\rho_p/\rho_f = 1.4$) acceleration in HIT for particles slightly larger than the Kolmogorov length ($\mathrm{D}_p/\eta \approx 3$). The normalized PDFs of acceleration and the normalized autocorrelation of acceleration show very little difference between the heavy particles and the tracer particles.

A large particle parameter space was explored by Qureshi *et al*[155] by using soap bubbles as particles in HIT in a wind tunnel . By tuning the bubble-making apparatus a large range of particles could be tested, from neutral-buoyant particles to particles 40 times heavier than air, and diameters from $\mathrm{D}_p/\eta = 12-25$. The normalized PDF of acceleration changed very little through out this parameter space, although the acceleration variance had a complex response to changing particle parameters.

Fully resolved heavy particles ($\rho_p/\rho_f \approx 2.2$) were simulated in turbulent channel flow DNS by Ulhmann and coworkers[156, 157]. Particles had diameters of 11 wall-units, which is twice that of the present study ($\mathrm{D}_p = 5.5$ wall-units). [3] Another important difference is the DNS domain was oriented vertically, such that gravity was parallel to the streamwise direction (in the present study gravity is parallel to the wall-normal direction). Particle acceleration mean and rms profiles are shown to quantitatively similar to those found by Gerashchenko *et al*[73], despite the differences in experimental parameters between the two studies. Acceleration rms profiles in the DNS are shown to be approximately 50% greater in the streamwise component than in the wall-normal component. Autocorrela-

[3] Although in the DNS the Reynolds number was much lower ($\mathrm{R}e_\tau = 221$) than in the present study ($\mathrm{R}e_\tau = 1440$), and so the particle in the DNS are much larger *relative to the channel width* than is the case in the present study.

tions of the particle accelerations also show a difference in components: the autocorrelation of the streamwise component of acceleration has a zero-crossing time approximately twice that of the wall-normal and spanwise components.

5.1.2 Large neutrally-buoyant particles

Particles larger than the Kolmogorov length scale of the turbulence and of similar density to the fluid present difficulties to understanding both theoretical: the Maxey-Riley-Gatignol equation is no longer applicable, and conceptual: the behavior of neutrally buoyant particles in vortices is much less intuitively clear than the simple model of heavy particles being ejected from vortices by the centrifugal force.

Voth *et al*[30]measured large neutrally buoyant particles in HIT, in the context of determining at what size neutrally buoyant particle may be considered tracer particles. Volk *et al*[153], and Xu *et al*[154] measured large neutrally-buoyant Lagrangian statistics in HIT for a single particle diameter, and compared the results to the results for heavy particles. These authors present different findings for the autocorrelation acceleration, with Xu *et al* reporting that the large neutrally buoyant particles ($D_p/\eta \approx 5$, $St = 1.5$) and the tracer particles have very similar acceleration autocorrelation curves, while Volk *et al* report a non-negligible difference in the autocorrelation of acceleration between the large neutrally buoyant particles ($D_p/\eta \approx 15$, $St = 10.7$) [4] and the tracer particles. Qureshi *et al*[84] and Brown *et al*[4] measured acceleration variance in HIT for several diameters of large neutrally buoyant particles. Figure 5.1 (reproduced from Brown *et al*[4]) assembles the normalized acceleration variance measurements from three sets of experimental measurements. Acceleration variance is constant for $D_p < 5$; for larger particle diameters the acceleration variance decreases in a manner consistant with the scaling proposed by Voth: $a_0 \sim (D_p/\eta)^{-2/3}$.

A more recent study by Volk *et al*[90] explored a large range of particle diameters ($D_p/\eta = 1-45$) in HIT. Previous acceleration variance results were largely confirmed. Acceleration autocorrelations were measured, and used to calculate particle acceleration time scales. Particles of diameter $D_p/\eta \approx 7$ are reported to have acceleration time scales of approximately 1.3 times that of the tracer particles; larger particles have time scales that increase linearly with their diameter ratio D_p/η.

Until the present study there has been no reported acceleration measurements of large neutrally-buoyant particles in inhomogeneous turbulence.

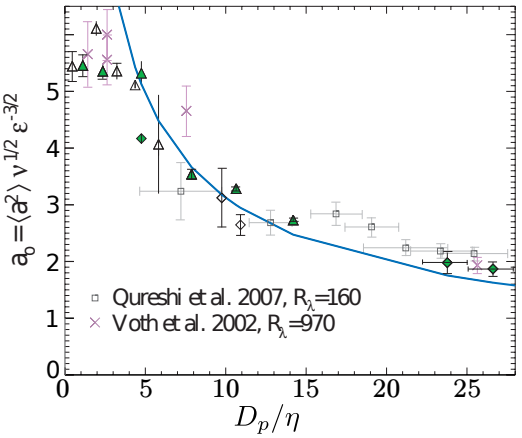

Figure 5.1: Normalized variance of acceleration of large neutrally-buoyant particles in HIT plotted against particle diameter normalized by the Kolmogorov length scale from three datasets: that of Voth *et al*[30] (crosses), that of Qureshi *et al*[84] (squares), and that of Brown *et al*[4](Triangles and diamonds). Figure reproduced from Brown *et al*[4].

[4]Volk *et al* reported a Stokes number of 16, but used and different definition of the Stokes number. $St = 10.7$ corresponds to the definition used by Xu *et al* so a direct comparison may be made.

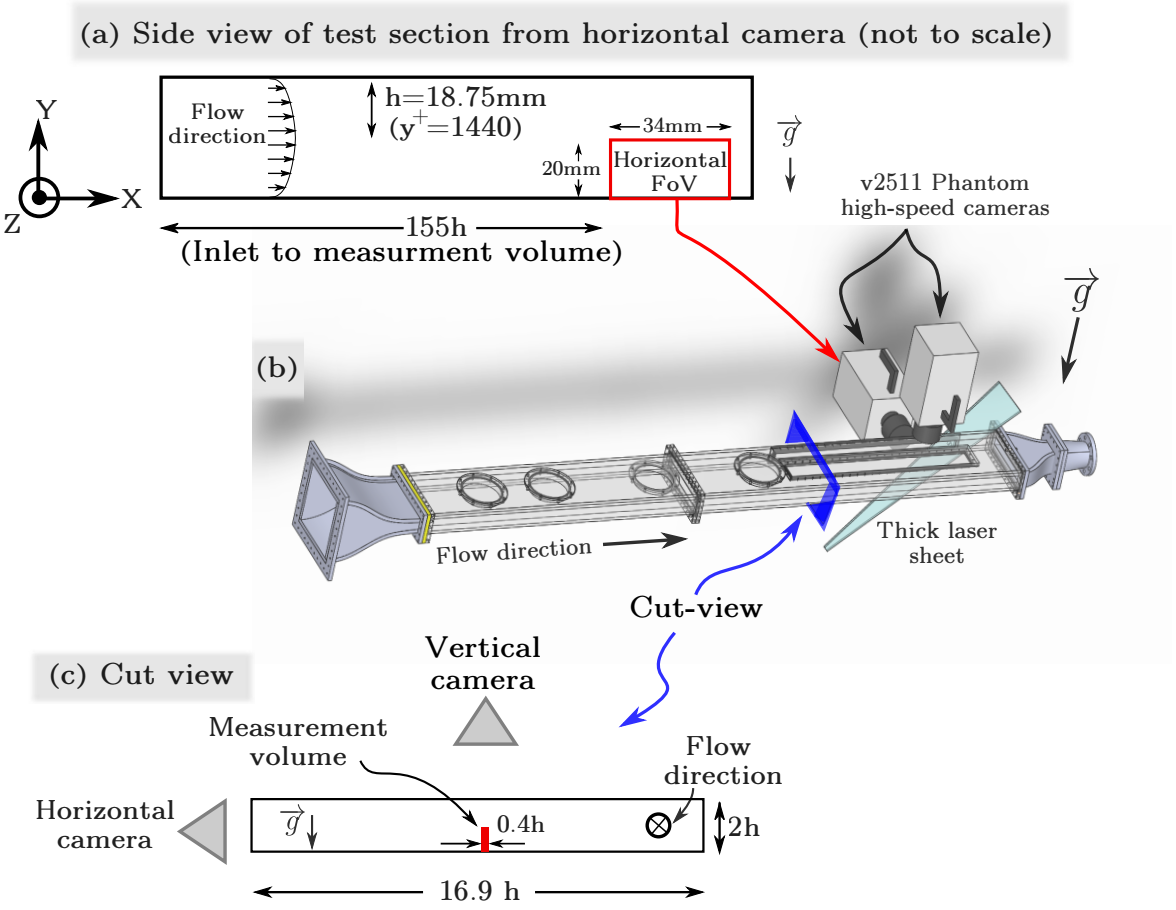

Figure 5.2: Schematic of the experimental setup used for the measurements of the heavy and large neutrally-buoyant particles reported in this chapter. **(a):** Schematic of the side view of the channel, from the viewpoint of the horizontal camera, including the field of view (FoV). **(b):** 3-D solid model of the channel, with the two high-speed cameras and thick laser sheet shown. **(c):** Schematic of the cut view (or end view) of the channel, with the measurement volume shown in red. The principal difference between this experimental configuration and the configuration used for the tracer particle measurements (figure 2.2) is the orientation of the channel (where gravity is now parallel to the wall-normal direction) and the orientation of the laser sheet (now oriented such that there is forward scattered light available to the vertical camera).

5.2 Experimental methods

The experimental methods described in chapter 2 were developed for Lagrangian measurements of tracer particles. The measurement of non-tracer particles, especially heavy particles, required some modifications to the experimental setup and data processing methods. This section explains the modifications to the experimental methods that were used in the measurement of the non-tracer particles; the experimental methods used for these measurements were the same as those described in chapter 2 unless explicitly noted here.

5.2.1 Changes in the experimental setup

Test section orientation

The principal change to the experimental setup is the rotation by 90 degrees of the channel test section, such that gravity is parallel to the wall-normal vector, and the transverse coordinate(z) is now horizontal. This arrangement is shown schematically in figure 5.2. The motivation for the change in orientation of the test section was practical: the settling velocity of the heavy particles was such that it was unclear if, had the test section remained in its previous orientation (gravity aligned with the transverse direction, see figure 2.2) the particles would have remained suspended in the test section. It is important to note that gravity has a complex role in the dynamics of heavy particles in the boundary layer[5], and that the choice made here to have the wall-normal direction aligned with gravity results in a system in which dynamics due to inertia and dynamics due to gravity are difficult to separate. A different choice, for example a channel in which the streamwise direction is aligned with gravity, would have also avoided the problem of particle settling.[6] Apart from the settling of particles in the test section, a large amount of settling was observed in other locations in the closed loop water tunnel , especially in the tranquilization chamber (shown in figure 2.3). After restarting the water tunnel from rest, the number of suspended particles climbed slowly, eventually reaching a quasi-steady state after approximately 30 minutes. This rate of resuspension is clearly highly dependent on the specific geometry of the water tunnel components, but it appears that the heavy particles used in this study were near the upper limit of size/density ratio for this water tunnel configuration. Tests with larger/heavier particles would have required either changing the the water tunnel geometry to encourage the resuspension of particles or a system for seeding the flow continuously during the measurements.

Laser sheet orientation

The other principle modification of the experimental setup is the orientation of the thick laser sheet. In the configuration used for the tracer particles illustrated in figure 2.2 the laser sheet is pointed away from the $x-z$ (horizontal) camera; in this configuration the laser sheet is pointed towards the $x-z$ (vertical in this new configuration) camera. This change was found to be necessary in order to have sufficiently illuminated images for the heavy particle measurements. The heavy particles are not fluorescent, and so scatter the laser light directly, and the optical filters used in the fluorescent particle measurements could not be used. Somewhat surprisingly, the non-filtered, non-fluorescent particles produced fainter images, and so the laser direction was changed in order to have the much more efficient forward scattered light available to the $x-z$ vertical camera.

De-gasification

The primary motivation to use fluorescent particles in conjunction with optical filters on the camera lenses is to be sure that only the fluorescent particles appear in the acquired images. Specifically, other particles that may be in the water, such as dust particles or micro-bubbles, are filtered from the image. This concern is not typically important in PIV applications, which often consider micro-bubbles and dust particles to be adequate flow

[5] See the work of Lavezzo *et al*[152] for a discussion of the role of gravity in this context.

[6] A vertical channel was not practically feasible for the present study, although it would certainly be helpful in elucidating the behavior of inertial particles in the boundary layer.

tracers. However, the dynamics of micro-bubbles especially are known to have significantly different dynamics that inertial particles[153], and it is therefore important to ensure that there is minimal contamination of the flow by micro-bubbles when acquiring PTV images without fluorescent particles and optical filters. This goal is quite challenging to achieve, and ideally requires a system designed for de-gasification. Lacking such a system, the following strategy was followed to minimize contamination of the measurements by micro-bubbles.

- **De-gasification:** The water in the tunnel (600L) was drained into a reservoir and heated to approximately 60 °C[7] and maintained at that temperature for several hours while being stirred. The water was then allowed to cool to a temperature cool enough to refill the water tunnel without deforming the acrylic test section (approximately 30 °C). The tunnel was refilled with a minimal agitation of the water.

- **Over-filling:** The water tunnel was designed to operate with a partially-full chamber between the downstream of the pump and upstream of the test-section (component (b) in figure 2.3) which then absorbs any variations in pressure in the system, for example when starting and stopping the pump.[8] This chamber was deliberately over-filled such that the system as a whole operating at a higher pressure. This eliminated any air infiltrations during water tunnel operation, as well as eliminating an air/water interface in the reservoir, therefore slowing the reabsorption of air by the water.

- **Repetition:** Despite the measures described above the system is not perfectly sealed from the external atmosphere, and the water slowly reabsorbs air over time. Furthermore, the low-pressure zones in the pump tend to transform any dissolved gases in the water into micro-bubbles. The de-gasification needed to be repeated regularly in order ensure a minimal number of micro-bubbles in the system.

Finally, the measurement volume was placed on the bottom wall (illustrated in figure 5.2 (c)) to increase the number of heavy particles—which tend to sink into the measurement volume—but also to decrease the number of bubbles, which tend to rise out of the measurement volume. This geometry effectively eliminates larger bubbles in the measurement volume and presumably decreases the concentration of micro-bubbles in the measurement volume, especially near the wall. This strategy was tested by collecting PTV videos before the addition of particles to system, and was found to be effective in eliminating micro-bubbles that could be mistaken for heavy particles.

5.2.2 Particles

The results presented in this thesis are from three classes of particles: tracer particles, large neutrally-buoyant particles, and moderately sized heavy particles. These particles are characterized by their distributions of density and diameter, which determine how the particles interact with a turbulent flow. The concentration of the particles is neglected as a significant factor of their behavior as particle concentrations are very low. The volume fraction of particles in this study never exceded $\Phi \approx 10^{-6}$, which is considered to be within

[7] This temperature was chosen simply because of the thermal resistance of the available reservoir; ideally the water would reach 100 °C

[8] This overfilling was only possible thanks to a variable pump controller which allowed the *gradual* operation of the pump, which would have otherwise broken the test section due the pressure surge.

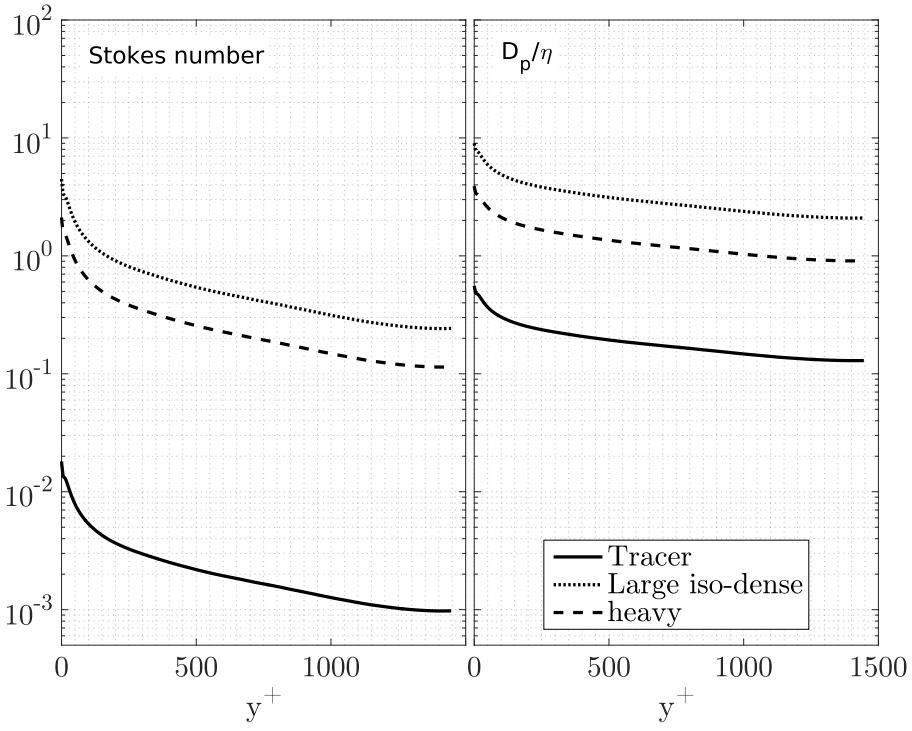

Figure 5.3: Stokes numbers and length scale ratios (based on particle diameter and Kolmogorov length scales) across the channel for the three classes of particle. Terms are defined in table 5.1.

the one-way coupling regime (i.e. the particles have a negligible effect on the turbulence) [158].

The behavior of particles in turbulence was classically thought to depend on the Stokes number[159], which may be thought of as a measure of inertia, or the ability of the particle to move with the flow. Recent work has shown that even particles with quite low Stokes numbers can produce significantly different acceleration results, and the density of the particle must be taken in to account even in the limit of $St \ll 1$ [83]. Mathai *et al* explain this dependence on density by noting that a particle drifting through the flow due to gravity will sample spatial gradients in a way that a fluid particle does not. Very little work has been published regarding the acceleration statistics in inhomogeneous flow, but by analogy we expect that the forces on the particle that result in drift (e.g. shear-induced lift [160]) to result in a similar effect. These mean-gradient effect depends only on length, so we must consider the length scale ratios independent of the Stokes number.

The key characteristics of the three classes of particles used in this study are given in table 5.1. These characteristics include the non-dimensional numbers that can be formed with the diameter and density of the particle and the properties of the flow (density, viscosity, turbulent scales, etc.). To avoid using results obtained from the experimental PTV using tracer particles in order to characterize the tracer particles themselves, the turbulent scales of the flow used to calculate the particle characteristics shown in table 5.1 and figure 5.3 were taken from the DNS results, the details of which are given in section 2.5.

Table 5.1: Characteristics of the three classes of particles used in the present study

	Definition	Tracer	Large neutrally-buoyant	Large heavy
ρ_p	Particle density	$1.05\,\mathrm{g\,cm^{-3}}$	$(0.995 \pm 0.010)\,\mathrm{g\,cm^{-3}}$	$(2.5 \pm 0.1)\,\mathrm{g\,cm^{-3}}$
Γ	Density ratio: ρ_p/ρ_f	1.05	0.995	2.5
β	Added mass ratio: $\frac{3\rho_f}{\rho_f + 2\rho_p}$	0.97	1.003	0.5
D_p	Particle diameter	$(10.2 \pm 0.8)\,\mu\mathrm{m}$ [a]	$(165 \pm 15)\,\mu\mathrm{m}$ [b]	$(72 \pm 8)\,\mu\mathrm{m}$
D_p/η	Length scale ratio based on Kolmogorov length η	Varies across channel, see figure 5.3		
D_p/δ_ν	Length scale ratio based on wall unit δ_ν	0.783	12.7	5.49
τ_p	Particle response time:[c] $\frac{D_p^2 \Gamma}{18\nu}$	$6.0 \times 10^{-6}\,\mathrm{s}$	$1.5 \times 10^{-3}\,\mathrm{s}$	$7.1 \times 10^{-4}\,\mathrm{s}$
St	Stokes number: τ_p/τ_η	Varies across channel, see figure 5.3		
Fr_p	Particle Froude number[d]: gSt/a_{rms}			0.2 - 0.27

[a] This uncertainty represents $\pm 3\sigma$

[b] According to the manufacturer >90% of particles fall into this size range

[c] Numerous definitions of particle response times exist in the literature, with many using β to account for added mass effects, and some adding correction terms for larger particles with finite Re_p. This definition given here is both classic and common, and used here in the interest of straight-forward comparison of results.

[d] Following the definition used by Gerashchenko *et al*[73]

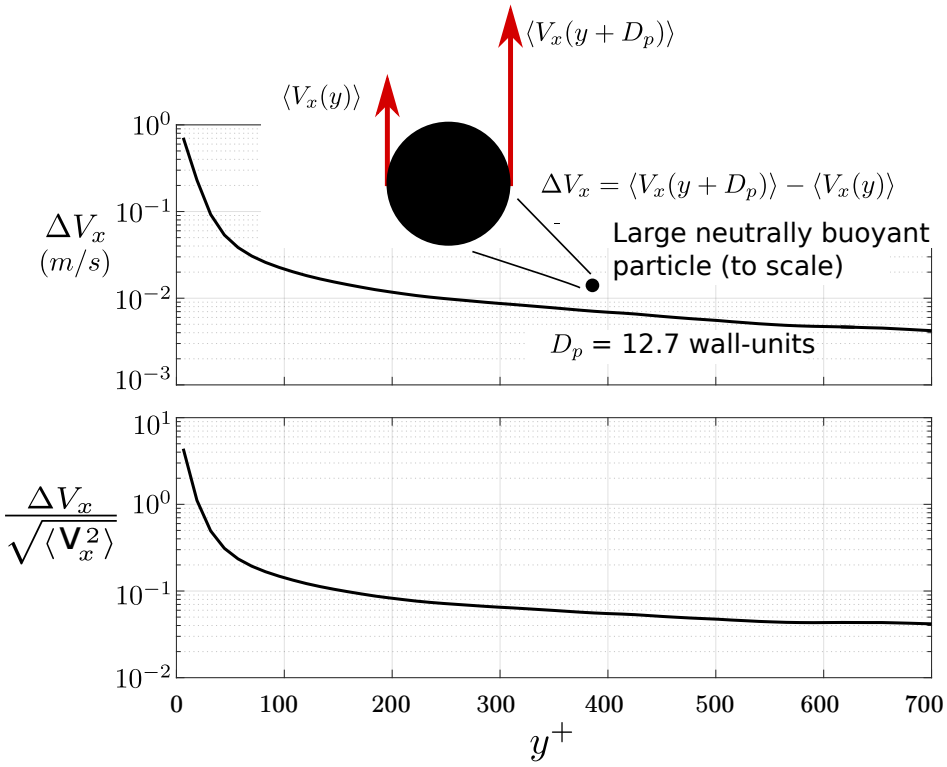

Figure 5.4: **Top:** Mean streamwise velocity difference on the scale of the large, neutrally-buoyant particle diameter. **Bottom:** Mean streamwise velocity difference on the scale of the large, neutrally-buoyant particle diameter, normalized by the rms of the streamwise velocity.

Large neutrally-buoyant particles

The class of big, neutrally-buoyant (or iso-dense) particles are fluorescent red polyethylene micro-spheres, distributed by Cospheric (Cospheric LLC, Santa Barbara, USA). Details provided by the manufacturer are listed in table 5.1; density and diameter distributions within the given ranges were not provided, and no independent measurements were performed. In the following results these particles are treated as mono-dispersed in diameter and density. The absorption and emission characteristics of the fluorescent material in these particles is similar to those of the tracer particles as described in section 2.1.5; no change in the laser or optical filters were necessary. The particle diameter was chosen such that the length scale ratio D_p/η would vary from close to 10 very near the channel wall to 2 at the channel center, as shown in figure 5.3. This choice represents a compromise between the range of parameters for which the acceleration variance (see figure 5.1) is expected to differ significantly from that of the fluid particle, and the diameter being too large, such that acceleration of these particles becomes too low and is lost in the measurement noise. Large neutrally-buoyant particles may also be affected by the mean shear in the flow; figure 5.4 plots the profile of the mean velocity difference on the length scale of the particle. For the diameter of particle tested this velocity difference is non-negligible, and near the wall is on the order of the rms of the fluid velocity.

Heavy particles

The class of heavy particles are spherical glass beads distributed by the Wheelabrator Group (Altrincham, UK) with a density specification of 2.4 g cm^{-3} to 2.6 g cm^{-3} (53 µm to 106 µm). Analytic sieves (VWR, Radnor, Pennsylvania) were used to reduce this range to

63 µm to 80 µm. The diameter and density distributions were not directly measured; the results presented treat these particles as mono-dispersed in diameter and density. These particles have Stokes numbers of 0.2-2 in the near-wall region, a range in which, at least for inertial particles in HIT, particles diverge significantly from fluid particle paths, preferential concentration becomes important, and particle acceleration statistics differ significantly from those of the fluid. These particles were judged to be the largest and heaviest that was practically possible to measure, given the twin constraints of particles settling and resisting re-entrainment (as discussed above), and the low signal-to-noise ratio that limits the measurement of particles with a low acceleration variance.

5.2.3 Changes in the data processing methods

No fundamental differences to the image processing and particle tracking algorithms described in chapter 2 were necessary for the treatment of the non-tracer particle data, although some adjustment was made to the image filtering and tracking parameters. The primary difference between the non-tracer particle datasets and the tracer particle dataset is the reduced signal-to-noise ratio and the reduced statistical convergence of the non-tracer particle datasets. The signal-to-ratio is illustrated by comparing the acceleration variance as a function of acceleration filter width, as was discussed in the context of the tracer particles in section 2.3, figure 2.19. When this analysis was performed on non-tracer trajectories the plateau of acceleration variance was found to be lower than the plateau found for the tracer particles, as illustrated in figure 5.5. Furthermore, the transition between the steep, insufficiently-filtered regime and the regime in which the acceleration variance is relatively flat, i. e. the "elbow" of the curves seen in figure 5.5 is less abrupt for the non-tracer particles. The more gradual transition between these two regimes for the non-tracer particles indicate that the signal-to-noise ratio is worse for these datasets than for the tracer particles. The ambiguity regarding where the under-filtered regime ends and the plateau regime begins does not allow a precise determination of the optimal filter width for these data. This uncertainty directly translates into large uncertainty regarding the true value of the acceleration variance.

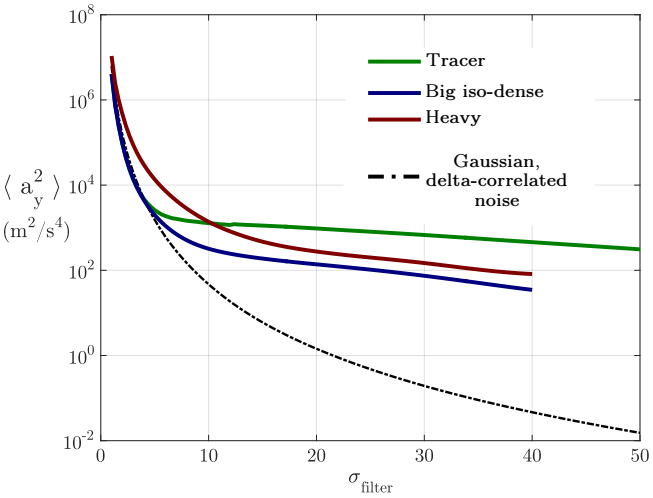

Figure 5.5: The variance of the wall-normal component of acceleration in the near-wall region for the three classes of particle as a function of filter width. Also plotted for reference is uncorrelated normally-distributed noise filter with the same acceleration filters, with the magnitude adjusted to match the tracer particle results at the smallest filter width.

The optimal filter width may be further refined by considering the autocorrelation of acceleration calculated with a range of filter widths. The time-scale separation between the noise and the acceleration results in a characteristic dip in the autocorrelation of acceleration calculated with a filter insufficiently wide. This characteristic dip is seen at a time corresponding to the width of the filter[9], which is shorter than the acceleration time scale. The strategy used to choose the optimal filter width was to increase the filter

[9]Here it is implicitly assumed that the noise is delta-correlated in time.

width until this characteristic dip disappears. If a larger filter with is used the acceleration variance continues to slowly decrease, but the autocorrelation of acceleration at longer time lags is relatively robust.

This strategy is illustrated by figure 5.6, which an example of an acceleration autocorrelation curve calculated with the optimal filter width(as chosen by the strategy described above), as well as the acceleration autocorrelation calculated with filter widths that both under-filter and over-filter. A slight characteristic dip may be seen on the under-filtered autocorrelation of acceleration. This choice of an optimal filter width is somewhat subjective, and a rigorous characterization of the errors resulting from this choice is therefore not possible. Instead, error bars as defined by using filter widths that are 10 time-steps wider than the optimal filter width, and 10 time-steps narrower. While the choice of 10 time steps is somewhat arbitrary, in nearly all cases it was clear that these filter widths over-filtered and under-filtered the data, respectively, and therefore act as confidence intervals. This method results in larger error bars for one-time statistics, such as acceleration variance, than two-time statistics, like Lagrangian correlations.

The fluid acceleration variance decreases as one moves from the wall to the channel center, and the non-tracer particle acceleration variance decreases along with it. Tracer particle acceleration measurements were possible near the center of the channel, but the signal-to-noise ratio of the non-tracer particle acceleration variance was found to be too low to accurately measure non-tracer particle acceleration near the channel center. Results in this chapter are therefore limited to the area of the channel from the wall to $y^+ = 638$, which is approximately halfway between the wall and the centerline of the channel.

In addition to the signal-to-noise concerns described above, the non-tracer datasets are smaller than the tracer particle dataset. In particular, the wider filters that were necessary to treat the non-tracer trajectories have the effect of shortening the mean trajectory length. Fewer trajectories results in less statistical convergence, especially for two-time Lagrangian statistics. For this reason the pdf's of acceleration are not presented, and the Lagrangian correlations are truncated at shorter times than for the tracer particles.

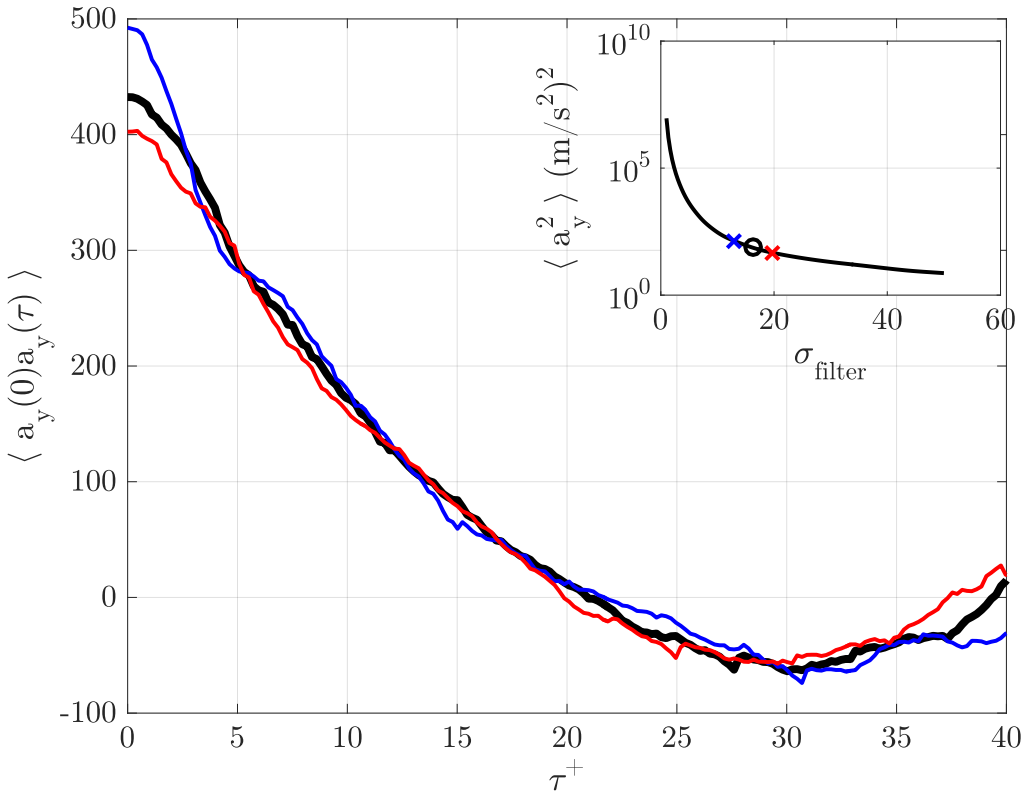

Figure 5.6: The autocorrelation of the wall-normal component of acceleration for large neutrally-buoyant particles at $y^+ = 75-150$. The thick black line is this autocorrelation using the optimal filter width, the blue line is this autocorrelation using a filter width 10 time-steps shorter than optimal (less filtering), and the red line is this autocorrelation using a filter width 10 time-steps longer than optimal (more filtering). **The inset plot** shows the variance of the wall-normal component of acceleration for these data plotted against the filter width. The position of the optimal filter width chosen is shown (black circle), as well as the filter widths corresponding to the "optimal - 10" (blue x) and "optimal + 10" (red cross) filter widths.

5.3 Acceleration variance

The variance of particle acceleration as a function of distance from the wall for the three classes of particles is shown in figure 5.7. Error bars are calculated using the method described in the preceding section: an optimal filter is chosen based on the appearance of the acceleration autocorrelation for each wall-bin, then the acceleration variance is calculated using a filter 10 time steps greater than optimal—which defines the lower extreme of the error bar—and a filter 10 time steps smaller than optimal—defining the upper extreme of the error bar. Similar trends are observed between the three components of acceleration variance: a monotonic decay of variance moving away from the wall, a much weaker acceleration variance in the heavy particles than the tracer particles, and the acceleration variance of large-neutrally buoyant between the two.

These tendencies are more easily compared in the normalized profiles of acceleration variance plotted in figure 5.8. The upper row of subplots shows the acceleration variance for the three classes of particles normalized by the variance of the transverse component

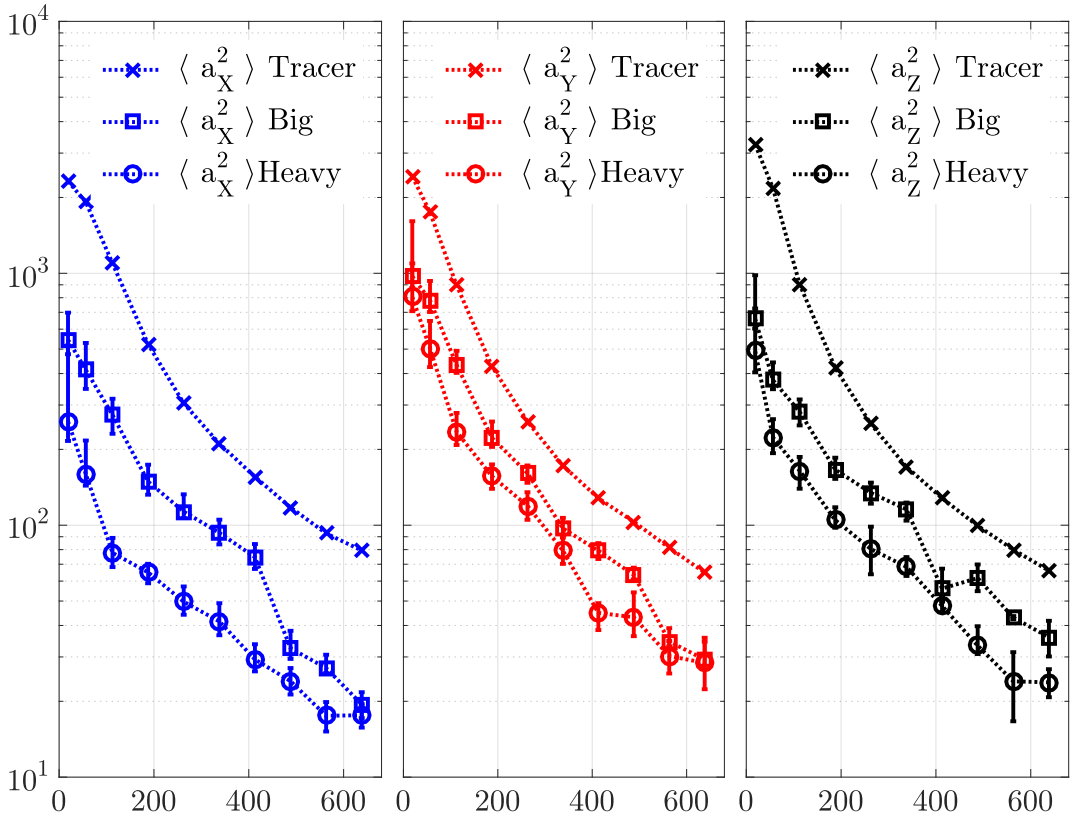

Figure 5.7: Acceleration variance for the three classes of particle (tracer: x's, big iso-dense: squares, and heavy: circles) from the wall to $y^+ = 638$, or approximately mid-way between the wall and the channel centerline. Error bars are calculated on the basis of the filter widths, as described in the text.

of acceleration of the tracer particles at $y^+ = 638$. While this choice is somewhat arbitrary[10], the variance of the transverse component of acceleration at this location is relatively far from the wall and acts as a reference value. Indeed the variance of the streamwise and wall-normal components of acceleration for the tracer particles are observed to be very similar to this value at $y^+ = 638$, i.e. the acceleration variance for the tracer particles is close to isotropic at this distance from the wall.

The acceleration variance normalized in this fashion for the tracer particles shows a large ratio (6-7) between the near wall value and the far wall value. By contrast this ratio for the heavy and large neutrally-buoyant particles are flatter, and the acceleration variance appears to be suppressed near the wall.

The lower row of subplots plot the accleration variance profiles of the heavy and large neutrally-buoyant particles normalized by the tracer particle acceleration variance profile, e. g $\langle a^2_{heavy} \rangle (y) / \langle a^2_{tracer} \rangle (y)$. As a general trend, the acceleration variance is most heavily suppressed relative to the tracer acceleration variance near the wall, and is less supressed farther away from the wall. A local maximum (which is interpreted at a minimum suppression relative to the fluid particle acceleration variance) is oberved at approximately $y^+ = 300$, although given the uncertainties of the data this may be simply the beginning of a plateau that is observed from approximately $y^+ = 300 - 600$.

The Heisenberg-Yaglom relation predicts the following scaling for the variance of

[10] Ideally this normalization would use the acceleration variance at the channel center, but this measurement was unreliable, as discussed in section 5.2.3

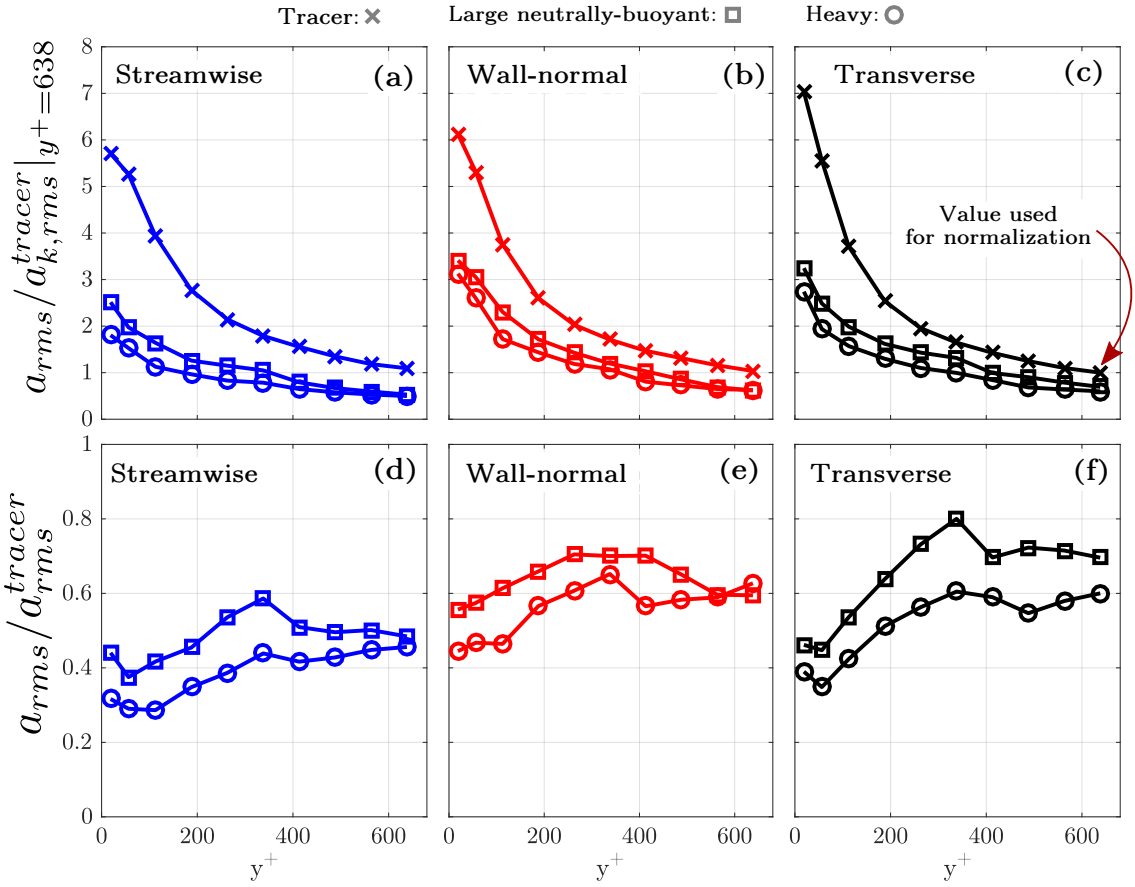

Figure 5.8: The rms of acceleration for the three classes of particles. **Subplots (a)-(c):** The acceleration rms of each component of the three classes of particle are normalized by the rms of the transverse component of the tracer particle acceleration at $y^+ = 638$, i. e. $\langle a^2_{z,tracer}\rangle^{1/2}|_{y^+=638}$ **Subplots (d)-(f):** The profiles of the ratio between the acceleration rms of the non- tracer particles and the tracer particles is plotted for each component.

acceleration in HIT in the limit of high Reynolds number

$$\langle a_i^2 \rangle = a_0 \nu^{-1/2} \langle \epsilon \rangle^{3/2} \tag{5.1}$$

where a_0 is thought be a universal constant. Normalizing the acceleration variance with this scaling permits comparison to previous acceleration measurements taken over a range of Reynolds numbers. Sawford *et al*[34] examined several measurements, from DNS and experiments, of a_0, and fitted the following relation

$$a_0 = \frac{5}{1 + 110/\mathrm{R}e_\lambda} \tag{5.2}$$

which was found to a good fit to the DNS measurements of a_0 in the range of $\mathrm{R}e_\lambda$ found in the turbulent channel used in this study. Figure 5.9 plots the normalized acceleration variance for the tracer and large neutrally-buoyant particles, using mean dissipation profiles calculated from the channel DNS[42]. The simple model from Sawford *et al*[34], equation 5.2, is also plotted using the local value of the Reynolds number ($\mathrm{R}e_\lambda(y^+)$) also calculated from the same DNS. Fairly good agreement is found with the curve-fit model from HIT, at especially for $y^+ > 100$. The normalized acceleration variance for the large neutrally-buoyant particles is plotted in figure 5.9 with respect to their local length scale ratio: $\mathrm{D}_p/\eta(y^+)$, where the Kolmogorov length scale η is again taken from the channel DNS.

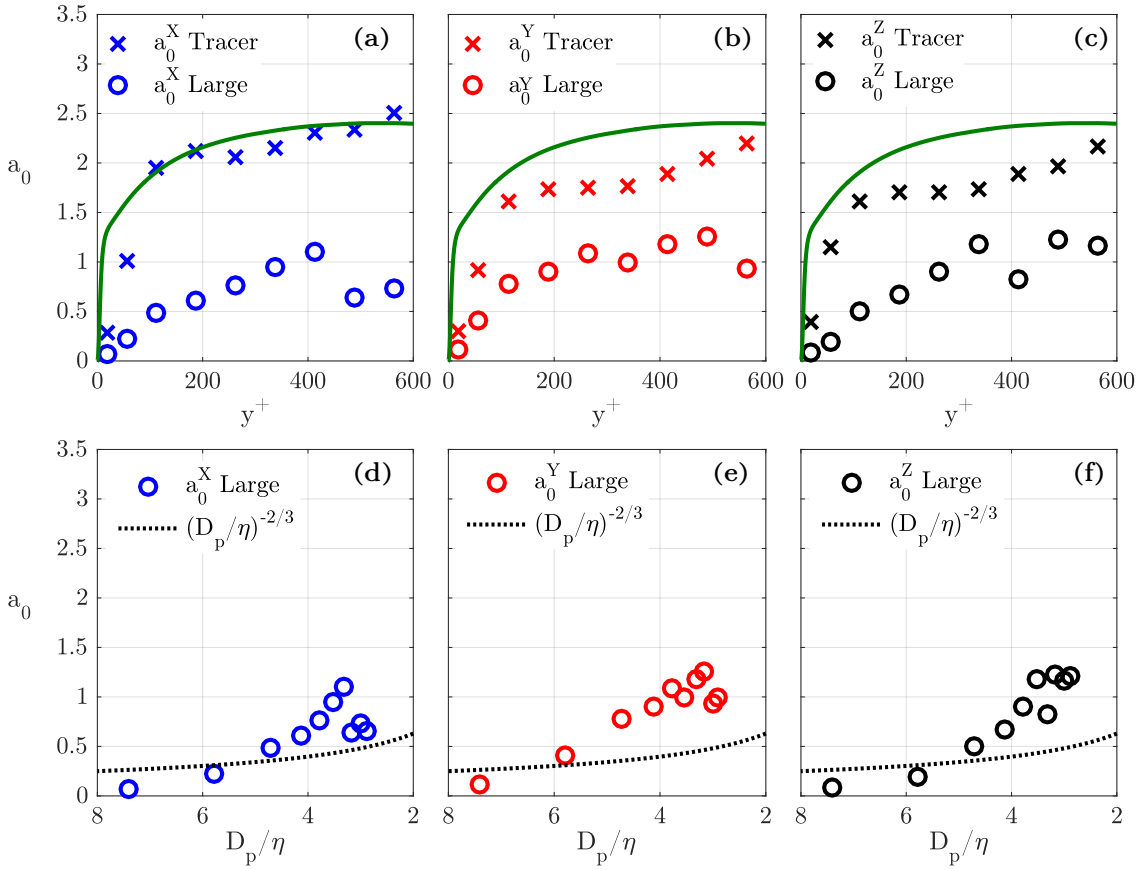

Figure 5.9: The Heisenberg-Yaglom "constant" a_0 as defined in equation 5.1 is calculated using the local value of the mean dissipation $\langle\epsilon\rangle(y^+)$ obtained from the DNS. **Subplots (a)-(c):** Plot a_0 as a function of distance from the wall for the tracer particles (x) and the large-neutrally buoyant particles for the streamwise (a), wall-normal (b), and transverse (c) components of acceleration. Also plotted is the curve-fit prediction $a_0 = 5/(1+110/Re_\lambda)$ from Sawford *et al*[34], calculated from the local Reynolds number $Re_\lambda(y)$ from the DNS. **Subplots (d)-(f):** are these same data plotted against the ratio of particle diameter and Kolmogorov length scale. Note that the horizontal axes of these subplots are flipped to be consistent with the subplots above, as D_p/η is greatest near the wall.

These plots show that even at $D_p/\eta < 5$ the acceleration variance of the large neutrally-buoyant particle remains significantly lower than the acceleration variance of the tracer particles.

A similar transformation of variables was performed for the heavy particles: figure 5.10 plots the normalized acceleration variance of the heavy particles against their local Stokes number, $St(y^+) = \tau_p/\tau_\eta(y^+)$, where the local $\tau_\eta(y^+)$ is taken from the channel DNS. The large Stokes numbers correspond to near wall locations; the small Stokes numbers correspond to locations farther from the wall. Also plotted are results from Bec *et al*[91] from DNS of HIT with inertial point-particles[11] for three Reynolds numbers. The relevant local Re_λ in the channel varies from $Re_\lambda \approx 100$ for the smallest Stokes numbers shown here, to $Re_\lambda \approx 40$ for the largest Stokes numbers. Large differences between the experimental results and the point-particle DNS results are observed at large Stokes numbers (close to the wall); these differences decrease at smaller Stokes number (farther from the wall).

The profiles of acceleration covariance, $\langle a_x a_y \rangle$, are shown in figure 5.11 for the three

[11]The simple Stokes drag truncation of the Maxey-Riley-Gatignol equation was used to integrate inertial particle paths.

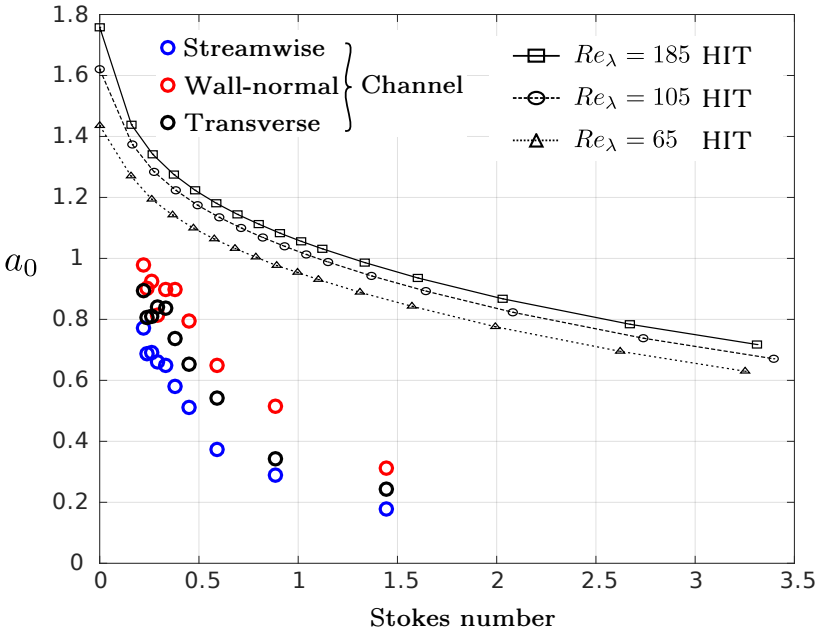

Figure 5.10: Normalized acceleration variance of the heavy particles in the channel (colored circles), plotted against the local Stokes number (τ_p/τ_η, where τ_η is the Kolmogorov time at $y(t_0)$ taken from the channel DNS). Large Stokes number results correspond to the near-wall region; Stokes numbers decrease monotonically with increasing distance to the wall (see figure 5.3). Also shown is the normalized acceleration variance from inertial point-particles in HIT over a range of Stokes number and for three Reynolds numbers, recreated from Bec *et al*[91], figure 1.

classes of particle. The fluid acceleration covariance is zero in HIT[35]; in a high-aspect-ratio channel the components of the acceleration covariance matrix that contain the transverse (z) component of acceleration are zero by symmetry[12], but the mean product of the streamwise and transverse components of acceleration is non-zero. As discussed in chapter 2, the strong negative covariance near the wall means that particle accelerations near the wall tend to be of opposite sign: either slowing in the streamwise direction and speeding up in the direction of the channel center or vice-versa. The acceleration covariance is smaller for the non-tracer particles than for the tracer particles. Comparing figure 5.11 (b) and figure 5.8 (d-e) the ratio of non-tracer to tracer covariance is slightly less than the ratio of the non-tracer to tracer variance, especially for the heavy particles.

5.3.1 Discussion

Large neutrally -buoyant particles

As mentioned in the introduction, previous work regarding large neutrally-buoyant particles in HIT have shown: 1) they do not cluster[161], and 2) their acceleration variance is approximately equal to that of tracer particles for $D_p/\eta < 5$[30, 4, 90]. Because these particles do not show any preferential concentration in HIT the "biased sampling" mechanism is not a factor, and therefore the reduced acceleration variance reported in the literature for neutrally-buoyant particles larger $D_p/\eta \approx 5$ is attributed to the temporal and spatial filtering mechanisms.

The acceleration variance for the large neutrally-buoyant particles reported here are typically 0.5-0.75 that of the fluid acceleration variance, *even in those regions of the flow*

[12] Also confirmed experimentally.

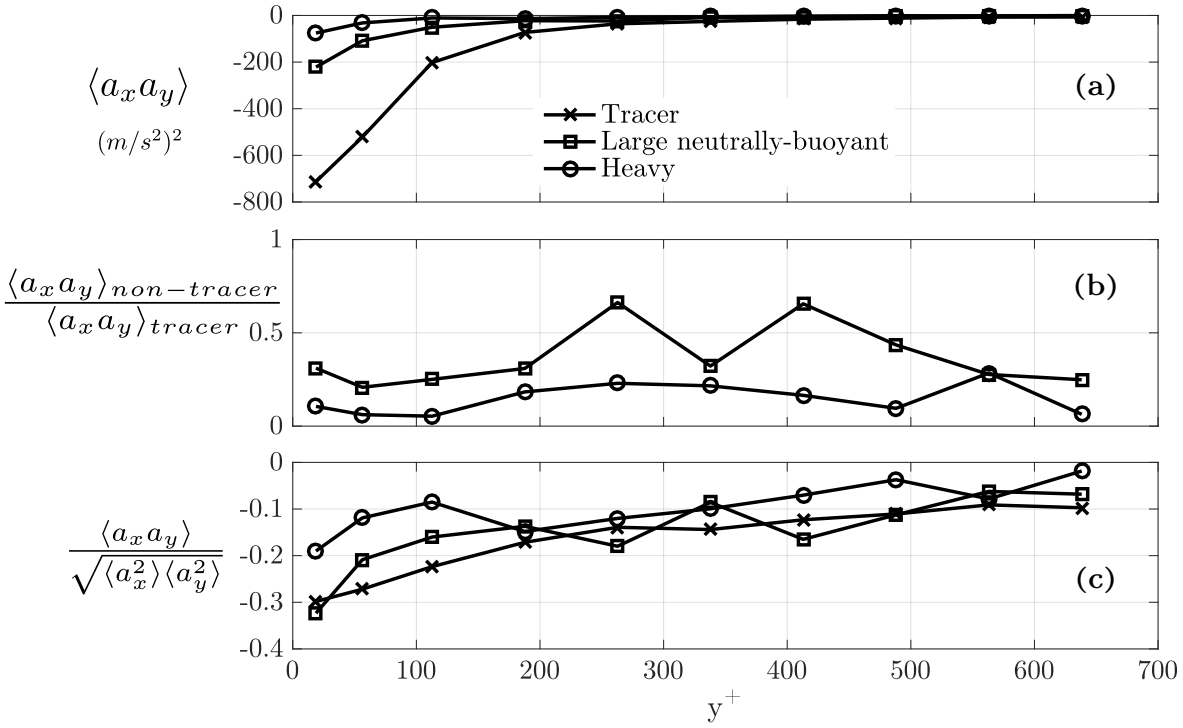

Figure 5.11: Covariance of acceleration for the three classes of particles. **Subplot (a):** The profiles of acceleration covariance $\langle a_x a_y \rangle$ for the three classes of particles. **Subplot (b):** The profiles of the ratios between the the covariance of acceleration of the non-tracer particles and the covariance of acceleration of the tracer particles. **Subplot (c):** The covariance of acceleration for the three classes of particles, normalized by the variance of their streamwise and wall- normal components of acceleration.

where $D_p/\eta < 5$ (see figure 5.9). How to explain the discrepancy between these results and well-established result in HIT that the acceleration variance of the particle is very close to that of the fluid up to D_p/η? One difference is that the experiments in HIT reported in the literature had higher Reynolds numbers l($Re_\lambda \approx 160-900$) than in the near wall of the channel($Re_\lambda < 80$), although this result seems quite insensitive to Reynolds number[4]. The more probable factor is that the difference between these results and the published results is that all of the published results were measured in HIT.

The discrepancy in acceleration variance results is explicable by the inhomogeneity and/or anisotropy of the turbulent channel only if one or more of the mechanisms that act to reduce particle acceleration variance behaves differently in the turbulent channel than in HIT. It is unclear how temporal and spatial filtering would behave differently in the inhomogeneous/anisotropic turbulence, especially in relation to the variance of acceleration. The sampling bias mechanism was thought to be irrelevant to the dynamics of the large neutrally-buoyant particles simply because no clustering was observed in HIT[161] for particles over a range of diameters $D_p/\eta = 4.5-17$ (St = 0.38-1.23), not from any theoretical concern. In fact, that are a few reasons to suspect that clustering could in fact occur in this context.

1) Large neutrally-buoyant particles are subject to drag and lift forces resulting from fluid shear and particle rotation[148][13] that act to separate the particle trajectory from the fluid trajectory. In HIT these forces do not induce clustering[161], but in a turbulent boundary layer containing features such as mean shear, preferential alignment of vortices,

[13]See Loth and Dorgan[148] for a thorough review of these forces in their effort to extend the Maxey-Riley-Gatignol equation to large particles.

and coherent structures (see the discussion in section 1.2) the effect of these forces on clustering may be substantially different.

2) Just as small, heavy particles accumulate in zones of low vorticity because of particle inertia[149], the forces described above imply that the particles accumulate in zones that minimize these forces. HIT therefore does not contain zones than minimize these forces, but the turbulent boundary layer may.

3) Recent efforts to better understand the clustering mechanism of inertial particles in HIT have resulted in the "sweep-stick" hypothesis[162, 163]. Briefly, clustering in the inertial range is explained by particles being swept through regions of zero fluid acceleration, then being stuck in these regions because the fluid acceleration is not large enough to cause the fluid and particle paths to diverge[14]. While this "sweep-stick" mechanism is not directly applicable to large neutrally-buoyant particles in HIT (or else clustering would have been observed in the results of [161]), it does make explicit the relationship between the topology of acceleration in the flow and the heavy particle clusters. There may be an analogous "stick" mechanism (something similar to that of small heavy particles: $\mathbf{v_p} \approx \mathbf{u} - \tau_p \mathbf{a}$) that relies on the finite-particle-size forces, and their topology in the channel.

Heavy particles

Heavy particle acceleration variance is found to be less than tracer particle acceleration variance across the channel. This reduction is especially notable near the wall, where figure 5.8 shows heavy particle acceleration variance is 30-45% (depending on the component) of the fluid acceleration variance. These results are consistent with the trend observed by Bec *et al*[91] in HIT: a monotonic decrease in heavy particle acceleration variance with increasing Stokes number. The heavy particle acceleration variance results of the present study are significantly lower than those found by Bec *et al* (see figure 5.10) even at approximately equivalent Reynolds numbers ($Re_\lambda = 80 - 100$ for $St < 0.5$). The trend visible in figure 5.10 shows a steeper decline of acceleration variance with increasing Stokes number for the channel results than for the HIT results of Bec *et al*.

There are two likely explanations for the discrepancy between the results from the channel and the result from HIT seen in figure 5.10. The first concerns the finite-size effects: the heavy particles have a length scale ratio of $D_p/\eta = 3.2$ (near the wall) to $D_p/\eta = 1.3$ (in the outer layer). Volk *et al*[153] reported a significant discrepancy between experimental measurements of the acceleration variance of a heavy particle ($D_p/\eta = 1.2$, $St = 0.58$) and the result from an inertial point-particle in DNS. The growing length scale ratio for particle closer to the wall is consistent with the steeper decline in the acceleration variance in the channel seen in figure 5.10.

The second explanation is that the bias sampling mechanism, which was shown to play an important role in the reduction of the acceleration of heavy particles in HIT[93], is almost certainly changing with wall distance. Heavy particles have been shown to concentrate in the near wall region due to turbophoresis, and particle clustering that is anisotropic and wall-distance dependent has been observed by Sardinia *et al*[164] in a turbulent channel DNS.

Gerashchenko *et al*[73] performed one of the rare experimental studies of inertial particle accelerations in a turbulent boundary layer[15]. Water droplets in air result in a high

[14] In 3-D turbulence this mechanism is more complex, see [162, 163] and references therein for a complete description.

[15] As of this writing this study remains the only such measurements in a turbulent system with a mean flow and mean shear that have been published.

density ratio, thus gravity plays an important role in particle dynamics. Particles were sub-Kolmogorov size, with Stokes numbers from 1.1 (close to the wall) to 0.5 (farther from the wall). Despite the similarity of Stokes numbers the results reported by Gerashchenko *et al* differ significantly from those reported here. In the near wall region they found the variance of the streamwise component of particle acceleration to be twice that of the variance of the wall-normal particle acceleration component. This is the inverse of what is seen in the present study, where the variance of streamwise component of heavy particle acceleration is shown in figure 5.7 to be less than the variance of the wall-normal component near the wall. Lavezzo *et al*[152] performed channel flow DNS using parameters as close as possible to the experimental parameters of Gerashchenko *et al* to elucidate the role of gravity in these results, and found that this increase of the variance of the streamwise particle acceleration near the wall is due to gravity. That conclusion is consistent with the results presented here, as the role of gravity is much less important in the present study. Gerashchenko *et al* found that the acceleration variance *increased* with decreased Stokes number, contrary to the results shown in figure 5.10 and the results for HIT from several sources, e. g. Bec *et al*[91]. This increasing acceleration variance with decreasing Stokes number was also found to be an effect of gravity by Lavezzo *et al*[152].

More puzzling is the substantial difference in normalized acceleration: Gerashchenko *et al* report a profile of a_0 across the boundary layer from $a_0 \approx 3$ near the wall to $a_0 \approx 4$ far from the wall. This is a substantial difference from the results reported here, seen in figure 5.10 as $a_0 \approx 0.2$ close to the wall to $a_0 \approx 0.8$ far from the wall (streamwise component). The increase in acceleration variance with decreased Stokes number, explained by the effects of gravity, suggests a complex interaction between gravity, bias sampling, and the turbulent boundary layer. This interaction is poorly understood, and requires further work.

5.4 Lagrangian acceleration statistics

The Lagrangian autocorrelations of the three components and magnitude of acceleration for each of the three classes of particle are plotted in figures 5.12 and 5.13. These figures include dimensional autocorrelations (top row) and normalized autocorrelations (bottom row). Figure 5.12 shows autocorrelations calculated from those trajectories close to the wall ($0 < y^+(t_0) < 37.5$), while figure 5.13 shows autocorrelations for the outer layer ($525 < y^+(t_0) < 600$). These two locations were chosen as representative; a full collection of figures for all available wall-bins is found in the appendix A.3. Note that the bin close to the wall (figure 5.12) is half the width of the bin in the outer layer (figure 5.13). This near-wall bin size is a compromise: it must be small enough such that important wall-distance-dependent dynamics are not lost, and large enough that the autocorrelations have adequate statistical convergence. The non-tracer particle results lose statistical convergence after $\tau^+ \approx 25$ in the near-wall bin (figure 5.12); in the outer layer bin (figure 5.13) these results show statistical convergence up to $\tau^+ \approx 40$. Despite this lack of statistical convergence at longer time lags several observations are possible regarding the autocorrelations of acceleration shown in these two figures. In the near wall region the normalized autocorrelation of the streamwise component of acceleration is quite similar for the three classes of particles, and none of them show strong negative correlations. The wall-normal and transverse components for the tracer particle show significant dips below zero, which was taken as evidence for vortex trapping in streamwise vortices near the wall. The non-tracer particles seem to decay to zero without significant dips below zero, with the exception of the transverse component of the large neutrally-buoyant particles. The autocorrelation of the magnitude of acceleration, both near the wall and in the outer layer, decays much more quickly for the non-tracer

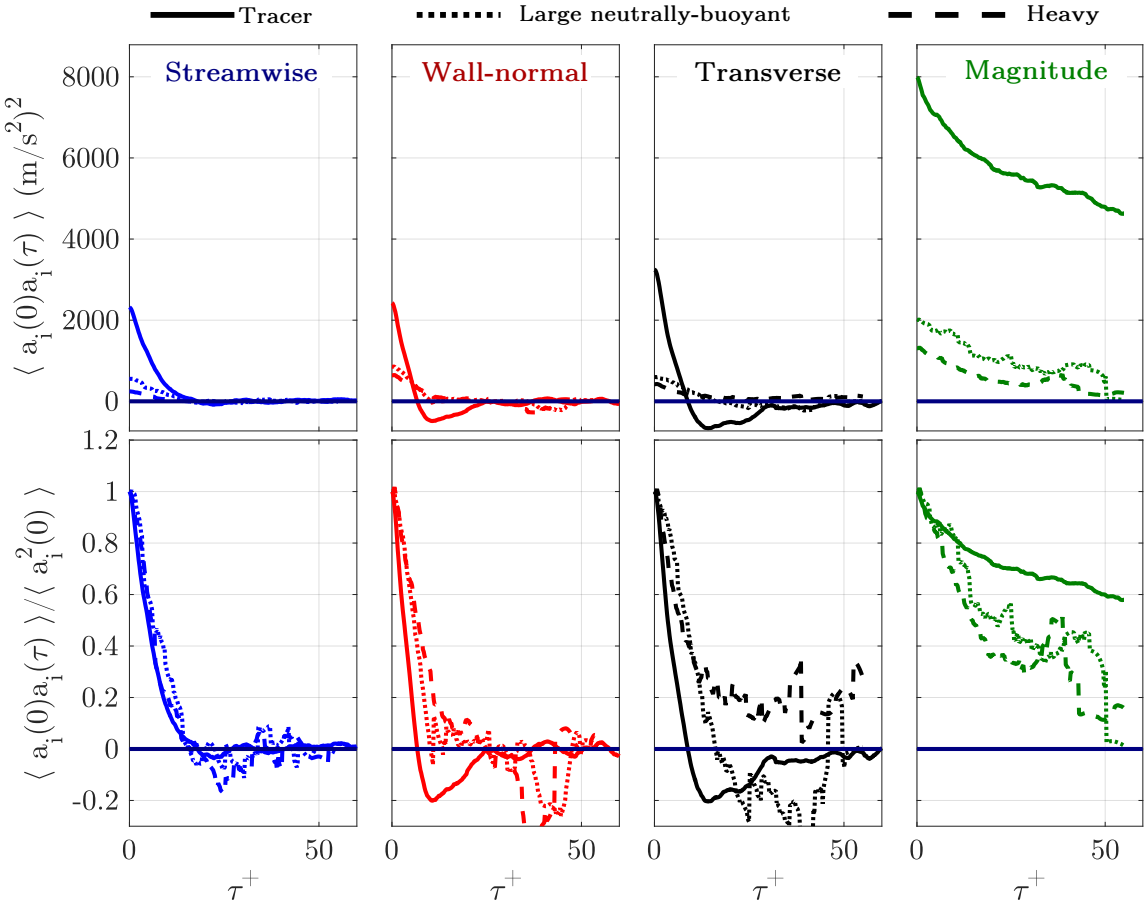

Figure 5.12: **Top:** Non-normalized autocorrelations of the three components of acceleration ($\langle a_i(0)a_i(\tau)\rangle$), and acceleration magnitude $\left\langle \sqrt{a_x^2(0)+a_y^2(0)+a_z^2(0)}\sqrt{a_x^2(\tau)+a_y^2(\tau)+a_z^2(\tau)} \right\rangle$, for the three classes of particle. **Bottom:** The same autocorrelations as above, normalized by their variance. The autocorrelations are calculated from trajectories that are in the bin $y^+ = 0-37.5$ at $t = 0$.

particles than for the tracer particles.

The Lagrangian cross-correlation between the streamwise and wall-normal components of acceleration were similarly calculated at the same locations in the channel, and are presented in figure 5.14. Non-negligible cross-correlation for the non-tracer particles is observed close to the wall; the cross-correlation decays to zero for all three classes of particles at approximately the same time lag ($\tau^+ \approx 10$). In the outer layer location this cross-correlation is effectively zero for the non-tracer particles, despite the clear (although much reduced in magnitude) cross-correlation of tracer particle acceleration.

The integration in τ of the normalized autocorrelations of acceleration form an acceleration timescale. The limits of this integral are typically taken to be zero and the zero-crossing time[151], or slightly before the zero-crossing time[16].

Due to the problems of statistical convergence observed in the normalized autocorrelations of acceleration in figures 5.12 and 5.13, the limits of integration were changed to between zero and the time at which the correlation decays below 0.2, i. e. (no sum over

[16] As was done for the acceleration timescales from the tracer particles calculated in chapter 3, which used the time at which the correlation decayed below 0.05

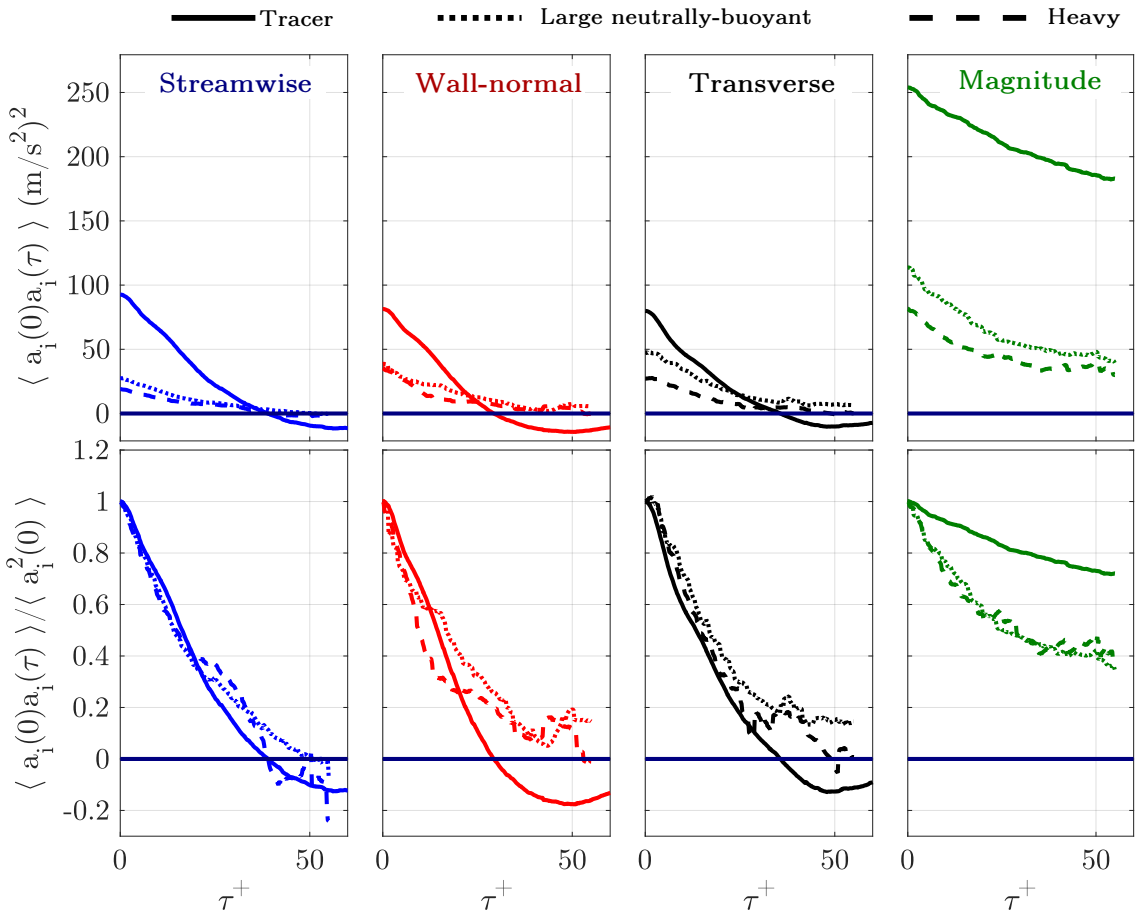

Figure 5.13: **Top:** Non-normalized autocorrelations of the three components of acceleration ($\langle a_i(0)a_i(\tau)\rangle$), and acceleration magnitude $\left(\left\langle\sqrt{a_x^2(0)+a_y^2(0)+a_z^2(0)}\sqrt{a_x^2(\tau)+a_y^2(\tau)+a_z^2(\tau)}\right\rangle\right)$, for the three classes of particle. **Bottom:** The same autocorrelations as above, normalized by their variance. The autocorrelations are calculated from trajectories that are in the bin $y^+ = 525-600$ at $t = 0$.

indices),

$$T_{i,acc} \equiv \int_0^{\tau_c} \langle a_i(0)a_i(\tau)\rangle/\langle a_i^2(0)\rangle d\tau \quad \text{where} \quad \langle a_i(0)a_i(\tau_c)\rangle/\langle a_i^2(0)\rangle = 0.2 \tag{5.3}$$

The limit of 0.2 was chosen to ensure that the calculation of the acceleration timescales is robust given the lack of statistical convergence. The tracer particle acceleration timescales were also recalculated according to this definition to allow direct comparison. Acceleration timescales calculated according to definition 5.3 are shown in figure 5.15 for the three classes of particles. The ratio between the non-tracer and tracer acceleration time scales is shown in figure 5.16. The non-tracer particles are observed to have a longer acceleration timescale than the tracer particles, up to almost 2.5 times that of the tracer particles in the near wall region for the wall-normal and transverse components. The results for the heavy and large neutrally-buoyant particles show quite similar trends, especially near the wall. The ratio between timescales for the streamwise component is closer to unity than for the other components.

The ratio between large neutrally-buoyant particle and tracer particle timescales shown in figure 5.16 may be compared to the results from Volk *et al*[90] (figure 4). The three measurements closest to the wall correspond to length scale ratios for the large neutrally-buoyant particles of $D_p/\eta \approx 5-7.5$. In this length-scale-ratio range Volk *et al* report

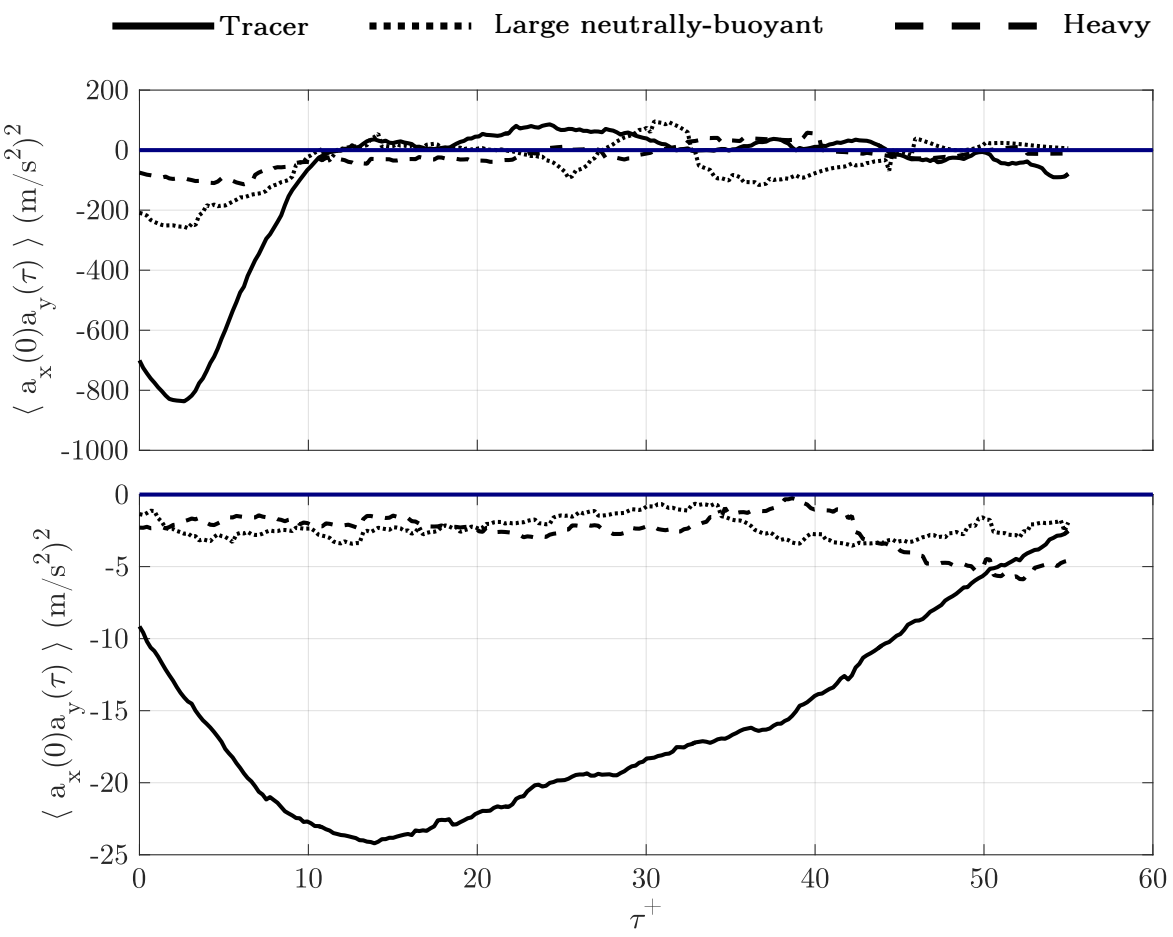

Figure 5.14: The Lagrangian cross-correlation of the streamwise and wall-normal components of acceleration for the three classes of particles. **Top:** The cross-correlation $\langle a_x(0)a_y(\tau)\rangle$ near the channel wall, $y^+ = 0-37.5$ at $t = 0$. **Bottom:** The cross-correlation $\langle a_x(0)a_y(\tau)\rangle$ near the channel wall, $y^+ = 525-600$ at $t = 0$.

measuring timescale ratios of approximately 1.5, which is consistent with the timescale ratio for the three closest points to the wall shown in figure 5.16.

5.4.1 Discussion

Salazar and Collins[93] studied the Lagrangian autocorrelations of acceleration of inertial particles in HIT ($Re_\lambda = 120$, $St = 0.025-2$) with a DNS point-particle approach. They were able to quantify the effect of temporal filtering and bias sampling on the autocorrelations of acceleration, and found that in the range of Stokes numbers relevant to the present study ($St = 2$ at the wall, $St = 0.2$ in the outer layer) the relative impact of these two mechanisms on the autocorrelation change notably. At $St = 2$, which occurs in the near wall region in the present study, the difference between the fluid and particle autocorrelations of acceleration are dominated by the temporal filtering mechanism. By contrast, at $St = 0.2$ (which occurs at the outer layer location in the present study), the difference in fluid and particle autocorrelations is dominated by the bias sampling mechanism. There are important differences between this DNS with inertial point-particles in HIT and the present study, including the finite-size of the heavy particles measured, the effect of gravity, and the structure of the turbulent boundary layer; these factors have unknown effects on the relative importance of the temporal filtering mechanism and the biased sampling

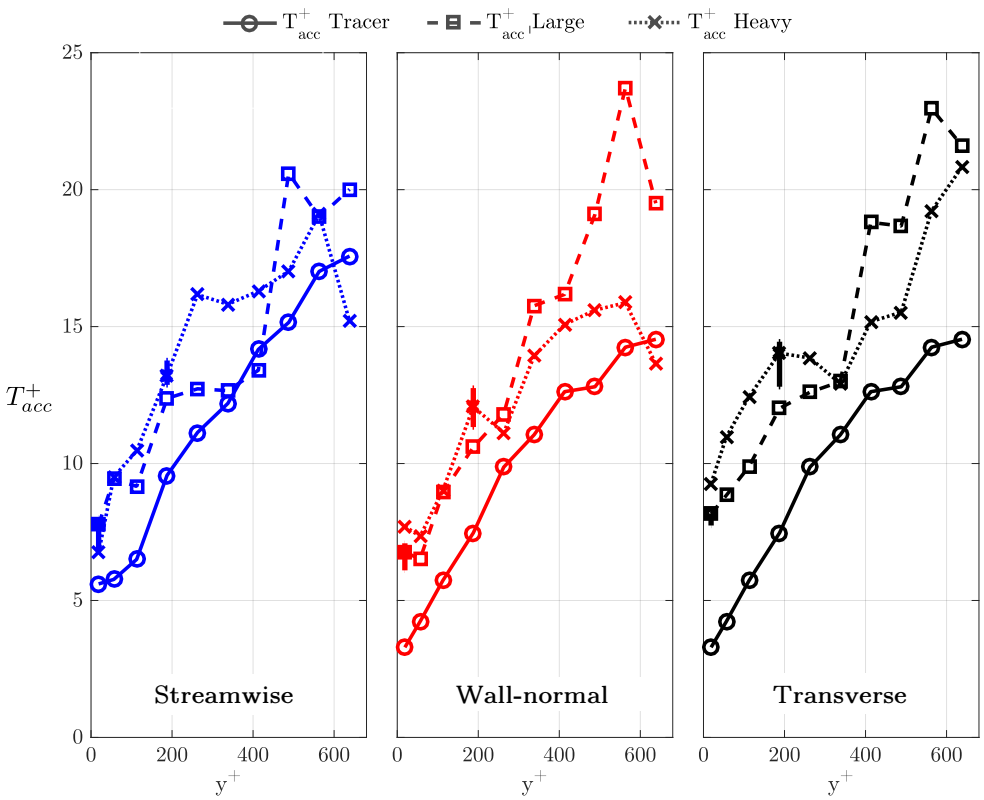

Figure 5.15: Acceleration timescales for the three classes of particle across the channel. Lines represent the timescales calculated with "best-fit" filter lengths; also shown are representative error bars (at $y^+ = 19$ for the large neutrally-buoyant particles and $y^+ = 188$ for the heavy particles) calculated with filter lengths ±10 relative to the "best-fit" length.

mechanism to the autocorrelation of particle acceleration.

For the large neutrally-buoyant particle there is no available analysis similar to that of Salazar and Collins for small inertial particles. Presumably the mechanisms affecting the autocorrelation of acceleration are related to those responsible for the acceleration variance, the nature of this relation is not clear. Volk *et al*[90] suggested that the scaling of the time scale ratio $\tau_p/\tau_f \sim D_p^{2/3}$, i. e. the particle response time is similar to the eddy turnover time of eddies at the scale of the particle diameter. This is similar to the argument for the scaling of acceleration variance by Voth *et al*[30] discussed in section 5.3, which was found to over-predict acceleration variance for the large neutrally-buoyant particles compared to the measurements reported here. The possibility of biased sampling of large neutrally-buoyant particles was discussed in section 5.3 as an explanation for this discrepancy; if bias sampling is in fact occurring in the channel flow for large neutrally-buoyant particles than it would presumably have an effect on the Lagrangian autocorrelations of acceleration.

Despite these differences in phenomenology between the heavy and large neutrally-buoyant particles their Lagrangian acceleration statistics are remarkably similar across the channel. Their normalized autocorrelations in figures 5.12 and 5.13 are quite similar, especially the rapid decorrelation of acceleration magnitude relative to the tracer particle. The long time correlation of acceleration magnitude has been attributed to the persistence of strong vortical structures in the turbulence[35, 37]; the shorter time correlation of this quantity indicates that non-tracer particles are ejected from these structures. This is expected in the case of heavy particles[149], but it is significant that large neutrally-

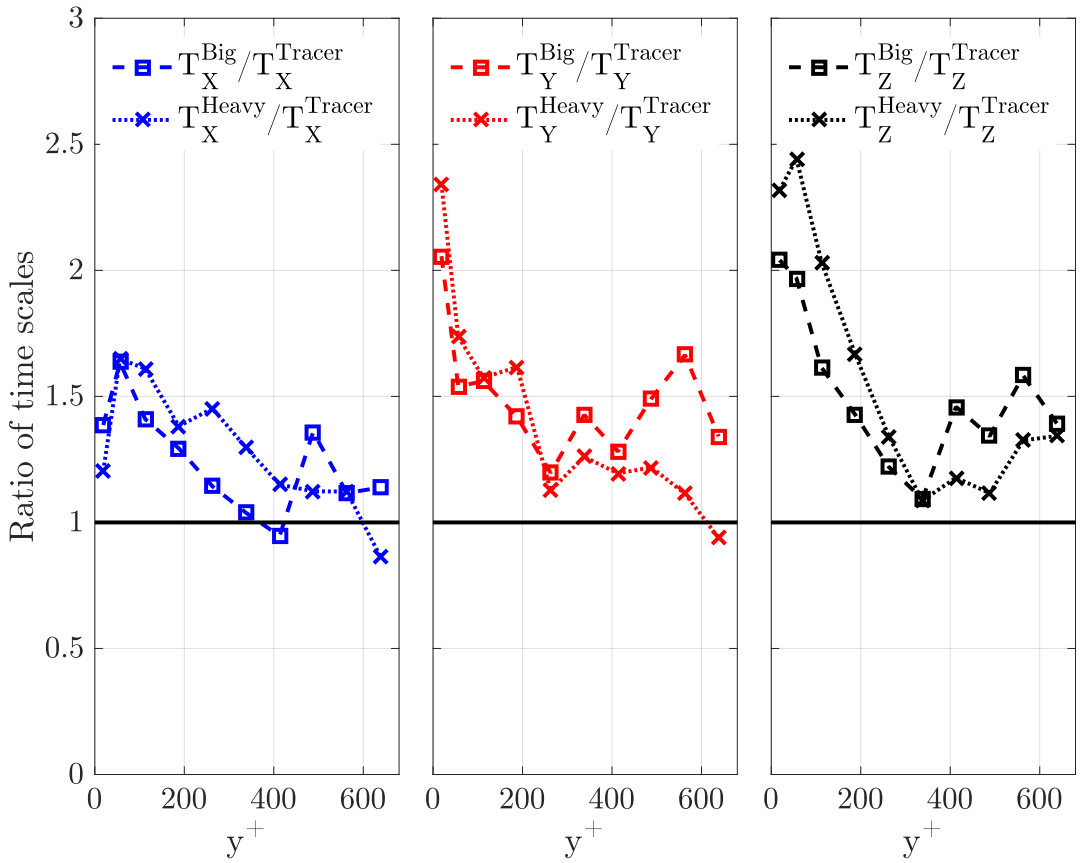

Figure 5.16: The ratio between acceleration timescales for the heavy particles and the big iso-dense particle (see figure 5.15) and the acceleration timescales across the channel.

buoyant particles show very similar behavior. This is consistent with the idea that there is some mechanism acting on the large neutrally-buoyant particles that causes preferential concentration. The similarities between the two particles is particularly notable in the ratio of particle and fluid acceleration timescales shown in figure 5.16. Despite the differences between the possible explanations for why the particle acceleration timescales differ from the fluid acceleration timescale (turnover timescale of the eddy at the particle diameter, biased sampling of zones of low vorticity, etc.) these ratios are quite similar.

5.5 Conclusion

A high-aspect ratio, moderate Reynolds number turbulent channel was adapted to allow the high-resolution, 3-D measurement of non-tracer particle trajectories. These particle trajectories allow Lagrangian statistics of position, velocity, and acceleration to calculated, conditioned on the distance to the channel wall. Two types of mono-dispersed non-tracer particles were measured, a large neutrally buoyant particle and a smaller, heavier particle. The large neutrally-buoyant particles allows the exploration of the effects of size on the particle statistics in the channel independent of inertial effects. The smaller heavy particles have a more complex phenomenology: effects of gravity, inertia, and finite-size are combined. For both particles the changing nature of the fluid turbulence as a function of wall distance results in a range of key parameters such as Stokes number and length scale ratio.

For both types of non-tracer particle the variance of the particle acceleration was significantly lower than the fluid acceleration across the channel, and particularly in the near-wall region. Large neutrally-buoyant particles smaller than $D_p/\eta \approx 5$ in HIT have particle acceleration variance equal to fluid acceleration variance, but the results presented here to not agree with that finding. This lack of agreement suggests a bias sampling effect that occurs in this turbulent system but not in HIT. Further work, including a characterization of the clustering of these particles in the channel, will be necessary to further explore this question.

The acceleration variance of the smaller, heavy particles was found to be lower than expected for similar Stokes numbers in HIT. Finite-size effects appear to play a role in this finding as well, even at relatively modest ($D_p/\eta \approx 3$) particle sizes. These results suggest a finite-size effect on the biased sampling in the turbulent channel.

Lagrangian correlations of the three components of acceleration, as well as the autocorrelation of the magnitude of acceleration, were presented for the near-wall and outer layer regions of the flow. The non-tracer particle results were quite similar, and both showed a rapid decorrelation of acceleration magnitude, comparable to the autocorrelation of one of the acceleration components. This suggests that the "vortex trapping", in which a fluid particle is trapped in a strong vortical structure of a relatively long period, occurs much more rarely for the non-tracer particles.

Lagrangian timescales of acceleration were extracted, and found to be greater than or approximately equal to the fluid particle timescales; near the wall the non-tracer acceleration timescales were up to 2.5 times the fluid acceleration timescale. These results, particularly the acceleration variances and timescales across the channel, are key ingredients in the development of Lagrangian stochastic models.

Chapter 6

Conclusions and perspectives

The symmetries of high-Reynolds number homogeneous isotropic turbulence have allowed fruitful exploration of this phenomenon from a Lagrangian point of view. Models that predict anomalous scaling of velocity increments, the long-correlations of acceleration magnitude, and dispersion in finite-Reynolds number turbulence, have been formulated in a Lagrangian framework. Over the last two decades there has been increasing experimental and numerical data to test these models.

There are many questions regarding how these results apply to inhomogeneous turbulence. Lack of stationarity, lack of small-scale isotropy, lack of independence between components even at the small-scales, break the typical assumptions made in the development of these models. This thesis has presented Lagrangian statistics in a turbulent channel obtained from high-resolution experimental measurements. These measurements have allowed the investigation of single-particle, three-component Lagrangian statistics in position, velocity, and acceleration. These statistics must be conditioned on position in inhomogeneous turbulence, and results are reported from the buffer layer near the wall to near the centerline of the channel. The measurements from this large domain, from the highly sheared, anisotropic near-wall region to the near-homogeneous central region, have allowed us to quantify where and how the Lagrangian statistics in the channel deviate from their expected values in homogeneous isotropic turbulence.

3-D particle tracking velocimetry in turbulence in inhomogeneous turbulence requires a delicate balance of parameters. One may take the approach of Gerashchenko *et al*[73] and translate the high-speed cameras and light source, an operation that is extremely technically challenging. The other approach is that discussed in chapter 2: a compromise between spatial resolution and measurement volume size. Future studies may use the results of this thesis to refine these compromises, and optimize experimental parameters. For example, a PTV system optimized for the measurement of acceleration near the wall could limit the size of the measurement volume based on the acceleration correlation times and the extent of particle dispersions that are reported here.

A complex chain of error and several statistical biases were described, some of which are unique to Lagrangian statistics in inhomogeneous flow. A rigorous treatment of the error in Lagrangian statistics in PTV measurements would be a significant contribution to the field. Statistical biases related to the finite measurement volume, extraction of Eulerian statistics, and conditioning should be tested in a systematic manner. This effort is perhaps best approached with DNS measurements, as these measurements often have the large numbers of particles necessary to converge results from narrow wall-bins. The anomalous velocity measurements reported in chapter 3 suggest that some correction scheme is necessary for these wall-bounded PTV measurements of velocity. Again, systematic test of

various strategies with experimental and DNS data would be a useful contribution.

Chapters 3 and 4 discuss Eulerian and Lagrangian statistics in the turbulent channel. The acceleration PDFs are shown to be highly skewed near the wall, which is not surprising given the degree of inhomogeneity near the wall. More surprising is that this skewness is non-zero very far from the wall, and indeed stays almost constant throughout the channel. This is only one aspect of the small-scale anisotropy that was found in the acceleration statistics: significant cross-correlation of components and anisotropy of the orientation of acceleration angles was also observed. We do not have a clear understanding of why and how such anisotropy persists, even far from the wall. An intriguing clue is found in the Lagrangian correlation of the streamwise and wall-normal components of acceleration (figure 4.20). This Lagrangian correlation suggests a preferential rotation direction in the $x-y$ plane along a particle trajectory, and may indicate that the mean shear is "organizing" the small-scale vorticity. The peak of this correlation at time-lags of approximately one Kolmogorov timescale indicates that, from a Lagrangian point of view, the acceleration components are more correlated than suggested by the simple one-time correlation of acceleration components (figure 3.12).

Further analysis of acceleration and velocity from a geometrical perspective, for example using the Frenet apparatus ($a_\parallel$, $a_\perp$, etc.), could help us to better understand the structure of Lagrangian turbulence. This perspective has been useful in exploring acceleration in vortex filaments[120] in HIT, and may be equally useful in describing organization in the turbulent boundary layer from a Lagrangian perspective. The inner product the acceleration and velocity vectors, the Lagrangian power, has been of recent interest as it relates to the time-irreversibility of the turbulence. A thorough analysis of this Lagrangian power, and how it relates to the transport of energy in a turbulent channel, would help us to understand the flow of energy in this system from a Lagrangian point of view.

A logical extension of this thesis is the development of a second-order Lagrangian stochastic model constrained by the results reported here. Terms in this model should be constrained the variances of velocity and acceleration and their Lagrangian timescales. A similar effort was published by Tanière *et al* [64] that used velocity statistics. A method for extracting model coefficients from primary statistics for a second-order model was proposed by Pope[55] for homogeneous shear flows. An adaptation of this method *à la* Tanière appears to be a reasonable first step in the use of these results to construct a second-order Lagrangian stochastic model. Lagrangian stochastic models have also been developed for non-tracer particles in inhomogeneous flow[165, 166]; direct comparisons are possible between the Lagrangian particle timescales and variances predicted by these models and the measurements reported in this thesis.

The Lagrangian statistics extracted from the DNS of a turbulent channel flow at similar Reynolds number (by J. I. Polanco and I. Vinkovic) have shown very good agreement with the experimental results reported in this thesis. Large increases in the Reynolds number for future Lagrangian experiments will be difficult to achieve, principally due to the mean flow. It seems likely that the role of future experiments will be focused on measurements of non-tracer particles, especially large particles which are difficult to simulate in DNS. The Lagrangian statistics of non-tracer particles reported in this thesis are just the beginning of the large effort necessary to understand how this particles interact with the turbulence from a Lagrangian point of view. The dynamics of large, neutrally-buoyant particles in turbulence is poorly understood, as are the mechanisms by which they filter and sample the underlying turbulent flow. A systematic study of the effect of particle size on acceleration dynamics in a turbulent channel would be useful in determining the upper limit of tracer particle diameter in wall-bounded flows. A study of particle clustering in this context would

also be useful. Large, neutrally buoyant particles have been shown to have no preferential concentration in HIT[161], but acceleration of these particles was shown in this thesis to be different than tracer particles. A systematic investigation of the various size effects may be possible using DNS in conjunction with experiments. Adding terms to the particle evolution equation, similar to the Faxen corrections discussed by Calzavarini[151] could help to untangle the influence of the various terms (Faxen terms, the history force, effects of mean shear, etc.) that drive the particle dynamics.

More broadly, exploration of the parameter space for non-tracer particles in inhomogeneous turbulence has barely begun. Understanding the difference in the Lagrangian statistics of non-tracer particles, and the mechanisms that govern their behavior, between homogeneous and inhomogeneous turbulence is important to the development of models that apply to real applications.

Ideally, non-tracer particle trajectories would be measured with simultaneous measurements of the surrounding fluid. Intriguing efforts in this direction have recently been reported by Elhimer *et al* [167]. Two- component PTV measurements of large particles along with simultaneous 2D-2C PIV measurement of the fluid allow direct *instantaneous* measurement of the relative velocity between the particle and the nearby fluid. Similar experiments using 3-D PTV are possible in the channel, and could allow us to measure local velocity gradients and particle accelerations simultaneously.

Appendix A

Appendices

A.1 Lagrangian time scale definition

We have defined our Lagrangian timescales for velocity, $T_{v,i}$, and acceleration $T_{a,i}$ from Lagrangian autocorrelation ρ_{ii} as follows:

$$T_{a,i}(y_0) = \int_0^{\tau_c} \rho_{ii}(\tau, y_0)\, d\tau, \tag{A.1}$$

where τ_c is the time lag at which the autocorrelation first crosses 0.05

The classic definition for this kind of time scale implicitly assumes that ρ_{ii} has an exponential decay, as for the autocorrelation of velocity in HIT, as so $\tau_c \to \infty$. This is an unsuitable definition for the time scale of acceleration, which as the derivative of a stationary process has an integral scale equal to zero. Yeung and Pope [16] used the zero-crossing time of the autocorrelation of acceleration as an acceleration time scale definition, and found it to be 2.2 times that of the Kolmogorov timescale.

In the turbulent channel we observe various forms of the autocorrelation of acceleration depending on the component of the acceleration and the initial distance to the wall. Specifically, the autocorrelation of the streamwise component of acceleration has a weak to non-existent tendency to be negatively correlated, meaning the zero-crossing time of these curves do not robustly characterize the time scales of the process.

As a compromise, we propose the definition shown in equation A.1, where τ_c is the time lag at which the autocorrelation first crosses 0.05, for both the acceleration and velocity timescales. This definition has the following advantages:

1. Small ($\approx$ %5) error between this definition and the classical definition for the time scale of velocity, which is A.1 with $\tau_c \to \infty$, as if we assume $\rho_v \approx \exp(-At)$, then

$$T_v = \int_0^{\tau_c} \exp(-A\tau)(\tau, y_0)\, d\tau$$
$$T_v = A(1 - \tau_c)$$

2. Less sensitive to measurement noise and/or lack of statistical convergence than the zero-crossing time.

3. Permits a consistent definition of time scales for acceleration and velocity.

A.2 Lagrangian correlations (complete)

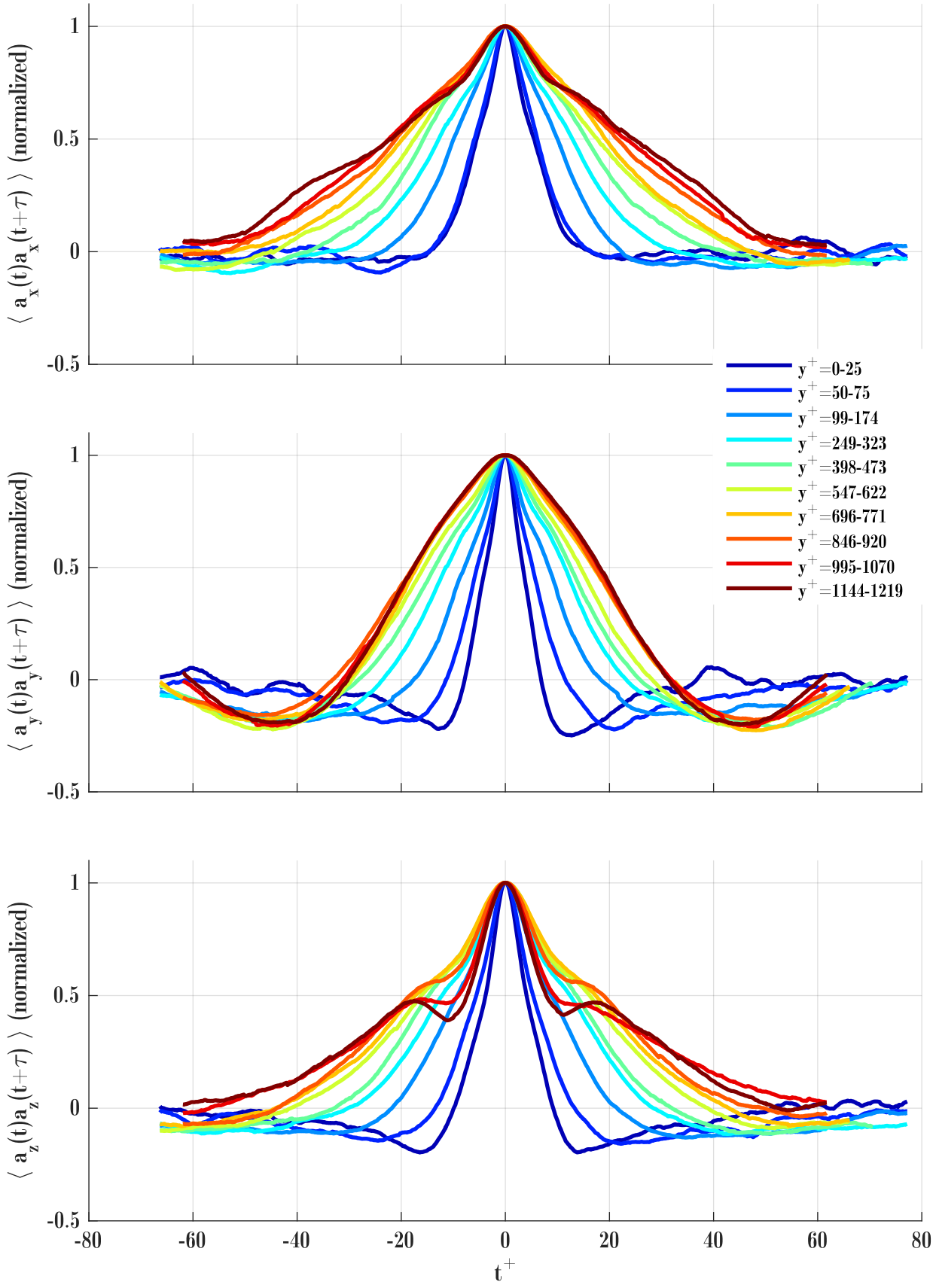

Figure A.1: Lagrangian autocorrelations of acceleration for the streamwise (x), wall-normal (y), and spanwise (z) components of acceleration.

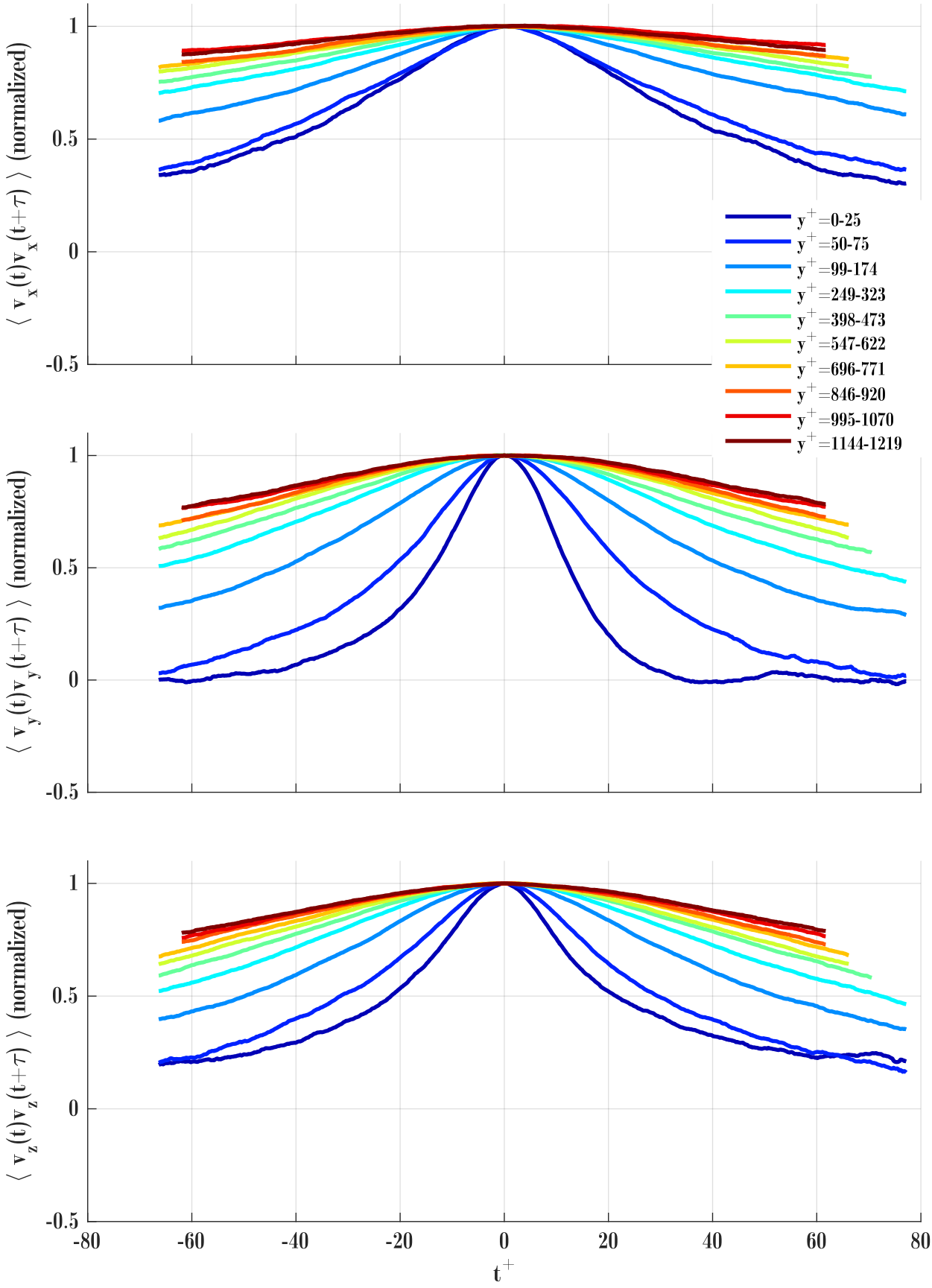

Figure A.2: Lagrangian autocorrelations of velocity for the streamwise (x), wall-normal (y), and spanwise (z) components of velocity.

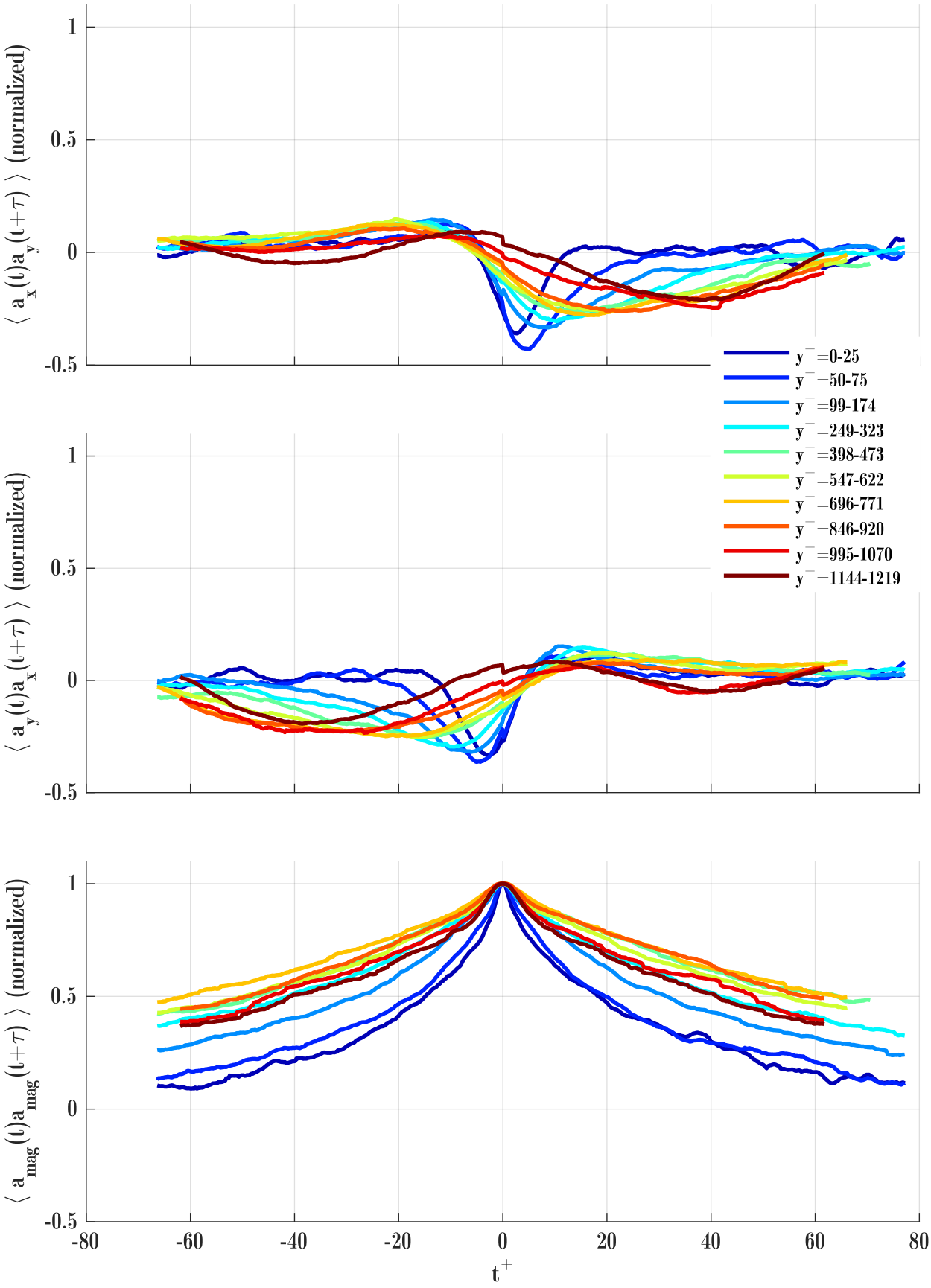

Figure A.3: Lagrangian correlations of the streamwise and wall-normal components of acceleration.

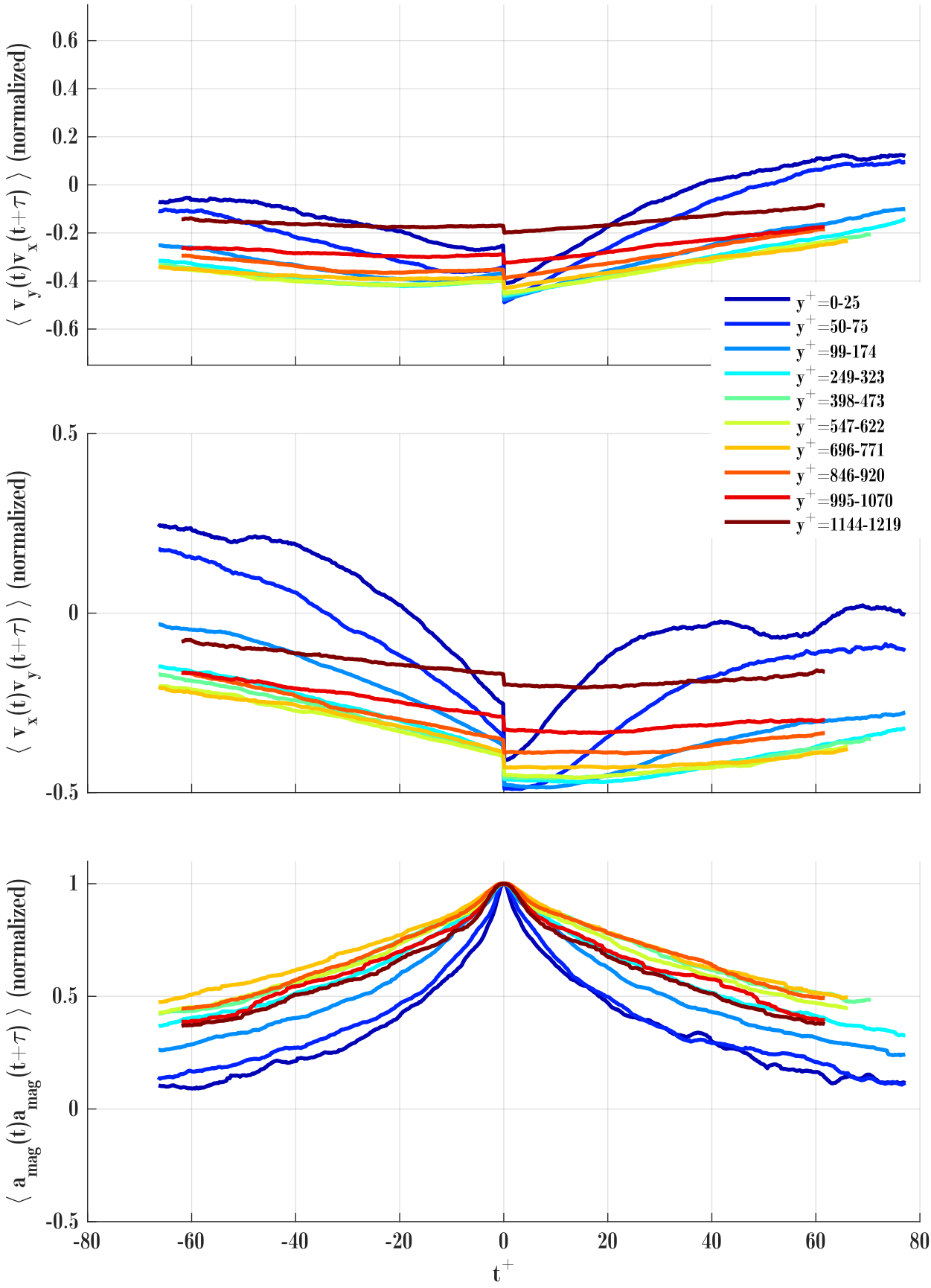

Figure A.4: Lagrangian correlations of the streamwise and wall-normal components of velocity.

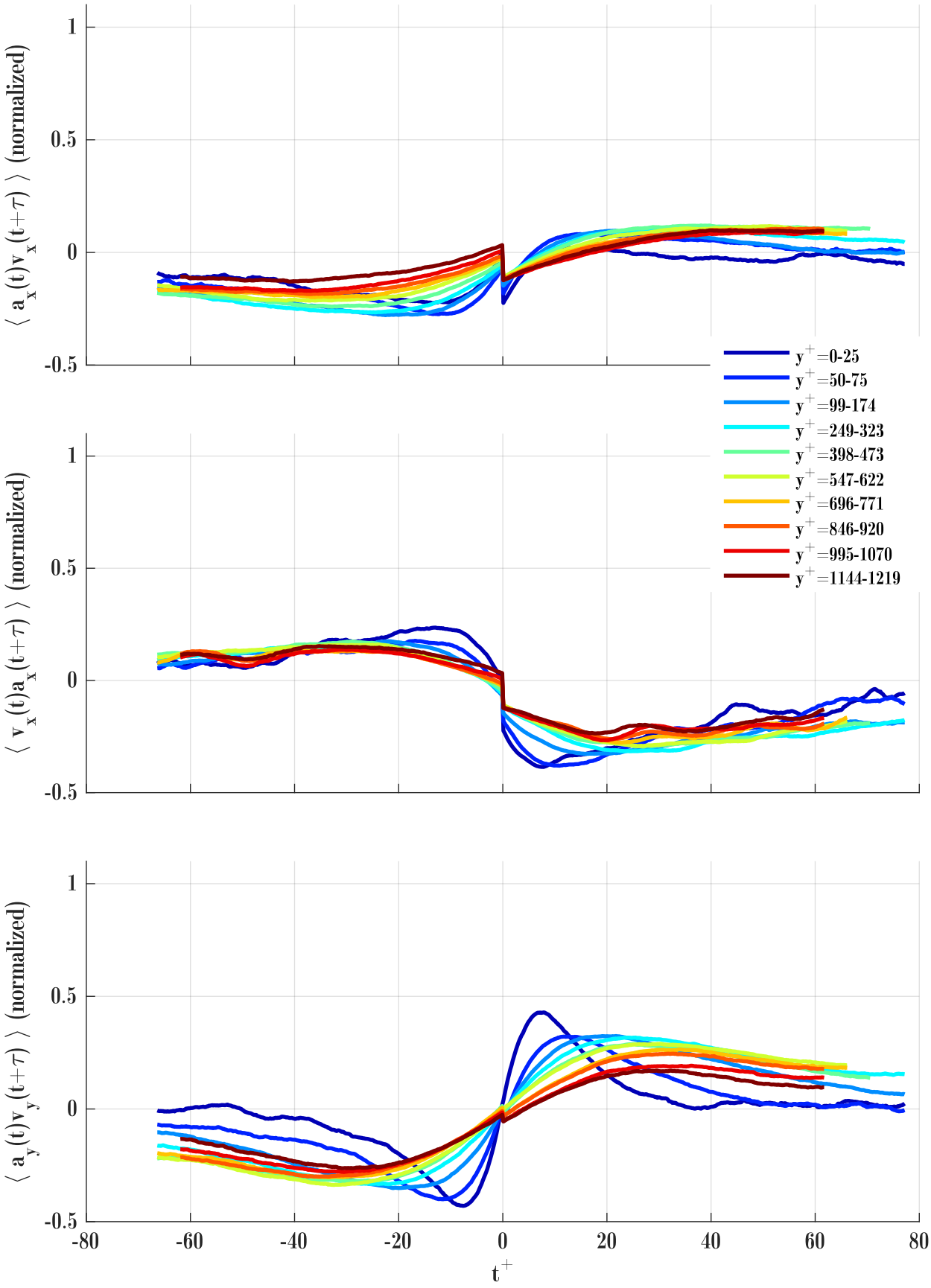

Figure A.5: Lagrangian cross-correlations of acceleration and velocity (same component)

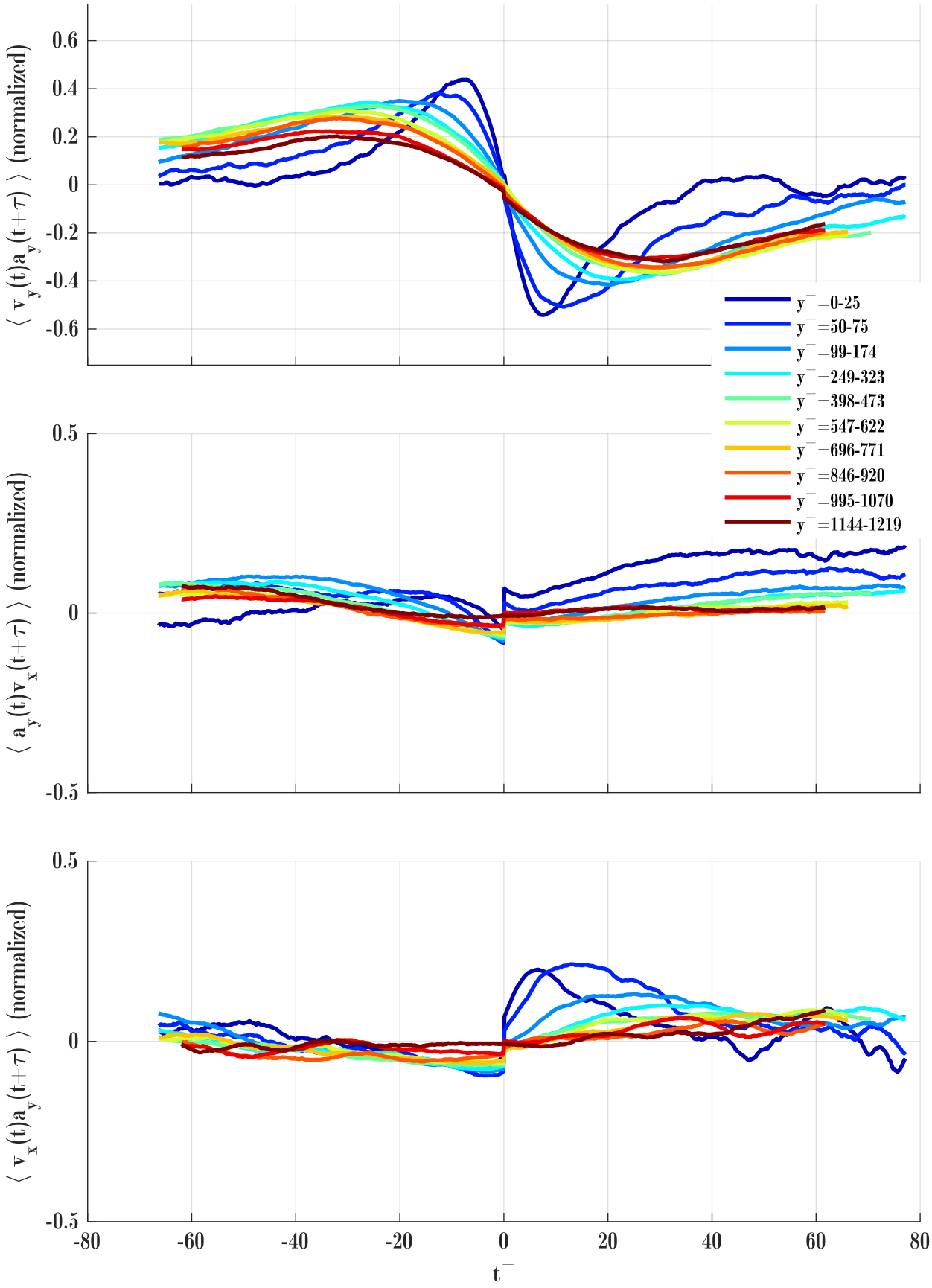

Figure A.6: Lagrangian cross-correlations of acceleration and velocity (different component)

A.3 Autocorrelations of acceleration for tracer and non-tracer particles

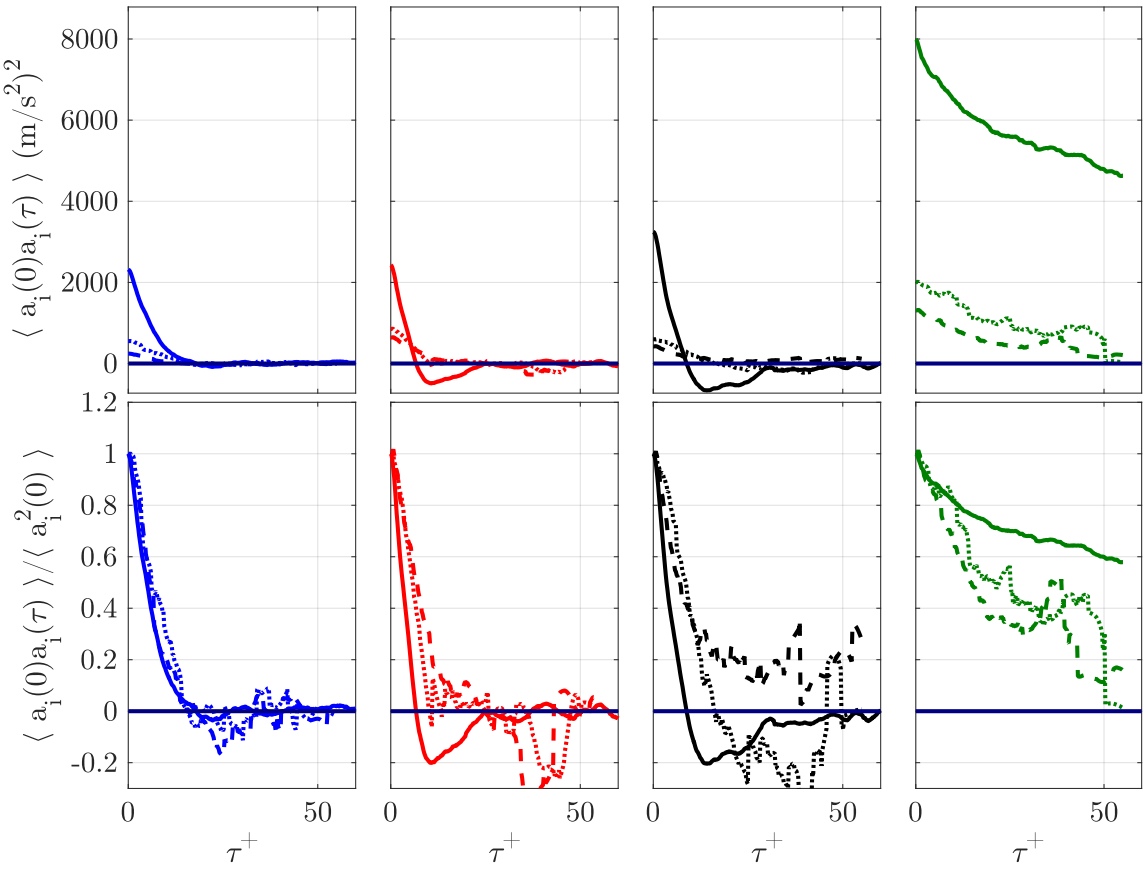

Figure A.7: Non-normalized autocorrelations of acceleration ($\langle a_i(0)a_i(\tau)\rangle$) for the three classes of particle. The autocorrelations are calculated from trajectories that are in the bin $y^+ = 0 - 37.5$ at $t = 0$.

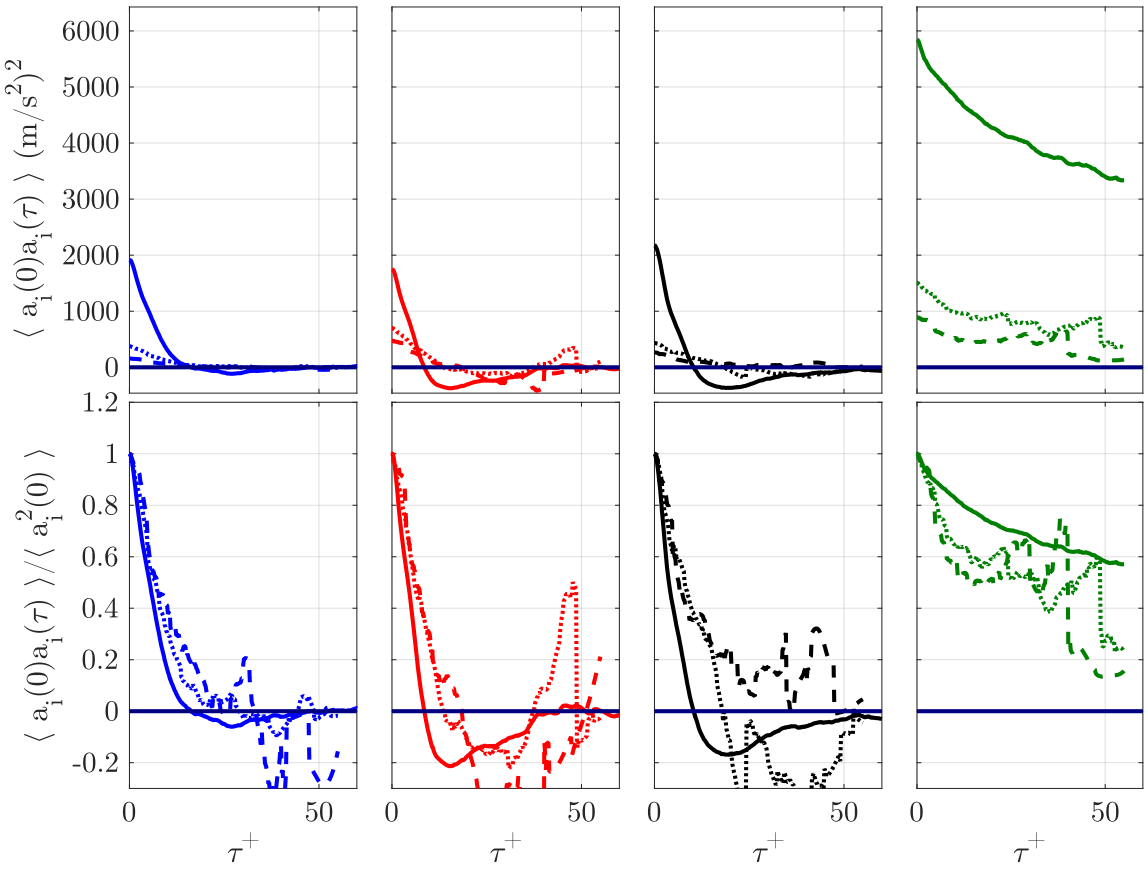

Figure A.8: Non-normalized autocorrelations of acceleration ($\langle a_i(0)a_i(\tau)\rangle$) for the three classes of particle. The autocorrelations are calculated from trajectories that are in the bin $y^+ = 37.5 - 75$ at $t = 0$.

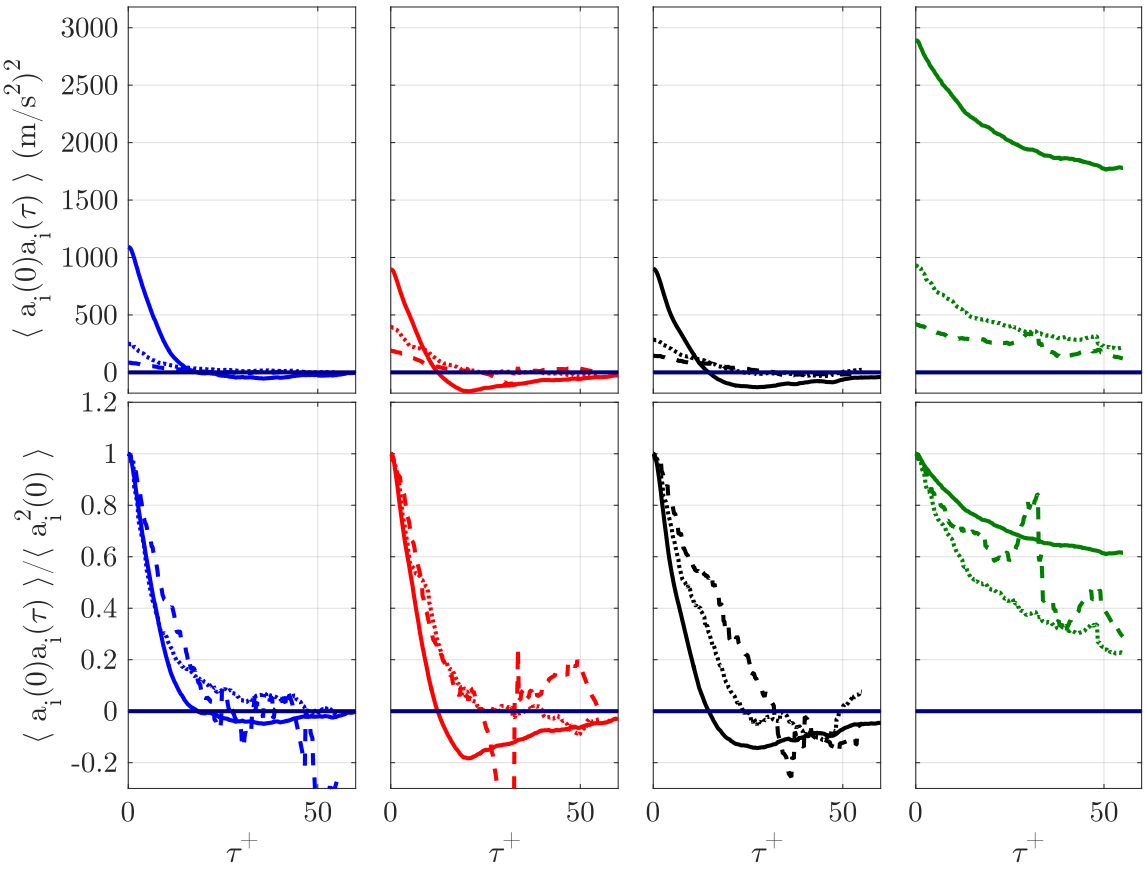

Figure A.9: Non-normalized autocorrelations of acceleration ($\langle a_i(0)a_i(\tau)\rangle$) for the three classes of particle. The autocorrelations are calculated from trajectories that are in the bin $y^+ = 75-150$ at $t = 0$.

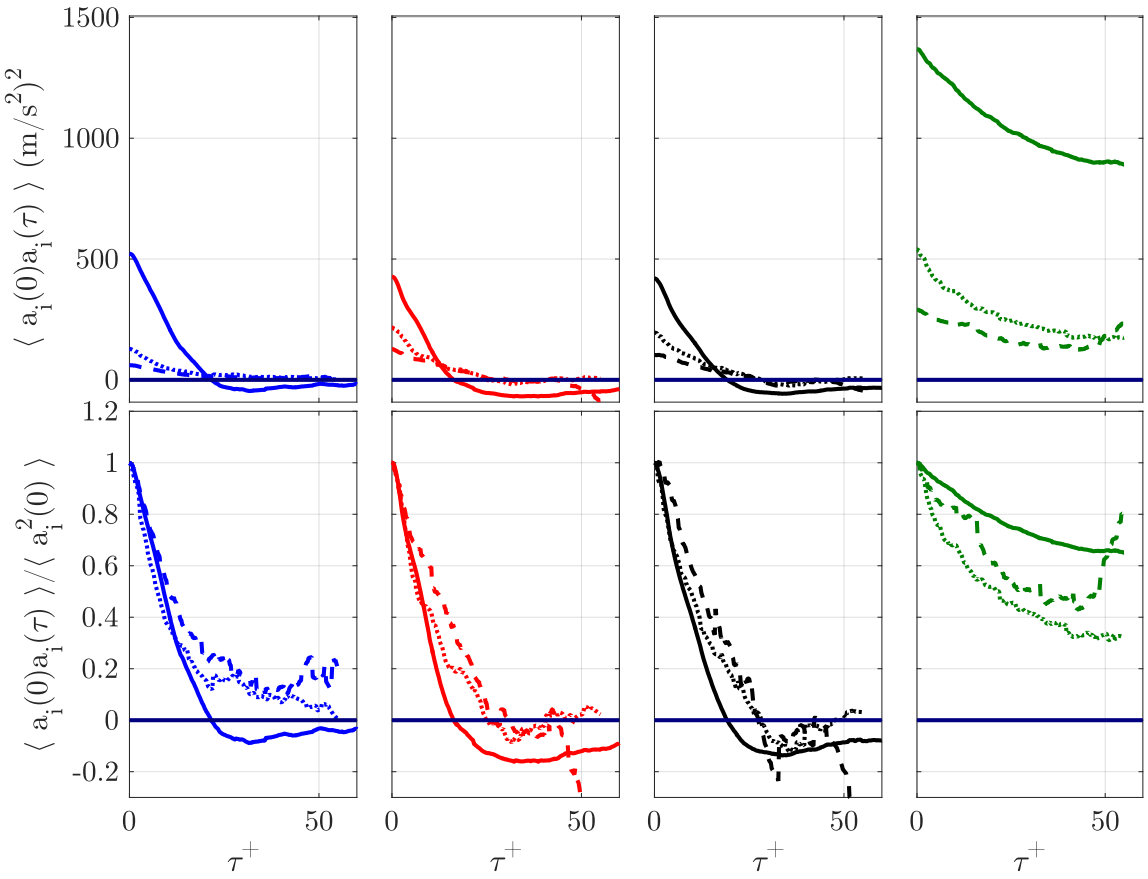

Figure A.10: Non-normalized autocorrelations of acceleration ($\langle a_i(0)a_i(\tau)\rangle$) for the three classes of particle. The autocorrelations are calculated from trajectories that are in the bin $y^+ = 150 - 225$ at $t = 0$.

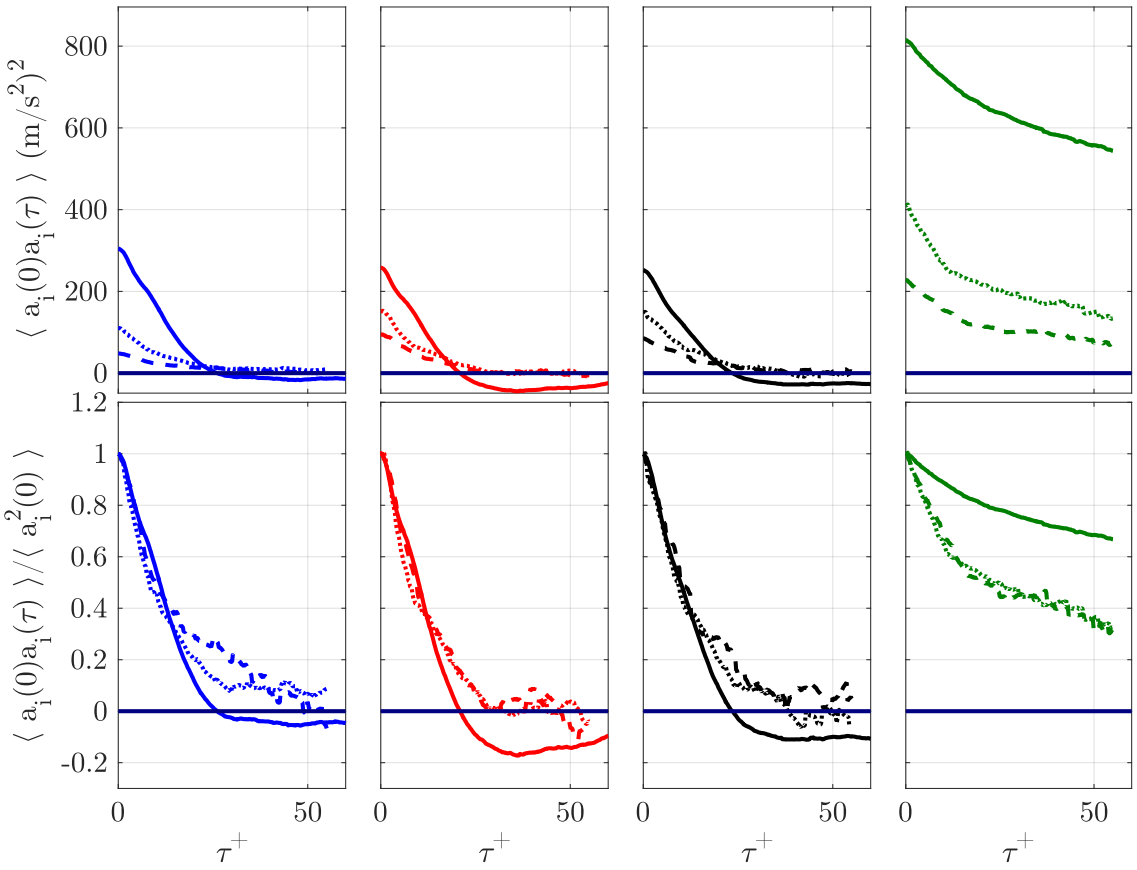

Figure A.11: Non-normalized autocorrelations of acceleration ($\langle a_i(0)a_i(\tau)\rangle$) for the three classes of particle. The autocorrelations are calculated from trajectories that are in the bin $y^+ = 225 - 300$ at $t = 0$.

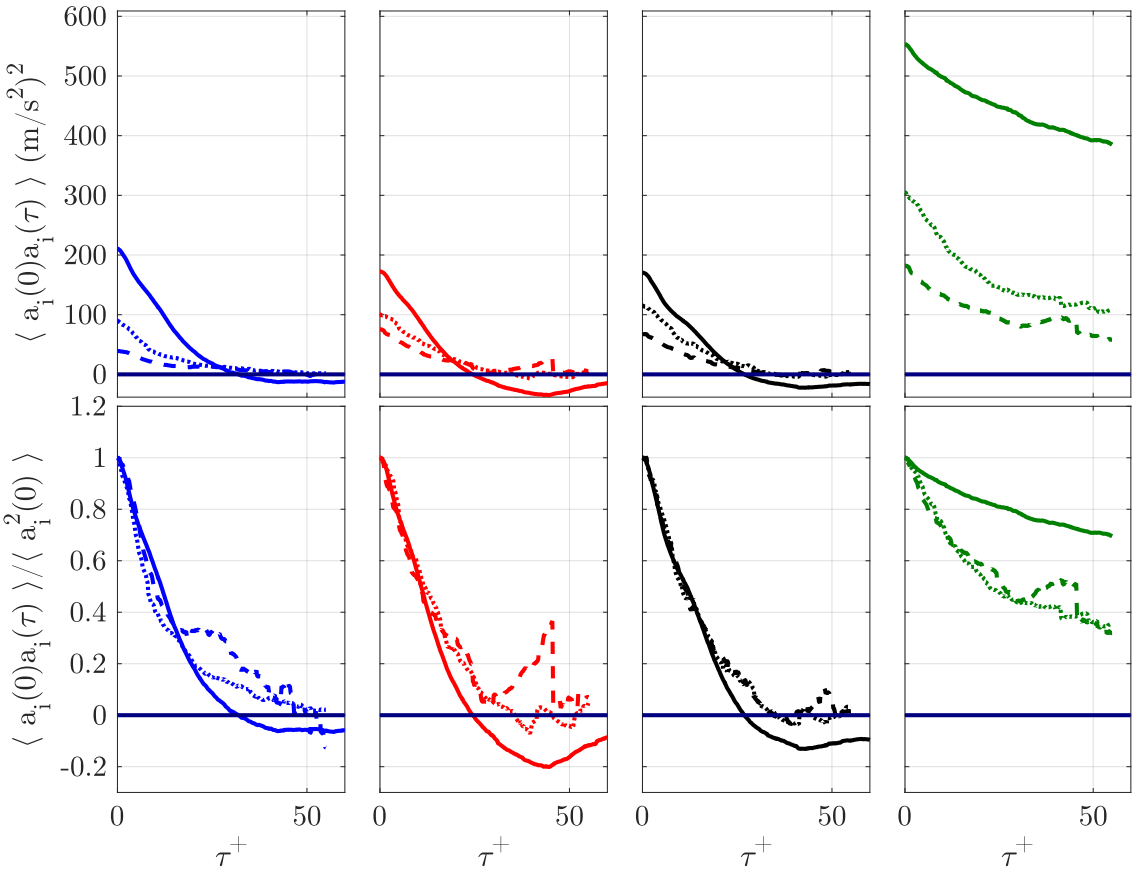

Figure A.12: Non-normalized autocorrelations of acceleration ($\langle a_i(0)a_i(\tau)\rangle$) for the three classes of particle. The autocorrelations are calculated from trajectories that are in the bin $y^+ = 300-375$ at $t = 0$.

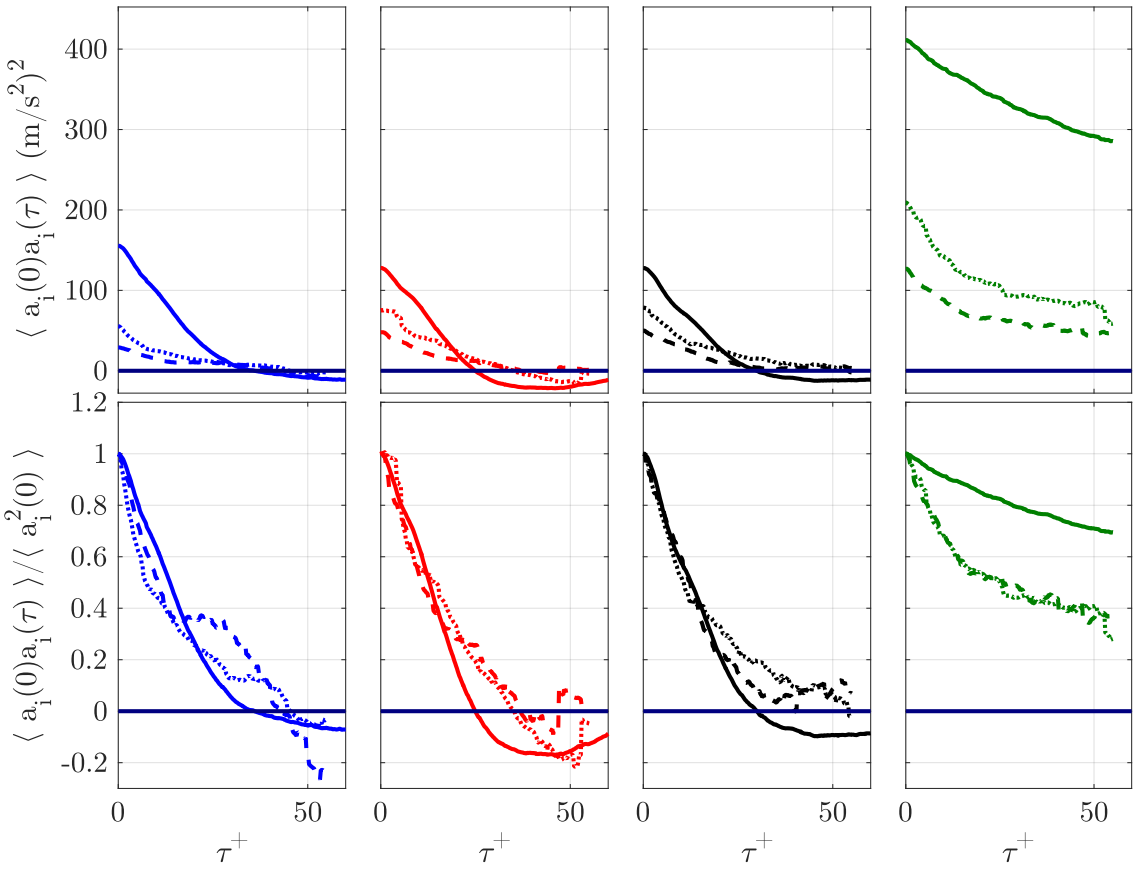

Figure A.13: Non-normalized autocorrelations of acceleration ($\langle a_i(0)a_i(\tau)\rangle$) for the three classes of particle. The autocorrelations are calculated from trajectories that are in the bin $y^+ = 375 - 450$ at $t = 0$.

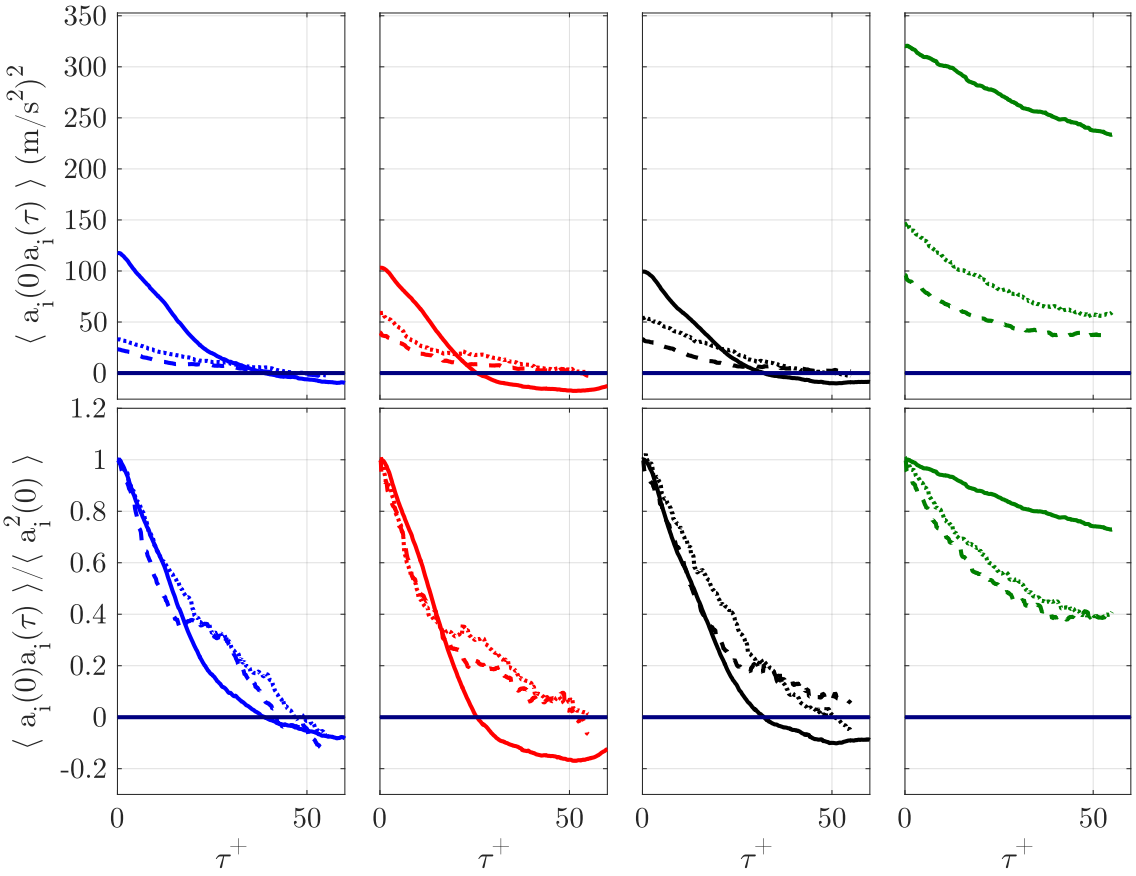

Figure A.14: Non-normalized autocorrelations of acceleration ($\langle a_i(0)a_i(\tau)\rangle$) for the three classes of particle. The autocorrelations are calculated from trajectories that are in the bin $y^+ = 450 - 525$ at $t = 0$.

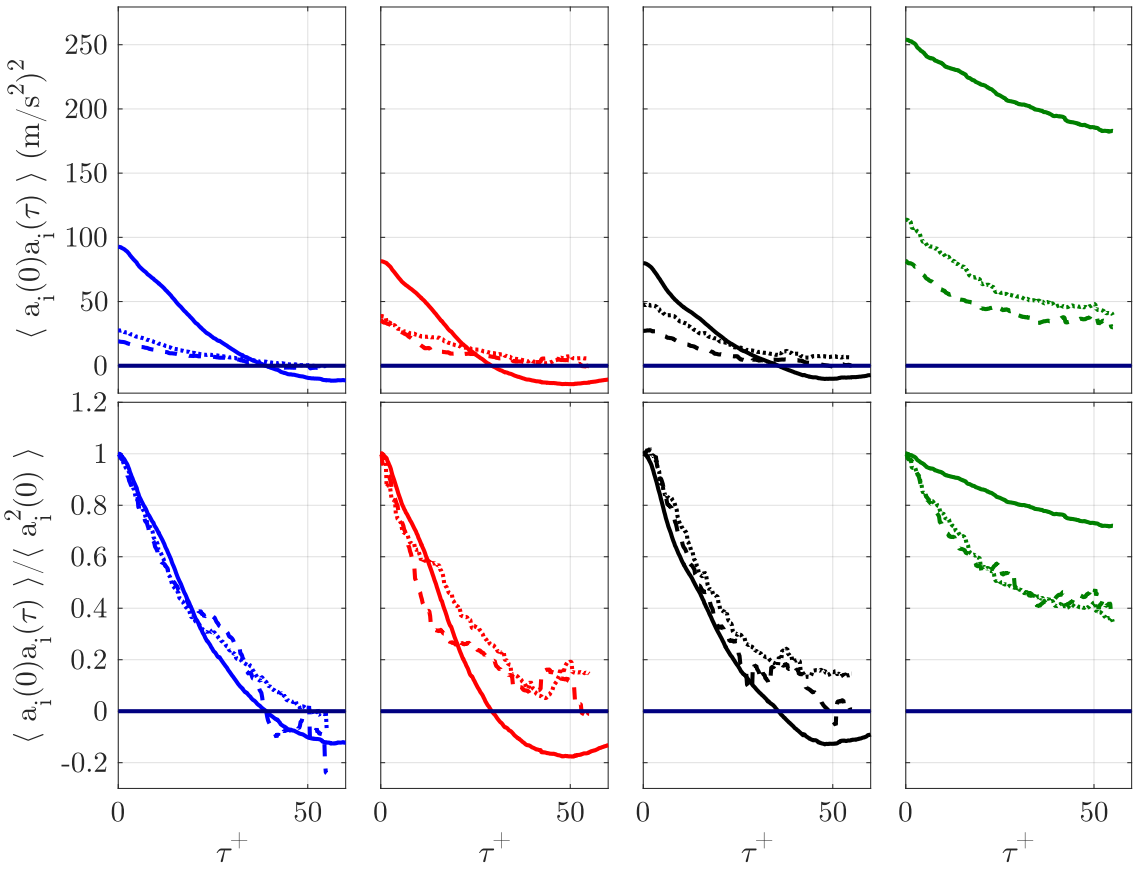

Figure A.15: Non-normalized autocorrelations of acceleration ($\langle a_i(0)a_i(\tau)\rangle$) for the three classes of particle. The autocorrelations are calculated from trajectories that are in the bin $y^+ = 525 - 600$ at $t = 0$.

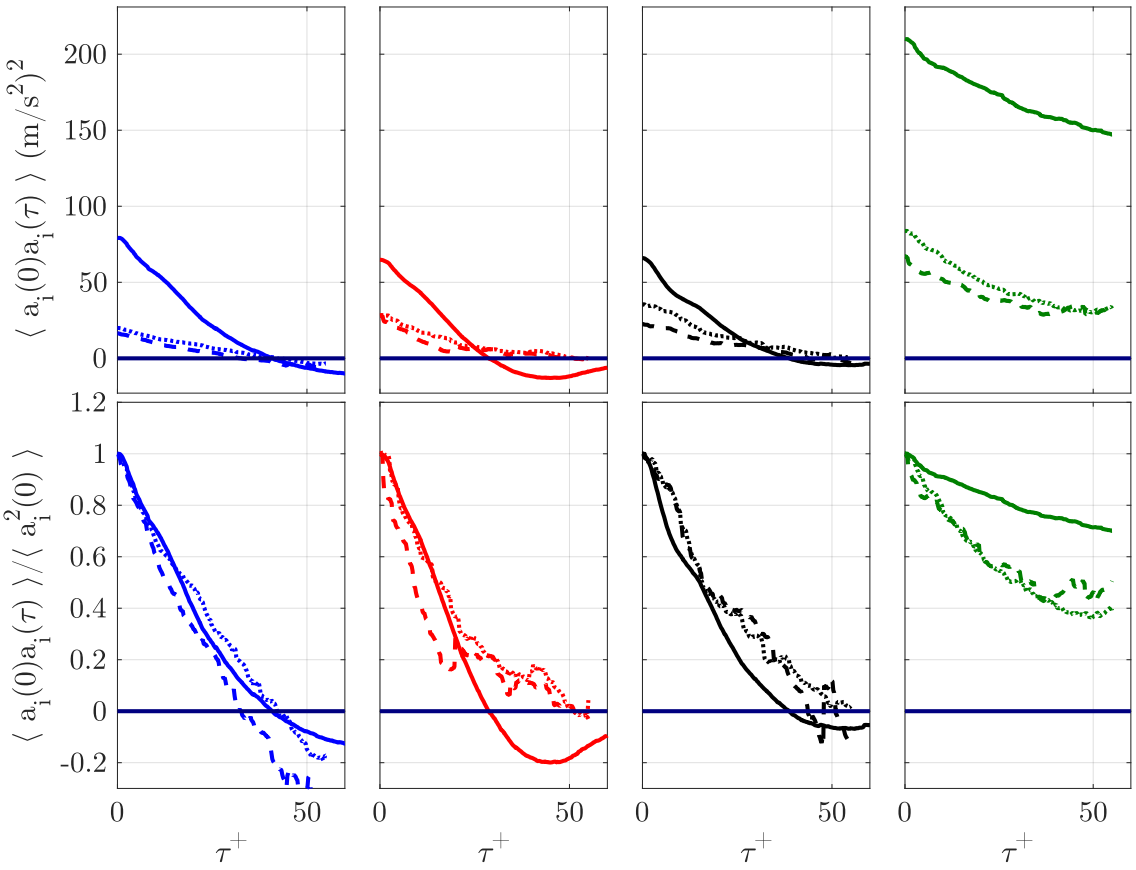

Figure A.16: Non-normalized autocorrelations of acceleration ($\langle a_i(0)a_i(\tau)\rangle$) for the three classes of particle. The autocorrelations are calculated from trajectories that are in the bin $y^+ = 600 - 675$ at $t = 0$.

Bibliography

[1] N. Mordant, P. Metz, O. Michel, and J.-F. Pinton, "Measurement of lagrangian velocity in fully developed turbulence," *Physical Review Letters*, vol. 87, no. 21, p. 214501, 2001. vii, 10, 13

[2] R. J. Adrian, "Hairpin vortex organization in wall turbulence," *Physics of Fluids*, vol. 19, no. 4, p. 041301, 2007. vii, 18

[3] R. Zamansky, I. Vinkovic, and M. Gorokhovski, "Acceleration in turbulent channel flow: universalities in statistics, subgrid stochastic models and an application," *Journal of Fluid Mechanics*, vol. 721, pp. 627–668, 2013. viii, 18, 27, 28, 74, 93, 94, 95, 96, 100, 119, 132

[4] R. D. Brown, Z. Warhaft, and G. A. Voth, "Acceleration statistics of neutrally buoyant spherical particles in intense turbulence," *Physical review letters*, vol. 103, no. 19, p. 194501, 2009. ix, 39, 141, 154, 155

[5] M. Van Dyke and M. Van Dyke, *An album of fluid motion*, vol. 176. Parabolic Press Stanford, 1982. 4

[6] N. Gnedin, S. Glover, R. Klessen, V. Springel, Y. Revaz, P. Jablonka, R. Teyssier, and L. Mayer, *Star Formation in Galaxy Evolution: Connecting Numerical Models to Reality: Saas-Fee Advanced Course 43. Swiss Society for Astrophysics and Astronomy*. Saas-Fee Advanced Course, Springer Berlin Heidelberg, 2015. 4

[7] O. Reynolds, "An experimental investigation of the circumstances which determine whether the motion of water shall be direct or sinuous, and of the law of resistance in parallel channels," *Philosophical Transactions of the Royal Society of London*, vol. 174, pp. 935–982, 1883. 4

[8] A. Tsinober, *An informal introduction to turbulence*, vol. 63. Springer Science & Business Media, 2001. 5, 15

[9] P. Kundu and I. Cohen, *Fluid Mechanics*. Elsevier Science, 2010. 5

[10] Pope, Stephen B., *Turbulent Flows*. Cambridge University Press, 2000. 5, 7, 15, 16, 20, 34, 61, 78, 108, 110

[11] U. Frisch and A. Kolmogorov, *Turbulence: The Legacy of A. N. Kolmogorov*. Cambridge University Press, 1995. 8

[12] A. Monin and A. Yaglom, *Statistical Fluid Mechanics: Mechanics of Turbulence, Vol. I and II*. MIT Press, Cambridge, Mass, 1971. 9, 102

[13] G. Falkovich, H. Xu, A. Pumir, E. Bodenschatz, L. Biferale, G. Boffetta, A. S. Lanotte, F. Toschi, and I. C. for Turbulence Research), "On lagrangian single-particle statistics," *Physics of Fluids*, vol. 24, no. 5, p. 055102, 2012. 9

[14] H. Tennekes and J. L. Lumley, *A first course in turbulence*. MIT press, 1972. 10, 106

[15] H. Xu, M. Bourgoin, N. T. Ouellette, E. Bodenschatz, *et al.*, "High order lagrangian velocity statistics in turbulence," *Physical review letters*, vol. 96, no. 2, p. 024503, 2006. 10, 13

[16] P. Yeung and S. Pope, "Lagrangian statistics from direct numerical simulations of isotropic turbulence," *Journal of Fluid Mechanics*, vol. 207, pp. 531–586, 1989. 11, 13, 26, 128, 131, I

[17] A. Reynolds, "Superstatistical mechanics of tracer-particle motions in turbulence," *Physical review letters*, vol. 91, no. 8, p. 084503, 2003. 11, 27

[18] A. Reynolds, "Superstatistical lagrangian stochastic modeling," *Physica A: Statistical Mechanics and its Applications*, vol. 340, no. 1, pp. 298–308, 2004. 11, 27

[19] Davidson, P. A., *Turbulence: An introduction for scientists and engineers*. Oxford University Press, 2004. 11

[20] H. Xu, N. T. Ouellette, E. Bodenschatz, *et al.*, "Multifractal dimension of lagrangian turbulence," *Physical review letters*, vol. 96, no. 11, p. 114503, 2006. 11

[21] L. Chevillard, S. Roux, E. Lévêque, N. Mordant, J.-F. Pinton, and A. Arnéodo, "Lagrangian velocity statistics in turbulent flows: Effects of dissipation," *Physical review letters*, vol. 91, no. 21, p. 214502, 2003. 11

[22] A. Arnéodo, R. Benzi, J. Berg, L. Biferale, E. Bodenschatz, A. Busse, E. Calzavarini, B. Castaing, M. Cencini, L. Chevillard, *et al.*, "Universal intermittent properties of particle trajectories in highly turbulent flows," *Physical Review Letters*, vol. 100, no. 25, p. 254504, 2008. 11, 13

[23] J. C. Hunt, "Lewis fry richardson and his contributions to mathematics, meteorology, and models of conflict," *Annual Review of Fluid Mechanics*, vol. 30, no. 1, pp. xiii–xxxvi, 1998. 11

[24] P. Yeung, "Lagrangian investigations of turbulence," *Annual review of fluid mechanics*, vol. 34, no. 1, pp. 115–142, 2002. 11

[25] P. Yeung, D. Donzis, and K. Sreenivasan, "Dissipation, enstrophy and pressure statistics in turbulence simulations at high reynolds numbers," *Journal of Fluid Mechanics*, vol. 700, pp. 5–15, 2012. 11

[26] R.-C. Lien and E. A. D'Asaro, "The kolmogorov constant for the lagrangian velocity spectrum and structure function," *Physics of Fluids*, vol. 14, no. 12, pp. 4456–4459, 2002. 12

[27] B. L. Sawford and P. Yeung, "Kolmogorov similarity scaling for one-particle lagrangian statistics," *Physics of Fluids*, vol. 23, no. 9, p. 091704, 2011. 13

[28] L. Biferale, E. Bodenschatz, M. Cencini, A. S. Lanotte, N. T. Ouellette, F. Toschi, and H. Xu, "Lagrangian structure functions in turbulence: A quantitative comparison between experiment and direct numerical simulation," *Physics of Fluids*, vol. 20, no. 6, p. 065103, 2008. 13

[29] M. Borgas and B. Sawford, "The small-scale structure of acceleration correlations and its role in the statistical theory of turbulent dispersion," *Journal of fluid mechanics*, vol. 228, pp. 295–320, 1991. 13

[30] G. A. Voth, A. la Porta, A. M. Crawford, J. Alexander, and E. Bodenschatz, "Measurement of particle accelerations in fully developed turbulence," *Journal of Fluid Mechanics*, vol. 469, pp. 121–160, 2002. 13, 27, 60, 69, 139, 141, 154, 161

[31] N. Mordant, A. M. Crawford, and E. Bodenschatz, "Experimental lagrangian acceleration probability density function measurement," *Physica D: Nonlinear Phenomena*, vol. 193, no. 1, pp. 245–251, 2004. 13, 56, 122, 126

[32] P. Vedula and P. Yeung, "Similarity scaling of acceleration and pressure statistics in numerical simulations of isotropic turbulence," *Physics of Fluids*, vol. 11, no. 5, pp. 1208–1220, 1999. 13

[33] L. Biferale, G. Boffetta, A. Celani, B. J. Devenish, A. Lanotte, and F. Toschi, "Multifractal statistics of lagrangian velocity and acceleration in turbulence," *Physical Review Letters*, vol. 93, no. 6, 2004-08-04. 00174. 13

[34] B. L. Sawford, P. K. Yeung, M. S. Borgas, P. Vedula, A. La Porta, A. M. Crawford, and E. Bodenschatz, "Conditional and unconditional acceleration statistics in turbulence," vol. 15, no. 11, p. 3478, 2003. 00058. 13, 152, 153

[35] N. Mordant, A. M. Crawford, and E. Bodenschatz, "Three-dimensional structure of the lagrangian acceleration in turbulent flows," *Physical review letters*, vol. 93, no. 21, p. 214501, 2004. 13, 128, 132, 133, 154, 161

[36] L. Biferale, G. Boffetta, A. Celani, A. Lanotte, and F. Toschi, "Particle trapping in three-dimensional fully developed turbulence," *Physics of Fluids*, vol. 17, no. 2, p. 021701, 2005. 13

[37] F. Toschi, L. Biferale, G. Boffetta, A. Celani, B. J. Devenish, and A. Lanotte, "Acceleration and vortex filaments in turbulence," *Journal of Turbulence*, vol. 6, p. N15, 2005. 14, 83, 126, 161

[38] B. Sawford, "Reynolds number effects in lagrangian stochastic models of turbulent dispersion," *Physics of Fluids A: Fluid Dynamics*, vol. 3, no. 6, pp. 1577–1586, 1991. 14, 23, 119, 130, 131

[39] A. Reynolds, "A second-order lagrangian stochastic model for particle trajectories in inhomogeneous turbulence," *Quarterly Journal of the Royal Meteorological Society*, vol. 125, no. 557, pp. 1735–1746, 1999. 14, 24

[40] A. M. Crawford, N. Mordant, and E. Bodenschatz, "Joint statistics of the lagrangian acceleration and velocity in fully developed turbulence," *Physical Review Letters*, vol. 94, no. 2, 2005-01-18. 14

[41] S. Hoyas and J. Jiménez, "Scaling of the velocity fluctuations in turbulent channels up to re_τ=2003," *Physics of Fluids*, vol. 18, no. 1, p. 011702, 2006-01. 16

[42] N. Stelzenmuller, J. I. Polanco, L. Vignal, I. Vinkovic, and N. Mordant, "Lagrangian acceleration statistics in a turbulent channel flow," *Physical Review Fluids*, vol. 2, no. 5, p. 054602, 2017. 17, 70, 74, 84, 152

[43] N. Mansour, J. Kim, and P. Moin, "Reynolds-stress and dissipation-rate budgets in a turbulent channel flow," *Journal of Fluid Mechanics*, vol. 194, pp. 15–44, 1988. 17

[44] S. Hoyas and J. Jiménez, "Reynolds number effects on the reynolds-stress budgets in turbulent channels," *Physics of Fluids*, vol. 20, no. 10, p. 101511, 2008. 17

[45] A. Pumir, H. Xu, and E. D. Siggia, "Small-scale anisotropy in turbulent boundary layers," *Journal of Fluid Mechanics.*, vol. 804, pp. 5–23, 2016. 18, 128

[46] A. J. Smits, B. J. McKeon, and I. Marusic, "High–Reynolds Number Wall Turbulence," *Annual Review of Fluid Mechanics*, vol. 43, no. 1, pp. 353–375, 2011. 18, 120

[47] J. Jeong, F. Hussain, W. Schoppa, and J. Kim, "Coherent structures near the wall in a turbulent channel flow," *Journal of Fluid Mechanics*, vol. 332, p. 185–214, 1997. 18

[48] K. T. Christensen and R. J. Adrian, "The velocity and acceleration signatures of small-scale vortices in turbulent channel flow," *Journal of Turbulence*, vol. 3, no. 23, 2002. 18

[49] S. Herpin, M. Stanislas, and J. Soria, "The organization of near-wall turbulence: a comparison between boundary layer spiv data and channel flow dns data," *Journal of Turbulence*, vol. 11, p. N47, 2010. 18

[50] G. I. Taylor, "Diffusion by continuous movements," *Proceedings of the London Mathematical Society*, vol. 2, no. 1, pp. 196–212, 1922. 19, 119

[51] D. S. Lemons and A. Gythiel, "Paul langevin's 1908 paper "on the theory of brownian motion"["sur la théorie du mouvement brownien," cr acad. sci.(paris) 146, 530–533 (1908)]," *American Journal of Physics*, vol. 65, no. 11, pp. 1079–1081, 1997. 20

[52] B. L. Sawford, P. K. Yeung, and J. F. Hackl, "Reynolds number dependence of relative dispersion statistics in isotropic turbulence," *Physics of Fluids*, vol. 20, no. 6, p. 065111, 2008. 22

[53] S. B. Pope, "Simple models of turbulent flows a," *Physics of Fluids*, vol. 23, no. 1, p. 011301, 2011. 23

[54] S. B. Pope, "Lagrangian pdf methods for turbulent flows," *Annual review of fluid mechanics*, vol. 26, no. 1, pp. 23–63, 1994. 23, 119

[55] S. B. Pope, "A stochastic lagrangian model for acceleration in turbulent flows," *Physics of Fluids*, vol. 14, no. 7, p. 2360, 2002. 24, 26, 120, 166

[56] D. Thomson, "Criteria for the selection of stochastic models of particle trajectories in turbulent flows," *Journal of Fluid Mechanics*, vol. 180, pp. 529–556, 1987. 24

[57] N. van Kampen, *Stochastic processes in physics and chemistry*. Elsevier, 2007. 24

[58] C. W. Gardiner, *Stochastic methods*. Springer-Verlag, Berlin–Heidelberg–New York–Tokyo, 1985. 24

[59] S. Pope, "A lagrangian two-time probability density function equation for inhomogeneous turbulent flows," *The Physics of fluids*, vol. 26, no. 12, pp. 3448–3450, 1983. 25

[60] D. C. Haworth and S. B. Pope, "A generalized langevin model for turbulent flows," *Physics of Fluids*, vol. 29, no. 2, p. 387, 1986. 25

[61] S. B. Pope, "Stochastic lagrangian models of velocity in homogeneous turbulent shear flow," *Physics of Fluids*, vol. 14, no. 5, pp. 1696–1702, 2002-05. 25

[62] M. P. B. Veenman, *Statistical analysis of turbulent pipe flow: A numerical approach*. Tue Universiteitsbibliotheek, 2004. 25

[63] R. J. E. Walpot, C. W. M. van der Geld, and J. G. M. Kuerten, "Determination of the coefficients of langevin models for inhomogeneous turbulent flows by three-dimensional particle tracking velocimetry and direct numerical simulation," *Physics of Fluids*, vol. 19, no. 4, p. 045102, 2007. 00023. 25, 28, 120

[64] A. Tanière, B. Arcen, B. Oesterlé, and J. Pozorski, "Study on langevin model parameters of velocity in turbulent shear flows," *Physics of Fluids*, vol. 22, no. 11, p. 115101, 2010. 25, 28, 120, 166

[65] A. M. Reynolds, "Stochastic simulation of lagrangian trajectories in near-wall turbulence," *Physics of Fluids*, vol. 18, no. 7, p. 075107, 2006. 26

[66] A. K. Aringazin and M. I. Mazhitov, "Stochastic models of lagrangian acceleration of fluid particle in developed turbulence," *International Journal of Modern Physics B*, vol. 18, no. 23, pp. 3095–3168, 2004. 26

[67] S. B. Pope and Y. L. Chen, "The velocity-dissipation probability density function model for turbulent flows," *Physics of Fluids A: Fluid Dynamics*, vol. 2, no. 8, pp. 1437–1449, 1990. 26, 27, 120

[68] A. La Porta, G. A. Voth, A. M. Crawford, J. Alexander, and E. Bodenschatz, "Fluid particle accelerations in fully developed turbulence," *Nature*, vol. 409, no. 6823, pp. 1017–1019, 2001. 27, 120, 132

[69] A. G. Lamorgese, S. B. Pope, P. K. Yeung, and B. L. Sawford, "A conditionally cubic-gaussian stochastic lagrangian model for acceleration in isotropic turbulence," *Journal of Fluid Mechanics*, vol. 582, p. 423, 2007-07. 27

[70] N. Mordant, J. Delour, E. Léveque, A. Arnéodo, and J.-F. Pinton, "Long time correlations in lagrangian dynamics: A key to intermittency in turbulence," *Physical Review Letters*, vol. 89, no. 25, 2002-12-03. 27, 120

[71] E. Bacry, J. Delour, and J.-F. Muzy, "Multifractal random walk," *Physical Review E*, vol. 64, no. 2, p. 026103, 2001. 27

[72] V. Sabel'nikov, A. Chtab-Desportes, and M. Gorokhovski, "New sub-grid stochastic acceleration model in LES of high-reynolds-number flows," *The European Physical Journal B*, vol. 80, no. 2, pp. 177–187, 2011-03. 27, 132

[73] S. Gerashchenko, N. Sharp, S. Neuscamman, and Z. Warhaft, "Lagrangian measurements of inertial particle accelerations in a turbulent boundary layer," *Journal of Fluid Mechanics*, vol. 617, 2008. 28, 29, 120, 139, 140, 146, 156, 165

[74] S. Ayyalasomayajula, A. Gylfason, L. R. Collins, E. Bodenschatz, and Z. Warhaft, "Lagrangian measurements of inertial particle accelerations in grid generated wind tunnel turbulence," *Physical Review Letters*, vol. 97, no. 14, 2006-10-05. 28, 39

[75] J.-I. Choi, K. Yeo, and C. Lee, "Lagrangian statistics in turbulent channel flow," *Physics of Fluids*, vol. 16, no. 3, pp. 779–793, 2004-03. 28, 29, 89, 120, 123

[76] C. Lee, K. Yeo, and J.-I. Choi, "Intermittent nature of acceleration in near wall turbulence," *Physical Review Letters*, vol. 92, no. 14, 2004. 28, 120, 124, 127, 128

[77] J. G. M. Kuerten and J. J. H. Brouwers, "Lagrangian statistics of turbulent channel flow at $re_\tau = 950$ calculated with direct numerical simulation and langevin models," *Physics of Fluids*, vol. 25, no. 10, p. 105108, 2013. 28, 120

[78] K. Yeo, B.-G. Kim, and C. Lee, "On the near-wall characteristics of acceleration in turbulence," *Journal of Fluid Mechanics.*, vol. 659, pp. 405–419, 2010. 28, 84, 88, 89, 124

[79] R. J. E. Walpot, J. G. M. Kuerten, and C. W. M. van der Geld, "Experimental determination of lagrangian velocity statistics in turbulent pipe flow," *Flow, Turbulence and Combustion formerly: Applied Scientific Research*, vol. 76, no. 2, pp. 163–175, 2006. 28, 104

[80] J. L. G. Oliveira, C. W. M. van der Geld, and J. G. M. Kuerten, "Lagrangian and eulerian statistics of pipe flows measured with 3d-PTV at moderate and high reynolds numbers," *Flow, Turbulence and Combustion*, vol. 91, no. 1, pp. 105–137, 2013. 28, 29

[81] A. Schröder, R. Geisler, K. Staack, G. E. Elsinga, F. Scarano, B. Wieneke, A. Henning, C. Poelma, and J. Westerweel, "Eulerian and lagrangian views of a turbulent boundary layer flow using time-resolved tomographic PIV," vol. 50, no. 4, pp. 1071–1091, 2011-04. 28, 29

[82] J.-T. Kim, A. Liberzon, and L. P. Chamorro, "Characterisation of the eulerian and lagrangian accelerations in the intermediate field of turbulent circular jets," *Journal of Turbulence*, vol. 18, no. 1, pp. 87–102, 2017. 28, 89

[83] V. Mathai, E. Calzavarini, J. Brons, C. Sun, and D. Lohse, "Microbubbles and microparticles are not faithful tracers of turbulent acceleration," *Physical Review Letters*, vol. 117, no. 2, p. 024501, 2016. 35, 39, 138, 145

[84] N. M. Qureshi, M. Bourgoin, C. Baudet, A. Cartellier, and Y. Gagne, "Turbulent transport of material particles: An experimental study of finite size effects," *Physical Review Letters*, vol. 99, p. 184502, 2007. 35, 141

[85] Zagarola, M. V., *Mean-Flow Scaling of Turbulent Pipe Flow*. Phd thesis, Princeton University, 1996. 35

[86] D. R. B., "Reynolds number dependence of skin friction and other bulk flow variables in two-dimensional rectangular duct flow," *Journal of Fluids Engineering*, vol. 100, no. 2, pp. 215–223, 1978. 36

[87] J. P. Monty, *Developments in smooth wall turbulent duct flows*. Phd thesis, University of Melbourne, Department of Mechanical and Manufacturing Engineering, 2005. 36, 81

[88] G. Comte-Bellot and A. Craya, *Écoulement turbulent entre deux parois parallèles*. Service de documentation scientifique et technique de l'armement, 1965. 36, 81

[89] C. Lindquist, *Contrôle électromagnétique d'écoulements*. PhD thesis, Université Joseph Fourier, 2005. 37, 38

[90] R. Volk, E. Calzavarini, E. LéVêQue, and J.-F. Pinton, "Dynamics of inertial particles in a turbulent von kármán flow," vol. 668, pp. 223–235, 2011-02. 39, 141, 154, 159, 161

[91] J. Bec, L. Biferale, G. Boffetta, A. Celani, M. Cencini, A. Lanotte, S. Musacchio, and F. Toschi, "Acceleration statistics of heavy particles in turbulence," *Journal of Fluid Mechanics*, vol. 550, p. 349, 2006. 39, 153, 154, 156, 157

[92] S. Ayyalasomayajula, Z. Warhaft, and L. R. Collins, "Modeling inertial particle acceleration statistics in isotropic turbulence," *Physics of Fluids*, vol. 20, no. 9, p. 095104, 2008. 39, 139

[93] J. P. L. C. Salazar and L. R. Collins, "Inertial particle acceleration statistics in turbulence: Effects of filtering, biased sampling, and flow topology," *Physics of Fluids*, vol. 24, no. 8, p. 083302, 2012. 39, 139, 156, 160

[94] J. Kim, P. Moin, and R. Moser, "Turbulence statistics in fully developed channel flow at low reynolds number," *Journal of Fluid Mechanics*, vol. 177, p. 133, 1987. 39, 74, 79, 81, 96

[95] N. Ouellette, *Probing the statistical structure of turbulence with measurements of tracer particle tracks*. PhD thesis, Cornell University, 2006. 39

[96] C. J. Kähler, S. Scharnowski, and C. Cierpka, "On the uncertainty of digital PIV and PTV near walls," *Experiments in Fluids*, vol. 52, no. 6, pp. 1641–1656, 2012. 40, 70

[97] N. T. Ouellette, H. Xu, and E. Bodenschatz, "A quantitative study of three-dimensional lagrangian particle tracking algorithms," *Experiments in Fluids*, vol. 40, no. 2, pp. 301–313, 2006. 45, 53, 65, 121

[98] M. K. Cheezum, W. F. Walker, and W. H. Guilford, "Quantitative comparison of algorithms for tracking single fluorescent particles," *Biophysical journal*, vol. 81, no. 4, pp. 2378–2388, 2001. 45

[99] J. C. Crocker and D. G. Grier, "Methods of digital video microscopy for colloidal studies," *Journal of Colloid and Interface Science*, vol. 179, no. 1, pp. 298 – 310, 1996. 46

[100] R. C. E. Gonzalez, S. L. Woods, R. E. R. E. R. C. Gonzalez, R. E. Woods, and S. L. Eddins, *Digital image processing using MATLAB*. No. 04; TA1637, G6., 2004. 46

[101] N. Otsu, "A threshold selection method from gray-level histograms," *Automatica*, vol. 11, no. 285, pp. 23–27, 1975. 46

[102] T. Dracos, "Particle tracking velocimetry (PTV)," in *Three-Dimensional Velocity and Vorticity Measuring and Image Analysis Techniques: Lecture Notes from the Short Course held in Zürich, Switzerland, 3–6 September 1996* (T. Dracos, ed.), pp. 155–160, Springer Netherlands, 1996. 47

[103] Joshi, Basanta, Ohmi, Kazou, and Nose, Kazou, "Comparitive study of camera calibration models for 3d particle tracking velocimetry," *International Journal of Innovative Computing, Information, and Control*, vol. 9, no. 5, pp. 1971–1986, 2013. 49

[104] N. Machicoane, M. López-Caballero, M. Bourgoin, A. Aliseda, and R. Volk, "Improvements on particle tracking velocimetry: model-free calibration and noiseless measurement of second order statistics of the velocity field," *arXiv preprint arXiv:1605.03803*, 2016. 49

[105] Richard Hartley and Andrew Zisserman, *Multiple View Geometry in Computer Vision*. Cambridge University Press, second edition ed., 2003. 50, 51

[106] D. Garcia, "Robust smoothing of gridded data in one and higher dimensions with missing values," *Computational Statistics & Data Analysis*, vol. 54, no. 4, pp. 1167–1178, 2010. 55

[107] R. L. Allen and D. Mills, *Signal analysis: time, frequency, scale, and structure*. John Wiley & Sons, 2004. 56, 58

[108] Jucha, Jennifer, *Time-Symmetry Breaking in Turbulent Multi-Particle Dispersion*. Phd thesis, 2014. 60

[109] Efron, B and Tibshirani, R., "Bootstrap methods for standard errors, confidence intervals, and other measures of statistical accuracy," *Statistical Science*, vol. 1, no. 1, pp. 75–77, 1986. 63, 70

[110] R. Dean, "Reynolds number dependence of skin friction and other bulk flow variables in two-dimensional rectangular duct flow," *J. Fluids Eng*, vol. 100, no. 2, pp. 215–223, 1978. 63

[111] H. W. Coleman and W. G. Steele, *Experimentation, validation, and uncertainty analysis for engineers*. John Wiley & Sons, 2009. 63

[112] N. Mordant, E. Lévêque, and J.-F. Pinton, "Experimental and numerical study of the lagrangian dynamics of high reynolds turbulence," *New Journal of Physics*, vol. 6, pp. 116–116, 2004. 69, 83, 126

[113] Y. Feng, J. Goree, and B. Liu, "Errors in particle tracking velocimetry with high-speed cameras," *Review of Scientific Instruments*, vol. 82, no. 5, p. 053707, 2011. 70

[114] M. Buffat, L. Le Penven, and A. Cadiou, "An efficient spectral method based on an orthogonal decomposition of the velocity for transition analysis in wall bounded flow," *Computers & Fluids*, vol. 42, no. 1, pp. 62–72, 2011. 70

[115] J. P. Monty and M. S. Chong, "Turbulent channel flow: comparison of streamwise velocity data from experiments and direct numerical simulation," *Journal of Fluid Mechanics*, vol. 633, p. 461, 2009. 74

[116] E. Lamballais, M. Lesieur, and O. Métais, "Probability distribution functions and coherent structures in a turbulent channel," *Physical Review E*, vol. 56, pp. 6761–6766, 1997. 74

[117] A. T. Popovich and R. L. Hummel, "Experimental study of the viscous sublayer in turbulent pipe flow," *AIChE Journal*, vol. 13, no. 5, pp. 854–860, 1967. 75

[118] J. L. Herrin and J. C. Dutton, "An investigation of LDV velocity bias correction techniques for high-speed separated flows," *Experiments in fluids*, vol. 15, no. 4, pp. 354–363, 1993. 76

[119] M. Lee and R. D. Moser, "Direct numerical simulation of turbulent channel flow up to $Re_\tau \approx 5200$," *Journal of Fluid Mechanics*, vol. 774, p. 395–415, 2015. 78, 81

[120] L. Biferale and F. Toschi, "Joint statistics of acceleration and vorticity in fully developed turbulence," *Journal of Turbulence*, no. 6, p. N40, 2005. 83, 166

[121] W. Braun, F. D. Lillo, and B. Eckhardt, "Geometry of particle paths in turbulent flows," *Journal of Turbulence*, vol. 7, p. N62, 2006. 84

[122] Y. Choi, Y. Park, and C. Lee, "Helicity and geometric nature of particle trajectories in homogeneous isotropic turbulence," *International Journal of Heat and Fluid Flow*, vol. 31, no. 3, pp. 482–487, 2010. 84

[123] A. Scagliarini, "Geometric properties of particle trajectories in turbulent flows," *Journal of Turbulence*, no. 12, p. N25, 2011. 84

[124] H. Xu, N. T. Ouellette, and E. Bodenschatz, "Curvature of lagrangian trajectories in turbulence," *Physical review letters*, vol. 98, no. 5, p. 050201, 2007. 84

[125] W. J. Bos, B. Kadoch, and K. Schneider, "Angular statistics of lagrangian trajectories in turbulence," *Physical review letters*, vol. 114, no. 21, p. 214502, 2015. 84

[126] E. Lévêque and A. Naso, "Introduction of longitudinal and transverse lagrangian velocity increments in homogeneous and isotropic turbulence," *EPL (Europhysics Letters)*, vol. 108, no. 5, p. 54004, 2014-12-01. 00007. 85, 89

[127] A. Pumir, H. Xu, G. Boffetta, G. Falkovich, and E. Bodenschatz, "Redistribution of kinetic energy in turbulent flows," *Physical Review X*, vol. 4, no. 4, p. 041006, 2014. 100

[128] H. Xu, A. Pumir, G. Falkovich, E. Bodenschatz, M. Shats, H. Xia, N. Francois, and G. Boffetta, "Flight-crash events in turbulence," *Proceedings of the National Academy of Sciences*, vol. 111, no. 21, pp. 7558–7563, 2014-05-27. 100

[129] J. Lumley, "The mathematical nature of the problem of relating lagrangian and eulerian statistical functions in turbulence," *Mécanique de la Turbulence*, no. 108, pp. 17–26, 1962. 103

[130] A. Bennett, *Lagrangian fluid dynamics*. Cambridge University Press, 2006. 107, 108

[131] P. Sagaut, *Large Eddy Simulation for Incompressible Flows: An Introduction*. Berlin, New York: Springer, 3rd ed ed., 2006. 119

[132] S. B. Pope, "Pdf methods for turbulent reactive flows," *Progress in Energy and Combustion Science*, vol. 11, no. 2, pp. 119–192, 1985. 119

[133] C. Beck, "Dynamical foundations of nonextensive statistical mechanics," *Physical Review Letters*, vol. 87, no. 18, 2001. 120

[134] A. M. Reynolds, "On the application of nonextensive statistics to lagrangian turbulence," *Physics of Fluids*, vol. 15, no. 1, 2003. 120

[135] L. Chen, S. W. Coleman, J. C. Vassilicos, and Z. Hu, "Acceleration in turbulent channel flow," *Journal of Turbulence*, vol. 11, p. N41, 2010. 120

[136] L. Del Castello and H. Clercx, "Lagrangian acceleration of passive tracers in statistically steady rotating turbulence," *Physical Review Letters*, vol. 107, 2011. 120

[137] M. Buffat, L. Le Penven, and A. Cadiou, "An efficient spectral method based on an orthogonal decomposition of the velocity for transition analysis in wall bounded flow," *Computers & Fluids*, vol. 42, no. 1, pp. 62–72, 2011. 122

[138] S. A. Orszag, "On the elimination of aliasing in finite-difference schemes by filtering high-wavenumber components," *Journal of the Atmospheric sciences*, vol. 28, no. 6, pp. 1074–1074, 1971. 123

[139] M. A. T. van Hinsberg, J. H. M. t. T. Boonkkamp, F. Toschi, and H. J. H. Clercx, "Optimal interpolation schemes for particle tracking in turbulence," *Physical Review E*, vol. 87, p. 043307, Apr. 2013. 123

[140] Z. Hu, C. L. Morfey, and N. D. Sandham, "Wall pressure and shear stress spectra from direct simulations of channel flow," *AIAA journal*, vol. 44, no. 7, pp. 1541–1549, 2006. 123

[141] L. H. Benedict and R. D. Gould, "Towards better uncertainty estimates for turbulence statistics," *Experiments in Fluids*, vol. 22, no. 2, pp. 129–136, 1996. 124

[142] Moffat, Robert J., "Describing the uncertainties in experimental results," *Experimental Thermal and Fluid Science*, vol. 1, no. 1, pp. 3–17, 1988. 124

[143] A. Pumir and B. I. Shraiman, "Persistent Small Scale Anisotropy in Homogeneous Shear Flows," *Phys. Rev. Lett.*, vol. 75, pp. 3114–3117, Oct. 1995. 128

[144] A. N. Kolmogorov, "The local structure of turbulence in incompressible viscous fluid for very large reynolds numbers," in *Dokl. Akad. Nauk SSSR*, vol. 30, pp. 299–303, 1941. 128

[145] M. R. Maxey and J. J. Riley, "Equation of motion for a small rigid sphere in a nonuniform flow," *The Physics of Fluids*, vol. 26, no. 4, pp. 883–889, 1983. 138

[146] R. Gatignol, "The faxén formulas for a rigid particle in an unsteady non-uniform stokes-flow," *Journal de Mécanique théorique et appliquée*, vol. 2, no. 2, pp. 143–160, 1983. 138

[147] E. Balkovsky, G. Falkovich, and A. Fouxon, "Intermittent distribution of inertial particles in turbulent flows," *Physical Review Letters*, vol. 86, no. 13, p. 2790, 2001. 138

[148] E. Loth and A. Dorgan, "An equation of motion for particles of finite reynolds number and size," *Environmental fluid mechanics*, vol. 9, no. 2, pp. 187–206, 2009. 138, 139, 155

[149] M. Maxey, "The gravitational settling of aerosol particles in homogeneous turbulence and random flow fields," *Journal of Fluid Mechanics*, vol. 174, pp. 441–465, 1987. 139, 156, 161

[150] A. Aliseda, A. Cartellier, F. Hainaux, and J. C. Lasheras, "Effect of preferential concentration on the settling velocity of heavy particles in homogeneous isotropic turbulence," *Journal of Fluid Mechanics*, vol. 468, pp. 77–105, 2002. 139

[151] E. Calzavarini, R. Volk, M. Bourgoin, E. Lévêque, J.-F. Pinton, and F. Toschi, "Acceleration statistics of finite-sized particles in turbulent flow: the role of faxén forces," *Journal of Fluid Mechanics*, vol. 630, pp. 179–189, 2009. 139, 158, 167

[152] V. Lavezzo, A. Soldati, S. Gerashchenko, Z. Warhaft, and L. Collins, "On the role of gravity and shear on inertial particle accelerations in near-wall turbulence," *Journal of Fluid Mechanics*, vol. 658, pp. 229–246, 2010. 140, 143, 157

[153] R. Volk, E. Calzavarini, G. Verhille, D. Lohse, N. Mordant, J.-F. Pinton, and F. Toschi, "Acceleration of heavy and light particles in turbulence: comparison between experiments and direct numerical simulations," *Physica D: Nonlinear Phenomena*, vol. 237, no. 14, pp. 2084–2089, 2008. 140, 141, 144, 156

[154] H. Xu and E. Bodenschatz, "Motion of inertial particles with size larger than kolmogorov scale in turbulent flows," *Physica D: Nonlinear Phenomena*, vol. 237, no. 14, pp. 2095–2100, 2008. 140, 141

[155] N. M. Qureshi, U. Arrieta, C. Baudet, A. Cartellier, Y. Gagne, and M. Bourgoin, "Acceleration statistics of inertial particles in turbulent flow," *The European Physical Journal B-Condensed Matter and Complex Systems*, vol. 66, no. 4, pp. 531–536, 2008. 140

[156] M. Uhlmann, "Interface-resolved direct numerical simulation of vertical particulate channel flow in the turbulent regime," *Physics of Fluids*, vol. 20, no. 5, p. 053305, 2008. 140

[157] M. García-Villalba, A. G. Kidanemariam, and M. Uhlmann, "Dns of vertical plane channel flow with finite-size particles: Voronoi analysis, acceleration statistics and particle-conditioned averaging," *International Journal of Multiphase Flow*, vol. 46, pp. 54 – 74, 2012. 140

[158] S. Elghobashi, "Particle-laden turbulent flows: direct simulation and closure models," *Applied Scientific Research*, vol. 48, no. 3, pp. 301–314, 1991. 145

[159] A. Melling, "Tracer particles and seeding for particle image velocimetry," *Measurement Science and Technology*, vol. 8, no. 12, p. 1406, 1997. 145

[160] L. Zeng, S. Balachandar, P. Fischer, and F. Najjar, "Interactions of a stationary finite-sized particle with wall turbulence," *Journal of Fluid Mechanics*, vol. 594, pp. 271–305, 2008. 145

[161] L. Fiabane, R. Zimmermann, R. Volk, J.-F. Pinton, and M. Bourgoin, "Clustering of finite-size particles in turbulence," *Phys. Rev. E*, vol. 86, p. 035301, Sep 2012. 154, 155, 156, 167

[162] S. Goto and J. Vassilicos, "Sweep-stick mechanism of heavy particle clustering in fluid turbulence," *Physical review letters*, vol. 100, no. 5, p. 054503, 2008. 156

[163] S. Coleman and J. Vassilicos, "A unified sweep-stick mechanism to explain particle clustering in two-and three-dimensional homogeneous, isotropic turbulence," *Physics of Fluids*, vol. 21, no. 11, p. 113301, 2009. 156

[164] G. Sardina, P. Schlatter, L. Brandt, F. Picano, and C. M. Casciola, "Wall accumulation and spatial localization in particle-laden wall flows," *Journal of Fluid Mechanics*, vol. 699, pp. 50–78, 2012. 156

[165] A. Innocenti, C. Marchioli, and S. Chibbaro, "Lagrangian filtered density function for LES-based stochastic modelling of turbulent dispersed flows," *arXiv preprint arXiv:1607.01709*, 2016. 166

[166] S. Chibbaro and J.-P. Minier, "Langevin PDF simulation of particle deposition in a turbulent pipe flow," *Journal of Aerosol Science*, vol. 39, no. 7, pp. 555–571, 2008-07. 166

[167] M. Elhimer, O. Praud, M. Marchal, S. Cazin, and R. Bazile, "Simultaneous piv/ptv velocimetry technique in a turbulent particle-laden flow," *Journal of Visualization*, vol. 20, no. 2, pp. 289–304, 2017. 167